UNIVERSITY OF CALIFORNIA

Santa Barbara

Optical Materials with a Genome: Nanophotonics with DNA-Stabilized Silver Clusters

A dissertation submitted in partial satisfaction of the

requirements for the degree Doctor of Philosophy

in Physics

by

Stacy M. Copp

Committee in charge:

Professor Elisabeth Gwinn, Chair

Professor Dirk Bouwmeester

Professor Joan-Emma Shea

December 2016

The dissertation of Stacy M. Copp is approved.

_____

Dirk Bouwmeester

_____

Joan-Emma Shea

_____

Elisabeth Gwinn, Committee Chair

November 2016

Optical Materials with a Genome: Nanophotonics with DNA-Stabilized Silver Clusters

by

Stacy M Copp

For David and Lydia

Acknowledgements

This thesis represents the culmination of many years of hard work, and certainly not only my own. I am indebted to a great many talented and selfless people who helped me become the scientist I am today. First, to my PhD advisor, Beth Gwinn: thank you for five years of guidance, patience, and mentorship. Thank you for giving me the freedom to explore the questions that interest me most, for supporting my development as both a researcher and a mentor, and for being patient with my particular opinions about commas. You have taught me that it is possible to be both an excellent physicist and a truly decent person.

To my labmates: Dani and Steven, thank you for being wonderful collaborators, for purifying many Ag_N-DNA for me, for putting up with my constant eating, and for making long days in the lab truly fun. Thanks to Sidsel for helping me transition back to work after maternity leave – it was great to have you here, if only for a short time. To Kira, Mark, Alex, Alexis, Jackie, and Hunter, thank you for all your help, creativity, and excitement about your research. I was privileged to work with such talented, hardworking undergraduates.

To my undergraduate mentors: To Koen Visscher, thank you for giving a freshman the chance to join your lab– having now mentored undergraduates myself, I much more fully appreciate your patience! My first research opportunity has made a world of difference for me. To Ben and Katie, thanks for teaching me how to be an experimentalist. Thanks to Ben for encouraging me to apply for fellowships and not sell myself short; you gave me the confidence to believe in myself. To my summer mentors at the national labs: Patrick McDaniel, Mike Kent, and especially Gabe Montaño, thank you for incredible experiences. To Jerry Moloney and Pavel Polynkin, thanks for a productive, exciting year.

To those outside of my research group: Thanks to Dirk Bouwmeester and Joan Shea for serving on my thesis committee. Thanks to Nemanja and Sumant for many transatlantic Skype calls. To Petko, Sruthi, and Alexander, thanks for an exciting collaboration that turned our unconventional idea into a reality. To Preeti, Claire, Kenny, Brian, Jenna, Trey, Matt, Eric, and John, thanks for being wonderful officemates. Thanks to Dan Morse, Mike Gordon, and the rest in the bioinspired photonics group for many fascinating discussions. Thanks to Mark Sherwin and Megan Valentine for research opportunities in your groups.

I owe thanks to a great many wonderful administrative and technical staff. Thanks to Jennifer Farrar for being the best graduate advisor in history; to Mike Deal for keeping Broida Hall intact, for helping us move our lab, and for finding me a fume-free place to work while I was pregnant; to Dave for being a continuous source of laughs and good cheer; to the great people at CNSI, Lynne, Marissa, Daniel, and Sonya, for making sure we get our packages and get paid; to Mary for running the NRI microscopy facility flawlessly; to Nelly for your help in the BNL; to Monte for patient help with Rosy the pipetting robot.

Thanks to my wonderful friends in Santa Barbara who have made graduate school fun and have made my heart full: to my classmates who suffered through first year classes in the trailer; to Kimberly, Netta, Claire, Jen, Anna, and the rest of Women in Physics for many lunches and discussions; to San Clemente Voices for musical divertions from research; to my church family for reminding me of what matters most; to the frisbee crew; and to our wonderful neighbors.

Most of all, I am grateful for my family. To Mom and Dad, thank you for your love and support in all my endeavors and for encouraging me to explore and to ask questions. I am a scientist today because of you! To my brother, David, thanks for being my childhood partner-in-crime and now my dear friend. To my grandparents, thank you for encouraging me to pursue

an education and for reminding me to have fun once in a while. To my daughter, Lydia, whose joy and curiosity inspire me every day. And to my best friend and husband, David, thank you for being my companion through our graduate school adventure and now through the much greater adventure of parenthood. I am so proud of what you have accomplished, and I could not have done this without you. This thesis is for you and Lydia.

Curriculum Vitae

Stacy M. Copp
November 2016

EDUCATION

2016	Ph.D. Physics, University of California, Santa Barbara
2013	M.A. Physics, University of California, Santa Barbara
2011	B.S. Physics and Mathematics, University of Arizona, *summa cum laude*

PROFESSIONAL EXPERIENCE

2017-2019	Los Alamos National Laboratory Director's Postdoctoral Fellow
2011-2016	Graduate Student Researcher, Department of Physics, University of California, Santa Barbara
Fall 2014	Teaching Assistant, University of California, Santa Barbara
Summer 2011	Post Baccalaureate Researcher, Los Alamos National Laboratory
2010-2011	Undergraduate Researcher, College of Optical Sciences, University of Arizona
Summer 2010	Undergraduate Researcher, Los Alamos National Laboratory
Summer 2009	Undergraduate Researcher, Sandia National Laboratories
Summer 2008	Undergraduate Researcher, Sandia National Laboratories
2008-2010	Undergraduate Researcher, Department of Physics, University of Arizona

SELECTED HONORS

2015	Materials Research Society Graduate Student Silver Award
2015	Best Student Talk in MRS Meeting Symposium E: Engineering and Application of Bioinspired Materials
2015	Materials Research Society Arthur Nowick Graduate Student Award
2015	Selected participant in the 65th Lindau Nobel Laureate Meeting
2015	Fiona Goodchild Award for excellence as a mentor of undergraduate research
2015	Chair's Outstanding Service Award, UCSB Physics Dept.
2013	Chair's Appreciation Award, UCSB Physics Dept.
2011-2016	NSF Graduate Research Fellowship
2011-2016	UCSB Chancellor's Fellowship
2011-2012	Yzurdiaga Graduate Student Fellowship
2010	Goldwater Scholar

PUBLICATIONS

1. Stacy M. Copp, D. Schultz, A. Faris, S. Swasey, and E. Gwinn. Cluster plasmonics: Dielectric and shape effects on DNA-stabilized silver clusters. *Nano Lett.*, **16**, 3594-3599 (2016).
2. Stacy M. Copp, A. Faris, S. Swasey, and E. Gwinn. Heterogeneous Solvatochromism of Fluorescent DNA-Stabilized Silver Clusters Precludes Use of Simple Onsager-Based Stokes Shift Models. *J. Phys. Chem. Lett.*, **7**, 698-703 (2016).
3. E. Gwinn, D. Schultz, Stacy M. Copp, and S. Swasey. DNA-Protected Silver Clusters for Nanophotonics. *Nanotechnology*, **5**, 180-207 (2015).
4. Stacy M. Copp, D. Schultz, S. Swasey, and E. Gwinn. Atomically Precise Arrays of Fluorescent Silver Clusters: a Modular Approach for Photonics on DNA Nanostructures. *ACS Nano*, **9**, 2303-2310 (2015).
5. Stacy M. Copp, P. Bogdanov, M. Debord, A. Singh, and E. Gwinn. Base Motif Recognition and Design of DNA Templates for Fluorescent Silver Clusters by Machine Learning. *Adv. Mater.* **26**, 5839-5845 (2014).
6. Stacy M. Copp, D. Schultz, S. M. Swasey, J. Pavlovich, M. Debord, A. Chiu, K. Olsson, and E. Gwinn. Magic Numbers in DNA-Stabilized Fluorescent Silver Clusters Lead to Magic Colors. *J. Phys. Chem. Lett.* **5**, 959-963 (2014).
7. D. Schultz, Stacy M. Copp, N. Markesevic, K. Gardner, S.S.R. Oemrawsingh, D. Bouwmeester, and E. Gwinn. Dual-Color Nanoscale Assemblies of Structurally Stable, Few-Atom Silver Clusters, as Reported by Fluorescence Resonance Energy Transfer. *ACS Nano* **7**, 9798-9807 (2013).
8. Stacy Shiffler, P. Polynkin, and J. Moloney. Self-focusing of femtosecond diffraction-resistant vortex beams in water. *Opt. Lett.* **36**, 3834-3836 (2011).

Abstract

Optical Materials with a Genome: Nanophotonics with DNA-Stabilized Silver Clusters

by

Stacy M. Copp

Fluorescent silver clusters with unique rod-like geometries are stabilized by DNA. The sizes and colors of these clusters, or Ag_N-DNA, are selected by DNA base sequence, which can tune peak emission from blue-green into the near-infrared. Combined with DNA nanostructures, Ag_N-DNA promise exciting applications in nanophotonics and sensing. Until recently, however, a lack of understanding of the mechanisms controlling Ag_N-DNA fluorescence has challenged such applications. This dissertation discusses progress toward understanding the role of DNA as a "genome" for silver clusters and toward using DNA to achieve atomic-scale precision of silver cluster size and nanometer-scale precision of silver cluster position on a DNA breadboard. We also investigate sensitivity of Ag_N-DNA to local solvent environment, with an eye towards applications in chemical and biochemical sensing.

Using robotic techniques to generate large data sets, we show that fluorescent silver clusters are templated by certain DNA base motifs that select "magic-sized" cluster cores of enhanced stabilities. The linear arrangement of bases on the phosphate backbone imposes a unique rod-like geometry on the clusters. Harnessing machine learning and bioinformatics techniques, we also demonstrate that sequences of DNA templates can be selected to stabilize silver clusters with desired optical properties, including high fluorescence intensity and specific fluorescence wavelengths, with much higher rates of success as compared to current strategies.

The discovered base motifs can be also used to design modular DNA host strands that enable individual silver clusters with atomically precise sizes to bind at specific programmed locations on a DNA nanostructure. We show that DNA-mediated nanoscale arrangement enables near-field coupling of distinct clusters, demonstrated by dual-color cluster assemblies exhibiting resonant energy transfer. These results demonstrate a new degree of control over the optical properties and relative positions of nanoparticles, selected almost solely by the sequence of DNA.

Ag_N-DNA are promising chemical and biochemical sensors due to the sensitivity of their fluorescence to local environment. However, the mechanisms behind many sensing schemes are not understood, and the nature of the excited state of the silver cluster itself remains unknown. To probe the fluorescence mechanisms of Ag_N-DNA, we investigate the behavior of purified solutions of these clusters in various solvents. We find that standard models for fluorophore solvatochromism, including the Lippert-Mataga model, do not describe Ag_N-DNA fluorescence because such models neglect specific interactions between the cluster and surrounding solvent molecules. Fluorescence colors are well-modeled by Mie-Gans theory,

suggesting that the local dielectric environment of the cluster does play a role in fluorescence, although additional specific solvent interactions and cluster shape changes may also determine fluorescence color and intensity. These results suggest that Ag_N-DNA may be sensitive to changes in local dielectric environment on nanometer length scales and may also act as sensors for small molecules with affinity for DNA.

Table of contents

List of Figures

List of Tables

1. Introduction

The universe is full of magical things patiently waiting for our wits to grow sharper.[1]

- Eden Phillpotts

As humans develop better ways to "look" at smaller and smaller things, we discover unexplored worlds, even in the most mundane of places. It was the development of new technologies, perhaps most notably scanning probe microscopy,[2,3] that allowed scientists to spatially map structures with dimensions much smaller than the wavelength of light. Suddenly, a whole new world was opened. Coupled with other advances in synthesis and characterization, these technologies fueled the formation of the field of nanoscience. With this discovery came many unanswered questions about how the properties of well-understood "ordinary" materials translate to particles having sizes on length scales of 10^{-9} m. It became clear, for example, that nanoscaled materials exhibit unexpected behavior due to quantum mechanical effects and that living cells were full of fascinating nanostructured "machines" previously hiding in plain sight.[4] Now a vast and interdisciplinary field, nanoscience seeks to create and understand nanoscaled materials of many types, combining elements of physics, chemistry, and biology. This dissertation focuses on a particular type of nanomaterial, DNA-stabilized silver clusters, thus requiring a knowledge of both metal cluster science and DNA nanotechnology. We provide a brief overview of these two fields to orient the reader.

1.1 Metal Clusters

Metal clusters are particles containing at least 2 metal atoms joined by metal-metal bonds. While the value that is considered to be the upper limit of "small" varies,[5] most studies concern clusters containing between N = 2 and N ~ 10^4 atoms. The study of metal clusters arose due to interest in the intermediate regime between atoms and bulk metals. For example, how do properties including conductivity and magnetism evolve as one moves from the discrete energy states of a single atom to the quasi-continuous density of states in the bulk?[6] To answer such questions, researchers developed sophisticated methods to produce gas-phase metal clusters in high vacuum environments and then characterize the distribution of cluster sizes by mass spectrometry.[7] Contrary to expectations that every cluster would have a unique, molecular electronic structure dependent on composition and geometry, even clusters of just a few metal atoms displayed evidence for electronic shell structure characteristic of delocalized valence electrons in a spherical potential well,[8] a trend that trandscends metal type.[7] Analogous to the nuclear and electronic shells of single atoms, the shell structure of metal clusters leads to the existence of certain "magic" clusters with enhanced stabilites whose sizes correspond to closed electronic shells.[5] Magic clusters are observed to have enhanced abundances due to their higher stabilities as compared to clusters without filled shells. By observing the abundance spectra for clusters of various metals, it became apparent that the magic numbers corresponding to shell filling for gas-phase metal clusters are the same as for nuclear shell filling (2, 8, 20, …) as opposed to electronic shell filling (2, 10, 18, …), due to the similarity in the nuclear and cluster potentials.[7] The successful description of cluster shell structure is detailed in several reviews from experimental[7] and theoretical[9] perspectives.

The initial motivation for cluster science was not purely fundamental; many researchers also noted the promise of metal clusters for exciting applications in electronics, photonics, and catalysis.[5,10] However, for several decades the study of metal clusters was largely confined to gas phase and surface-supported clusters formed and studied in ultra-high vacuum, due to the propensity of naked metal clusters to aggregate into larger metal particles or to oxidize. This made it nearly impossible to form stable metal clusters outside of the vacuum, prohibiting the realization of envisioned technologies. This barrier was finally broken by the use of small molecule ligands to protect metal clusters from aggregation, a breakthrough that has revolutionized cluster science by allowing clusters to leave the vacuum and "enter the real world." The rapidly growing field of ligand-stabilized metal cluster science focuses on both the fundamental properties of these composite structures and technological applications, about which gas-phase cluster scientists had only speculated.[11]

Metal clusters are now employed in myriad applications that capitalize on the special properties arising from their reduced sizes.[12–14] Due to the large fraction of atoms that lie on the surface of a cluster, metal clusters can be used as efficient catalysts,[15] with many examples provided in a recent review.[14] Because monodisperse populations of some types of ligand-stabilized metal clusters can be produced, these materials are also being used as contrast agents of small defined size for biological structure determination by transmission electron microscopy.[16] Clusters whose dimensions are on the order of or less than the Fermi wavelength can exhibit fluorescence, due to the reduction in nonradiative decay paths in these ultrasmall clusters. This fluorescence has enabled a huge number of applications, including fluorometric detection of metal ions and biomolecules, biological imaging, as reviewed by several groups.[12–

[14] While photonic applications of metal clusters still remain limited, thiolate-stabilized gold clusters were recently used in light-emitting diodes (LEDs).[17]

Gold clusters are by far the most studied species of condensed phase cluster, in part due to its inert chemical nature in the bulk. In particular, thiolate-stabilized gold clusters have become a model system for ligand-stabilized metal clusters. Since the first structure was solved crystallographically in 2007,[18] numerous structures for thiolate-stabilized gold clusters have now been determined with molecular precision, allowing a detailed understanding of their structural, optical, and chemical properties.[19] Of particular interest was the discovery that gold clusters with enhanced thermodynamic stabilities display the magic number behavior previously found for gas phase clusters.[20] For these and other ligand-stabilized clusters, the so-called "superatom model" proposed by Häkkinen and others[20,21] shows that it is not the total number of metal atoms within a cluster that displays magic number behavior; this is because the ligands protecting the cluster withdraw electrons from the metal atoms to which they are bonded. Rather, it is the remaining number of free electrons within the cluster core that is magic. Thus, when a cluster contains n^* free electrons, where n^* corresponds to electronic shell filling, the resulting cluster is a magic "superatom:"

$$n^* = Nv_A - L - Z \qquad (1.1)$$

where N is the number of metal atoms in the cluster, v_A is the valency of the metal, L is the number of electron-withdrawing ligands surrounding the cluster (assuming one electron is withdrawn per ligand), and Z is the cluster charge.[20,21] Eq. 1.1 rationalizes the composition of many ligand-stabilized metal clusters that have been observed to have enhanced stabilities. It is clear that magic number behavior in metal clusters is not just a curiosity arising from quantum mechanics applied to few-electron systems; rather, it is a key property on which all

of metal cluster technology may hinge. The existence of ultrastable ligand-stabilized metal clusters has enabled a wide range of exciting applications,[22] with countless more doubtless to arise in coming years.

1.2 DNA Nanotechnology

Biology has engineered a remarkably elegant mechanism for storing information. DNA, a vital ingredient of life's rich complexity, stores the entire genetic code of an organism in a linear sequence of just the four natural nucleic acids, adenine (A), cytosine (C), guanine (G), and thymine (T), which are arranged in sequential order on a phosphate backbone. Two strands of DNA with complementary sequences can bind together by Watson-Crick base pairing of A to T and C to G, forming the now-famous DNA double helix. It is this base pairing that preserves the fidelity of an organism's genome by protecting the bases from chemical alteration.[23] In the early 1980's, crystallographer Nadrian Seeman proposed a revolutionary idea: that the information stored in a DNA base sequence and DNA's propensity for complementary base pairing could be harnessed to predictably form two- and three-dimentional structures.[24] Although it took several decades for the first DNA nanostructures to be realized,[25] this idea gave birth to the vibrant field of structural DNA nanotechnology.

It is now possible to predictively design a huge range of custom two-dimensional and three-dimensional nanostructures that self-assemble from strands of DNA. Notable examples include the first 2D DNA lattices,[25] DNA tubes of prescribed diameters,[26] and the well-developed design and assembly methods for finite 2D and 3D structures: DNA origami, where a long piece of single-stranded viral DNA is "stapled" together by DNA oligonucleotides (short pieces of single-stranded DNA),[27–29] and DNA bricks, which utilize only oligonucleotides for

construction.[30] DNA crystals with ~100 μm sizes have even been created,[31] and, more recently, dynamics have also been programmed into DNA nanostructures.[32,33] These and many other examples illustrate the versatility of DNA as a building material for self-assembling nanoscale structures.

Nanostructures of DNA are not simply curiosities; these nanostructures can act as "breadboards" to arrange nanoparticles and molecules with nanoscale precision,[34,35] even allowing resolutions on the scale of the Bohr radius.[36] This control over the relative positions and orientations of light-active nanoparticles has enabled creation of self-assembling hybrid DNA-metal nanomaterials exhibiting special optical properties, including fluorescence resonance energy transfer (FRET),[37] chiral plasmonic response,[38,39] and surface-enhanced Raman spectroscopy (SERS),[40] rivaling what is achievable by even the most sophisticated and labor-intensive lithographic techniques. (We note that, in addition to its use as a molecular breadboard, DNA has also been harnessed for self-assembly of many colloidal particles and nanoparticles by coating these particles in DNA with selectively engineered sequences for controlled particle binding.[41,42] We do not discuss these further here.) These and other exciting features of structural DNA nanotechnology may find important applications in biomedicine, sensing, and nanophotonics.[43]

1.3 DNA-stabilized silver clusters

In 2004, Petty and coauthors merged the fields of metal cluster science and DNA nanotechnology. Inspired by the well-known affinity of silver cations (Ag^+) for the bases of DNA,[44] and motivated by the bright fluorescence of few-atom silver clusters stabilized in other ways,[45,46] they discovered that a particular DNA oligonucleotide could stabilize clusters of

silver atoms exhibiting bright fluorescence.[47] Later work then established that the fluorescence of these "Ag_N-DNA" depends on the sequence and secondary structure of the DNA template used to stabilize the cluster,[48] producing emission wavelengths spanning the visible to near-infrared (IR).[49] Fluorescence can be excited at a peak wavelength 50 – 100 nm shorter than the emission wavelength and universally in the UV through the DNA bases.[50] Ag_N-DNA are synthesized by simple reduction of an aqueous solution of Ag^+ and DNA template strands using sodium borohydride,[49] with Ag^+ typically supplied by addition of $AgNO_3$. Because silver clusters form by reduction of base-bound Ag^+, double-stranded DNA can prohibit formation of fluorescent cluster solutions.[48]

Due to the wide range of silver-bearing DNA products of varying compositions produced during synthesis, initial studies of as-synthesized Ag_N-DNA solutions misidentified the composition of the fluorescent species, significantly underestimating the content of the emissive cluster to be only a few silver atoms.[47,48,51] To isolate and accurately determine the sizes of fluorescent Ag_N-DNA, Schultz and Gwinn developed a method combining high performance liquid chromatography with in-line mass spectrometry (HPLC-MS) and tandem UV-Vis spectroscopy.[52] This method enables correlation of the composition and optical properties of various Ag_N-DNA that are sufficiently robust to survive the purification process. Schultz and Gwinn found that, contrary to previous reports, all fluorescent Ag_N-DNA contained between 10 and 24 Ag atoms, approximately half of which were cationic, with fluorescence color correlating to cluster size.[52,53] (Smaller and/or larger clusters may also exist but were not detected for the studied host strands.) Many nonfluorescent Ag-DNA products were also detected.[52] The complex product mixture necessitates purification for applications

that require monodisperse Ag_N-DNA, including those discussed in Chapter 4 and Chapter 5 of this dissertation.

These studies of purified Ag_N-DNA also provided insights into their structure.[53,54] If Ag_N-DNA had globular cluster geometries, as do nearly all stable gas-phase and condensed-phase metal clusters, then for clusters in their size range of 10 – 24 silver atoms, it would be expected that Ag_N-DNA absorbance spectra would have multiple transitions at blue to UV wavelengths. Instead, the absorbance spectra of pure Ag_N-DNA have single dominant peaks in the visible to near-infrared whose wavelengths scale strongly with cluster size, with an additional peak in the UV corresponding to the absorbance of the DNA template.[53] Such distinctive absorbance features in the visible to IR that increase in wavelength with cluster size are predicted for clusters with rod-like shapes.[55,56] Additional evidence for a rod-like cluster geometry is provided by cryogenic microscopy of single pure Ag_N-DNA, which display strong polarization dependence.[53,57] Later studies of the magic numbers of Ag_N-DNA,[58] discussed in Chapter 2, and their chiroptical properties[59] also point to elongated cluster geometries. Such a rod-like geometry is unique among metal clusters and rationalizes the impressive tunability of Ag_N-DNA emission wavelengths by changes of just a few atoms in size.[53]

While the detailed structure of Ag_N-DNA is still not established, their bright, sequence-tunable fluorescence has already enabled many applications.[60] Early studies suggested the utility of Ag_N-DNA as new fluorophores for biological imaging,[61] demonstrated their two-photon properties,[62] and proposed that Ag_N-DNA could replace larger semiconductor quantum dots.[63] Publications demonstrating such nanophotonic applications have since been limited, in part due to infrequent use of purification to produce monodisperse products. However, Ag_N-DNA have been successfully used for a huge range of chemical and biochemical sensing

schemes, including single-nucleotide mutation detection,[64–66] metal ion sensing,[64,67] and microRNA identification.[68,69] Nearly all of these applications utilize impure, as-synthesized Ag_N-DNA solutions, and, despite numerous publications reporting these schemes, the mechanisms enabling readout of analyte detection by fluorescence color or intensity changes are still not well understood. This lack of understanding of the mechanisms underlying many properties of Ag_N-DNA limits the development and scope of applications.

This dissertation seeks to further our understanding of the properties of Ag_N-DNA, motivated by a fundamental interest in cluster science and with an eye towards applications. For most studies, we employ pure solutions of Ag_N-DNA obtained by the HPLC methods developed previously.[52] Due to the extremely time-consuming nature of HPLC-MS characterization, it is impossible to examine large numbers of Ag_N-DNA species with this method; therefore, Chapter 2 and Chapter 3 employ large-scale studies of hundreds of Ag_N-DNA templates with random sequences for generality. The topics discussed in each chapter of this dissertation are detailed in the following paragraphs.

Chapter 2 presents the first large-scale studies probing the origins of Ag_N-DNA fluorescence color.[58] We employ a set of 684 randomly chosen 10-base DNA template sequences to determine what selects Ag_N-DNA emission wavelengths and whether certain fluorescence wavelengths are more abundant than others. Rather than a flat distribution, we find that specific color bands dominate. Cluster size data indicate that these "magic colors" originate from the existence of magic numbers for DNA-stabilized silver clusters, which differ from those of spheroidal gold clusters stabilized by small-molecule ligands. Elongated cluster structures, enforced by multiple base ligands along the DNA, can account for both magic

number sizes and color variation around peak wavelength populations. This study provides further evidence for the previously proposed rod-like structure of Ag_N-DNA.[53]

The sensitivity of Ag_N-DNA fluorescence to the host DNA template sequence[48] is one of the most exciting properties of Ag_N-DNA, yet how certain base sequences select for bright emission of various colors remains unknown. To overcome this hurdle and design DNA templates for brightly fluorescent Ag_N-DNA of specific colors, Chapter 3 combines the large data set produced in Chapter 2 with machine learning tools for pattern recognition.[70] We discover certain "discriminative" base motifs within the DNA templates that are predictive of whether a DNA template will stabilize brightly fluorescent silver clusters. Combining these multibase motifs with a generative algorithm, the probability of selecting DNA templates that stabilize fluorescent Ag_N-DNA is increased by more than 300%. This is a significant improvement to previous "informed guessing" design strategies. The discoveries in Chapter 3 are used to design new DNA template strands in following chapters.

Despite the promise of combining Ag_N-DNA and structural DNA nanotechnology to realize nanoscale cluster arrays,[48] it is unknown if such few-atom metal clusters can actually be assembled with nanoscale separations on a DNA breadboard. In fact, successful sensing schemes use the sensitivity of certain Ag_N-DNA to changes in local DNA environment to sense single nucleotide polymorphisms.[65,66] These results question whether Ag_N-DNA of different sizes can remain stable when in nanoscale proximity, a step that necessarily changes their local DNA environment. In Chapter 4, we answer this question by forming bicolor, dual cluster assemblies using purified Ag_N-DNA with spectral properties that would enable Fluorescence Resonance Energy Transfer (FRET) if each silver cluster of different size retained its structural integrity.[71] We design DNA clamp assemblies that incorporate a N = 10 atom Ag cluster and

a N = 15 or N = 16 atom Ag cluster. Thermally modulated FRET verifies assembly formation and stability. Comparison to Förster theory indicates that DNA clamps hold Ag_N-DNA within ~ 5 – 6 nm separations, in the range of the finest resolutions achievable on DNA scaffolds. The absence of spectral shifts in dual-cluster FRET pairs, relative to the individual Ag_N-DNA, shows that select few-atom silver clusters of different sizes are sufficiently stable to retain structural integrity within a single nanoscale DNA construct. The spectral stability of the cluster persists in a FRET pair with an organic dye molecule.

Building on the results of Chapter 4, Chapter 5 extends the ability to form multi-cluster constructs for atomically precise arrays of silver clusters with nanoscale separations on DNA.[72] Prior work has shown that methods relying on *in situ* synthesis of Ag_N-DNA onto a DNA breadboard[73] cannot achieve the labeling precision necessary for custom cluster arrays due to the range of fluorescent and dark products produced during Ag_N-DNA synthesis.[52] For this reason, we develop a modular design and assembly method for Ag_N-DNA-decorated DNA nanotubes, a prototypical DNA nanostructure. Using the information learned about sequence control of Ag_N-DNA fluorescence from Chapters 2 and 3, we design bifunctional Ag_N-DNA host strands that combine the cluster template sequence with an appended linker sequence, enabling isolation of specific clusters by HPLC prior to assembly on nanotubes. Through hybridization with complementary docker strands appended to DNA nanotubes, we show that both Ag_{15} and Ag_{14} can assemble onto DNA nanotubes with high attachment yields, as evidenced by comparision with dye-labeled nanotubes. The modularity of this approach generalizes to Ag_N-DNA of diverse sizes and DNA scaffolds of many types.

Chapters 6 and 7 address the challenge of developing a common model for Ag_N-DNA. Although correlations between cluster geometry and fluorescence color have begun to shed

light on how the optical properties of Ag_N-DNA are selected, the exact mechanisms responsible for fluorescence in these materials remain unknown, in part due to their diverse optical and chemical properties. To explore possible universal mechanisms in Ag_N-DNA, Chapter 6 describes the behavior of four distinct purified Ag_N-DNA in ethanol–water and methanol–water mixtures,[74] finding that the solvatochromism (the spectral shifts due to changes in solvent properties) of Ag_N-DNA varies widely among different cluster species and differs markedly from prior results on impure material.[75] Placing Ag_N-DNA within the context of standard Lippert–Mataga solvatochromism models based on the Onsager reaction field, we show that such nonspecific solvent models are not universally applicable to Ag_N-DNA. Instead, alcohol-induced solvatochromism of Ag_N-DNA may be governed by changes in hydration of the DNA template, with spectral shifts resulting from cluster shape changes and/or dielectric changes in the local vicinity of the cluster.

Chapter 7 investigates the effects of dielectric environment and cluster shape on electronic excitations of fluorescent Ag_N-DNA. We first establish that the longitudinal plasmon wavelengths predicted by classical Mie-Gans (MG) theory agree with previous quantum calculations for excitation wavelengths of linear silver atom chains, even for clusters of just a few atoms. Application of MG theory to Ag_N-DNA with $400 - 850$ nm cluster excitation wavelengths indicates that these clusters are characterized by a collective excitation process and suggests effective cluster thicknesses of $\sim$2 silver atoms and length to diameter aspect ratios of 1.5 to 5. To investigate Ag_N-DNA sensitivity to the surrounding medium, we measure the wavelength shifts produced by addition of glycerol, a high refractive index cosolvent. These shifts are smaller than reported for much larger gold nanoparticles but easily detectable

due to narrower line widths, suggesting that Ag_N-DNA may have potential for fluorescence-reported changes in dielectric environment at length scales of ~1 nm.

Chapter 8 concludes this dissertation by summarizing the results presented in this dissertation and placing them in the context of the broader field of nanoscience. Together, Chapters 2-7 show that DNA is a powerful tool for self-assembly across multiple length scales. DNA base sequence orders magic-sized silver clusters with rod-like clusters on lengths scales of ~0.1-1 nm. By careful engineering of multi-functional silver cluster template strands, DNA can also be used to bring silver clusters within ~5-10 nm and mediate inclusion of Ag_N-DNA onto DNA breadboards with length scales of 100-1000 nm. While many questions about Ag_N-DNA remain to be answered, new discoveries regarding the interactions between Ag^+ and DNA bases provide a clearer picture of the fundamental interactions between silver and DNA that underlie the formation of Ag_N-DNA.[76–78] As our understanding of these materials grows, and as our abilities to manipulate their placement on the nanoscale improve, many exciting nanophotonic applications may be realized.

2. Magic Numbers in DNA-Stabilized Fluorescent Silver Clusters Lead to Magic Colors

This chapter is adapted from Copp, S. M.; Schultz, D.; Swasey, S.; Pavlovich, J.; Debord, M.; Chiu, A.; Olsson, K.; Gwinn, E. Magic Numbers in DNA-Stabilized Fluorescent Silver Clusters Lead to Magic Colors. *J. Phys. Chem. Lett.* **2014**, *5* (6), 959–963.[58] *This open-access article can be found online at* *http://pubs.acs.org/doi/10.1021/jz500146q*.

2.1 Introduction

Ligand-stabilized metal nanoclusters are an exciting class of materials due to their remarkable chemical, electrical, and optical properties[79,80] and their promise for applications in catalysis,[80,81] nanoelectronics,[79] and biosensing.[80] By preventing aggregation, ligands enable cluster sizes that are not otherwise stable in solution,[81] allowing clusters to be formed and studied outside of the high vacuum environment that has dominated several decades of cluster research.[7] The physical, chemical, and optical properties of a ligand-stabilized metal cluster are intimately connected to the properties of the ligand itself, and ligand-metal bonds at the cluster surface can even dictate the so-called "magic numbers" of gold clusters that occur due to enhanced stability of certain clusters with select numbers of metal atoms, reflecting electronic shell closings.[18,20]

Most ligand-stabilized noble metal nanoclusters have quasi-spherical geometries. However, a new class of DNA-stabilized silver clusters[47] (Ag_N-DNA) displays evidence for rod-like shapes,[53] an exciting feature due to the possibility of new functionalities based on shape-tuned color and anisotropic polarization response. The challenge of isolating these small

fluorescent clusters, which are surrounded by bulky DNA ligands, was recently overcome.[52,82] This has enabled identification of total silver content and DNA content; thus far, all identified Ag_N-DNA have sizes in the range of N = 10-24 Ag atoms, with 1-2 DNA oligomers associated with each cluster.[52] The optical properties reported for Ag_N-DNA vary widely, depending on DNA strand specifics.[52] Some are brightly fluorescent, with emission wavelengths spanning the visible and near-IR,[50] bandwidths of ~40 – 90 nm that are narrow compared to larger plasmonic particles,[83] and quantum yields exceeding 90%.[53] High photostabilities have also been reported for an Ag_N-DNA embedded in polymer film[63] (this property may not be universal for all Ag_N-DNA or for Ag_N-DNA free in solution). Due to these unique fluorescence properties, Ag_N-DNA are now employed in a number of fascinating sensing applications, including detection of metal ions,[64,67] microRNAs,[69,84] target DNA strands in the presence of serum[85] and single base mutations relevant to human diseases.[66,86]

Despite a growing list of applications, little is known about the origins of cluster color in Ag_N-DNA. Strategies for selecting cluster-stabilizing DNA oligomers generally focus on experimentally testing small sets of cytosine (C)-rich or guanine (G)-rich oligomers, which are important for forming fluorescent products,[65,87,88] to find sequences that produce attributes appropriate to a specific application. Here we instead use a large set of 684 distinct 10-base oligomers with widely varying composition to probe the origins of clusters with varying emission colors.

2.2 Parallel Cluster Synthesis and Characterization

We randomly selected sequences containing at least three total C plus G bases from a larger set produced using a MATLAB random number generator with equal probability of placing A,

C, G or T bases at each site. Sequences containing fewer than a total of three C plus G bases were excluded to increase the probability of obtaining fluorescent Ag_N-DNA solutions. Because the total number of distinct ten-base sequences of the four natural bases is 4^{10}, and the number of distinct ten-base sequences with two or fewer C plus G bases is $(2^{10} + 2^9 * 4 + 2^8 * 4^2)$, this exclusion removes less than 0.7% of possible sequences, only slightly changing the base content of the random sequence set (see Appendix Figure A.1 for distribution of base frequency).

Robotic parallel synthesis of Ag_N-DNA under identical conditions was performed in well plate format (Figure 2.1b). DNA was ordered in 384 deep well plate format, pre-suspended in water with standard desalting from Integrated DNA Technologies. Several wells contained a control oligomer known to produce bright fluorescence in order to confirm proper synthesis. A Beckman Coulter Biomek 2000 pipetting robot was used to synthesize Ag_N-DNA at four synthesis conditions: 10 μM and 20 μM DNA, with $[AgNO_3]/[DNA]$ = 5 and 10. Synthesis was performed at pH 7 in 10 mM NH_4OAc, with $[NaBH_4]/[AgNO_3]$ = 0.5. These synthesis conditions were chosen to span the range of Ag^+/base ratios used in published studies. In each well, the hydrated DNA oligomer was mixed with $AgNO_3$, followed by $NaBH_4$ reduction (details in Appendix A.2).

All clusters were excited *via* the DNA bases using 280 nm excitation.[50] Fluorescence spectra were measured using a Tecan Infinite® 200 PRO reader and fitted to single Gaussian lineshapes as a function of energy to extract spectral parameters using Igor Pro 6 software. Ag_N-DNA solutions with dim fluorescence or multiple peaks were excluded from histograms (see Appendix A.3 for details). Here we examine results from oligomers that stabilize clusters having (1) fluorescence brightness well above the noise level and (2) single, rather than

multiple, fluorescence peaks, corresponding to one dominant fluorescent product. We do so because achieving formation of a single Ag_N-DNA species by a single oligomer under certain synthesis conditions is most desirable for the majority of applications.[89,90] Such oligomers comprised up to 25% of the total strand set, depending on synthesis conditions. Apparently, sequences producing one dominant fluorescent product are fairly common amongst randomly selected strands. The remaining 75% of the strands either did not stabilize silver clusters, stabilized "dark" clusters that were not measurably fluorescent, or stabilized clusters that produced very low fluorescent signals due to low chemical yields or low quantum yields of fluorescent products. These strands are presumably not favorable hosts for silver clusters, perhaps due to insufficient attachment of Ag^+ to the bases or because silver clusters stabilized by these strands are not in environments that favor radiative over nonradiative decay.

2.3 Results and discussion

2.3.1 Bimodal color distribution

To examine whether some Ag_N-DNA emission colors are more common than others, we consider the distribution of all peak fluorescence wavelengths measured for solutions of Ag_N-DNA having one dominant fluorescent peak (as described in 2.2). Histograms of fluorescence wavelengths from these single-peak solutions demonstrate bimodal color distributions with enhanced abundances of "green" Ag_N-DNA near 540 nm and "red" Ag_N-DNA near 630 nm (Figure 2.1a and S2). Although relative heights vary somewhat, histogram peaks are invariant over time (one day, one week, and four weeks after synthesis) and synthesis conditions (data for additional synthesis conditions and time points are in Appendix A.4). This suggests that enhanced stabilities of Ag_N-DNA that possess colors near 540 nm and 630 nm lead to the

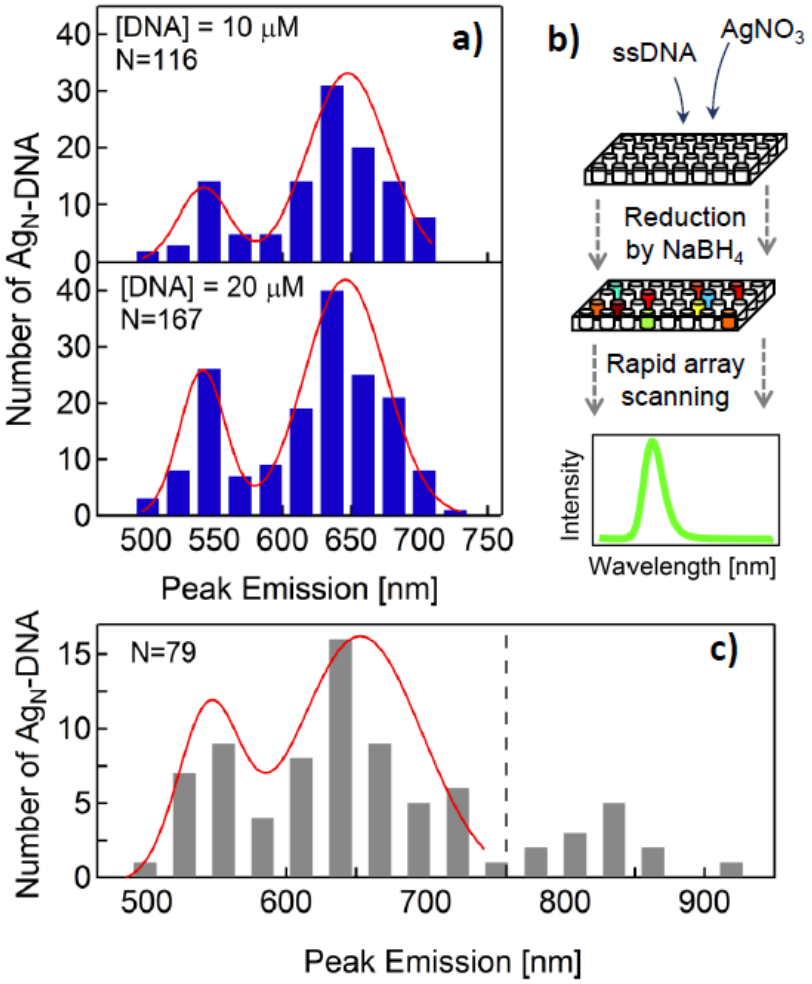

Figure 2.1: a) Peak fluorescence wavelength histograms for Ag_N-DNA stabilized by randomly generated 10-base oligomers, synthesized at 10 μM DNA and 20 μM DNA with Ag^+:DNA = 5:1 and measured 1 week after synthesis to ensure stability of measured products. The number of data, N, indicated on each graph, represents the number of brightly fluorescent Ag_N-DNA with single-Gaussian spectra that are histogrammed in each plot. Maximum likelihood estimation fits to a sum of two normal distributions (MATLAB R2012a) are in red. **b)** Cartoon schematic of parallel robotic synthesis and fluorescence characterization. **c)** A histogram of published Ag_N-DNA fluorescence wavelengths[47,48,51–53,64,66,67,82,86,88,92–94] is strikingly similar to those resulting from the randomly chosen 10-base strands (Figure 2.1a).

enhanced abundances in Figure 2.1.[91] The 850 nm sensitivity limit of the well plate reader precludes detection at longer wavelengths.

To investigate whether these color bands are specific to 10-base oligomers, we surveyed results on 79 strands previously reported to form fluorescent Ag_N-DNA,[47,48,51–53,64,66,67,82,86,88,92–94] with widely varying sequence lengths (6–34 bases) and synthesis conditions. Care was taken to avoid duplicating reported results on identical strands (many

oligomers are utilized across multiple studies). A histogram of reported peak fluorescence wavelengths shows a similar color distribution (Figure 2.1c), with abundances of green and red species as compared to other colors (an additional peak in the near-IR may also indicate a third abundance that is not detectable with our plate reader, which has poor sensitivity beyond ~750 nm.) Apparently "magic colors" are generic, rather than special to strands of specific length.

2.3.2 Ag_N-DNA sizes

We next consider whether Ag_N-DNA within a "magic color" grouping also share similar cluster properties, regardless of sequence specifics. Previous work used high-performance liquid chromatography with in-line mass spectrometry (HPLC-MS) to identify total numbers of silver atoms, N, and silver cations, N_+, for 51 different Ag_N-DNA products[53] that formed on 10 different mixed base sequences with 16–34 bases. From this data we extract the number of neutral silver atoms, N_0, in each cluster: $N_0 = N - N_+$ (Figure 2.2a,b). Distinct groupings are apparent for even N_0, despite wide-ranging numbers of silver cations (Figure 2.2a; for $N_0 = 6$, N_+ ranges from 6 to 10). A histogram of N_0 (Figure 2.2b) displays marked enhancement at even values. Thus, it appears that even magic numbers of N_0 correspond to enhanced abundances of Ag_N-DNA species, regardless of N_+. Additionally, brightly fluorescent Ag_N-DNA (colored circles in Figure 2.2a; RGB colors match peak fluorescence) demonstrate color groupings, with green and red clusters grouped separately, mirroring the histogram color peaks in Figure 2.1b.

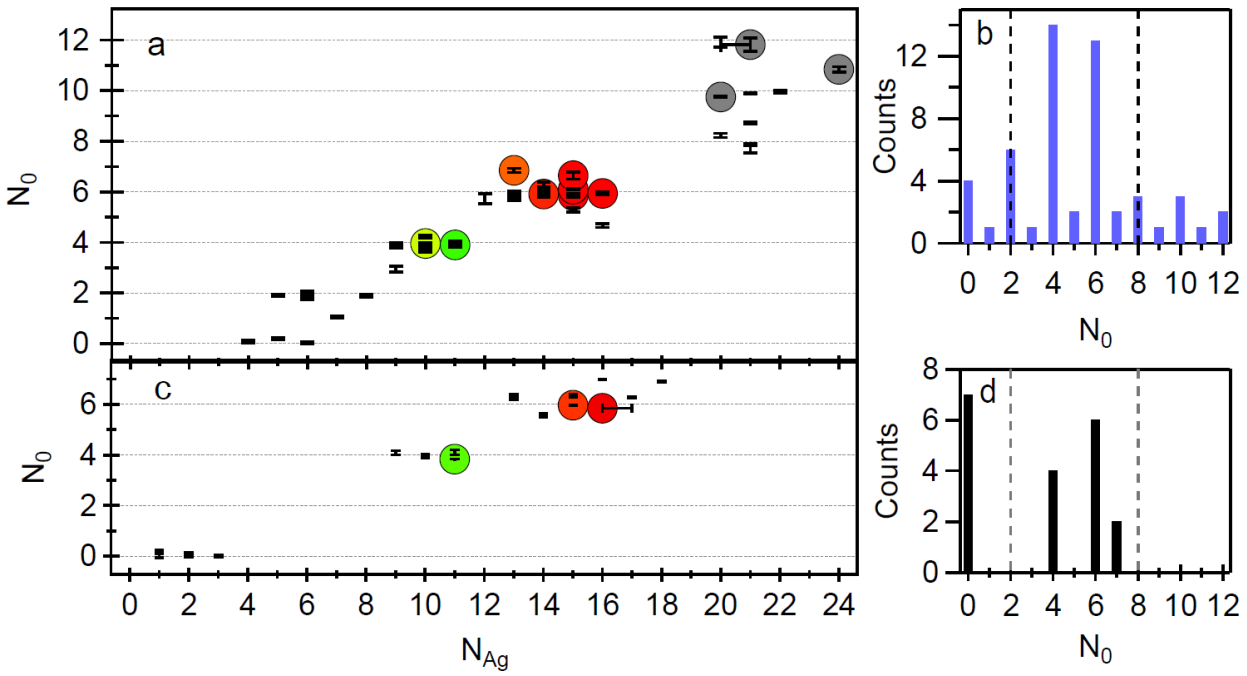

Figure 2.2: a-b) Neutral Ag atom numbers, N_0, extracted from previous Ag$_N$-DNA size data[53] and **c-d)** measured for select 10-base well plate strands that produced bright fluorescence and HPLC-stable products. **a,c)** *N_0 vs. N* for HPLC-purified Ag$_N$-DNA, determined by MS. Brightly fluorescent clusters are indicated by colored dots; RGB colors match fluorescence wavelength (IR-emitting clusters are grey). Black data points represent Ag$_N$-DNA that were not measurably fluorescent but still sizable by MS. Vertical error bars are standard errors in the cluster charge, N_+, and horizontal error bars represent uncertainty in *N*. **b,d**) Histograms of N_0 values show abundances of clusters with even N_0. Magic numbers predicted by the spherical superatom model (dashed lines) differ from those observed for Ag$_N$-DNA.

To investigate whether Ag$_N$-DNA forming on 10-base template strands also contain the magic numbers of N_0 exhibited in Figure 2.2a,b, and whether these Ag$_N$-DNA lie in the same magic color bands, we selected three 10-base strands that produced bright fluorescence and characterized these using HPLC-MS. For this process, synthesis of select bright Ag$_N$-DNA was scaled to 1 ml, and aliquots of the main synthesis products were collected by HPLC separation and examined by negative ion MS (electrospray ionization) (see Appendix A.6). Figure 2.2c,d show that Ag$_N$-DNA formed by the three selected 10-base strands, both fluorescent and dark, indeed show an overwhelming propensity for even N_0, and that colors lie in the same bands exhibited in Figure 2.2a.

Counts of neutral silver atoms do not in themselves imply that all counted neutral atoms are connected into a single cluster. However, if the neutral silver atoms were not included in a single cluster, there would be no reason for color to red-shift with larger N_0. This color-shifting trend, predicted to be a feature of rod-like clusters,[55,56] is clear in Figure 2.2 and is discussed in more detail in Ref. 53.

2.3.3 "Superatom" model

To better understand the magic nature of certain N_0 rather than certain N, we consider the well-studied spherical, ligand-stabilized gold clusters.[20] In these "superatoms," total Au atom number, N, is not magic because ligands effectively remove some gold atoms from the cluster core.[20] For thiolate- and phosphine-stabilized Au clusters, ligands bind to surface Au atoms and withdraw a fraction of the cluster's electrons, forming protective units around the cluster and leaving behind a magic number of electrons, and thus *neutral* gold atoms, in the cluster core.[18,20] Magic numbers of these core electrons are predicted by electronic shell closings in the spherical "superatom" model (see 1.1). While ligand-stabilized silver clusters developed much later than their gold counterparts,[95,96] the existence of magic number silver clusters was recently established using thiolate ligands.[97–99]

For DNA-stabilized silver clusters, the most prominent magic numbers of neutral Ag atoms observed are 4 and 6 (Figure 2.2), not 2 and 8 as predicted by the spherical "superatom" model (dashed lines, Figure 2.2b,d). For non-spherical clusters, superatom magic numbers no longer hold special significance due to lifting of degeneracies by spherical symmetry breaking,[7] such as cluster reshaping by ligand-metal interactions.[100] Instead, the ellipsoidal shell model predicts even-odd oscillation of stability as a function of metal cluster atom number,[7] as we observe in

Figure 2.2. The distinct magic numbers of Ag_N-DNA, relative to spherical gold clusters, thus are consistent with non-spherical cluster shapes.

The presence of both neutral and cationic Ag in Ag_N-DNA, as well as the magic nature of only neutral silver content, indicate different roles for neutral and cationic silver. Because silver cations are thought to bind to ring nitrogens in DNA bases,[47,51,76] we infer that base-Ag^+ complexes act as ligand units, analogous to thiolate- and phosphine-bonded Au units. One crucial difference is that DNA presents multiple base ligands arrayed along a line-like backbone, which could favor elongated, rod-like cluster shapes, as are also needed to account for the optical properties of Ag_N-DNA.[53] This suggests a quasi-linear perimeter of base-attached Ag^+ around a rod-like cluster that exhibits enhanced abundances at even magic numbers of neutral Ag atoms.

2.3.4 Magic Ag_N-DNA sizes lead to magic colors

We now turn to the relation between color distribution and magic numbers. Ag_N-DNA from the two prominent peaks in Figure 2.1a, centered at 540 nm and 630 nm, respectively, fall within the high abundances of clusters having N_0 = 4 and N_0 = 6, respectively (Figure 2.2c). We thus infer that "magic" green clusters within the 540 nm color band correspond to Ag_N-DNA with N_0 = 4, and "magic" red clusters within the 630 nm color band correspond to Ag_N-DNA with N_0 = 6. This is consistent with a previously established trend of longer wavelength fluorescence for Ag_N-DNA with larger silver clusters[52] and also agrees with the previously sized fluorescent clusters in Figure 2.2a: the 7 fluorescent Ag_N-DNA with N_0 = 6 clusters emit within 60 nm of the 630 nm color peak, and the 3 fluorescent Ag_N-DNA with N_0 = 4 clusters emit within 25 nm of the 540 nm color peak. Additional IR emitters in Figure 2.2a,

corresponding to the near-IR band in Figure 2.1c, may indicate another magic N_0. IR emitters stabilized by the 10-base random strands were not detectable with the plate reader, however, so we make no conjectures here as to the corresponding value of N_0.

The 540 nm and 630 nm histogram peaks (Figure 2.1a) have standard deviations of 20 and 30 nm, respectively. To understand why the color peaks corresponding to magic N_0 are so wide, we consider the well-known sensitivity of transition wavelengths of rod-shaped metal nanoparticles and clusters to aspect ratio[101–103] and bending.[59,104–106] Because small changes in aspect ratio or small deviations from a linear chain shift transition wavelengths, a range of aspect ratios and/or curvatures could qualitatively account for observed color spreads at magic N_0. We expect base-Ag+ units to influence color by determining cluster shape. The existence of dark Ag_N-DNA with $N_0 = 0$ and up to six Ag^+ (Figure 2.2a) shows that fluorescent clusters may also contain Ag^+ that are not incorporated into the base-Ag^+ ligand units surrounding the neutral cluster core. Ag^+ content varies from $N_+ = 6$ - 9 in red-emitting clusters with $N_0 = 6$, suggesting that up to three Ag^+ are associated with bases detached from the cluster, where they may still affect wavelength by altering the potential seen by the cluster's delocalized electrons.

Figure 2.3 shows variants on such a silver cluster nanorod, adapted from previously suggested structures,[53,107] (AMBER structure generation details in Appendix A.6[108–113]). Like ligand-protected Au clusters, this schematic shows base-Ag^+ units that protect a neutral cluster core containing a magic number of neutral silver atoms, even N_0, due to spin degeneracy (Figure 2.3 a,b). Ag-Ag bond angle variation within the core can produce a range of aspect ratios for a fixed N_0, avoiding energetically costly changes in Ag bond length caused by modifying Ag bond angles and base stacking energies. Molecular dynamics simulations[108] show that clusters may assume curved shapes due to Coulomb interactions, and addition or

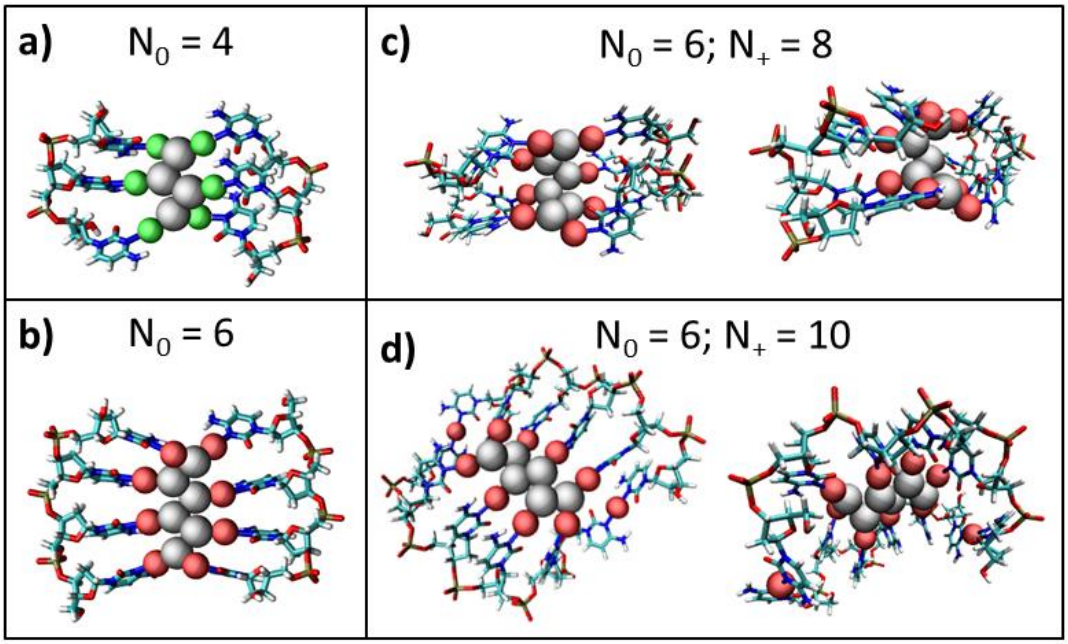

Figure 2.3: Cluster schematics from AMBER simulations for **a)** a green-emitting $N_0 = 4$ Ag_N-DNA and **b)** a red-emitting $N_0 = 6$ Ag_N-DNA. **c)** AMBER simulations of the $N_0 = 6$ cluster structure after 1 ns for front and side views, as compared to **b)**. Simulations suggest that Ag_N-DNA may assume curved shapes, influenced by location of Ag ions. **d)** Simulations of a $N_0 = 6$, $N_+ = 10$ cluster structure after 1 ns. Additional Ag ions that are not directly bound to the cluster's neutral core but still associated with the Ag_N-DNA complex may cause additional shape and/or fluorescence wavelength changes, as seen by comparing the shapes of $N_0 = 6$ clusters with 8 Ag^+ (Figure 2.3c) to $N_0 = 6$ clusters with 10 Ag^+ (Figure 2.3c).

subtraction of silver ions near the cluster can modify cluster shape (Figure 2.3c,d). We expect that a combination of such shape factors account for the breadth of histogram peaks in Figure 2.1b. It is noted that the structures shown in Figure 2.3 are simple models, and not crystalographically determine exact structures.

2.3.5 DNA sequence and Ag_N-DNA color

Finally, we consider the specificity of Ag_N-DNA color to the particular DNA template sequence, an important issue for Ag_N-DNA colorimetric sensing schemes. Our array data studies show that many distinct sequences produce nearly the same fluorescence color. In particular, for red emitters we find 26 distinct ten-base strands that produce the same peak fluorescence color to within 10 nm (Table A.3, Appendix A.8). This will challenge the

development of sensing schemes aimed at distinguishing the presence of specific sequences amidst a background of other DNA.

2.4 Conclusions

We observe significantly enhanced abundances of Ag_N-DNA stabilized by random DNA oligomers with fluorescence peaks near 540 nm and 630 nm. HPLC-MS data shows that these color groupings correspond to cluster populations with even numbers of neutral silver atoms, different from magic numbers for spherical clusters. Due to the dependence of fluorescence wavelength on neutral silver atom number, we conclude that magic numbers of silver atoms result in the observed "magic color" bands. Variants on rod-like cluster models qualitatively explain the breadth of the color histogram peaks relative to magic numbers by permitting variations in cluster geometry and immediate environment. The existence of such "magic colors" has implications for the palette available to colorimetric assays and could be exploited in sensing applications where transitions between green and red emissive clusters, caused by changes in the magic number of neutral silver atoms through oxidation or reduction of existing Ag_N-DNA, act as signals for a desired process.

3. Base Motif Recognition and Design of DNA Templates for Fluorescent Silver Clusters by Machine Learning

Adapted with permission from Copp, S. M.; Bogdanov, P.; Debord, M.; Singh, A.; Gwinn, E. Base Motif Recognition and Design of DNA Templates for Fluorescent Silver Clusters by Machine Learning. *Adv. Mater.* **2014**, *26* (33), 5839–5845.[70] *Copyright 2014 John Wiley and Sons.*

3.1 Introduction

In the previous chapter, we showed that Ag_N-DNA fluorescence colors are selected by the number of neutral silver atoms in the cluster core and that the enhanced abundances of certain colors of Ag_N-DNA correspond to magic numbers of these neutral silver atoms that are consistent with a rod-like cluster geometry. Next, we seek to understand selection of fluorescence properties by DNA sequence.

It remains unknown how the sequence of DNA template strands selects the fluorescence properties of Ag_N-DNA.[48,86,87] Particular template choices select for fluorescent silver clusters with peak emission wavelengths throughout the visible and near-IR spectrum,[50,93] corresponding to 10-24 silver atoms bound to the DNA.[53] This wide color palette, combined with proposed low toxicity, high quantum yields of some clusters,[53] low synthesis costs, small cluster sizes and compatibility with DNA have enabled many applications employing Ag_N-DNA, as discussed in 1.3. Yet despite the rapid growth of applications for Ag_N-DNA, it is not understood why certain sequences produce brightly fluorescent solutions while other apparently similar sequences do not. This question of the influence of biopolymer host

sequence on the structure of templated inorganic particles[114–116] is scientifically rich, with potential for high payoff if approaches can be developed to address the complexities introduced by sequence diversity and flexibility of polymeric templates. In the specific context of Ag_N-DNA, robust design methods for DNA template strands are sorely needed to aid future applications development.

In the emerging physical picture of silver cluster formation on DNA host molecules, silver cations (Ag^+) assist attachment of bases in a DNA template to the silver cluster, subject to backbone-imposed geometrical constraints. This view is based on the presence of both neutral (Ag^0), which tend to form magic-sized clusters (Chapter 2), and cationic silver atoms in Ag_N-DNA[53] and on the known affinity of Ag^+ for the nucleobases.[117] Prior studies showed that homopolymers of cytosine (C) or guanine (G) stabilize fluorescent Ag_N-DNA, albeit often with poor temporal stability, while adenine (A) or thymine (T) homopolymers produce negligible yields of fluorescent products.[88] Beyond the recognition that C- and G-rich DNA strands favor fluorescent cluster solutions,[48,65,89] very little is known about how the composition of mixed-base templates relates to fluorescent cluster formation. For this reason, template design[69] relies on experimentally testing oligomers with sequences selected by "informed guessing," using random changes to previously identified DNA template strands to attempt to improve fluorescence brightness or change fluorescence color.

More systematic template prediction is challenged by the huge space of possibilities: for templates of base length L, there exist 4^L distinct sequences of the four canonical bases, with typical values of L ~10-20 corresponding to 10^6-10^{12} unique sequences. Even for an individual template, DNA flexibility and the ability of Ag^+ to reconfigure native Watson-Crick pairing[76] typically result in many distinct cluster products in a single solution environment, most of them

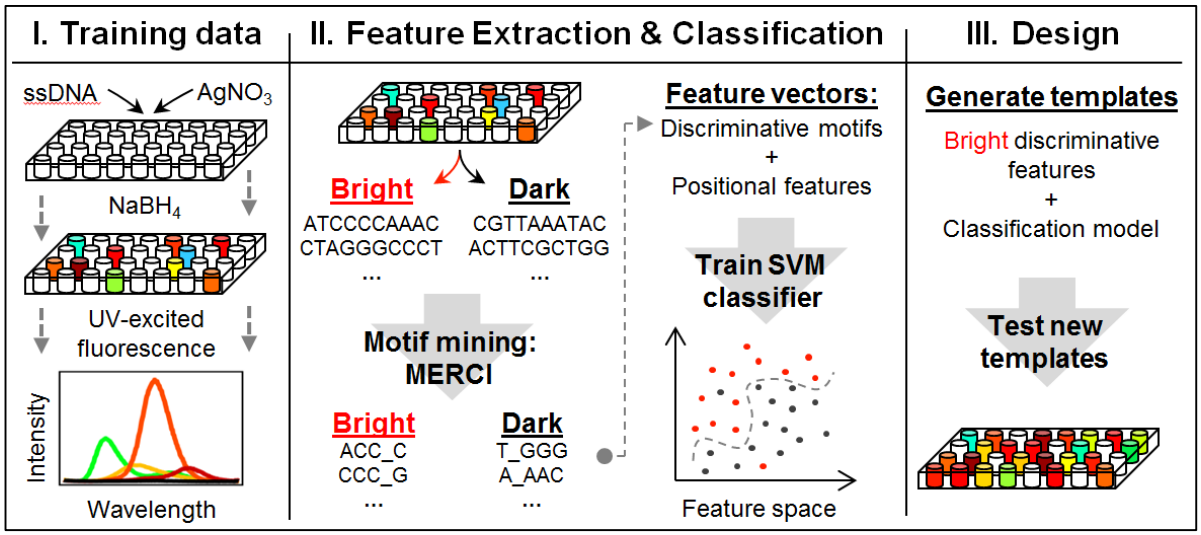

Figure 3.1. Schematic of methods used to recognize discriminative base motifs within DNA templates for fluorescent Ag_N-DNA and to construct new templates for solutions with increased brightness.

nonfluorescent.[52] As understanding improves of the interactions among DNA, Ag^+, and Ag^0, and of the interactions of all constituents with solvent molecules in modes that favor radiative over non-radiative decay, first-principle theoretical methods like density functional theory may eventually become predictive. However, given these undetermined fundamental issues, a systematic data-driven approach to template selection is currently necessary.

To develop predictive power for selecting DNA templates that stabilize fluorescent Ag_N-DNA, we adopt an approach that combines large experimental data sets with computational machine learning tools for pattern recognition (Figure 3.1). We identify short, consecutive sets of bases, called "base motifs," that preferentially select for fluorescent Ag_N-DNA. We then demonstrate the power of a motif-based method to design DNA templates producing brightly fluorescent Ag_N-DNA solutions. This new understanding of the connection between base motifs and fluorescence brightness builds a basis for statistically predictive design methods for templates that stabilize Ag_N-DNA with desired characteristics for specific applications.

3.2 Experimental Details

To limit the scope of the problem, we consider only L = 10 templates. Specifically, we examine clusters stabilized by 684 distinct 10-base oligomers with random sequences of the canonical bases, corresponding to < 0.07% of all possible 10-base oligomers. Because C and G are important for stabilizing fluorescent silver clusters, random sequences containing fewer than three C plus G bases were excluded.

Standard Ag_N-DNA synthesis by $NaBH_4$ reduction was performed on templates in parallel using robotic pipetting in well plate format. 10-base DNA template strands were ordered from Integrated DNA Technologies with standard desalting, suspended in RNase-free H_2O in well plate format. A Beckman Coulter Biomek 2000 pipetting robot was used to synthesize Ag clusters on each template strand in parallel. DNA was mixed with a solution of $AgNO_3$ in NH_4OAc buffer and incubated at room temperature for 20 min before $NaBH_4$ reduction, for final concentrations of 20 μM DNA, 100 μM $AgNO_3$, and 50 μM $NaBH_4$ in 10 mM NH_4OAc. Of the synthesis conditions tested, these conditions produced the largest number of brightly fluorescent Ag_N-DNA solutions. Products were stored at 4°C until measurement.

Emission spectra were measured from 400-850 nm using a Tecan Infinite® 200 PRO well plate reader. 280 nm light was used to simultaneously excite all fluorescent Ag_N-DNA products formed by a given template, *via* UV absorbance of the bases.[50] Products were measured 1 day, 1 week, and 4 weeks after synthesis to test fluorescent product stability. Stable products typically peaked in brightness at 1 week and decayed only slowly thereafter. Here we focus on the data sets collected one week after synthesis.

The fluorescence intensity integrated across 450-850 nm, I_{int}, is used as a brightness metric for products formed on a given template (data in Table B.3). (Because scattered excitation light

was detected from 400-430 nm, integrated intensity values were integrated from 450-850 nm.) I_{int} represents the product of chemical yields, fluorescence quantum yields and extinction coefficients summed over all the different fluorescent Ag_N-DNA produced in a single solution. About 25% of spectra corresponding to fluorescent solutions exhibited two distinct peaks, typically with one dominant, which arise when the template stabilizes more than one main fluorescent Ag_N-DNA species. To include fluorescence from templates producing high yields of multiple silver clusters in the brightness metric, we chose I_{int} over peak intensity I_{peak}.

3.3 Results and Discussion

3.3.1 Machine learning classifier selection

To elucidate trends connecting template sequence to Ag_N-DNA brightness, we considered several pattern recognition schemes that are widely used in machine learning and data mining: artificial neural networks, support vector machines (SVM), random forest, and logistic regression, all available in the Weka library.[118] While all schemes had comparable performance, we selected SVMs due to slight gains. SMVs are classifiers that learn to separate two classes of training data, which are represented in a high-dimensional "feature space" discussed below, by fitting an optimal hyperplane between the two classes.[119] SVMs are widely employed in bioinformatics tasks such as protein-protein binding site prediction[120] and gene classification.[121] Here we use SVMs to categorize base sequences favorable for forming fluorescent Ag_N-DNA. We use the random template data to train the SVM to make predictions of the probability of brightness for new, untested DNA templates. The two training data classes correspond to "bright" DNA templates that stabilize fluorescent Ag_N-DNA and "dark" templates that do not. Each template is represented by a feature vector that includes information

on sequence, as well as Ag_N-DNA solution brightness.

Any classification scheme requires categorization criteria. We chose to classify DNA templates stabilizing Ag_N-DNA with I_{int} values in the top 30% as "bright" and the bottom 30% as "dark." The middle 40% of templates are excluded from analysis to avoid an arbitrary single threshold distinguishing "bright" from "dark."

3.3.2 Feature vector selection and motif discovery

SVMs rely on selecting feature vectors that successfully capture the class-determining characteristics. To compare different choices of feature vector composition and thus elucidate template features that are most important for selecting for Ag_N-DNA brightness, we use the SVM accuracy, $A = (t_B+t_D)/(t_B+f_B+t_D+f_D)$, where t_B is the number of true predictions the SVM makes for bright strands, f_B is the number of false bright predictions, and t_D and f_D are the number of true and false dark predictions, respectively. A is the fraction of test template sequences that the SVM correctly selects as "bright" or "dark". To evaluate A for a given choice of feature vector space, the data is divided into a training set (85% of the templates) and a test set. The SVM chooses the optimal hyperplane dividing bright and dark sequences in the training set, and A is evaluated using the remaining 15% of the data. Multiple subdivisions of the data are used to obtain stable values for A.

Initially we chose feature vectors containing the entire template sequence, coding each base as an integer ({A,C,T,G}~{1,2,3,4}). Trained SVMs using these feature vectors gave poor accuracy, $A \approx 60\%$, for bright-dark predictions, indicating that use of sequence in the feature vectors gives rather poor separation between bright and dark. This poor separation results from an insufficient representation of the features of a sequence that actually determine its fitness as

a template for fluorescent Ag_N-DNA. Feature vectors containing only integer-encoded sequence appear not to capture salient features that are invariant with position in the sequence, such as multi-base motif patterns. For example, consider two distinct sequences containing the same multi-base motif. If the motif occurs in different positions in the two sequences, these sequences can be arbitrarily distant from one another in a sequence-only feature space. Now, if that motif plays an important role in determining if sequences stabilize fluorescent Ag_N-DNA, regardless of position within a sequence, then this crucial information will not be captured by the feature vectors and will not be conveyed to the SVM. In such a poorly chosen feature vector space, the fitted hyperplate will not separate bright and dark classes very efficiently, resulting in low predictive power, *ie*, low accuracy, *A*. Therefore, to gain insight into the defining aspects of bright *versus* dark templates, we use *A* as a metric to assess different choices of feature vector.

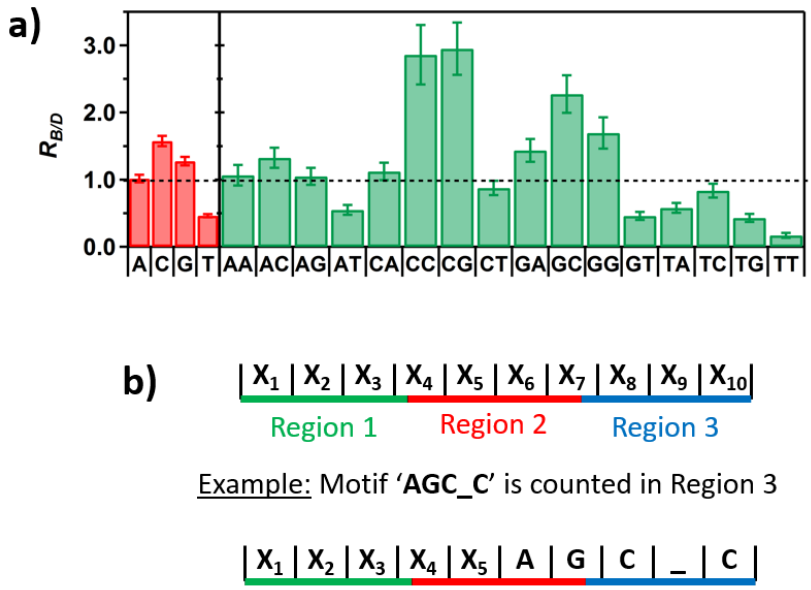

Figure 3.2: a) Ratios of average motif counts, $R_{B/D}$, per strand in bright to dark templates, with standard error bars. Single base counts (red) show that C and G occur more frequently in templates stabilizing fluorescent clusters while T occurs twice as frequently in dark templates than in bright templates. The spread of $R_{B/D}$ values increases for 2-base motifs (green) and still more for 3-base motifs (Figure B.1). **b)** Schematic of the three regions considered within a template. Positional features are summed in each region, and motifs are counted in the region containing their middle base(s) (see example).

Under the hypothesis that there exist certain multi-base patterns that determine a template's fitness for hosting fluorescent Ag clusters, regardless of these patterns' positions within the template, we next considered vectors composed of information about base motifs instead of only information about base sequence. Figure 3.2a further motivates this choice, displaying average ratios, $R_{B/D}$, of the total counts of individual bases and of 2-base motifs in bright templates to the counts in dark templates. For individual bases (Figure 3.2, red) $R_{B/D}$ confirms the expectation that bright templates contain higher C and G counts and lower T counts than dark templates. A counts do not, on average, distinguish bright *versus* dark. For longer motifs, the range of $R_{B/D}$ values also increases. Two-base motifs (Figure 3.2a, green) show a 10:1 spread, and 3-base motifs (Appendix Figure B.1) show a 25:1 $R_{B/D}$ spread, suggesting that predictive power of motifs will increase with length until motif length is sufficient to fully define a fluorescent cluster. SVM-based prediction methods may thus benefit from considering motifs at least 3-4 bases in length. Another recent study has also related 4-5 base subsets of DNA sequences to characteristics of Ag_N-DNA fluorescence.[122]

Also apparent in Figure 3.2 and Figure B.1 are motifs with $R_{B/D}$ near unity, which do not, on average, distinguish between bright and dark templates. To test whether including these possibly non- discriminative motifs would degrade *A*, we constructed 64-element motif feature vectors composed of the occurrence numbers of *all* 3-base motifs in the template. For example, the feature vector for the template AAAAATTTTT contains '3' for the two entries corresponding to motifs AAA and TTT, '1' for entries corresponding to AAT and ATT, and '0' for the remaining 60 elements. These 64-element motif feature vectors gave even poorer predictive accuracy, $A \approx 50\%$, than the feature vectors containing the entire sequences. Because inclusion of irrelevant information in feature vectors reduces SVM accuracy, we then

selected only the ten, 3-base motifs with $R_{B/D}$ farthest from unity. The 10-element feature vectors increased A to ~75%. Thus, many motifs are apparently *non*discriminative for brightness: removing them dramatically improves SVM performance for DNA template classification.

To efficiently and systematically select discriminative motif features, we employ a motif-miner called MERCI[123] that has been applied to various bioinformatics applications.[124,125] For a set of sequences separated into positive (P) and negative (N) classes, MERCI identifies motifs occurring with frequency $\geq F_P$ in class P and $\leq F_N$ in class N. Maximum motif lengths and the maximum length and number of gaps that act as wildcards are specified as parameters. For example, 'AA_GC,' where the gap '_' represents any base or no base, is either a 5-base motif with a 1-base gap or the 4-base motif AAGC. (Gaps add additional flexibility to the features representing template sequences by accounting for possible similarities of multi-base patterns with similar function. Such similar motifs might otherwise be discarded by MERCI if each individual motif does not occur with sufficient frequency.) Our feature vectors describe the set of bright:dark discriminative motifs selected by MERCI by using a binary variable for every identified motif. The feature vector entry for a given motif is '1' if that motif occurs in the template and '0' otherwise. We found that using motifs of at most 10 bases in length with gaps of at most 1 base and setting $F_P = 10$, $F_N = 10$ results in optimal training and testing accuracies for the 684, ten-base training templates. Since the frequency constraints (F_P, F_N) are not symmetric for bright and dark classes, we run MERCI twice, using bright and then dark as the positive class, to separately extract motifs that discriminate for bright and for dark templates.

With the above optimal parameters, all discriminative motifs identified by MERCI contained 3 to 5 bases, with 4 and 5 base motifs making up 98% of those identified (Tables

B.4 and B.5). Thus, motifs 3-5 bases in length appear to define Ag clusters with the requisite structures for emission within the detection bandwidth of our well plate reader (~ 400-850 nm). It is notable that MERCI does not identify any discriminative 2-base motifs under the conditions necessary for optimal SVM training and testing accuracies, indicating that 2-base motifs are too small to independently template fluorescent Ag clusters.

The 10 most common motifs associated to bright and dark templates are listed in Table 3.1. Several of the bright motifs contain consecutive C bases, consistent with previous findings

Bright Motifs		
Motif	**#Bright / #Dark**	**Avg. I_{int}**
CC_C	6.0	$4.7 \pm 0.9\times10^5$
C_CC	10.4	$4.8 \pm 0.9\times10^5$
GCG	4.7	$1.8 \pm 0.3\times10^5$
CCG	5.3	$2.9 \pm 0.5\times10^5$
GCC	6.0	$3.0 \pm 0.6\times10^5$
CGC	6.7	$2.2 \pm 0.2\times10^5$
CCC	18.0	$6 \pm 1\times10^5$
GG_AC	2.8	$2.0 \pm 0.4\times10^5$
G_GAA	1.9	$3.0 \pm 0.9\times10^5$
AGC_G	1.8	$1.2 \pm 0.3\times10^5$
Dark Motifs		
Motif	**#Bright / #Dark**	**Avg. I_{int}**
T_TT	0.13	$7 \pm 3\times10^4$
TT_T	0.10	$7 \pm 3\times10^4$
AT_T	0.19	$3.3 \pm 0.6\times10^4$
A_TT	0.15	$4 \pm 2\times10^4$
TTG	0.19	$5 \pm 2\times10^4$
TTT	0.07	$7 \pm 4\times10^4$
TTC	0.21	$1.1 \pm 0.5\times10^4$
CTT	0.25	$1.2 \pm 0.5\times10^4$
TTA	0.19	$1.1 \pm 0.5\times10^4$
ATT	0.11	$2.5 \pm 0.5\times10^4$

Table 3.1: Top 10 most frequently occurring discriminative motifs, as identified by MERCI, for both bright and dark random templates, with motif sequence, the ratio of the number of occurrences in bright templates to dark templates, and the average I_{int} with standard error for templates containing each motif. All motifs identified for random templates are tabulated in Tables B.4 and B.5.

of fluorescent Ag_N-DNA formed on C-rich templates. [69,93,122] Multiple G bases are also common in bright motifs.[48,66] The particular combination of one G with two C bases and bright motifs containing A bases were unanticipated (Table 3.1).

Prior work that focused on small sets of "patterned" templates, obtained by single to few-base mutations of certain C-rich parent sequences, could not test for global significance of specific motifs.[69,93,122] In contrast, our application of pattern-recognition algorithms to large random template sets establishes that particular 3-5 base motifs participate in stabilizing Ag_N-DNA. Apparently these motifs have special Ag-binding characteristics that favor formation of clusters with visible fluorescence wavelengths.

In addition to motif composition, the number of bright motifs required to stabilize an emissive Ag cluster is important. Prior studies identified the numbers of Ag atoms and DNA strands contained in fluorescent Ag_N-DNA with 15-34 base templates.[52,53] For templates with 19 or more bases, the Ag_N-DNA contained just one DNA strand, but for shorter, 15-16 base templates, *two* copies of the same strand simultaneously stabilized the clusters. This implies that at least two bright motifs are required to stabilize fluorescent clusters. In longer templates, this cluster "sandwiching" between bright motifs can be achieved by folding the strand around the cluster. With shorter templates, it appears that clusters engage multiple bright motifs by simultaneously attaching to two strands. For 10-base templates, the fluorescent clusters with known composition were indeed found to be stabilized by two copies of the template strand.[58]

We therefore expect the Ag_N-DNA in this study to be stabilized *via* attachment to two 10-base template copies. For these "strand dimer" Ag_N-DNA, a cluster would engage a 3-5 base motif in each strand, with Ag-base bonds holding strands together around the encapsulated cluster. Because the lengths of bright motifs are well below half the single-stranded DNA

persistence length,[126] they can act as stiff, linear cluster scaffolds, rationalizing the elongated, rod-like cluster shapes indicated by Ag_N-DNA optical properties.[53] The cluster size range of 4-6 neutral silver atoms in most visible-emitting Ag_N-DNA[58] may also arise from the requirement that atoms arranged in an elongated cluster make contact the 3-5 bases of linear motif scaffolds within two template strands. For Ag_N-DNA stabilized by single, longer template strands, we expect that these templates must contain at least two bright motifs as well as sufficiently long, flexible runs of intervening bases to allow the strand to present both bright motifs to the cluster.

In addition to motif inclusion features, we consider positional features describing motif location along the 10-base random template sequences. Templates are partitioned into 3 equal regions, and dark and bright discriminative motifs are counted in each region (Figure 3.2b); a motif is counted in the region containing its middle symbol(s). We also tested use of positional features describing average nucleotide size and "stickiness", a metric of each base's interaction strength with Ag clusters (parameters in Table B.1). The single base dependence in Figure 3.2a ($R_{B/D} > 1$ for G and C bases, $R_{B/D} < 1$ for T, $R_{B/D} \sim 1$ for A) is parameterized by this rough "stickiness" categorization, for comparison to results assuming equal stickiness. The LIBSVM library[127] was used for classification. While including the positional features improved SVM accuracy from 82% to 86%, with stable accuracies across multiple SVM runs, base size and stickiness had little effect. Improved SVM accuracy upon inclusion of positional motif information suggests that locations of 3- 5 base motifs within a template are also somewhat important. In summary, the propensity of a DNA template strand to stabilize fluorescent Ag clusters is determined by certain select 3-base to 5-base motifs within the template as well as by the relative positions of these motifs with respect to one another.

3.3.3 DNA template generation

To generate new DNA templates for bright Ag_N-DNA solutions, we adopt a simple model that draws on the extracted motif features and the I_{int} values measured for Ag_N-DNA solutions. Let $p(M,P)$ be a probability density function describing the probability of motif M being incorporated at position P (P={1,2,3} our case) in a bright template. For the set of training templates, T, and the set of MERCI-identified motifs, M, we define the probability of bright template inclusion for every position p and motif m as:

$$p(M = m, P = p) = \frac{\sum_{t \in T} I_t x(t, m, p)}{\sum_{n \in M} \sum_{t \in T} I_t x(t, n, p)} \qquad (3.1)$$

where I_t is the intensity of template t and $x(t,m,p)$ is '1' if motif m occurs in training template t at position p and '0' otherwise. (Here $p(m,p)$ can be interpreted as the intensity-weighted probability that motif m occurs at position p, across all training sequences.) Starting with an empty sequence, we iteratively sample motifs to include in consecutive regions of the new template according to the motif's value of $p(m,p)$, rejecting motifs that are incompatible with the previously included motifs. This process continues until all base positions are assigned. Only sequences differing by at least two and at most three mutations from any of the 684 template data set are retained, corresponding to ~10^6 distinct sequences. We then classify each newly generated template as bright or dark using our previously trained SVM.

3.3.4 Experimental verification

We tested the effectiveness of this motif-based design method by experimentally testing the 374 template sequences to which the SVM assigned the highest brightness probabilities (Table B.6). The average I_{int} value for Ag_N-DNA solutions synthesized with this designed template set is much brighter, by a factor of > 3 at one week after synthesis, than for the random

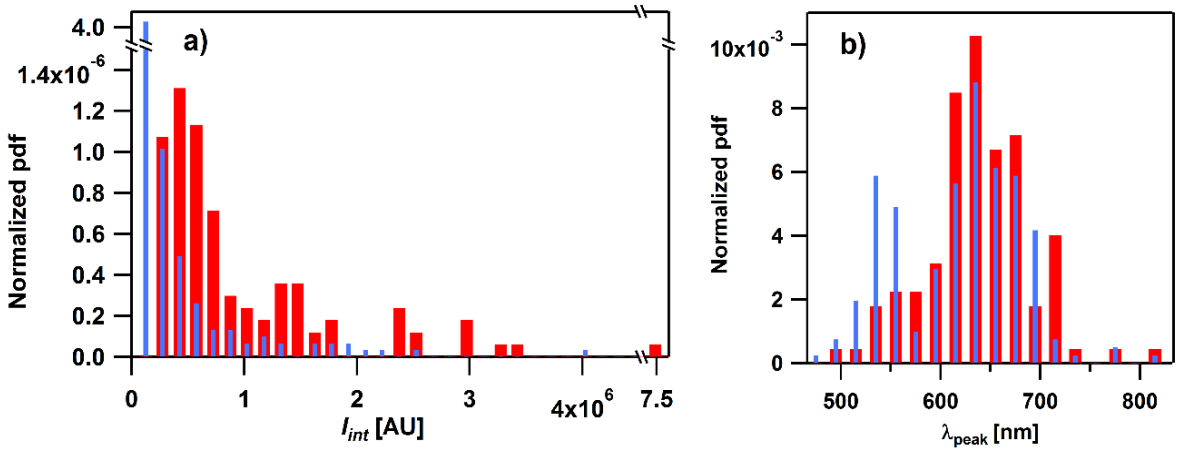

Figure 3.3: **a**) Normalized probability density (pdf) functions of the top 30% of I_{int} values for strands with randomly generated sequences (blue) and with sequences designed by motif selection (red). The distribution of I_{int} shifts towards higher values for designed templates. **b**) Pdfs of peak wavelengths for bright clusters stabilized by random (blue) and designed templates (red).

template set used to train the SVM. Figure 3.3a demonstrates this shift to higher solution fluorescence by comparing probability distribution functions (pdfs) for the top 30% of I_{int} values from random and designed templates. For the random template set, low-fluorescence solutions were by far the most probable outcome, while in striking contrast, none of the top 30% of designed templates produced solutions in the lowest brightness bin (Figure 3.3a; note the scale break in the pdf axis). By the I_{int} threshold definitions used to classify random template sequences as "bright" or "dark", 293 of the 374 generated templates are bright, while only 3 are dark (the remaining 78 lie between bright and dark thresholds). This dramatic increase in the ability to select bright DNA templates corresponds to an accuracy A = 78% for the motif-based design method, somewhat below the SVM accuracy, A = 86%, obtained from the random sequence training data. The decrease in realized *versus* predicted accuracy may reflect the small training set size, < 0.07% of the possible space of templates. Larger training sets may yield even higher accuracies. Accuracy may also be reduced by formation of larger, infrared clusters (not detectable due to the plate reader's low sensitivity above ~750 nm), as might be expected from the inclusion of higher numbers of "bright" motifs in the designed

versus random templates.

The hypothesis that greater numbers of "bright" base motifs in template sequences lead to formation of larger Ag clusters is consistent with the red-shift in the Ag_N-DNA color distribution for the designed *versus* random template set (Figure 3.3b). Ag_N- DNA color reddens with increasing numbers of Ag atoms in the cluster,[52] which has been attributed to elongation of the free-electron path in rod-shaped[53,58,107] clusters. We expect the higher average number of bright motifs in the designed templates to increase the numbers of Ag^+ associated to the template's bases before reduction, causing an increase in the average neutral silver cluster size formed by reduction and thus longer fluorescence wavelength.

An examination of the 10 brightest template sequences (Table B.2) hints at why motifs in Table 3.1 are predictive of fluorescence intensity and which nucleotides interact with Ag clusters. Nine of the 10 brightest templates contain two or more adjacent C bases, matching cytosine's accepted role in forming fluorescent Ag_N-DNA. The sixth "brightest" sequence, however, contains no adjacent C's, and of the 497 random and generated "bright" templates (Tables B.3 and B.6), 27% contain no consecutive C's, and 58% contain no more than two consecutive C's. The discriminative 3-5 base motifs leading to optimal SVM performance suggest that Ag clusters interact with at least 3 consecutive bases on each template. Thus, while C's have often appeared to play a dominant role in stabilizing fluorescent Ag_N-DNA, our motif mining and SVM results suggest that Ag clusters must also be engaged to at least one A, G, or T in the majority of these bright templates. Previous studies suggest that thymines do not associate with Ag clusters at neutral pH,[88] and the role of adenine is still unclear. It may be that thymines act as termination sites to limit Ag cluster growth during synthesis and prevent cluster migration after synthesis, both important aspects for visible and near-IR emission wavelengths

and time stability. This would explain the presence of T's in 15% of identified bright motifs. Future tests of this hypothesis for the role of thymines in truncating Ag_N-DNA cluster growth should be performed.

Thus, a plausible model of Ag cluster association with DNA template(s) consists of at least two 3-5 base motifs, rich in C's, G's, and/or A's. These motifs occur either in two separate template strands or in a single longer strand separated by a dark linker long enough to allow two bright motif regions to encapsulate the cluster. T's likely serve to limit cluster size, while variations in C, G, and perhaps A content likely further control cluster size and thus wavelength. As past studies show that a single DNA strand often stabilizes multiple fluorescent and nonfluorescent Ag-DNA products,[52] formation of an Ag_N-DNA with significant fluorescence brightness would require a template sequence whose motifs select a *small* number of different products to improve chemical yield of any high quantum yield Ag_N-DNA. Thus, Ag_N-DNA template strand design should select a DNA sequence that not only stabilizes brightly fluorescent silver clusters but also avoids stabilizing other products that would compete for silver atoms during synthesis.

3.3 Conclusions

We have used large array data sets and machine learning tools to show that multi-base motifs govern the fluorescence brightness of Ag_N-DNA solutions formed on DNA templates. We separately identify sets of motifs that select for brightness and sets of motifs that discriminate against bright products. Both motif types will be important for realizing designed multi-cluster constructs. By selecting motifs that discriminate between bright and dark templates and representing templates with feature vectors composed of information about these

discriminative motifs, SVM-based classifiers can be trained to predict template brightness with high accuracy. Combining this predictive power with an intensity-weighted, motif-based generative model, we experimentally demonstrate ~80% accuracy for generating templates that produce bright Ag_N-DNA solutions. Even higher accuracies may be achieved in the future by using larger training data sets and/or by employing techniques such as feature selection to better select feature vectors for classification. These are currently being pursued in ongoing work.

The lengths of identified discriminative motifs suggest that Ag clusters engage with regions of DNA templates containing 3-5 consecutive bases. While many of the identified bright motifs are rich in C and G bases, more complex roles of multi-base motifs still need to be investigated. Motifs identified as discriminative for low-fluorescence Ag_N-DNA solutions may also be utitilized in sensing schemes to create regions of DNA that do not stabilize fluorescent Ag clusters. We expect that both dark and bright motifs may enable design of DNA strands mediating attachment of Ag_N-DNA to larger DNA nanostructures, as discussed in the following chapters.

The techniques used here, motif selection by the MERCI algorithm and classification by SVM techniques, were developed for use in contexts quite different from stabilization of fluorescent silver clusters. Thus, in terms of the broader context of biopolymer-templated inorganic nanomaterials, we expect that the approaches developed here may be generally useful for studies of polypeptides, proteins, and RNA as templates for other inorganic materials such as metal and semiconductor clusters.

4. Dual-Color Nanoscale Assemblies of Structurally Stable, Few-Atom Silver Clusters, as Reported by Fluorescence Resonance Energy Transfer

Adapted with permission from: Schultz, D.; Copp, S. M.; Markešević, N.; Gardner, K.; Oemrawsingh, S. S. R.; Bouwmeester, D.; Gwinn, E. Dual-Color Nanoscale Assemblies of Structurally Stable, Few-Atom Silver Clusters, as Reported by Fluorescence Resonance Energy Transfer. *ACS Nano* **2013**, *7* (11), 9798–9807.[71] *Copyright 2013 American Chemical Society.*

4.1 Introduction

DNA self-assembly offers the opportunity to create nanostructures with unique optical properties that arise from the spatial organization of metal particles at length scales much smaller than visible light wavelengths. Recent efforts to exploit this potential used double-stranded DNA constructs to control near-field interactions in noble metal nanoparticle arrays,[38,128–131] resulting in modified optical phenomena such as visible-wavelength chirality and Fano-like resonances. Because fluorescence quantum yields are low (10^{-7} – 10^{-6}) for bulk-like metal particles with diameters of a few to tens of nanometers,[132] photon emission is difficult to detect. Instead, the spatial organization of metal particles by the DNA was reported by changes in photon absorption and scattering. [38,128–131]

As size is reduced from the bulk nanoparticle regime to the limit of quantum-size clusters with 10-20 atoms and dimensions of up to a few Fermi wavelengths, the availability of non-radiative decay paths falls and fluorescence quantum yields rise.[13,133] Thus, the organization of quantum-size metal clusters on DNA constructs has the potential to produce optical

functionalities based on photon emission, rather than absorption or scattering, to report interactions that arise from near-field couplings. Fluorescence detection has numerous advantages, including intrinsically low background, high specificity, and availability of sophisticated techniques for single emitter detection and for direct imaging at length scales down to ~ 10 nm.

Producing such small metal clusters in aqueous solution requires the use of stabilizing ligands to prevent agglomeration. Fluorescent clusters of silver have been realized using a variety of ligands,[134] including dendrimers,[46] peptides,[135] and polymers.[136] Fluorescent silver clusters have also been stabilized by small molecules such as thiols,[137] glutathione,[138] and dihydrolipoic acid[139] as well as in microemulsions.[140] Particularly promising are Ag_N-DNA.[47] Recent work has demonstrated that monodispersed clusters with fluorescence quantum yields close to unity[53,90] can be isolated for sizes ranging from 10-24 silver atoms when these clusters are stabilized by suitably chosen DNA sequences. The ability to separate DNA-wrapped clusters that differ in cluster size by just one metal atom is essential to controlling optical properties: contrary to 10 nm metal nanoparticles which contain ~10^4 - 10^5 atoms,[141] and are consequently insensitive to single atom changes in size, metal clusters at the 10 atom size scale exhibit significant changes in optical properties with addition or subtraction of just one atom.[142,143]

Emerging applications for Ag_N-DNA include fluorescence signaling of target strands,[65,68,69,144] biosensors based on photoinduced electron transfer,[145] and logic devices that employ ion-tuned fluorescence.[146] The ability to tune silver cluster color throughout the visible and near-IR spectrum using sequence modification[13,48,93,147] is a unique feature that makes silver clusters particularly promising candidates for photonic elements within DNA-based,

nano-optical structures. An order of magnitude smaller than semiconductor quantum dots, the 1-2 nm hydrodynamic radii of Ag_N-DNA[148] would permit incorporation into DNA scaffolds at spacings that fully exploit the high resolution positioning attainable through current techniques of DNA nanotechnology.[27–30] Select oligomers have been shown to template silver clusters that are more photostable than high quality organic dyes,[63] facilitating detection of the emission spectra from individual silver clusters.[149] Lastly, the high polarization dependence of silver cluster emission, which appears to arise from a rod-like cluster structure,[53] is promising for realization of directional information processing along DNA-based optical arrays.

Despite these unique features of Ag_N-DNA, there is no evidence that such few-atom metal clusters can actually be assembled within nanoscale proximity. DNA nanotubes have been decorated with silver cluster emitters that were stabilized by single-stranded DNA extrusions from the double-stranded tube scaffold, but the separation distance between clusters was large (~1000 nm), and each emitter was held in the same cluster-templating sequence.[73]

Here we focus on assembling clusters of *different* size at 100 times smaller separations. Achieving such multi-cluster, nanoscale constructs is a challenging goal for DNA nanotechnology. For bare silver clusters, size-dependent free energies and electrochemical potentials[7,150] tend to drive structural reorganization of different sized clusters in an aqueous environment. The interaction of silver clusters with the DNA bases might, in principle, provide stability. However, solutions containing various Ag_N-DNA of unknown composition exhibited changes in fluorescence color and brightness when mixed with additional DNA oligomers,[66,151] indicating that the initially formed clusters were structurally altered when the overall DNA surroundings changed.

These results raise the question of whether silver clusters of different size, held in their particular DNA templates, can remain stable when brought together into one nanoscale construct, a step that necessarily alters the DNA environment. Currently this question cannot be answered from first principles because the mechanisms by which the DNA base composition sets the sizes and stabilities of fluorescent silver clusters are not understood.

Thus, whether DNA constructs can hold fluorescent silver clusters of different size at nanometer-scale separations is an open question that must be addressed in order to determine whether the unique properties of these clusters can be exploited in nanoscale, multi-color constructs. We approach this question by seeking to form bi-color, dual cluster assemblies using clusters with spectral properties that would enable Fluorescence Resonance Energy Transfer (FRET) if each silver cluster of different size retained its structural integrity.

4.2 Design and Experimental Methods

4.2.1 Dual cluster assembly schemes

In FRET,[152,153] an excited "donor" fluorophore transfers energy non-radiatively to a nearby "acceptor" fluorophore, which then emits a photon. The signature of FRET is emission from the acceptor (A) for excitation of the donor (D). FRET requires donor and acceptor to be at separations less than or comparable to a characteristic length scale, R_0, which depends on the spectral overlap of the donor emission spectrum with the acceptor absorbance spectrum. Since the underlying resolution of DNA scaffolds is typically 5-10 nm, testing whether silver clusters can be arrayed at length scales that exploit this resolution requires stable donor and acceptor clusters for which R_0 is in the 5-10 nm range. Here we design nanoscale DNA assemblies to incorporate such clusters and establish that select clusters exhibit both the requisite spectral

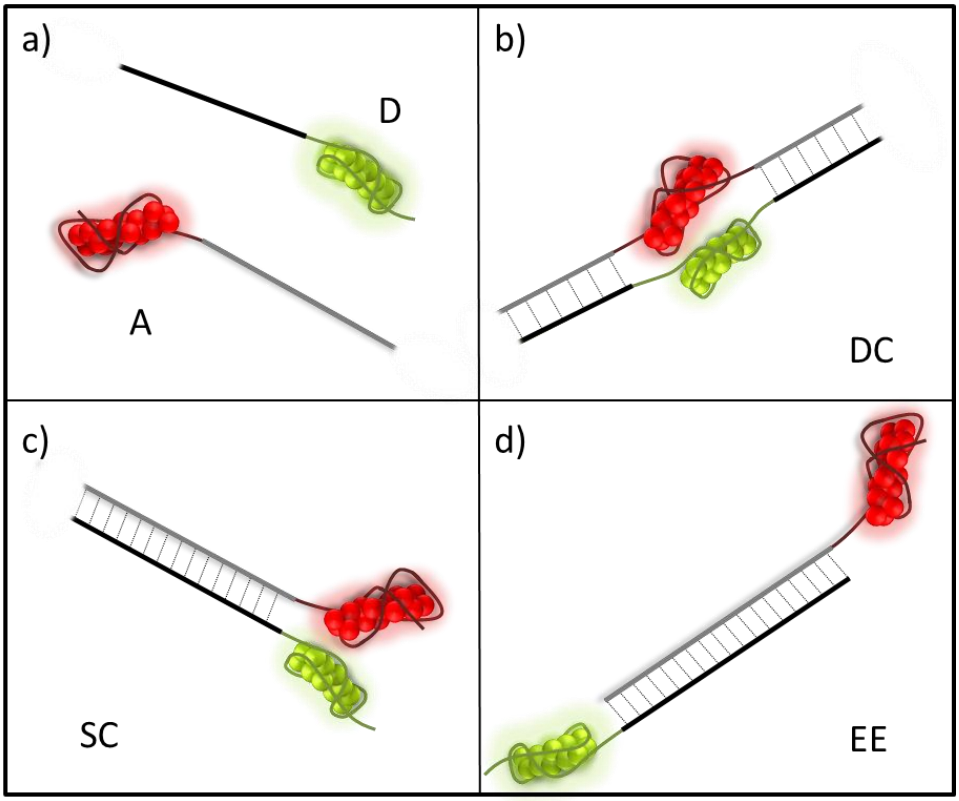

Figure 4.1. Designs for dual cluster assemblies. **(a)** Cartoons of the individual DNA-stabilized donor (D) and acceptor (A) silver clusters. Distinct cluster-templating sequences, shown as wrapped around the clusters, select cluster size and corresponding color. The extensions represent hybridization tail sequences. **(b)** The double clamp (DC) assembly design has complementary tails on both sides of the cluster-templating sequences. **(c)** The single clamp (SC) assembly design has hybridization tails on just one side of the cluster templating sequences. **(d)** The hybridization tails in the end-to-end (EE) assembly are designed to hold the clusters apart.

properties for FRET and the requisite structural stability to enable assembly into a single, nanoscale construct.

Figure 4.1 shows schematics for the dual cluster assembly designs. In each case, the green and red cartoons represent the donor (D; green) and acceptor (A; red) clusters, which are held within their respective DNA templates. The double-clamp (DC) assembly flanks these templates with complementary regions designed to clamp the clusters together at both ends. The single-clamp (SC) assembly holds the clusters together at just one end, on the same side of the hybridization clamp. The end-to-end (EE) assembly places the cluster templates at opposite ends of the clamp. The hybridization tails are sequences of A and T bases, with 13

Name	Sequence
A1 (SC, EE)	CACCGCTTTTGCCTTTTGGGGACGGATA – TTTT – ATTAATAAATAATATTTAAAATTTATTATA
A1 (DC)	AAAATTTATTATA – TTT – CACCGCTTTTGCCTTTTGGGGACGGATA – TTT – ATTAATAAATAAT
D (SC)	TATAATAAATTTTAAATATTATTTATTAAT – TTTT – TGCCTTTTGGGGACGGATA
D (EE)	TGCCTTTTGGGGACGGATA – TTTT – TATAATAAA TTTTAAATATTATTTATTAAT
D (DC)	ATTATTTATTAAT – TTT – TGCCTTTTGGGGACGGATA – TTT – TATAATAAATTTT
A2 (SC)	TTCCCACCCACCCCGGCCCGTT – TTTT – ATTA ATAAATAATATTTAAAATTTATTATA

Table 4.1. Names and sequences of DNA oligomers used in dual clamp assemblies

bases for each of the two tails in the DC assembly, and 30 bases in the SC and EE assemblies. Sequences are listed in Table 4.1. Melting temperatures were calculated using 1 μM DNA and 50 mM Na^+ in the DINAMelt[154,155] web server. We use ammonium acetate rather than buffers containing Na^+, but prior work[156] has shown that equal concentrations of Na^+ and NH_4^+ ions give similar T_m results.

4.2.2 Synthesis, purification, and assembly

Samples were prepared by mixing DNA, NH_4OAc and $AgNO_3$ (pH 7). Following 20 minute incubation at 4°C, solutions were reduced with freshly prepared $NaBH_4$. For A1 and D, final concentrations were 15 μM DNA, 188 μM $AgNO_3$, 94 μM $NaBH_4$ and 10 mM NH_4OAc. For A2, final concentrations were 5 μM DNA, 50 μM $AgNO_3$, 25 μM $NaBH_4$ and 10 mM NH_4OAc.

To obtain unequivocal evidence for or against formation of the desired bicolor assemblies, we separately purify the DNA strand monomers that contain the donor and acceptor clusters and then assemble the monomers into dual cluster constructs by hybridization of their

complementary tails. This approach is necessitated by the heterogeneity of as-synthesized silver-DNA solutions. Prior work has shown that reduction of silver ions on DNA strands typically produces multiple fluorescent and non-fluorescent products that contain different numbers of silver atoms.[52,53] Because the color, Stokes shift, and chemical stability vary widely amongst these products, hybridizing the unpurified solutions typically produces multiple fluorescence peaks at wavelengths that shift over time, providing little insight into whether the desired construct forms as one of many possible hybridization products.

Use of homogeneous solutions containing sufficiently stable clusters of known size is key to the work presented here. We identify DNA templates that previous studies have found to produce Ag_N-DNA with good quantum yields that are also stable enough to purify and identify by high performance liquid chromatography with in-line mass spectrometry (HPLC-MS),[53] and that have spectral characteristics suitable for FRET. The selected donor, D, is a green emitting cluster (560 nm peak emission) containing 10 silver atoms in a 19-base DNA template, as previously established by mass spectrometry on the purified material.[53] The primary acceptor, A1 (670 nm peak emission), a 15 Ag atom red-emitting cluster in a 28 base template,[53] was used in all design schemes (DC, SC and EE). A second acceptor, A2 (635 nm peak emission), a 16 Ag atom cluster in a 22 base template,[53] is used in the SC scheme to test the generality of silver cluster FRET. The fluorescence quantum yields of these clusters are 40%, 75% and 90% for D, A1 and A2, respectively.[53] All clusters are stable after HPLC isolation and re-concentration by spin filtration on time scales of several weeks to several months.

All silver-DNA solutions were purified using a Waters 2695 Separations Module with auto-injector and a Waters 2487 Dual Wavelength absorbance detector (10 μL volume), set to

monitor the visible peak of each Ag_N-DNA. Separations used linear gradients from 15% to 35% of B) 35 mM TEAA/MeOH with A) 35 mM TEAA/H2O on a 50 mm x 4.6 mm Kinetex C18 core-shell column with 2.6 μm particle size and 100 Å pore size (Phenomenex). Directly following HPLC purification, samples were dialyzed overnight into 50 mM NH_4OAc using 10 kDa MWCO MINI dialysis units (Thermo Scientific). The higher concentration buffer, relative to synthesis conditions, is used to promote hybridization of AT complementary tails.

Purified components were mixed with an estimated 2-fold excess of A strands and spun in 10 kDa MWCO centrifugal filters (Millipore) to remove solvent and increase total DNA concentration to ~1 μM. Solutions were left at room temperature for at least 30 minutes to allow complete hybridization. Hybridized solutions were then spun three times using 30 kDa centrifugal filters (Millipore) to remove excess DNA strand monomers. Following each spin, buffer was added to ensure a final concentration of at least 50 mM NH_4OAc.

4.3 Results and Discussion

4.3.1 Förster theory

According to standard Förster theory,[152,153,157] the spectral overlap integral, donor quantum yield, and relative orientations of the transition dipole moments of D and A determine the Förster distance, R_0:

$$R_0^6 = \frac{9\ln(10)Q_0\kappa^2(\int f_D(\lambda)\varepsilon_A(\lambda)\lambda^4 d\lambda)}{128\pi^5 n^4 N_A} \qquad (4.1)$$

Here, Q_0 is the donor fluorescence quantum yield, n is the index of refraction (1.33 for water), f_D is the donor emission spectrum normalized to unity integral over wavelength λ, ε_A is the extinction spectrum of the acceptor in SI units (cm^2/mole), N_A is Avogadro's number, and κ^2 is a unitless factor describing the relative orientation of donor and acceptor.

The FRET efficiency,

$$E_{FRET} = 1/[1 + (r/R_0)^6] \qquad (4.2)$$

gives the probability that excitation of the donor will result in emission from the acceptor, where r is the separation between the D and A silver clusters. For $r = R_0$, $E_{FRET} = 0.5$; efficiency decays rapidly for larger r. Because energy transfer to the acceptor reduces donor emission, E_{FRET} can be measured by comparing the peak emission intensity of the donor monomer, I_D, to the peak donor emission intensity from the D-A assembly, I_{DA}.[157] Assuming all donor clusters in solution are paired with acceptor clusters, the FRET efficiency is:

$$E_{FRET} = 1 - I_{DA}/I_D \qquad (4.3)$$

We note that fluorescence lifetime measurements can also be used to determine FRET efficiencies without assumptions about the fraction of donors paired to acceptors, if the lifetime difference between paired and unpaired donors is sufficiently large.[157] Here we present only intensity-based measurements.

4.3.2 FRET pair design

Figure 4.2 shows the well-separated emission spectra (solid lines) and absorbance spectra (dashed lines) of the HPLC-purified solutions of the donor cluster D (green traces) and acceptor cluster A1 (red traces). Spectra for acceptor A2 are shown in Appendix C.1 (Figure C.1). For each D-A pair, the absorbance peak of the acceptor is significantly redder than the donor absorbance peak. Thus excitation of the donor will not produce significant excitation of the acceptor, except in the case of FRET.

Significant overlap between donor emission and acceptor absorbance is also evident in Figure 4.2 and Figure C.1 (illustrated by shaded region). R_0 values depend on this spectral

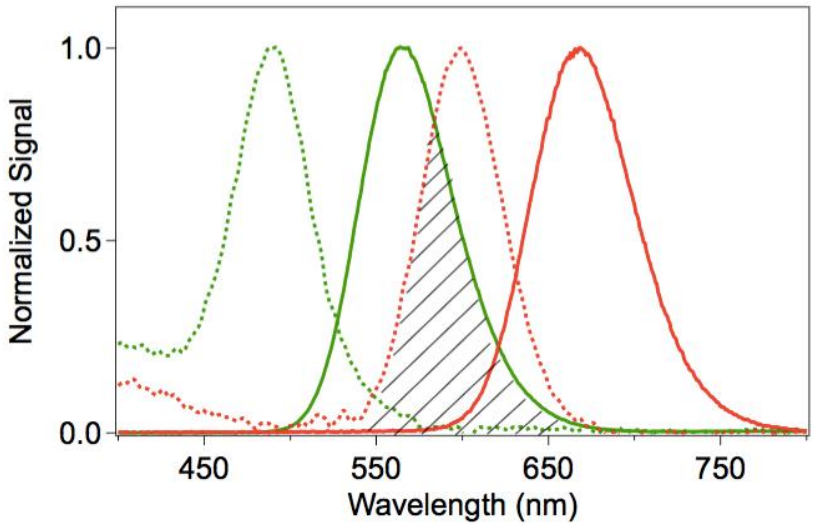

Figure 4.2. Normalized absorbance and emission spectra of donor D (green) and acceptor A1 (red) cluster. Dashed lines: absorbance. Solid lines: emission. The shaded region marks the range of spectral overlap between donor emission and acceptor absorbance.

overlap. We estimated visible extinction coefficients, ε_{vis}, of the clusters from absorbance spectra of the HPLC-purified solutions together with the fluorescence ($F_{\lambda max}$) and UV absorbance (A_{260}) chromatograms recorded during HPLC[52] (Figure C.2), where $F_{\lambda max}$ is the peak visible emission wavelength of the cluster.[53] Comparison of time-dependences of A_{260} and $F_{\lambda max}$ chromatograms provides an estimate of the purity after one round of HPLC. To estimate concentrations, we assume that A_{260} of the DNA-bound cluster is dominated by the DNA, as indicated by the similarity of UV spectra to the bare oligomers (Figure C.3). It appears that high energy transitions of the clusters contribute relatively little to absorbance near 260 nm, where the DNA bases absorb strongly, as expected from calculations for atomic silver chains.[56,158] The purity-scaled A_{260} and the known DNA extinction coefficient of the strand provide the estimated concentration of the cluster, which together with the peak A_{vis} gives the peak visible extinction coefficient, ε_{vis}. We find $\varepsilon_{vis} = 0.9 \pm 0.2 \times 10^5$, $1.4 \pm 0.2 \times 10^5$ and $2.1 \pm 0.7 \times 10^5$ $M^{-1}cm^{-1}$ for D, A1 and A2, respectively.

Because the orientations of the D and A clusters with respect to their DNA templates are unknown, we have no *a priori* knowledge of the orientation factor, κ^2. Thus we included a flexible linker sequence of three to four T bases between the cluster templates and the hybridization sequences to promote orientational averaging of the relative transition moments of D and A clusters in the SC and EE assemblies. In the case of randomized transition moment orientations, $\kappa^2 = 2/3$. Using this standard orientation-averaged value gives R_0 values of 6.2 ± 0.2 nm and 6.7 ± 0.4 nm for D-A1 and D-A2, respectively. The same T-linkers were used at both ends of the cluster template sequences for the DC assembly, although in this case the constraints imposed by the double clamp will tend to reduce orientational freedom. If such constraints, or Van der Waals or other interactions between the DNA-wrapped clusters, were to produce a net, time-averaged alignment of the transition dipoles, values for κ^2 could range from $\kappa^2 = 0$, for perpendicular alignment, to $\kappa^2 = 4$, for end-to-end parallel alignment.[157]

All three D-A1 assemblies are designed to form by hybridization of complementary tails appended to the cluster-nucleating templates. Prior work demonstrated that changes of just one base in a DNA strand can cause formation of different clusters.[86,159–161] Thus, appending a hybridization tail sequence to the cluster templating sequence could potentially destabilize the desired cluster in favor of other silver-DNA products. Because homopolymer strands of A and T bases do not form fluorescent clusters,[88] we chose to append complementary tails comprised of mixed A and T sequences[65] to the D and A1 (or A2) cluster templating sequences. The calculated melting temperatures for these complementary tails are $T_M = 42$, 30 and 42 °C for the SC, DC and EE assemblies, respectively.

Because the lengths of the templating sequences with appended tails exceed 50 bases, cluster sizes could not be determined using mass spectrometry (the propensity for DNA-salt

associations results in poor ionization efficiencies and challenge mass spectrometry of long DNA strands).[162] Thus, to test whether the addition of hybridization tail and linker bases resulted in formation of differently structured clusters, we compared spectral properties of purified D and A clusters formed on only the template strands with properties of clusters formed on the template strands with appended tails. The strand alterations leave spectral properties of unhybridized D, A1 and A2 emitters unaltered (Figure C.4). Because the optical properties of Ag_N-DNA are sensitive to changes in cluster size of just one atom, as well as to cluster shape,[53,56,158] the lack of spectral changes with hybridization tails shows that the clusters themselves are essentially unaltered.

The AT tails we append might still bind non-fluorescent silver products,[88] which could potentially hinder hybridization. To demonstrate that any such non-fluorescent clusters do not inhibit donor-acceptor binding, 10% native PAGE gels were run to compare D-A1 and D-A2 pairs with their respective monomer components. We additionally measured melting curves for hybridized pairs (Figure C.5) and found good agreement with calculated melting temperatures for the complementary tails. Measured melting temperatures for the SC and DC assemblies are $T_{M,meas}$ = 49 and 30 °C, respectively.

The hybridization was carried out with roughly a 2-fold excess of A-bearing cluster strands in order to minimize the presence of D clusters that are not incorporated into D-A pair assemblies. This is important because estimated FRET efficiency, $E_{FRET} = 1\text{-}I_{DA}/I_D$, is accurate only if the D-A pair solution contains no unhybridized D monomers and no hybridized assemblies containing D clusters but not A clusters. The pair solutions were prepared by mixing purified D and A components in 50 mM NH_4OAc at room temperature and incubating for 30

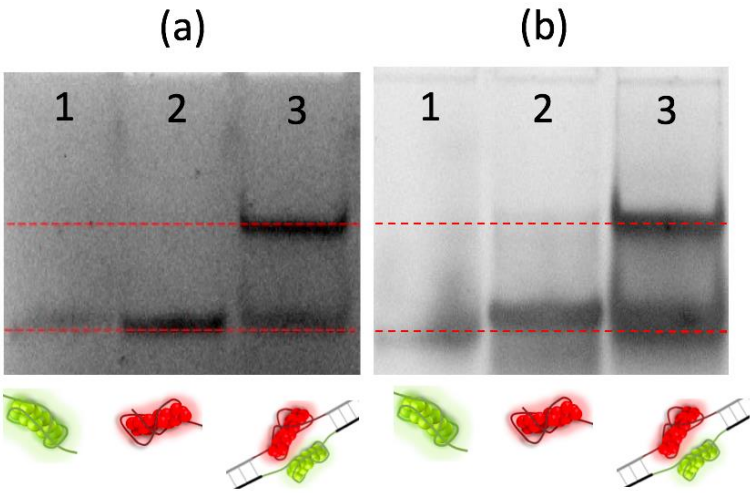

Figure 4.3. Gel shift assay of the silver cluster monomers and the double-clamp (DC) assembly. (a,b) Lane 1 contains the D cluster monomer, Lane 2 contains the A1 cluster monomer, and Lane 3 contains the D-A1 pair. The lower red lines mark the monomer bands and the upper red lines mark the DC assembly. (a) Unstained gel. The UV lightbox excites the fluorescent silver clusters in all lanes (b) Stained gel.

minutes. To remove unassembled donor strands that would mask FRET, hybridized solutions were then spin-filtered using 30 kDa centrifugal filters (SI, Figure C.6).

Figure 4.3 shows a representative gel shift assay of the double-clamp D-A1 pair solution. The purified D and A1 monomers and the D-A1 pair solution were run in lanes 1, 2 and 3, respectively. In the unstained gel (Figure 4.3a), UV excitation reveals the bands that contain fluorescent Ag_N-DNA, while SYBR gold staining (Figure 4.3b) shows all DNA products. The upper gel bands in the pair lanes confirm hybridization and fluorescence from the D-A assembly (Figure 4.3a,b). The lower gel bands in lanes 3 that co-traveled with the unassembled cluster-bearing strands in lanes 1 and 2 show the additional presence of unassembled strands in the pair lane. This is likely due to partial melting of the assembled pair (T_M = 30°C) by the heat generated during electrophoresis, though excess A1 cluster-bearing monomers that were not removed by spin filtering could also contribute.

The clear presence of D-A bands in the gel suggests that FRET should be observable in solution if SC and DC assembly designs do succeed in holding intact D and A clusters at

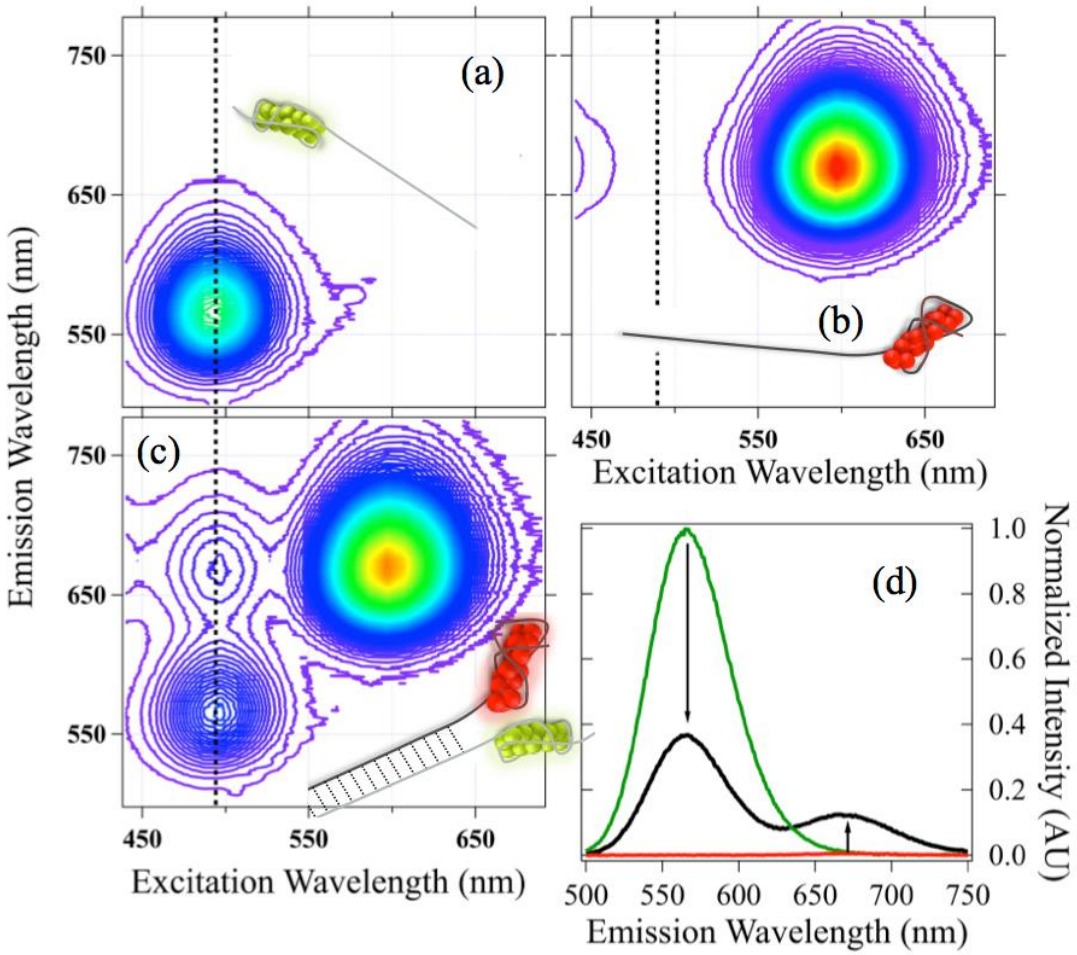

Figure 4.4. Inter-silver cluster FRET. (a) Fluorescence contour map for the 10 silver atom donor cluster, D. (b) Fluorescence contour map for the 15 silver atom acceptor cluster, A1. (c) Fluorescence contour map for D-A1 single clamp (SC) assembly. Acceptor emission appears at donor excitation wavelengths, a signature of FRET. (d) Data for 490 nm excitation (dotted line in (a)-(c)). Black line: emission spectrum of the D-A1 assembly. Green line: emission spectrum from D alone. Red line: emission spectrum from A1 alone. In the D-A1 SC and DC assemblies, FRET quenches the donor emission and dramatically increases the acceptor emission.

separations comparable to R_0. Both SC and DC schemes (Figure 4.1) are expected to bring distinct Ag clusters within the 6 nm range and thus enable FRET. The EE design, however, separates D-A pairs by at least 10 nm, so in this case we expect negligible FRET.

4.3.3 Spectral evidence of FRET

Figure 4.4 shows emission contour plots for the single-clamp D and A1 monomers (Figure 4.4a, b) and hybridized single-clamp D-A1 solution (Figure 4.4c). The monomer emission

spectra have been normalized by their respective concentrations relative to the spin-filtered D-A1 solution, as measured from the corresponding visible absorbance peaks (SI, Figure C.7), and all spectra have been normalized to the intensity of the Xe arc lamp used for excitation. Figure 4.4b shows that emission from the A1 monomer is not observed within the excitation range of the donor cluster (peak donor excitation is 490 nm, indicated by the dashed line). However, upon hybridization, excitation of the donor cluster produces emission from the A1 cluster, while simultaneously reducing donor emission (Figure 4.4c). These are unambiguous signatures of FRET.

Both of these phenomena are also clearly seen in the contour slice at the D cluster's maximum excitation wavelength, 490 nm (Figure 4.4d). Emission of the isolated donor (green line) is partially quenched in the hybridized construct (black line), while acceptor emission rises dramatically relative to the isolated A1 monomer (red line). Spectral characteristics for FRET displayed by SC (Figure 4.4) and DC (Figure C.8) D-A1 pairs demonstrate that D and A1 clusters are successfully brought within nanometer proximity. Similar spectra were observed for the SC D-A2 assembly (Figure C.9).

4.3.4 Thermal cycling

To confirm that the observed FRET signal does, in fact, result from strand hybridization and not an accidental transfer of one cluster onto the other strand, fluorescence from D-A1 pair solutions was monitored during thermal cycling. Figure 4.5 shows representative thermal data for the D-A1 double clamp (DC) assembly, after correcting for the temperature dependence of the emission from D and A1 individually (Figure C.10). The melting point of the double-clamp

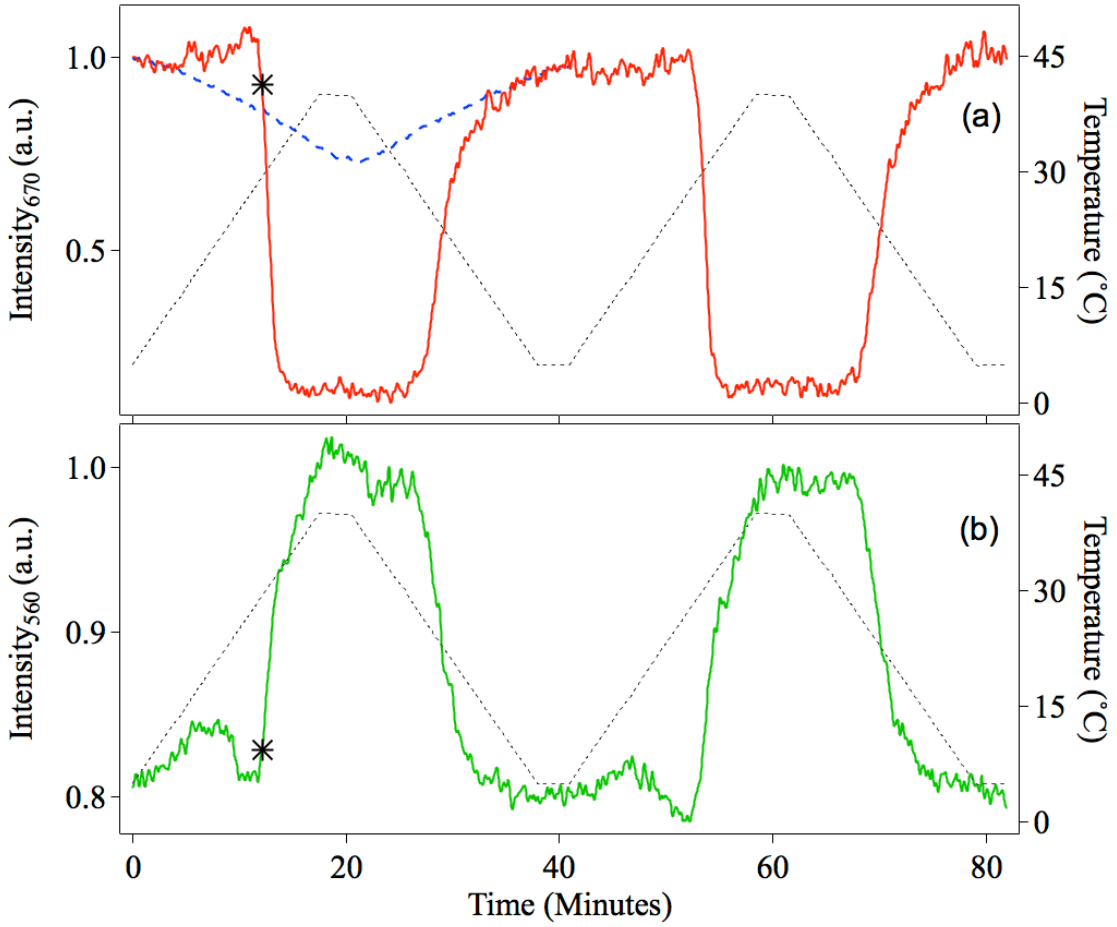

Figure 4.5. Fluorescence signals from (a) acceptor, with detection at 670 nm and (b) donor, with detection at 560 nm in the double clamp (DC) D-A1 pair, using 490 nm excitation, as the temperature is cycled twice from 5 to 40°C (black dashed lines, right axes). Black stars indicate the melting temperature of the assembly as determined by A_{260} (Figure C.5). The blue dashed line (a) shows the temperature dependence of A1, using 600 nm excitation. Data were normalized to remove effects of photobleaching and temperature-dependent monomer brightness (Figure C.10)

assembly was determined to be $T_M \sim 30°C$ by monitoring absorbance at 260 nm as a function of temperature (Figure C.5).

Exciting D-A1 at 490 nm, we monitor both 670 nm emission intensity, corresponding to fluorescence from A1 (Figure 4.5a), and 560 nm emission intensity, corresponding to fluorescence from D (Figure 4.5b), as the temperature is cycled twice from 5°C to 40°C over a period of 80 minutes. At low temperatures, the FRET pairs are hybridized and 670 nm fluorescence from D-A1 is observed. As the temperature is increased past the melting point

(indicated by black stars), 670 nm emission drops by roughly a factor of 7, which is significantly greater than the expected heating effects[163] for the A1 monomer (dashed blue trace, Figure 4.5a). We note that residual 670 nm emission is expected for the D-A1 pair at the maximum temperature of 40°C due to incomplete melting of the hybridization tails.

Thermal modulation of 670 nm emission in D-A1 is anti-correlated with the temperature dependence of 560 nm emission from the donor cluster (Figure 4.5). At low temperatures, well below T_M, donor quenching by FRET produces lower intensity emission, while increasing T above T_M removes the FRET loss channel for the donor, resulting in brighter emission (Figure 4.5b).

4.3.5 Non-complementary tails

As an additional control to confirm the correlation between strand hybridization and FRET, we performed the same experiment on D and A1 clusters formed on strands with *non*–complementary tails and did not observe FRET. The requirement for complementary tails and the observed intensity modulation around the hybridization melting point demonstrates that FRET pairs are indeed forming *via* strand hybridization.

4.3.6 FRET efficiency estimates

The FRET efficiency varied amongst the three dual-cluster design schemes. As expected, the EE scheme produced no discernable FRET signal. This lack of FRET signal is reasonable because, with a cluster separation distance of 10 nm or more, the calculated FRET efficiency for this D-A1 pair in the EE scheme is 4% or less. FRET was observed for both SC and DC schemes. For the SC assembly, we used two normalization methods to determine the decrease

in donor emission from the assembled D-A cluster pair solution relative to the D cluster monomer (Figure 4.4d, Eq. 4.3). The first method of normalizing relative concentrations involved using the ratio of 560 nm emission intensities from D monomer and SC D-A pair solutions at temperatures well above T_M, where there is no FRET quenching. These relative concentrations agreed well with those made using the second method, comparing the visible peak absorbance values at 490 nm in solutions of the D monomer alone and of D-A assemblies (Figure C.7). The two estimates from these methods yielded E_{FRET} = 0.6-0.65. For the DC assembly, we found E_{FRET} = 0.6 by again using the relative 560 nm intensities above T_m. These estimates of E_{FRET} from the partial quenching of donor emission provide a lower bound on the true FRET efficiency because the possible presence of hybridized strands that lack an acceptor, or unhybridized strands containing only the donor cluster, will reduce the apparent FRET-induced quenching. We conclude that the SC and DC assemblies hold the D and A acceptors at separations within ~ 5-6 nm.

4.3.7 Silver cluster and organic dye pair

For comparison to inter-silver cluster FRET, we also studied a D-A pair in which the donor is an organic dye and the acceptor is a silver cluster. For this construct, the 3' end of the DNA template sequence for silver cluster A1 was labeled with a donor Rhodamine (Rh) dye molecule, with peak excitation at 570 nm and peak emission at 590 nm. Four T bases were inserted between the dye and the template sequence to promote orientational averaging of the relative moment alignments of the dye and the cluster. The A1 cluster was synthesized directly on the Rh-labeled DNA and purified by HPLC.

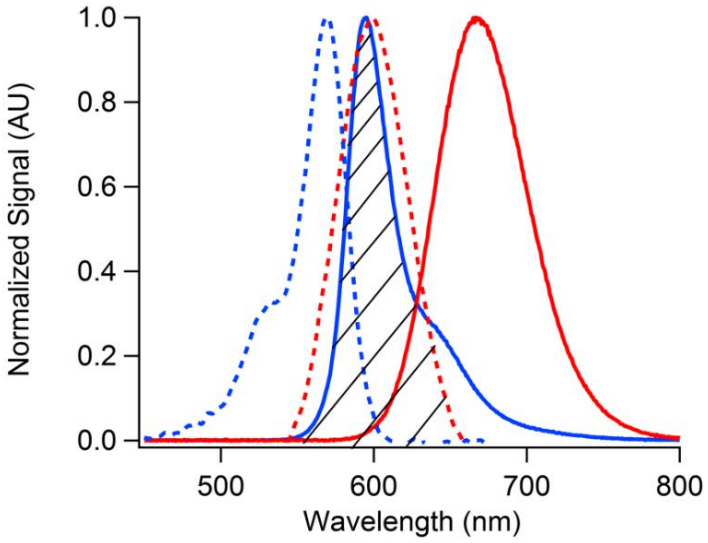

Figure 4.6. Spectra of the Rh dye attached to the A1-templating DNA strand, without the A1 cluster (blue) and spectra of the A1 silver cluster (red). Dashed lines are absorbance and solid lines are emission.

The characteristic vibronic sidebands of organic dye molecules are apparent for the Rh-labeled DNA in Figure 4.6 as the short wavelength shoulder in the absorbance and the long wavelength shoulder in the emission spectrum. These features are also apparent in the corresponding fluorescence contour map (Figure 4.7a). Such structure is strikingly absent in the corresponding spectra for the Ag_N-DNA synthesized on the DNA template alone (Figure 4.6 and 4.7b). This absence of vibronic structure in emission spectra from Ag_N-DNA is also a feature of individual silver clusters measured in the limit of very low temperatures (2K), attesting to the clusters' metal-metal bonding character.[53]

Due to the vibronic shoulders on the Rh donor absorbance and emission spectra, the Rh-A1 spectra (Figure 4.7c,d) have a more complex appearance than for the dual silver cluster pair spectra (Figure 4.4). Nonetheless, we observe clear FRET signals from the Rh-A1 pair. From spectral characteristics of Rh and A1, we calculated R_0 to be 7.2 ± 0.2 nm, assuming $\kappa^2 = 2/3$. The decrease in donor emission gives $E_{FRET} \approx 67\%$ (a lower limit estimate since Rh-labeled DNA strands that do not hold a A1 cluster may also be present). For comparison, dye-based

FRET studies of thymine homopolymer DNA strands with lengths of 10 to 40 bases found comparable FRET efficiencies at 18-base strand lengths,[164] after correcting for the smaller R_0 (6 nm) of the dye pair used in that study. Prior studies[53] indicated that the A1 cluster attaches to several bases within the 28-base DNA template, effectively making those bases part of the cluster itself. Thus ~ 18 bases is a reasonable overall length for the single-stranded DNA between the Rh dye molecule and the A1 cluster.

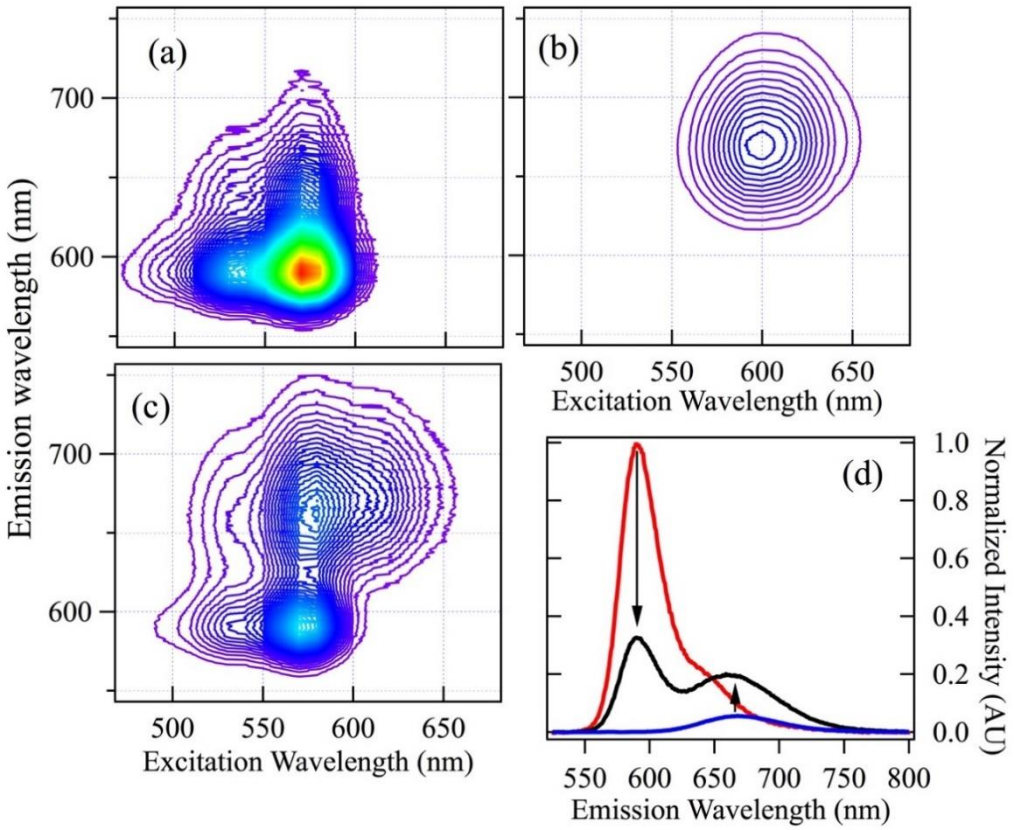

Figure 4.7. Rhodamine-silver cluster FRET. (a) Fluorescence contour map for the Rh donor dye, attached to the DNA strand. (b) Fluorescence contour map for the 15 silver atom acceptor cluster, A1, attached to the same DNA strand in (a), but with no dye (c) Fluorescence contour map for Rh-A1 assembly. (d) Data for 570 nm excitation (dotted line in (a)-(c)). Black line: Emission spectrum of the Rh-A1 assembly. Blue line: emission spectrum from donor alone. Red line: emission spectrum from acceptor alone. In the Rh-A1 assemblies, FRET quenches donor emission and dramatically increases acceptor emission.

4.3.8 Spectral and structural fidelity

We now turn to the issue of the structural stability of the Ag_N-DNA. If assembly into dual cluster structures altered the number of silver atoms or significantly changed cluster shape, we would expect large spectral shifts in the spectra of D-A assemblies relative to those of individual clusters. Figure 4.8 shows that instead, the clusters in the bi-color assemblies exhibit the same spectral features as the individual clusters. To display the lineshapes, the emission data is plotted *versus* energy for the single clamp D-A1 assembly and its individual cluster components (Figure 4.8a) and for the Rh-A1 cluster assembly and components (Figure 4.8b). The D-A1 data can be fitted accurately by superposition of two Gaussians, with peak wavelengths that match those of the individual clusters within 2 nm. We conclude that the D and A clusters retain their individual structures when incorporated into nm-scale, dual-cluster assemblies.

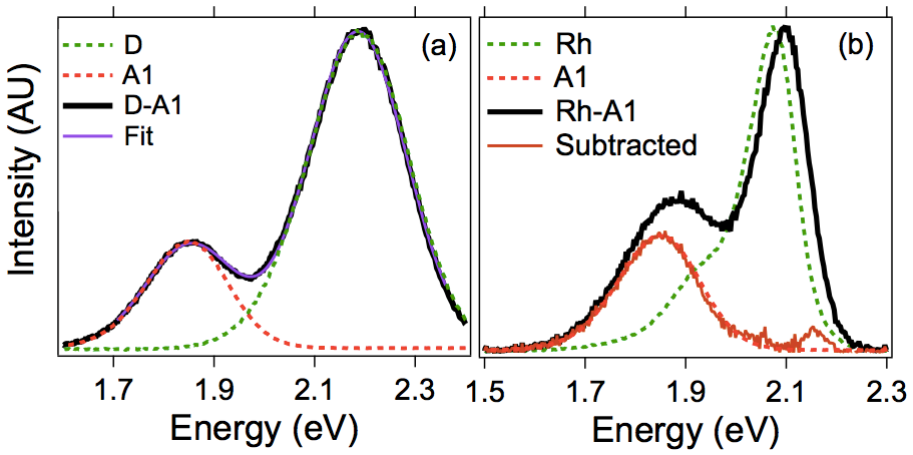

Figure 4.8. Analysis of the spectral stability of silver clusters in bi-color assemblies. Data are plotted *versus* energy to display lineshapes. (a) Black line: data for the SC dual silver cluster assembly. Green and red lines: data for D and A1 clusters. Purple line: dual Gaussian fit to dual cluster assembly data. The fitted wavelengths agree with those of the separate clusters to within 2 nm. (b) Black line: data for the Rhodamine-A1 pair. Green and red lines: Spectra of Rh dye only on the DNA strand and A1 cluster only on the templating DNA strand, respectively. Orange line: Data after subtracting a blue-shifted Rh spectrum overlie the spectrum of the A1 cluster.

For the Rh-A1 pair, the Rh dye peak blue-shifts 6 nm relative to the dye on the same DNA strand but without the cluster. To extract the spectrum of the A1 cluster, we subtracted a rigidly shifted dye spectrum. The resulting estimate of the cluster spectrum (orange line, Figure 4.8b) is nearly indistinguishable from that of the cluster alone (red dashed line). Apparently cluster formation affects the dye molecule fluorescence, perhaps due to altered dye-base pi stacking arising from changes in base orientation upon cluster formation. Variations in the spectral properties of another commonly used fluorescent dye molecule, Cy3, due to changes in the dye molecule's local environment have also been demonstrated.[165] However, the silver cluster in the Rh-A1 assembly appears to be unchanged in the presence of the dye.

4.3.9 Necessity of purification

All results discussed thus far pertain to D-A pairs assembled from solutions of purified Ag_N-DNA. It would be desirable to create dual cluster constructs more simply, without purifying the individual Ag_N-DNA components. An obstacle to this approach is the heterogeneity of products produced by reduction of silver ions on DNA templates. To investigate the necessity of a purification stage, we attempted several different strategies to observe FRET without pre-purification for the EE, DC and SC configurations using the silver clusters D and A1. These one- and two-pot methods rely instead on sufficient chemical yields of D and A1, with respect to other products, to result in a clear spectral signature of FRET. A summary of these attempts is in Appendix C.11. None resulted in any significant FRET signal, indicating insufficient chemical yields of the desired dual cluster assembly when using the D and A1 templates. When the relation between DNA sequence and cluster structure is better

understood, it may become possible to select stabilizing templates that produce good yields of multi-cluster constructs without preliminary purification stages.

4.4 Conclusions

We have brought distinct silver nanoclusters, with sizes in the range of 10-20 atoms, into nanometer proximity. This was accomplished by using strand hybridization to merge distinct clusters of different size into nanoscale constructs. The success of the assemblies was verified using gel shift analyses and by monitoring FRET, an optical readout only occurring when donor-acceptor pairs are separated by just a few nanometers. To date, the FRET signatures are also temporally stable over times exceeding one month.

We find that both of the Ag_N-DNA participating in FRET preserve their spectral properties, indicating that each cluster maintains its original structure. The absence of vibronic structure in the cluster spectra simplifies the recognition of FRET features, relative to organic dyes. We find that Rhodamine is less spectrally stable upon assembly than the silver clusters themselves.

Prior studies of heterogeneous solutions produced by different template strands reported spectral changes upon altering the DNA environment. The structural stability we observe shows that appropriate strand selection results in clusters that are suitable for use in DNA-based nano-optical structures.

5. Atomically Precise Arrays of Fluorescent Silver Clusters: a Modular Approach for Photonics on DNA Nanostructures.

Adapted with permission from: Copp, S. M.; Schultz, D. E.; Swasey, S.; Gwinn, E. G. Atomically Precise Arrays of Fluorescent Silver Clusters: A Modular Approach for Metal Cluster Photonics on DNA Nanostructures. *ACS Nano* **2015**, *9* (3), 2303–2310. [72] *Copyright 2015 American Chemical Society.*

5.1 Introduction

Chapter 4 showed that two Ag_N-DNA can be held at nanoscale separations while retaining their individual structures and demonstrated that this arrangement is thermodynamically stable with proper choice of DNA templates. Now, we pursue the challenge of arranging multiple atomically precise silver clusters on a DNA breadboard. This potential was proposed by early works on Ag_N-DNA,[48] yet the challenges of obtaining high chemical yields of monodisperse Ag_N-DNA solutions hindered its realization. Now, combining the efficient HPLC-MS purification methods for Ag_N-DNA[52,53] with the improved understanding of the role of sequence for selecting fluorescent silver clusters[70] (Chapter 3), we develop a modular approach to arrange atomically precise silver clusters at programmed locations on a DNA nanostructure.

DNA nanotechnology enables nanoscale arrangement of optical elements, such as organic fluorophores, noble metal nanoparticles, and colloidal quantum dots, onto DNA scaffolds that self-assemble in diverse shapes and sizes.[25,27,28,34,35,166] Attachment of a single-stranded DNA oligomer (ssDNA) to a molecule or nanoparticle enables positioning at programed sites on DNA scaffolds, by hybridization with complementary ssDNA extrusions on the scaffolds.

Several groups have already employed hybridization to position optical elements on DNA nanostructures[34,35,128] and to demonstrate intriguing optical phenomena, including fluorescence resonance energy transfer (FRET),[37] optical chirality,[38,39] and surface-enhanced Raman scattering.[40]

Achieving desired optical properties from arrays of many elements demands stringent control over the individual elements. This is challenging for nanoparticles due to the difficulty of precisely controlling size, shape and surface morphology.[167] In contrast, ligand-protected metal clusters provide a route to atomically precise control of size and shape,[21] and therefore precise control over the optical response of cluster assemblies. Metal clusters are remarkable for their unique combination of metallic and molecular attributes, which can produce metal-like optical response from collective excitations of delocalized valence electrons while also exhibiting molecule-like high fluorescence quantum yields, related to the sparse density of states.[21,53,168,169] Crystallization of superlattices[170] comprised of silver clusters protected by *p*-MBA ligands[97] was recently achieved. However, nanoscale arrangement of metal clusters by DNA-mediated methods, or by any other method achieving controlled nanoscale placement, is still an unrealized goal. Developing methods for arranging atomically precise metal clusters on the nanoscale is therefore a critical step towards harnessing their unique potential for applications in nanoscience.[171,172]

Ag_N-DNA[47] are a new class of optical nanomaterial with unique advantages for arrangement on DNA scaffolds. Now employed in many applications,[60] Ag_N-DNA are appealing for their tunable fluorescence colors, ranging from blue-green to near-IR,[48,93] high fluorescence quantum yields,[53] and proposed bio-compatibility. Containing only N ~ 10-30 Ag atoms,[53] each silver cluster is stabilized by base motifs within a DNA template,[70] whose

sequence selects the size of the cluster core and thus fluorescence color,[58] and whose linear arrangement, as constrained by the DNA backbone, imposes a unique, rod-like cluster shape.[53,58,59,107] This anisotropic shape is responsible for the wide color range of Ag_N-DNA and for their strong polarization dependence,[53,57] which has fascinating potential for directionally-dependent DNA-based optical materials.

These properties make Ag_N-DNA uniquely suited for arrangement into atomically precise arrays on DNA scaffolds. While previous studies have used the preference for Ag cluster formation onto ssDNA to synthesize Ag_N-DNA in linear arrays,[73,173] control of optical properties and spatial separations was not achieved due to the heterogeneous products formed during synthesis: typical templates give < 10% chemical yields of a specific Ag_N-DNA, along with non-fluorescent majority products that have wide-ranging silver and DNA compositions.[52,53] Thus, in addition to the intended cluster, dark Ag products and Ag_N-DNA with the wrong fluorescence color decorate DNA scaffolds that are directly subject to Ag cluster synthesis. This heterogeneity of synthesis products is a nearly universal feature of Ag_N-DNA that has been ignored in most prior studies.

Achieving atomically precise arrays of metal clusters requires a different approach. To realize decoration of DNA nanostructures with monodisperse silver clusters, we develop a modular, generalizable method to attach N-atom silver clusters (Ag_N-DNA) onto individual selected double helices of 10-helix tiled DNA nanotubes (NT)[26] (Figure 5.1), chosen as prototypical scaffolds for linear arrays. We demonstrate this method with clusters of two sizes and distinct colors, N = 15 with 670 nm peak emission and N = 14 with 640 nm peak emission. We first describe design methods for the bifunctional DNA host strands that combine templates for fluorescent Ag_N-DNA with linker sequences, which both preserve cluster structure and

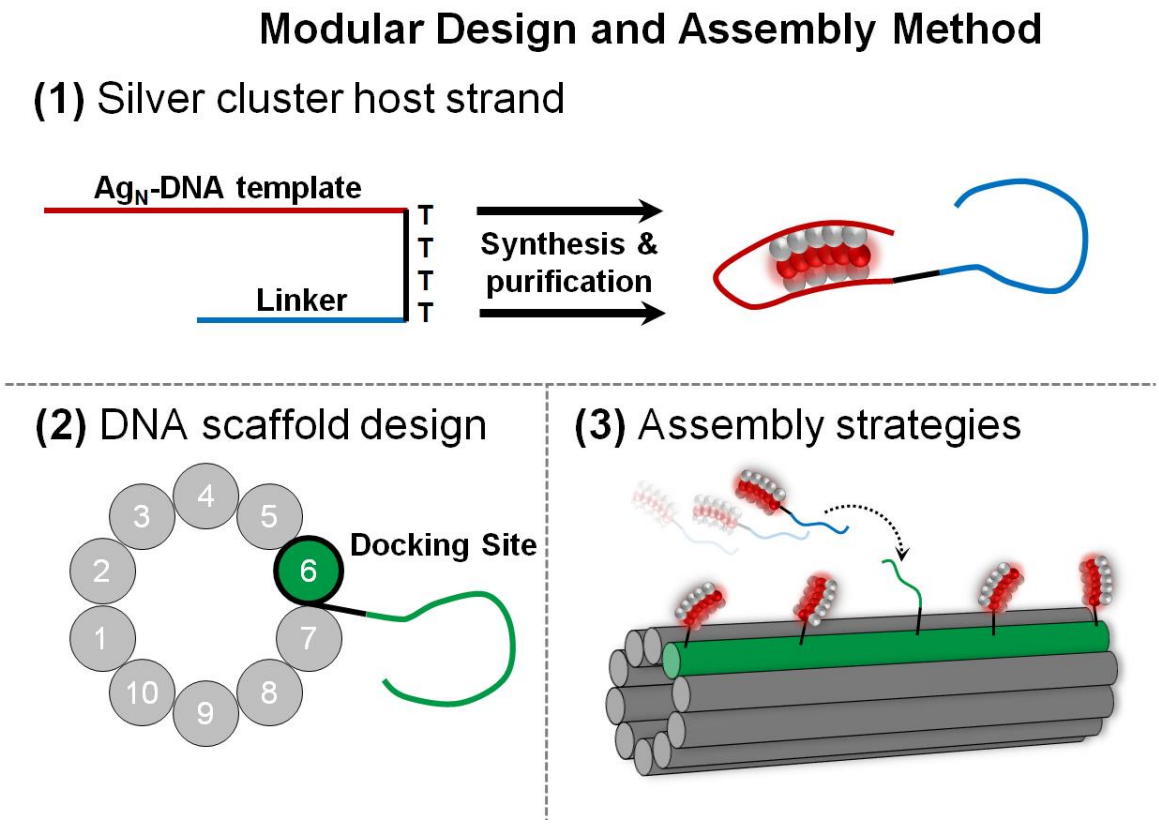

Figure 5.1: Attachment of monodiperse Ag_N-DNA to DNA nanotubes (NT). NT self-assemble as ten interwoven helices from ten 42-base strands reported previously,[26] with one strand extended here by a select 18-base "docker" sequence. a) Modular cluster host strands constrain clusters to templating regions (red) with selection of non-interacting linker regions (blue). This allows Ag_N-DNA purification, and thus selection of cluster size, N, prior to assembly on NT. b) The docker (green), complementary to the linker, is appended to one of the strands that forms the NT and extrudes from the NT (end-view schematic). c) NT decoration is mediated by Watson-Crick base pairing between diffusing linkers and extruding dockers that are spaced by 7.1 nm on the NT.

hybridize to densely-spaced attachment sites on NT. Next, NT attachment site design is presented. Confocal microscopy verifies NT decoration with Ag_N-DNA, and fluorescence spectroscopy verifies structural stability of Ag_N-DNA on NT.

5.2 Experimental Methods

5.2.1 Synthesis, purification, & characterization

DNA templates for Ag_N-DNA were ordered from Integrated DNA Nanotechnologies (IDT) with standard desalting. Template DNA was mixed with $AgNO_3$ in a 10 mM NH_4OAc

ammonium acetate buffer and incubated at room temperature for 20 minutes. DNA-silver solutions were then reduced using $NaBH_4$ and mixed well. Final concentrations for synthesizing Ag_{15}-DNA and Ag_{14}-DNA were 15.0 μM DNA, 188 μM $AgNO_3$, and 93.8 μM $NaBH_4$ (corresponding to 12.5 Ag atoms per host strand; Ag/base ratios vary with host strand length). Ag_{14}-DNA purified by HPLC was synthesized using 25 μM DNA, 313 μM $AgNO_3$, and 156 μM $NaBH_4$ (12.5 Ag atoms per host strand). Samples were stored at 4°C overnight prior to spectral characterization and/or purification using reverse-phase high-performance liquid chromatography (HPLC). Emission spectra were collected with a thermoelectrically cooled array detector (Ocean Optics QE65000) and SpectraSuite software (Ocean Optics). A UV LED was used to universally excite fluorescence of Ag_N-DNA.[50]

A 2695 Separations Module with auto-injector and 2487 Dual Wavelength absorbance detector (10 μL volume), set to monitor the visible peak of each silver cluster, were used to perform HPLC (Waters). Full emission spectra were also collected every second by the Ocean Optics QE65000, using the UV LED to universally excite all Ag_N-DNA products. A first separation of different Ag_N-DNA species was achieved using linear gradients of H_2O and MeOH in the ion-pairing agent, 35 mM triethylamine acetate (TEAA), to a 50 mm × 4.6 mm Kinetex C18 core-shell column (Phenomenex). The second round of purification, by the same instrument and column but in-line with the MS, used running buffers with 400 mM 1,1,1,3,3,3-hexafluoro-2-propanol in separate H_2O and MeOH solutions adjusted to pH 7 with triethylamine. Samples were purified using a 1% per minute linear gradient of 15-35% methanol running buffer. Ag_N-DNA were returned to 10 mM NH_4OAc by spin filtration with Amicon Ultra 3 kDa membrane centrifugal filters (EMD Millipore).

Mass spectra were collected every second over a 500-3000 *m/z* range on a Waters QTOF2 in electrospray ionization negative mode. Instrument parameters were set to 2 kV capillary voltage, 30 V cone voltage, 10 V collision energy, 100 ^{O}C source and 120 ^{O}C desolvation temperatures. Samples were introduced into the MS at 10 μL/min through a splitter connected to the HPLC, allowing simultaneous collection and characterization.

5.2.2 DNA nanotube assembly

10-helix DNA nanotubes[26] (NT) were formed with HPLC-purified oligomers from IDT (sequences provided in Table D.1). For fluorescein-labeled NT, U1 oligomers were ordered from IDT with a fluorescein dye (FAM) attached to the 5' end. The ten NT-forming oligomers were mixed in 0.2 mL PCR tubes, each oligomer at a final concentration of 1.4 μM, in 40 mM NH_4OAc and 12 mM MgOAc for a final volume of 50 μL. Mixtures were annealed using a Mastercycler personal (Eppendorf) to heat solutions to 90°C for 5 minutes and then cool solutions from 65°C to 50°C in 0.5°C steps, 50 minutes per step. After annealing, NT were stored at 4°C for no more than several days until use. For NT with varying % dockers, U6 and U6-docker site oligomers were mixed at appropriate ratios for a total final concentration of [U6 + U6-linker] = 1.4 μM.

5.2.3 Nanotube decoration with Ag_N-DNA

To attach Ag_N-DNA to NT, Ag_N-DNA was added to solutions of annealed NT, at 5 times greater Ag_N-DNA concentration than the concentration of docker sites appended to NT, for final NT concentration of 0.14 μM and a final Ag_N-DNA concentration of $5 \times$ (% docker) $\times$ 0.14 μM. For NT decorated with twice-purified Ag_{15}-DNA, final NT and Ag_{15}-DNA

concentrations were halved to conserve material. Buffer concentration was maintained at 40 mM NH_4OAc and 12 mM MgOAc after mixing. Mixtures were stored for at least 1 hour at room temperature in the dark before imaging.

5.2.4 Microscopy

Standard microscopy coverslips (#1.5) were sequentially sonicated for 15 minutes in acetone, ethanol, and 18.2 MΩ·cm H_2O (Milli-Q, Millipore) and then dried in an oven. Glass slides were rinsed well in 18.2 MΩ·cm H_2O and then ethanol and subsequently dried under filtered N_2. For samples embedded in polyvinyl alcohol (PVA), 16 kDa PVA (Acros Organics) was dissolved in H_2O at 5 mg/mL. 1 μL of NT-Ag_N-DNA mixture was added to 90 μL of PVA and 9 μL H_2O and immediately spun-cast on clean coverslips at 1680 RPM for 100 s. Coverslips were fixed above the microscope objective on a clean glass slide. Widefield and confocal fluorescence microscopy were performed using an inverted Olympus DSU (Spinning Disk) confocal with a Hamamatsu ImaEM CCD camera (C9100-13) and Hg arc lamp illumination. A 89000 ET Sedat Quad Filter Set (Chroma) was used to image fluorescein-labeled NT and Ag_{14}-DNA, and a Cy5-4040A filter set was used for imaging Ag_{15}-DNA (Semrock). A UPlanSApo 100X oil immersion objective, with 1.4 numerical aperture (NA) (Olympus) was used to collect all images, with standard acquisition times of 1 s. For widefield images of NT with 10% docker sites (Figure 5.2e, not including inset), the spinning disc was removed to increase collected fluorescence signal. Confocal images of NT with 10% docker sites were collected with 10-15 s exposure times. MetaMorph software was used to control image acquisition (Molecular Devices, Inc).

5.3 Results and Discussion

5.3.1 Ag_N-DNA host strand design

We illustrate the design process for host strands for N = 15 clusters (Ag_{15}); the same approach was successful for Ag_{14} (see Figure D.3 and surrounding text). This Ag_{15}-DNA exhibits peak excitation and emission at 600 nm and 670 nm, respectively, and has a 75% fluorescence quantum yield.[53,71] The cluster's red emission results from a magic number of six neutral silver atoms in the cluster core.[58] Ag_{15}-DNA can be isolated by high performance liquid chromatography (HPLC).[59] The DNA template sequence (Table D.1) was selected to produce this highly fluorescent, time-stable cluster, which is also robust at Mg^{2+} concentrations necessary for stable NT formation.

The bifunctional Ag_N-DNA host strand combines the cluster template sequence with an appended linker sequence. This linker attaches Ag_N-DNA to larger nanostructures that are decorated with complementary ssDNA "docker" sequences (Figure 5.1a). Using purification[52] prior to assembly, we recently showed that select Ag_N-DNA can be joined into simple dual-cluster assemblies with nanoscale separations, using suitable complementary linkers.[71] "Suitable" linkers are essential: because the characteristics of base motifs for specific fluorescent clusters[70] are not well understood, intended linker sequences can disrupt the desired cluster structure when appended to the cluster template, causing altered color and/or loss of fluorescence.

Preservation of the structure of the selected Ag_N-DNA when the linker is present is established by preservation of the fluorescence spectrum, due to the strong correlation between emission wavelength and the elongated Ag_N cluster shape.[58,59] In addition to structure preservation, the linker must not form other silver products that would hinder hybridization to

the complementary docker, and insertion of dockers into the DNA nanostructure must not disrupt nanostructure formation. Finally, the complementary linker and docker must have a hybridization melting temperature sufficiently above room temperature but still be short enough to enable attachment of Ag_N-DNA at the high spatial densities that are a key advantage of DNA nanostructures.

Previously, DNA sequences rich in A and T were selected to link Ag_N-DNA to other DNA strands because neither A nor T strongly associates with Ag_N.[65,66,71,88] These (A,T) linkers must be long, ~ 30 bases, to achieve high enough melting temperatures. We attempted to use a 30 base (A,T) sequence introduced by Yeh, *et al.*[65,66] as a linker for Ag_{15}-DNA to NT. This was previously used to link Ag_{15}-DNA to a separate Ag_{10}-DNA, forming dilute solutions of dual-color cluster pairs exhibiting FRET.[71] However, the (A,T) sequence resulted in no detectable attachment of Ag_{15}-DNA and only very low attachment of linkers labeled with Cy5 to NT (Figure D.1). The failure of these long (A,T) linkers in the dense DNA environment on NT likely arises from a combination of steric crowding and partial linker self-complementarity caused by using only two base types.

For successful NT decoration, bifunctional host strands evidently require shorter, mixed-base linkers. Designing such a linker is challenged by the propensity of C and G to participate in templating Ag_N: appending these bases to a cluster template can change the species of Ag_N-DNA that forms. We evaluated several 10-base candidate linkers chosen from a set of 684 ssDNA strands with random (A,C,G,T) sequences, described elsewhere.[58,70] Selected linker candidates were chosen because they did not stabilize fluorescent Ag_N-DNA and had melting temperatures > 40°C with perfect complements (determined by UNAFold[154,155] for relevant salt concentrations). Candidate linkers were appended to the 3' end of the Ag_{15}-DNA template.

Comparison of the fluorescence spectra of unpurified Ag_N-DNA solutions, stabilized by the candidate host template-linker strands, to the spectrum with the template strand alone (Figure D.2) indicates that all linkers were successful, *i.e.* Ag_{15} was the major fluorescent product in all cases. We selected the linker TCCGTTGTAT to use for attachment of the purified silver cluster to NT. Four additional A,T bases were appended to reach a linker-docker melting temperature > 45°C, and four thymine bases were inserted between template and linker. The final Ag_{15}-DNA host strand is then 'template'-TTTT-TCCGTTGTATAAAT. After one round of HPLC purification using triethylamine acetate as the ion-pairing agent, peak emission wavelengths produced by the template alone and by the template-linker host strand agree within 1 nm, suggesting that the structure of the Ag_{15}-DNA is unperturbed by the linker.

We performed a second round of HPLC with in-line electrospray mass spectrometry (ESI-MS) in negative ion mode to confirm that addition of this tail to the Ag_{15}-DNA template does not alter the composition of the fluorescent silver cluster (details in Section 5.2.1). The second HPLC round used 1,1,1,3,3,3 hexafluoro- 2-propanol/triethylamine as the ion-pairing agent to ensure sufficient ionization rates for high sensitivity MS.[52] MS confirms that the cluster stabilized by the modified Ag_{15}-DNA host strand contains 15 silver atoms (Figure D.4). The eluting Ag_{15}-DNA is estimated to be $\geq 70 \pm 1\%$ pure. HPLC-MS also confirms that the size of the Ag_{14}-DNA remains unchanged after addition of a tail and is isolated to $77.0 \pm 0.1\%$ purity (Figure D.5).

5.3.2 DNA scaffold design

We selected 10-helix DNA nanotubes[26] (NT) as scaffolds for Ag_N-DNA for two reasons: their architecture allows ssDNA docker extrusions at separations of just 7.1 nm along specific

individual double helices of the NT, so that decorating elements are arrayed in a line (Figure 5.1), and their ~ 10 μm length allows facile visualization by fluorescence microscopy**.** To adapt published NT sequences[26] for decoration with Ag_N, we appended "docker" sequences (complementary to the linkers) to the end of one of the ten, 42-base oligomers that weave together to form the NT. A similar approach was previously taken to attach much larger colloidal gold nanoparticles to NT.[174] The ten NT strands offer 20 distinct docker sites. For Ag_{15}-DNA attachment, we chose to append the docker sequence to the 3' end of strand U6, separated by TTTT to avoid perturbing the NT structure (see Table D.1 for nomenclature and sequences). Ag_{14}-DNA was attached to a U9-appended docker (see Appendix D.4). To verify NT formation with docker strands, we used a fluorescein (FAM) dye label at the end of a different NT strand (U1) and imaged by confocal microscopy. Figures D.6, D.7 show properly formed FAM-labeled NT.

5.3.3 Labeling efficiency control experiments

FAM-labeled NT are models for 100% labeling with fluorescent elements spaced at 7.1 nm, because FAM-labeling by the manufacturer is nearly 100% efficient and because the FAM-labeled U1 strand is necessary for NT assembly. Intensity profiles of NT decorated with Ag_N-DNA can therefore be compared to FAM-NT to investigate efficiency of docker site labeling by Ag_N-DNA. This comparison is necessary because previous studies of similar Cy3-labeled NT measured unexpected intensity modulations along NT contours.[174,175] Such modulations along the 100%-labeled Cy3-NT were attributed to deformations of NT structure caused by the strand extensions added to attach the dye labels. While such deformations do not alter the packing density of Cy3 dyes along the NT, they do modulate the coupling of emitted

light into the microscope objective, causing the intensity modulations. Because we used the same strand extension modification (addition of two T bases, a dye linker, and a dye molecule to one end of a NT-forming oligomer) to label U1 strands with FAM we expect, and observe, such intensity modulations. We also expect similar deformations of the NT decorated by Ag_N-DNA, due to the docker strand extensions.

To avoid confusing intensity modulations caused by such geometric deformations with regions of lower Ag_N-DNA labeling efficiency, we develop a numerical procedure to quantify intensity modulations along FAM-labeled NT and Ag_N-DNA-labeled NT. We used MATLAB-based software[176] to trace individual NT contours in confocal microscopy images. A custom MATLAB script, inspired by previous work,[175] then calculates the average standard deviation of the background-corrected intensity along each contour, normalized to the contour's average intensity, denoted by *M* (see Figure D.8 and surrounding text). *M* is a measure of the size of intensity fluctuations along a NT and thus correlates to average labeling efficiency. The most probable value of *M* is ~ 0.2 for FAM-NT (Figure 5.3).

M values for FAM-NT are larger than expected if the orientation of the dye-labeled helix does not vary along an NT (see simulations, Figure D.9). The microscope point spread function brings ~30 FAM molecules, spaced 7.1 nm apart, within a diffraction limited spot. Thus $M \sim 0$ if emitted light collection is uniform along NT and if emission dipole directions randomize during the collection time. Assuming random, fixed dipole orientations raises the expected *M* to ~ 0.1 (Figure D.9), still below the most probable observed $M \sim 0.2$ (Figure 5.3). Apparently the strand extensions protruding from the NT do perturb its shape, as previously observed.[174,175]

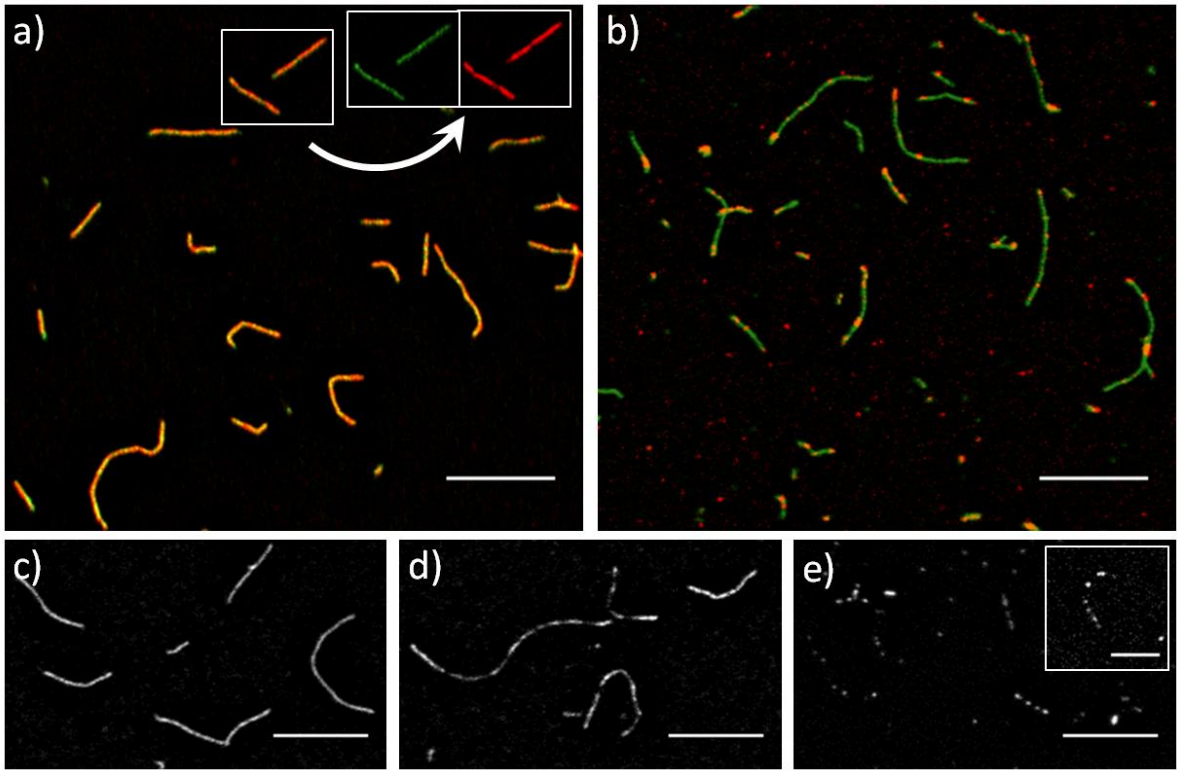

Figure 5.2: Fluorescence microscopy of NT decorated by Ag_{15}-DNA. a-d) Spinning disc confocal images of 10-helix DNA nanotubes (NT) labeled with Ag_{15}-DNA and spin-cast in polyvinyl alcohol (PVA) film. Scale bars: 10 μm (except inset). a-b) NT with FAM-labeled U1 strands and with a) 100% of U6 strands with dockers and twice-purified Ag_{15}-DNA or b) 10% of U6 with dockers and once-purified Ag_{15}-DNA. Yellow color indicates overlap of green (FAM) and red (Ag_{15}-DNA) fluorescence, and thus attachment of Ag_{15}-DNA on NT. Inset in a): FAM and Ag_{15}-DNA channels for boxed region. c-e) Images of once-purified Ag_{15} (red) fluorescence only, with no FAM label. The percentage of U6 strands containing dockers controls the density of NT labeling by Ag_{15}-DNA. c) 100% U6 dockers. d) 50% U6 dockers. e) Widefield image of Ag_{15}-DNA on NT with 10% dockers shows more sparsely decorated NT. Inset: Confocal image of NT with 10% dockers, decorated by Ag_{15}-DNA. Inset scale bar: 5 μm.

5.3.4 Microscopy of decorated NT

Assembly of NT decorated with Ag_N-DNA demonstrates the modularity of our method (Figure 5.1). First, Ag_N are synthesized on a cluster host strand, which combines the cluster template sequence with a linker sequence. Silver clusters of particular size, N, are then isolated to remove dark cluster products that would otherwise occupy NT sites. Next, NT-forming DNA strands, with docker sites attached to one of these strands, are annealed by heating to 90°C and then cooling slowly across the NT melting transition. Decoration of NT with select Ag_N-DNA

(N = 14 or 15) is then simply mediated by the designed linker and docker regions, whose $> 45°C$ melting temperature allows room temperature assembly (full assembly details in Section 5.2.2). Confocal microscopy confirms decoration of NT with Ag_{15}-DNA (Figure 5.2; Ag_{14}-DNA decoration in Figure D.10). NT in Figure 5.2a, b are co-labeled with FAM, and colocalized fluorescence from FAM (green) and Ag_{15}-DNA (red) confirms Ag_{15}-DNA attachment. No Ag_{15}-DNA attachment is observed for NT without docker sites (data not shown). Figure 5.2c-e shows that the density of dockers on the NT controls Ag_N-DNA labeling density, confirming that Ag_{15}-DNA attach by hybridization of linkers and dockers. For NT with dockers appended to 100% of the U6 strands, NT appear continuously-labeled by fluorescent clusters (Figure 5.2c). In comparison, coverage is less uniform for dockers on just 50% of the U6 docker sites, with some micron-scale variations in intensity along the NT (Figure 5.2d). NT with 10% U6 docker sites are sparsely decorated (Figure 5.2b,e), and individual Ag_{15}-DNA emitters can be identified by stepwise blinking and bleaching (Movie D.1, Figure D.11).

5.3.5 Labeling efficiency

To investigate the labeling efficiency of NT by Ag_{15}-DNA, we compared intensity modulations along NT with 100% U6 dockers that were decorated by Ag_{15}-DNA (Figure 5.2a,c) to FAM-labeled NT with both 100% U6 dockers and FAM-labeled U1 (Figure D.6), using the previously described numerical measure *M*. The probability density functions (PDFs) of *M* for 100% labeled FAM-NT (green) and NT, with 100% U6 dockers, labeled by twice-purified Ag_{15}-DNA (red) show close similarity (Figure 5.3). Because FAM-NT are models for

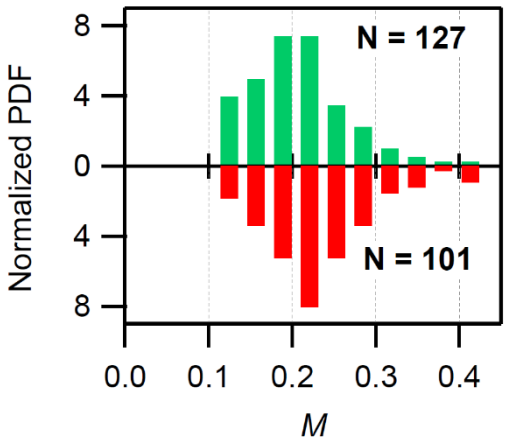

Figure 5.3: Intensity fluctuations along NT. Normalized probability density functions (PDFs) for *M*, the average standard deviation of the background-corrected intensity, normalized to average intensity, along *N* individual NT contours. Top (green): FAM-NT, with 100% U6 docker sites and 100% U1-FAM, are a model for 100% labeling. Intensity variations that arise from NT deformations modulate the coupling of emitter dipoles in the objective, resulting in non-zero measured values of *M*. Bottom (red): The same NT with 100% U6 dockers decorated by twice-purified Ag_{15}-DNA. Similar PDFs suggest that % labeling with Ag_{15} is similar to that for 100% FAM (7 nm spacing).

100%-labeled NT, this similarity suggests that average NT labeling efficiency with Ag_{15}-DNA is also near 100%.

5.3.6 Spectroscopy

In addition to NT deformations caused by decorating elements and/or docker site extrusions, NT may also deform the structures of the decorating Ag_N-DNA themselves. It is well-known that an Ag_N-DNA's optical properties can be extremely sensitive to the local cluster environment, a feature that is the basis for a number of fascinating sensing applications.[60,65,66] Thus, it is important to investigate whether the proximity of Ag_N-DNA to much larger NT DNA scaffolds affects the structure of the decorating clusters. Possible structural reconfigurations include changes in the number of neutral Ag atoms, which correlates strongly with color, and changes in the number of Ag cations, which may have finer control of Ag_N-DNA shape.[58] The proximity of Ag_N-DNA to NT containing orders of magnitude more DNA than the cluster host strands, may also affect cluster geometry and/or

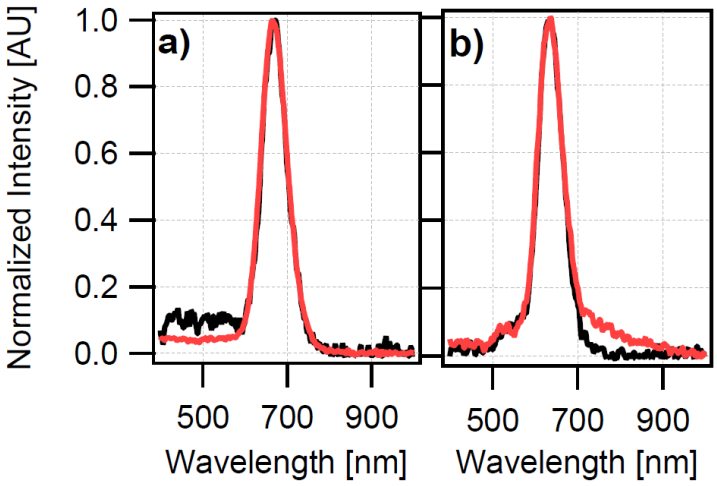

Figure 5.4: Ag_N-DNA emission on and off NT. UV-excited fluorescence spectra of a) Ag_{15}-DNA and b) Ag_{14}-DNA free in solution (black) and attached to NT (red). a) Ag_{15}-DNA mixed with 5x excess of NT containing 100% U6 docker sites, to ensure complete Ag_{15}-DNA binding, and incubated at room temperature for 75 min (red) show unchanged spectral features compared to Ag_{15}-DNA at identical concentrations and incubation times but in the absence of NT (black). b) Ag_{14}-DNA, mixed at 5x excess of NT with U9 docker sites (red) maintain a dominant 640 nm peak, the same as Ag_{14}-DNA free in solution (black).

radiative properties. To investigate whether Ag_N-DNA properties are changed by attachment to NT scaffolds, we compared fluorescence spectroscopy for Ag_N-DNA free in solution to Ag_N-DNA attached to NT with 100% docker sites. UV excitation was used to universally excite all Ag_N-DNA products simultaneously.[50]

The UV-excited fluorescence spectra of Ag_{14}-DNA and Ag_{15}-DNA (Figure 5.4) have unshifted emission peaks and unaltered peak widths when bound to docker sites (red) on NT as compared to free in solution (black). Because the fluorescence spectrum of an Ag_N-DNA is highly sensitive to changes in cluster geometry,[58,59] such unchanged spectral shapes indicate that these Ag_N-DNA are unaltered by scaffolding on NT.

5.4 Conclusion

We have demonstrated a modular design and assembly method for decorating DNA nanotube structures with atomically precise arrays of fluorescent silver clusters. Bifunctional

host strands constrain the cluster to a templating region of the strand, while a separate linker region allows attachment to ssDNA "docker" extrusions from a prototypical scaffold, a DNA nanotube, after the crucial step of isolating a particular cluster species. Positioning of individual Ag_N-DNA of known size, N, at selected locations on the nanotubes *via* ssDNA docker sites, is verified using fluorescence microscopy. Fluorescence spectroscopy shows that the optical properties of these Ag_N-DNA, and thus cluster structure, are unaffected by proximity to the DNA nanostructure. This modular approach to scaffold decoration with Ag_N of select size, N, represents the first demonstration of nanoscale assembly of atomically precise metal clusters at programmed positions on a nanoscale scaffold. The approach should generalize across a diverse spectrum of DNA scaffold sizes and geometries, as well as to patterned scaffolding of silver clusters with different N and different emission colors.

6. Heterogeneous Solvatochromism of Fluorescent DNA-Stabilized Silver Clusters Precludes Use of Simple Onsager-Based Stokes Shift Models

This chapter is adapted from: Copp, S. M.; Faris, A.; Swasey, S. M.; Gwinn, E. G. Heterogeneous Solvatochromism of Fluorescent DNA-Stabilized Silver Clusters Precludes Use of Simple Onsager-Based Stokes Shift Models. *J. Phys. Chem. Lett.* **2016**, *7*, 698–703.[74]

This open-access article can be found online at:

http://pubs.acs.org/doi/10.1021/acs.jpclett.5b02777.

6.1 Introduction

DNA-stabilized silver clusters (Ag_N-DNA) are powerful tools for sensing,[177] promising fluorescent markers for bioimaging,[178] and have precisely controllable sizes for DNA-based photonic arrays.[72] Yet despite a growing number of applications for Ag_N-DNA, including those presented in Chapters 4 and 5, the mechanisms behind their sequence-tunable fluorescence are not fully understood. Most properties of Ag_N-DNA are highly heterogeneous: different DNA sequences select widely varying photostabilities, chemical stabilities, quantum yields, and fluorescence colors from blue-green into the near IR. These wide-ranging attributes have hindered the development of a common model for Ag_N-DNA.

One commonality that fluorescent Ag_N-DNA do appear to share is a rod-like cluster core.[49] While the detailed structure of Ag_N-DNA has not been solved, there is considerable evidence for elongated cluster geometries, with cluster length selecting color.[53,57–59,107] By isolating Ag_N-DNA with monodisperse sizes,[52,93] previous studies showed that the distinctive form of optical absorbance spectra, dependence of peak absorbance wavelengths on silver content,[49,53]

non-spherical values of magic cluster sizes,[58] circular dichroism spectral features,[59] and strongly polarization-dependent emission[57] all point to a rod-like cluster geometry.[53] Another feature shared by all fluorescent Ag_N-DNA is excitation *via* the UV absorbance band of the stabilizing DNA strand, in addition to the visible or IR wavelength excitation band selected by cluster length.[50] These commonalities raise the question of whether processes governing fluorescence might also be universal across distinct Ag_N-DNA colors and stabilizing DNA strands.

For ligand-stabilized metal clusters in general, the factors controlling fluorescence quantum yields (QY) remain obscure. The nature of the initial excited state, non-radiative pathways, and roles of ligands *versus* cluster structure are all open questions. Recent studies that varied ligand composition while preserving the same cluster structure found that the QY of weakly fluorescent thiol-protected Au_{25} clusters increased from $2x10^{-5}$ to $1x10^{-4}$ upon addition of ligand substituents with higher electron donating power.[179] This implicated charge transfer from the ligands to the cluster upon excitation, consistent with long (~μs) fluorescence lifetimes arising from low spatial overlap between a cluster-centered ground state and excited states with high weight on ligands. Contrasting studies of phosphine-protected $Au_{25-x}Ag_x$ clusters used fixed ligand composition and cluster geometry to investigate effects of altering cluster composition. Increasing the silver content *x* from 12 to 13 atoms increased the QY dramatically, from ~ $1x10^{-3}$ to 0.4. This was attributed to reaching nearly complete Ag 5s character in ground and excited states upon addition of the 13th Ag atom and greater electron delocalization over the cluster.[180] Such an increase to a QY approaching unity would be difficult to understand for an excited state with significant charge transfer to the ligands, due

to low overlap with a cluster-centered ground state. Thus, the nature of excited states may differ between ligand-stabilized clusters with high QY ~ 1 and low QY << 1.

Here we investigate the fluorescence of high QY (0.3 – 0.9) purified Ag_N-DNA with wide-ranging colors (Table 6.1). To better understand the influence of DNA base ligands and the nature of the initial excited state, we use methanol-water and ethanol-water mixtures to investigate the solvatochromic behavior of these Ag_N-DNA. Solvent effects on fluorophore absorption and emission spectra have been studied for decades, and models for solvatochromism have played an important role in understanding how electron distributions within select types of molecules change upon excitation.[181] Patel, *et al.*, made the interesting suggestion that fluorescent Ag_N-DNA generally have an initial excited state characterized by significant charge transfer from the cluster to the DNA, producing a large change in static dipole moment.[75] This widely cited[145,182–184] idea was based on modeling the solvatochromic behavior of a single unpurified Ag_N-DNA in ethanol-water mixtures. However, as discussed below, the reported behavior was incompatible with the Lippert-Mataga model[185,186] used to infer the change in static dipole moment between ground and initial excited states.

Our studies instead reveal distinctly different dependences of Stokes shift on the bulk dielectric properties of the solvent for Ag_N-DNA with different silver content, N, ranging from 10-20 atoms (see Table 6.1 for aqueous optical properties and DNA templates).[53] In addition to this heterogeneity, we find much smaller solvatochromic shifts of the pure Ag_N-DNA studied here than was reported for the single, impure solution studied previously,[75] questioning the existence of universal charge transfer from silver cluster to DNA upon excitation. We find that Onsager-based continuum models,[187] including the Lippert-Mataga (LM) model,[185,186] fail to universally describe Ag_N-DNA solvatochromism, and thus cannot be used uncritically to

infer differences in ground and excited state dipole moments. Rather than charge transfer, our data suggest that template-specific sensitivity of Ag_N-DNA structural details to solvent environment may instead be responsible for the observed solvatochromism. To aid the emerging field of fluorescent ligand-stabilized metal clusters, in addition to these new results on Ag_N-DNA, we also provide a brief general review of the requirements for applicability of Onsager-based models for solvatochromism.

6.2 Experimental Methods

Each Ag_N-DNA was purified by high performance liquid chromatography (HPLC) to ensure that fluorescent Ag_N-DNA were sufficiently isolated for accurate determination of Stokes shifts (Figures E.1-E.4),[52] avoiding the heterogeneous silver cluster mixtures identified by previous studies.[188] Ag_N-DNA excitation and emission spectra were measured in mixtures of ethanol (EtOH) or methanol (MeOH) and aqueous buffer (Figure 6.1). To separate effects due to solvent composition from possible effects of varying salt concentration, all mixtures contained 10 mM NH_4OAc. Impure solutions were also studied (Figures E.5 and E.6), but because many DNA templates produce multiple fluorescent products, with different solvatochromic behavior of the impure mixture from that of a specific purified Ag_N-DNA (Figure E.6), we show only pure Ag_N-DNA data here.

6.2.1 Synthesis and purification

Custom DNA oligomers (Integrated DNA Technologies, standard desalting) were washed by solvent exchange in DNAse-free distilled water (Life Technologies) using Amicon Ultra centrifugal filters to remove residual salts. Ag_N-DNA were synthesized by mixing DNA with

$AgNO_3$ in 10 mM NH_4OAc. Final concentrations for synthesis were: 15.0 μM DNA and 188 μM $AgNO_3$ for Ag_{10} and Ag_{15}, 20.0 μM DNA and 200 μM $AgNO_3$ for Ag_{14}, and 20 μM DNA and 250 μM $AgNO_3$ for Ag_{20}. DNA and $AgNO_3$ mixtures were allowed to rest at room temperature for 20 min before adding $NaBH_4$ at a ratio of 0.5 [$NaBH_4$]/[$AgNO_3$]. Reduced mixtures were stored overnight at 4°C prior to purification.

We use a previously described high performance liquid chromatography (HPLC) method:[52] Ag_N-DNA species were concentrated five times by spin filtration, injected into a 50 mm x 4.6 mm Kinetex C18 core-shell column with 2.6 μm particle size and 100 Å pore size (Phenomenex), and separated by ion pair reversed-phase HPLC (Waters 2695 Separations Module) with 35mM ion-pairing (IP) buffer triethylamine acetate (TEAA) in HPLC grade water and MeOH at pH 7. Ag_N-DNA were then solvent exchanged into 10 mM NH_4OAc and stored at 4°C until use.

6.2.2 Spectral measurement and analysis

Ag_N-DNA were studied in solutions of 10%, 20%, 30%, 40%, and 50% w/w EtOH and 20%, 40%, 60%, and 80% w/w MeOH, with constant 10 mM NH_4OAc concentration. 4 μL of Ag_N-DNA was mixed with appropriate volumes of H_2O, 100 mM NH_4OAc, and EtOH or

Name	DNA Sequence	n_{DNA}	λ_{ex}	λ_{em}	QY	# Ag
Ag_{10}	TGCCTTTTGGGGACGGATA	1	497 nm	560 nm	44 %	10
Ag_{14}	TTCCCACCCACCCCGGCCCGTT	1	574 nm	640 nm	93 %	14
Ag_{15}	CACCGCTTTTGCCTTTTGGGGACGGATA	1	602 nm	676 nm	75 %	15
Ag_{20}	CCCACCCACCCGCCCA	2	709 nm	770 nm	30 %	20-21

Table 6.1: Ag_N-DNA properties. Each is named for the total number of silver atoms in the cluster, as previously reported, and n_{DNA} is the number of DNA strands.[53] Peak excitation (λ_{ex}) and emission (λ_{em}) wavelengths are for Ag_N-DNA in aqueous buffer. Quantum yields (QY) for Ag_{10}, Ag_{14}, and Ag_{15} are reported by Schultz, *et al.*,[53] and Petty, *et al.* report the QY of Ag_{20}.[93]

MeOH in low volume 384 well plates (Corning #3544). To minimize evaporation, alcohol was added immediately prior to measurement. Emission and excitation spectra were collected by a Tecan Infinite® 200 PRO, with a 9 nm excitation bandwidth and a 20 nm emission bandwidth. Emission was scanned from 400 nm to 850 nm at a 2 nm step. Excitation scans were conducted by monitoring at the peak emission wavelength of each Ag_N-DNA (Table 6.1). Excitation wavelength was scanned from 230 nm to 40.0 nm less than the emission peak wavelength, with a 2 nm step size. For Ag_{14}, Ag_{15}, and Ag_{20}, experiments were repeated 2-3 times and averaged for Stokes shift analysis. Igor Pro 6 software was used to extract peak excitation and emission energies by fitting spectra to single Gaussians[149] as a function of energy. Refractive index measurements for mass ratio alcohol-water mixtures[189] and dielectric constant measurements for weight ratio alcohol-water mixtures[190] were used to calculate Δf.

6.3 Results and Discussion

6.3.1 Solvatochromism of excitation and emission

Figure 6.1 displays peak excitation and emission wavenumbers (ν_{ex} and ν_{em}, respectively) for each Ag_N-DNA in varying w/w % EtOH and MeOH. Both ν_{ex} and ν_{em} show qualitatively different solvatochromism for different Ag_N-DNA: for Ag_{10}, ν_{ex} and ν_{em} blueshift with increasing alcohol content, while Ag_{14}, Ag_{15}, and Ag_{20} display smaller redshifts and/or nonmonotonic behavior.

To interpret Figure 6.1, we first test whether changes in ν_{ex} and ν_{em} might arise solely from non-specific solvent effects,[191] rather than from specific interactions between Ag_N-DNA and solvent molecules, such as hydrogen bonding. Non-specific solvent models are premised on

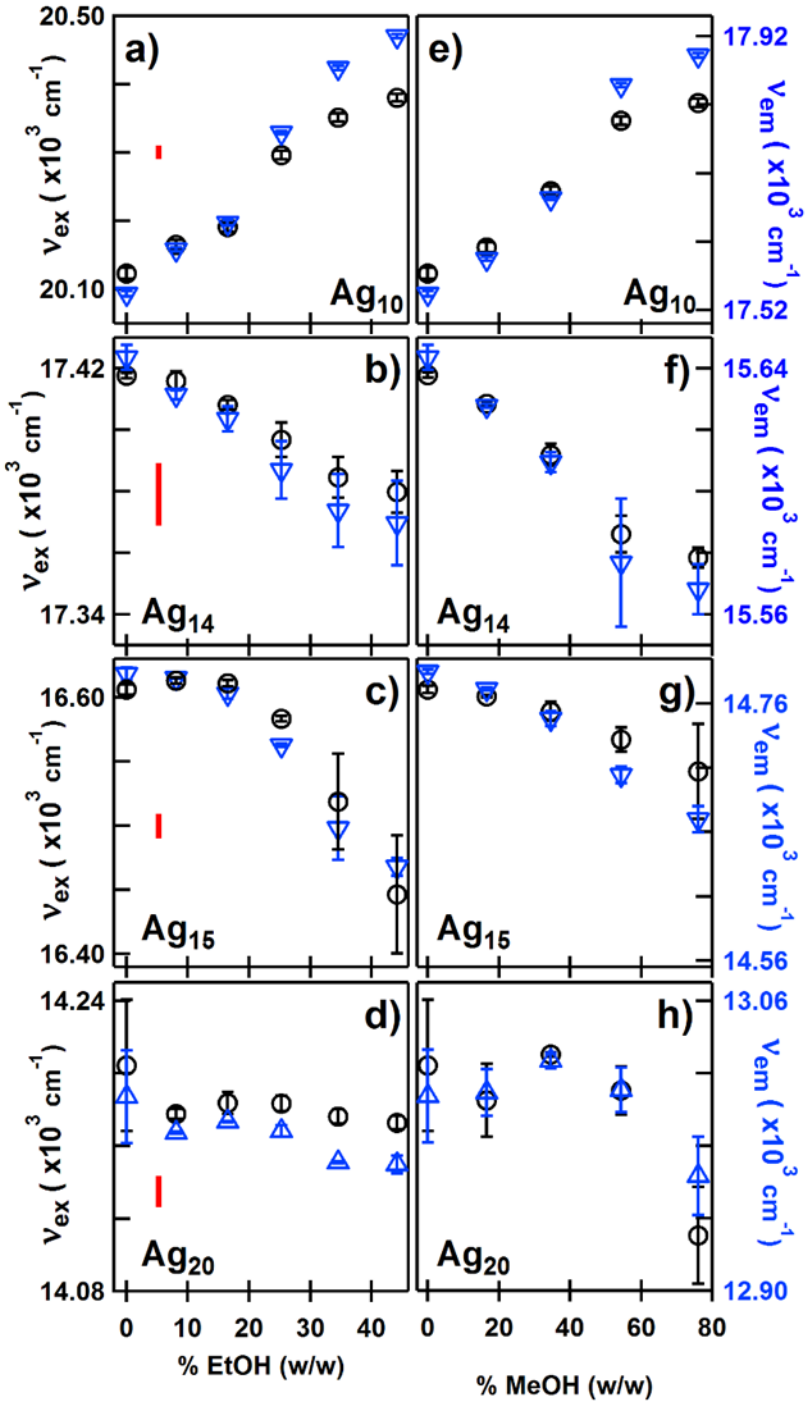

Figure 6.1: Solvatochromism in **(a-d)** EtOH- and **(e-h)** MeOH-buffer mixtures for **a)**, **e)** Ag_{10}, **b)**, **f)** Ag_{14}, **c)**, **g)** Ag_{15}, and **d)**, **h)** Ag_{20}. Peak excitation values ν_{ex} (black circles) and emission values ν_{em} (blue triangles) are plotted in cm^{-1} on the left and right axes, respectively. Axis ranges are identical for a given Ag_N. Vertical red bars (left) are 20 cm^{-1} in height to provide a visual reference for relative magnitudes of changes for different Ag_N. Error bars represent standard deviation of duplicate experiments, except for Ag_{10}, where error bars represent Gaussian fit errors. w/w % values were chosen to achieve similar Δf values for EtOH and MeOH (see Figure 6.2).

the Franck-Condon principle that electronic transitions occur on much shorter time scales than nuclear motion. Thus, during photon absorption and emission, solvent molecules do not have time to reorient, while electrons in individual solvent molecules do. The refractive index *n* represents the nearly instantaneous electronic response of the bulk solvent upon absorption and emission, while the zero frequency dielectric constant ε represents both electronic response and the much slower process of solvent molecule reorientation.[191]

Ag_N-DNA lifetimes of 1 ns have been reported,[75,90] suggesting that free solvent molecules in the bulk solvent have ample time to reorient prior to Ag_N-DNA emission. In this case, non-specific solvent models would predict that changes in ε shift ν_{em}, while changes in *n* shift both ν_{ex} and ν_{em}.[191] We would then expect ν_{em} to shift more than ν_{ex} with changing solvent composition. However, this behavior is only convincingly exhibited by Ag_{10} (Figure 6.1a, 6.1e).

6.3.2 Lippert-Mataga model

To draw more quantitative conclusions, we consider perhaps the most commonly used model for non-specific solvent effects, the Lippert-Mataga (LM) model.[185,186] Based on the Onsager reaction field,[187] the LM model applies to fluorophores that interact with the surrounding solvent through purely dipolar interactions with solvent molecules that reorient freely.[187] We consider this model because it was previously applied to Ag_N-DNA[75] and to Ag clusters stabilized by synthetic polymers.[192]

Because the LM model makes several significant assumptions that have resulted in incorrect application when overlooked, and because few others[193] have discussed such mistakes, we summarize it here. The LM model is an extension of Ooshika's absorption

spectrum theory,[194] in which a solute molecule is approximated as a dipole embedded in the solvent within a spherical, vacuum cavity of Onsager radius *a*.[187] The solvent is approximated as an isotropic, homogeneous sea of dipoles with bulk dielectric constant ε and index of refraction *n*, and the structure of the solute is assumed to be independent of the surrounding solvent. Combining these approximations with the Franck-Condon principle, perturbation theory is used to calculate energy shifts in ground and excited states of the solute induced by dipolar interactions with the solvent, and Onsager's classical reaction field[187] is used to approximate several challenging expectation values.[194] Lippert and Mataga, *et al.*, then extended Ooshika's theory to the process of fluorescence.[185,186]

The LM model yields an equation relating the Stokes shift of a fluorophore, defined as the difference between peak absorbance and emission wavenumbers ($\nu_{ab} - \nu_{em}$), to the change in static dipole moment of the fluorophore between the ground state, $\overrightarrow{\mu_G}$, and excited state, $\overrightarrow{\mu_E}$:

$$\nu_{ab} - \nu_{em} = \frac{2(\overrightarrow{\mu_E} - \overrightarrow{\mu_G})^2}{hca^3}\Delta f + const. \qquad (6.1)$$

where $\Delta f = \frac{\varepsilon-1}{2\varepsilon+1} - \frac{n^2-1}{2n^2+1}$ is the orientation polarizability of the bulk solvent.[185,186] The constant in Eq. 6.1 expresses intrinsic properties of the fluorophore that are independent of solvent composition. In practice, Δf is taken to be that of the bulk, macroscopic solvent: differences between bulk solvent properties and inner shell hydration of the solute are beyond the scope of such "simple" application of the LM model. Thus, for a fluorophore in a dielectric medium where the previously listed approximations are valid, a "Lippert-Mataga plot" of $\nu_{ab} - \nu_{em}$ *versus* Δf yields a straight line with positive slope, and $|\overrightarrow{\mu_E} - \overrightarrow{\mu_G}|$ may be extracted from this slope if the cavity radius *a* is known.

Because $(\overrightarrow{\mu_E} - \overrightarrow{\mu_G})^2 \geq 0$, the slope of a LM plot must be greater than or equal to zero for a fluorophore that is correctly modeled by Eq. 6.1; it is not sufficient for plots to exhibit linear

behavior. Others also note that $(\overrightarrow{\mu_E} - \overrightarrow{\mu_G})^2$ must increase with increasing Δf.[195,196] Similar to nonlinearity, a negative slope implies that the system *does not* satisfy the assumptions of the LM model (see Appendix E.1). In such cases, the LM model cannot describe a fluorophore, *i.e.* the change in dipole moment between ground and excited states cannot be extracted from a negative slope. Thus, the previously inferred large changes in the dipole moment of one Ag_N-DNA upon excitation were not meaningful because the LM plot for this impure solution exhibited negative slope.[75] This peculiar behavior may relate to poor stability of the fluorescent species, which degraded during our attempts to purify by HPLC, as did the other two fluorescent species studied in Ref. 75. Misuse of the LM model has led to other misleading results in the literature (including invalid dipole moment changes reported for molecules[197] and larger gold nanoparticles[198] from LM plots with negative slopes).

6.3.3 Lippert-Mataga plots

To explore the more general applicability of the LM model to robust Ag_N-DNA of known N, Figure 6.2 shows LM plots for the four purified Ag_N-DNA in EtOH and MeOH mixtures. Stokes shifts were calculated from excitation and emission spectra. (Although excitation and absorbance spectra of monodisperse fluorescent Ag_N-DNA display identical peaks in the visible to near-IR range,[50] we use excitation spectra to avoid the possibility of shifts in absorbance that could arise from non-fluorescent impurities that co-elute with the fluorescent Ag_N-DNA from the HPLC column; see Figure E.7 for example). The magnitude of the Stokes shift changes previously reported for unpurified solutions[75] were roughly 7 times larger than for Ag_{10} (Figure 6.2a) and roughly 60 times larger than for Ag_{14} (Figure 6.2b) in ethanol-water mixtures. Thus the solvatochromic changes in Stokes shift are much smaller for the Ag_N-DNA

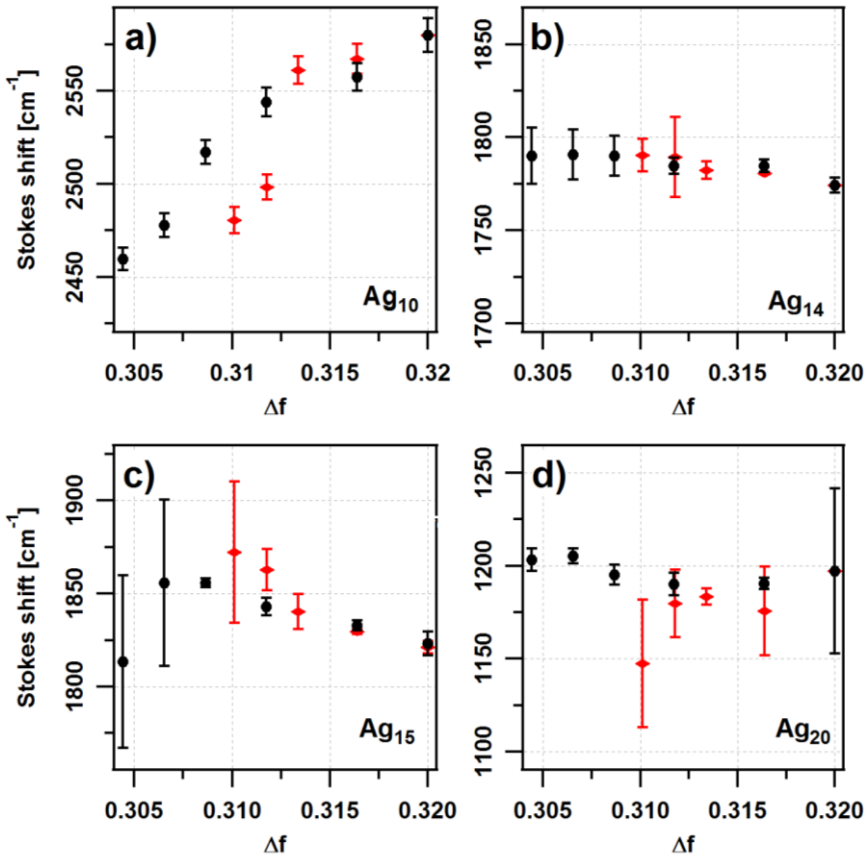

Figure 6.2: Lippert-Mataga plots for **a)** Ag_{10}, **b)** Ag_{14}, **c)** Ag_{15}, and **d)** Ag_{20} in EtOH-buffer mixtures (black) and MeOH-water mixtures (red). Y-axis ranges are equal for all plots to enable comparison. Error bars represent standard deviation.

studied here than for the silver-DNA solutions studied previously,[75] which were not stable enough to purify by the HPLC methods employed here.

LM plots for Ag_{14} and Ag_{15} in both EtOH and MeOH exhibit overall negative slope (Figure 6.2b – 6.2d), invalidating use of the LM model to extract dipole changes using Eq. 6.1. The LM plots for Ag_{10} alone exhibit positive slope. One mechanism for this could be a change in dipole moment upon excitation; however, Ag_{10} was previously shown to exist in two conformational states, one dark and one emissive, in a solvent-controlled equilibrium.[59] Shape changes are outside the scope of the LM model (Appendix A.1). Further, the differing behavior of LM plots for Ag_{10} in EtOH as compared to MeOH (Figures 2a and 2d, red and black data)

and the nonlinear behavior of Ag_{10} indicate specific solvent effects. We note that other studies have used modifications of the LM model with more realistic approximations for the reaction field that lead to modified expressions for Δf.[193] However, modifications to Δf alone only stretch the x-axis of a Stokes shift *versus* Δf plot and thus cannot transform a plot exhibiting negative slope or nonmonotonic behavior to the form required for validity of the model, a linear plot with positive slope. For Ag_{20}, slight shifts in ν_{em} with respect to ν_{ex} (Figure E.4) may be indistinguishable from the small changes in Stokes shift in EtOH (Figure 6.2d), and thus we do not comment on the applicability of the LM model for Ag_{20}.

6.3.4 Alternative mechanisms

Due to the failure of the LM model to describe the Ag_N-DNA studied here, we conclude that Ag_N-DNA solvatochromic behavior provides no evidence for charge transfer to the bases upon initial excitation, as previously proposed.[75] [75] also proposed a long-lived dark state resulting from charge transfer from the initial excited state. The measurements here do not address such a dark state, or any other type of dark state, as was probed by transient spectral data.[75]) The diverse responses of different Ag_N-DNA to changes in solvent composition, combined with known base-dependent effects of hydration on DNA structure[199,200] and known changes in DNA conformation in response to alcohol cosolvents,[201,202] instead suggest that solvatochromism may arise from changes in hydration that are specific to the DNA surrounding the clusters. In particular, transition energies of Ag_N-DNA could be altered by alcohol cosolvents *via* hydration-induced changes of DNA conformation that perturb cluster structure or modify the ligand properties of the DNA bases supporting the clusters. Prior studies established that solvent composition controls a reversible equilibrium between two

forms of Ag_{10}, the fluorescent form studied here (peak aqueous absorbance at ~ 490 nm) and a dark form (peak aqueous absorbance at ~ 410 nm).[59] Thus, it is reasonable to expect that solvent changes may produce structural perturbations to fluorescent forms of Ag_N-DNA, as well. (Ag_{14}, Ag_{15} and Ag_{20} exhibit no detectable dark forms).

Sensitivity of calculated Stokes shifts to ligand arrangement was found in computational studies of smaller, 2-3 atom Ag clusters by Gell, *et al*.[203] It has also been postulated that the ligands surrounding Ag_N-DNA control cluster color by controlling cluster shape.[53,58,107] (Such structural changes are entirely absent in the LM model, which presumes that the structure of the fluorophore itself is unaffected by solvent composition.) Thus, if solvent-DNA interactions alter cluster geometry *via* changes in ligand arrangement, solvent composition would also tune Ag_N-DNA excitation and emission, even in the absence of charge transfer. Such solvent-tuned changes in structure may depend on the specific sequence of the DNA stabilizing the fluorescent cluster, resulting in a diverse range of solvatochromism in Ag_N-DNA. Alternatively, Ag_N-DNA might sense changes in the local, sequence-specific dielectric properties of the DNA hydration shell.[199,204] Such sequence-specific dielectric variations, combined with the well-known inhomogeneity of alcohol-water mixtures on molecular scales,[205] challenge the use of a continuous, bulk dielectric model for the local environment of Ag_N-DNA. Further studies of interactions between Ag_N-DNA and solvent molecules, as well as of potential solvent-induced conformational changes of Ag_N-DNA, may lead to a better understanding of these effects.

6.4 Conclusion

We studied the optical properties of four Ag_N-DNA with widely ranging sizes and colors in a variety of alcohol-buffer mixtures and found that none of these Ag_N-DNA is well-modeled by traditional Onsager-based models for solvatochromism, including the often-used Lippert-Mataga model. Careful examination of the assumptions made by such models shows that Ag_N-DNA are likely not compatible with non-specific solvent interaction models because other phenomena, such as hydrogen bonding and solvent-induced structural changes, can play a larger role in determining the Stokes shift of Ag_N-DNA. Additionally, the solvatochromism observed for the four purified Ag_N-DNA is both heterogeneous and much smaller in magnitude than observed for an impure sample formed on a different DNA template,[75] questioning the universal existence of any significant charge transfer from the cluster to the DNA bases upon excitation. Instead, the solvatochromism of Ag_N-DNA may be governed by changes in hydration of the DNA template, with spectral shifts resulting from cluster shape changes and/or dielectric changes in the local vicinity of the cluster, potentially providing a mechanism for fluorescence sensing of changes that are highly local to DNA.

7. Cluster Plasmonics: Dielectric and Shape Effects on DNA-Stabilized Silver Clusters

Adapted with permission from: Copp, S. M.; Schultz, D.; Swasey, S. M.; Faris, A.; Gwinn, E. G. Cluster Plasmonics: Dielectric and Shape Effects on DNA-Stabilized Silver Clusters. *Nano Lett.* **2016**, *16* (6), 3594–3599.[206] *Copyright 2016 American Chemical Society.*

.

7.1 Introduction

Current interest in noble metal nanorods arises from the special properties produced by elongated particle shapes. These properties include absorbance wavelengths that are tunable throughout the visible and infrared by simply altering the rod's length, ℓ, relative to its diameter, D, as parameterized by the rod aspect ratio, $AR = \ell/D$.[101–103] The elongated shape also enhances near-fields[207] and enables directional plasmonic coupling[208] as well as sensing of the particle's local dielectric environment. An additional advantage of an elongated shape is a narrower plasmon linewidth,[83] which enables more frequency-selective coupling schemes than afforded by spherical particle geometries.

Most studies of metal nanorods focus on the nano*particle* size regime, $\ell \sim 10 – 100$ nm and $D \sim 5 – 20$ nm.[103] For such "classical" nanorods, proximity-induced shifts in plasmonic absorbance are detected for inter-rod and rod-analyte separations comparable to near-field length scales that depend on nanorod size.[208] As size is reduced to the nano*cluster* regime, where particles contain a few to some tens of atoms, near-field length scales decrease.[209] Thus, the cluster regime may enable near-field sensing at scales comparable to cluster sizes of up to a few times the Fermi wavelength, ~ 0.5 nm in silver, which is well below the 5 – 10 nm range

accessible to standard FRET techniques. But despite many theoretical investigations of high *AR* clusters of silver and gold[55,56,106,210–212] and early experimental work that used a STM to position atomic Au chains on atomically flat substrates,[213] metal cluster rods have been largely unavailable for experimental study due to the challenge of controlling cluster shape.

Recently, however, studies found evidence that silver cluster rods can be realized using select DNA oligomers as stabilizing ligands.[53,58,59] Such "Ag_N-DNA" exhibit fluorescence quantum yields that can exceed 90%,[53] much higher than those of globular Au clusters of similar size.[214] The rod shape rationalizes the tunability of Ag_N-DNA color across the visible and near infrared spectrum[53] by different choices of the DNA template,[48] the magic number behavior of Ag_N-DNA sizes,[58] and their chiroptical properties.[59] Studies strongly suggest that this rod shape results from the unique nature of DNA as the cluster-stabilizing ligand: the Ag^+-base ligands thought to stabilize the clusters[58] are arranged on the linear phosphate backbone, imposing an elongated[58] and chiral shape.[59] Ag_N-DNA are inherently compatible with DNA nanotechnology, leading to their use in FRET schemes,[71] miRNA detection,[68] cellular imaging,[61] and logic gates.[144,146] Beyond these demonstrated applications, the small cluster sizes and high fluorescence quantum yields of Ag_N-DNA may enable new sensing schemes at sub-nanometer length scales, for example, as sensors for local changes in DNA hydration patterns thought to be important for DNA function,[215] and in novel cluster-based nano-optics just now being explored theoretically[216] and realized experimentally.[72]

For such short-range phenomena, the aspect ratio, *AR*, of Ag_N-DNA and their sensitivity to the local dielectric environment are key undetermined properties. Here we use the cluster excitation energy of compositionally pure Ag_N-DNA solutions to estimate *AR* for fluorescent clusters with excitation wavelengths from 406 to 850 nm. To test the sensitivity of Ag_N-DNA

to changes in the surrounding medium, we increase the range of dielectric properties relative to previous studies[74,75] by using glycerol as a cosolvent. These studies seek to advance the emerging field of cluster-based molecular plasmonics.[49,212,216] (While use of the term "plasmon" to describe excitations of small free electron systems has been debated, there is no contradiction between having both a discrete density of states and well-developed collective excitations, in particular for silver clusters with linear shapes.[49,212]) Our results suggest that, even for clusters with as few as ~ 10 atoms, near-fields may be strong enough to enable local dielectric sensing, with an expected range of ~ 0.1 – 1 nm given the small cluster size.

7.2 Experimental and Computational Methods

7.2.1 Cluster synthesis and purification

Ag_N-DNA were synthesized as described in Appendix F.1. Table F.1 lists the different mixed-base DNA templates for these clusters (10-34 bases in length) with their abbreviations (DNA1 – DNA13), estimated neutral silver atom numbers, N_0, and peak absorbance wavelengths, λ_{res}. Ag_N-DNA with $\lambda_{res} > 700$ nm were developed by Petty, *et al.*;[82,93] other clusters were developed by our group.[53,58] Ag_N-DNA were purified by one stage of high performance liquid chromatography (HPLC),[52] which typically produces 60-90% purity. Remaining impurities are non-fluorescent byproducts with similar column retention. To determine λ_{res} and its associated standard deviation, absorbance spectra were fitted to a single Gaussian as a function of energy, and values were then converted to wavelength. Note that in the visible to near-infrared spectrum, the peak absorbance and peak fluorescence excitation wavelengths of a pure solution of Ag_N-DNA coincide.[50]

7.2.2 Computational details

Fits to the bulk dielectric functions of silver and gold (Figures F.1 and F.2) are provided in Appendix F.2. To determine *w*, data in Figures 7.1b and 7.1c were fitted to the appropriate form of Eq. 7.7 by least squares fitting.

7.2.3 Dielectric effects

To study dielectric effects, aqueous solutions of pure Ag_N-DNA were well-mixed with glycerol to achieve various w/w % glycerol. To isolate effects of glycerol-induced changes in medium dielectric from possible effects due to changing salt concentration, solutions were maintained at 10 mM NH_4OAc. Excitation and absorption spectra were collected using an Ocean Optics QE65000 spectrometer. Excitation light was produced by a Xenon arc lamp, with wavelength scanning using a Monoscan 2000 monochromator (Ocean Optics). Excitation spectra were appropriately normalized for variations in lamp brightness and monochromator transmission. Index sensitivities were calculated using the bulk refractive index of glycerol-water mixtures.[189] Figures F.5 – F.11 display individual Ag_N-DNA spectra at various w/w % glycerol.

7.3 Results and Discussion

7.3.1 Evidence for collective excitation

Multiple factors suggest that the low energy electronic excitations of Ag_N-DNA share distinctive physical properties with the longitudinal plasmon modes of larger metal nanorods. Prior studies found that the total silver content of Ag_N-DNA is comprised of N_0 neutral atoms, with associated magic values as expected for a non-spherical cluster core (Figure 7.1a), and

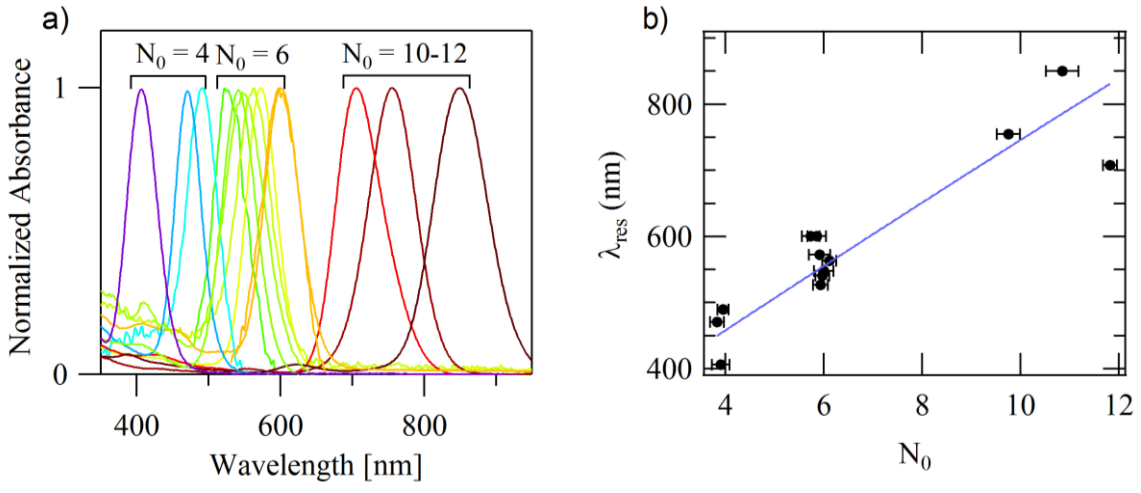

Figure 7.1. (a) Absorbance spectra of purified Ag_N-DNA with neutral silver content N_0 exhibit single excitation peaks at λ_{res} and cluster extinction coefficients that grow with N_0 (Figure F.3). **(b)** Dependence of λ_{res} on N_0 (black points) and fit to MG theory (blue line). Horizontal error bars represent estimated uncertainty from charge determination by mass spectrometry. **(a),(b)** Data taken in aqueous solution with 10 mM NH_4OAc.

N_+ cations that may incorporate as part of base-cluster ligands.[53,58] Consistent with the "superatom" concept for ligand-stabilized metal clusters,[20] N_0 also represents the number of electrons within the cluster core. All fluorescent Ag_N-DNA sized to date have N_0 values ranging from 4 to 12,[58] and thus multiple delocalized electrons exist in the cores of these Ag_N-DNA. Purified fluorescent Ag_N-DNA, including those studied here (see Table F.1 and Appendix F.1 for experimental details), display a single dominant absorbance peak, λ_{res}, coincident with the cluster's peak fluorescence excitation,[50] that moves to longer wavelength as N_0 increases (Figure 7.1). Additionally, the cluster extinction coefficient at λ_{res} increases with N_0 (Figure F.3). Such a single dominant peak that redshifts approximately linearly with increasing cluster size and increases in strength with cluster length is characteristic of the longitudinal collective electronic excitation of both rod-shaped metal clusters[55,56,210] and much larger rod-shaped metal nanoparticles.[102,103,209] Low temperature single emitter spectral studies additionally suggest a collective excited state in Ag_N-DNA, as emitter linewidths remain broad at 2K.[149] Thus, while Ag_N-DNA display molecular-like high quantum yields

typically associated with single electron transitions, the excitation leading to fluorescence shares a number of the distinctive metallic, or collective, attributes that are recognized as signatures of larger metal particles with elongated shapes. This behavior suggests that models for larger metallic systems, such as metal nanoparticles, may be applicable to Ag_N-DNA.

The criterion for defining a cluster excitation as collective or single-electron in character varies within the literature and remains an outstanding question within molecular plasmonics.[217] Earlier work[55] considered "plasmon" excitations in few-atom metal clusters to be those with the distinctive attributes found in classical electromagnetic models for metal rods.[218,219] Later studies additionally state that a plasmonic excitation must originate from multiple transitions between the single particle ground state orbitals, the Kohn-Sham (KS) levels in density functional theory. However, for linear chains of 2 - 40 Ag atoms,[211] the intense longitudinal excitation arises from a single KS transition, despite having the classical dependences of λ_{res} and intensity on *N*. Thus, there has been a lack of consensus on whether these excitations can be regarded as plasmons.[211] For thicker Ag cluster rods with pentagonal cross sections, three KS transitions contribute,[158,211] so their longitudinal excitations might be regarded as somehow more plasmonic. Such an interpretation is challenged by a lack of a clear trend with rod cluster cross section; for example, a single KS transition dominates the strong longitudinal excitation of ligand-stabilized, rod shaped "super-clusters" of repeating Au_{13} subunits.[220] Thus, it appears that the number of KS states involved may not always be useful as a defining characteristic for the nature of cluster excitations.

Recently, a more physical distinction between plasmonic and single-particle excitations was investigated for metal clusters and organic molecules, based on the defining nature of plasmons as density waves that arise from the Coulomb interaction.[212,221] Using a scaling

parameter to vary the overall interaction strength, plasmonic excitations were identified as those whose energies strongly increased with increasing interaction strength, while excitations with mainly single particle character exhibited little shift. Application to N = 20 Na and Au atomic chains identified the intense longitudinal excitations as plasmonic, despite their origin in a single KS transition and consistent with their MG-like properties. Given this result, we take the point of view that agreement with MG theory is indicative of plasmonic behavior.

7.3.2 Mie-Gans theory

To test whether models for larger metallic systems may be applied to Ag_N-DNA, and to probe Ag_N-DNA cluster shape and dielectric sensitivity, we interpret the dependences of λ_{res} on cluster size and solvent composition using classical Mie-Gans (MG) theory for ellipsoidal particles.[218,219] MG theory successfully predicts λ_{res} for metal nanoparticle rods with ~10 – 100 nm sizes and can also be used to describe smaller gas-phase "bare" metallic clusters (without ligands).[142] In MG theory, λ_{res} is the long wavelength solution to Eq. 7.1,[208]

$$\varepsilon(\lambda_{res}) = -\left(\frac{1-P}{P}\right)\epsilon_M \qquad (7.1),$$

corresponding to charge oscillations along the long axis of a metal ellipsoid with bulk dielectric function $\varepsilon(\lambda)$, embedded in a medium with dielectric constant ϵ_M. The depolarization factor P depends differently on AR for oblate and prolate particle shapes.[222] In the prolate case ($\ell > D$) that describes a rod-like cluster,

$$P = \frac{1-e^2}{2e^3}\left(ln\left(\frac{1+e}{1-e}\right) - 2e\right) \qquad (7.2)$$

$$e = \sqrt{1-(1/AR)^2} \qquad (7.3)$$

In the oblate case ($D > \ell$),

$$P = \frac{1+e^2}{e^3}(e - tan^{-1}e) \qquad (7.4)$$

$$e = \sqrt{(1/AR)^2 - 1} \qquad (7.5)$$

Eqs. 7.1 – 7.5 can thus be used for continuously varying *AR* values, as is necessary for fitting data for Ag_N-DNA of unknown *AR*.

We use ε(λ) for pure bulk silver as measured by Johnson and Christy[223] (widely used in studies of much larger metal nanorods[83,102,103,208,224,225]), which has the form:

$$\varepsilon(\lambda) = a\lambda^2 + c \qquad (7.6)$$

at sufficiently long wavelengths, with $a < 0$ and $c > 0$ (we neglect the small imaginary part of ε). For silver, the fitted values are $a = -5.55 \pm 0.02 \times 10^{-5}$ nm^{-2} and $c = 4.00 \pm 0.06$ for wavelengths greater than 470 nm (Appendix F.2 and Figures F.1 and F.2). Solving Eqs. 7.1 and 7.6 for λ_{res} (and avoiding a linear approximation used in prior studies[102]) yields the wavelength of the longitudinal collective resonance:

$$\lambda_{res} = \frac{\sqrt{-4a\left(c + \left(\frac{1-P(AR)}{P(AR)}\right)\epsilon_M\right)}}{-2a} \qquad (7.7)$$

7.3.3 Application to simulated linear silver clusters

Before applying this classical model to Ag_N-DNA, we test the applicability of MG theory to linear silver clusters by comparison to the theoretical results of Guidez and Aikens[56] for straight atomic Ag chains in vacuum ($\epsilon_M = 1$). Their time-dependent density functional theory (TDDFT) calculations found that, for Ag atom chains with $N = 2$-20 atoms, the longitudinal collective excitation wavelength, λ_{res}, scales linearly with *N*. Results varied somewhat between TDDFT with the statistical average of orbital potentials (SAOP) and LB94 model potentials[56]

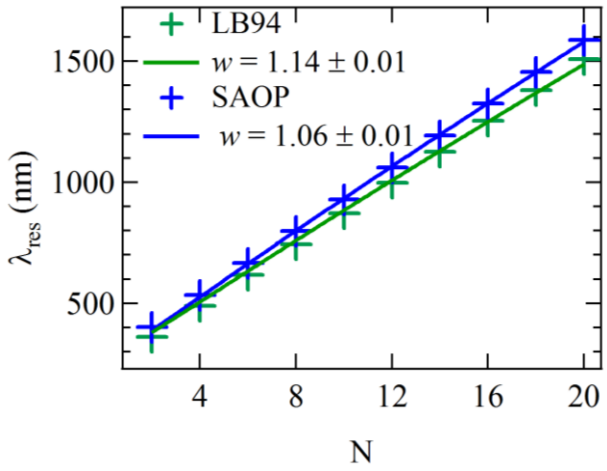

Figure 7.2: Crosses: λ_{res} of vacuum-embedded *N*-atom Ag chains with one-atom cross sections, previously calculated by TDDFT using LB94 (green) and SAOP (blue).[56] Solid lines: Fits to MG theory using $AR = N/w$ and $\varepsilon_M = 1$ to determine the least-squares values for *w*.

(crosses, Figure 7.2), giving a rough sense of the uncertainties still inherent in modern quantum calculations.

To apply MG theory to Ag cluster rods of known atom size *N* but unknown *AR*, we make the *ansatz* that cluster aspect ratio is $AR = N/w$, where *w* is a dimensionless correction factor (see schematic example in Figure 7.3). For linear Ag atom chains with bond lengths equal to the effective diameter of a silver atom, we expect $w = 1$. Fits of the TDDFT calculated results of Guidez and Aikens (Figure 7.2) to Eq. 7.7 return $w = 1.06 \pm 0.01$ (SAOP) and $w = 1.14 \pm 0.01$ (LB94), close to the ideal value of $w = 1$, validating the use of MG theory for linear Ag atom clusters. This success is despite several underlying approximations of the MG model: 1) the nonlocality of the dielectric response[226] is ignored, as are all quantum effects beyond those inherent to the bulk silver dielectric function; 2) the bulk silver dielectric function is applied to "rods" just 1 atom across; and 3) geometric differences between atomic Ag chains and the ellipsoidal shape assumed in MG theory are ignored. Despite these approximations, we find that MG theory appears trustworthy for linear clusters to within ~ 10% accuracy. This finding

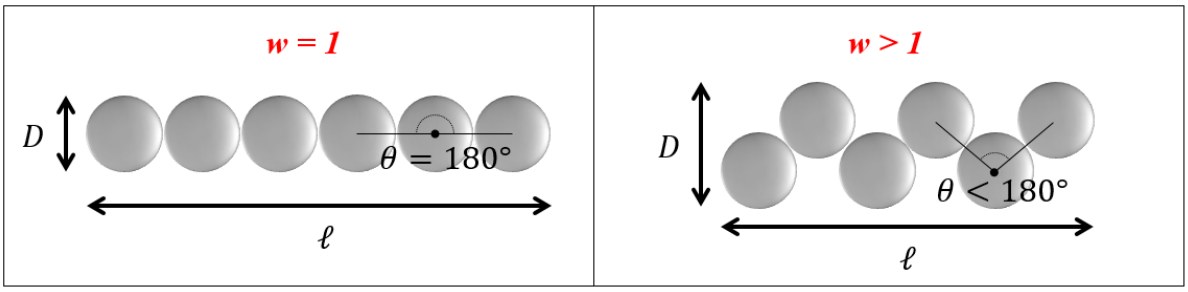

Figure 7.3. Two-dimensional example of dependence of w on cluster shape. θ represents Ag-Ag-Ag bond angle.

agrees qualitatively with previous studies of globular gas-phase Ag clusters that reported agreement between predictions of absorbance spectra by MG theory and by TDDFT.[142]

7.3.4 Application to Ag_N-DNA

For Ag_N-DNA, which have known Ag atom numbers but unknown *AR*, we make the same *ansatz*, $AR = N/w$, to relate cluster size to *AR*. We expect that shape deviations from a linear chain, associated with attachment of the cluster to the DNA, may reduce overall cluster length, ℓ, due to an increase in diameter D that could arise from Ag-Ag-Ag bond angles below 180°,[59,107] and this would effectively increase w (two-dimensional example in Figure 7.3). (We note that other Ag_N-DNA studies also suggest $w > 1$. Experimental and computational studies of the chiroptical properties of Ag_N-DNA presented evidence for helical cluster core shapes, with Ag-Ag-Ag bond angles below 180°.[59,106] Also, TDDFT calculations for a different proposed structure with Ag-Ag-Ag bond angles below 180° shows that excitation energies increase as w increases,[107] in qualitative agreement with MG theory.)

Because it is the neutral silver content, N_0, that determines the size of the metallic cluster core,[58] we take N_0 to be the size of the Ag_N-DNA cluster, and define $AR = N_0/w$. We use

$\varepsilon_M = 1.77$, corresponding to water at visible frequencies, as the homogeneous dielectric medium assumed by MG theory.

Fitting experimental values of λ_{res} for compositionally pure Ag_N-DNA as a function of N_0 (data points in Figure 7.1b) gives $w = 2.15 \pm 0.09$ (blue line in Figure 7.1b), corresponding to an effective thickness of approximately 2 atoms for Ag_N-DNA cluster rods. Thus, within a model that assumes all clusters belong to a similar structural family with constant w, Ag_N-DNA aspect ratios are $AR \sim N_0/2$. Of course, the selected value of ε_M also affects the fitted value of w: lower ε_M values result in lower w values and *vice-versa*. We are not aware of reliable estimates of the optical dielectric constant in the hydration shell of dilute DNA, which likely differs from bulk solution. We note that computational studies found that the *static* dielectric constant of water within several angstroms of B-form DNA is lower than bulk water,[227] consistent with confinement of liquid to a cavity.[228] Recent experiments on double-stranded DNA inside a bacteriophage measured the static dielectric constant of DNA to be lower than bulk water, as well.[229] However, it is unclear how these static dielectric constant measurements relate to the optical dielectric constant relevant to plasmonic response. All of these effects (variations in structural details and/or dielectric environment[106]) are lumped into the single parameter w, likely accounting for the spread in λ_{res} values of Ag_N-DNA with the same N_0 (Figure 7.1a, 1b).

7.3.4 Dielectric sensitivity

The high sensitivity of λ_{res} to the medium surrounding rod-shaped metal nanoparticles[101,224,225,230] is of great interest for nanoscale sensing of dielectric properties. Figure 7.4a plots MG predictions for index sensitivity, $d\lambda_{res}/dn_M$, for medium refractive index

$n_M = \epsilon_M^{1/2}$, as a function of *AR* for silver particles (grey line) and gold particles (yellow line). Published results for Au nano*particle* rods (red symbols, Figure 7.4a)[231–233] show that even for relatively large nanoparticles (~10 – 100 nm), experimental index sensitivity is reduced relative to MG predictions. While the reasons for this are not fully understood, spatial variation

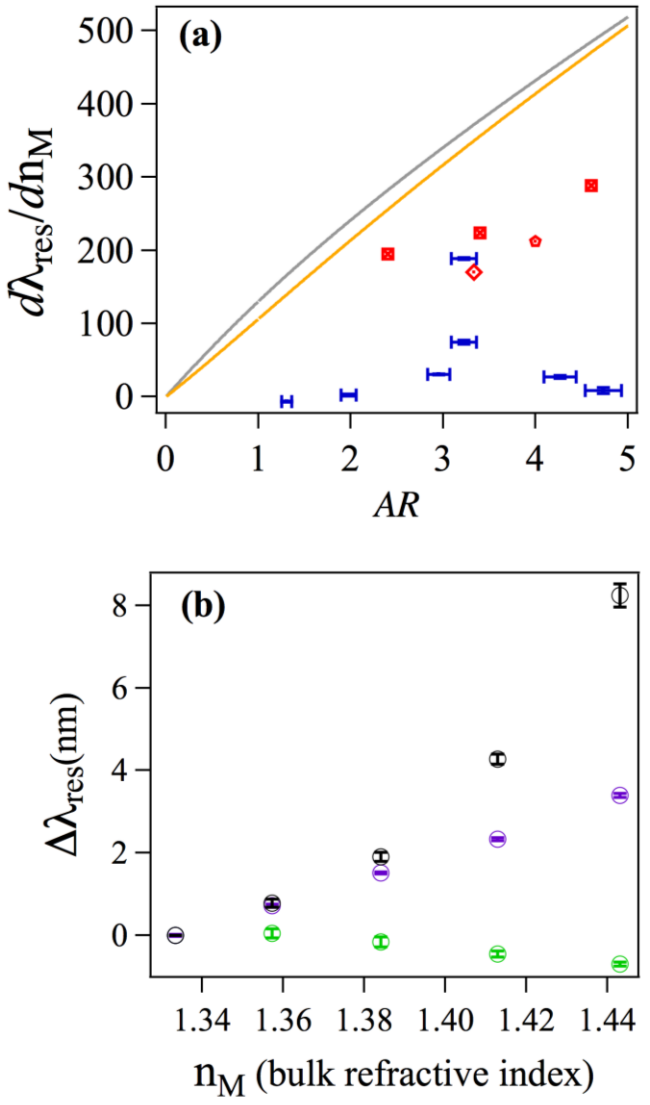

Figure 7.4. a) Index sensitivity predicted by MG theory for Ag (grey line) and Au (yellow line), previously reported for Au nanorods[231–233] (red symbols), and measured for Ag_N-DNA in water-glycerol mixtures (blue symbols, Table F.2). *AR* values for Ag_N-DNA are assigned based on wavelength and the fitted MG model in Figure 7.1b. **b)** Shift in λ_{res} as a function of bulk refractive index, n_M, measured for DNA1 (green), DNA8 (purple), and DNA9 (black).

of n_M close to the metal nanoparticle is a likely candidate[234] because $d\lambda_{res}/dn_M$ is weighted by local field enhancements that decay over length scales comparable to nanoparticle sizes.[235]

To test index sensitivity in the nano*cluster* (rather than nano*particle*) regime, we add glycerol as a cosolvent to pure aqueous solutions of Ag_N-DNA. We chose glycerol because it produces large changes in n_M while leaving DNA structure nearly unperturbed to well above 80% w/w glycerol,[236] the highest fraction employed here. Values of $d\lambda_{res}/dn_M$ for Ag_N-DNA are estimated using λ_{res} measured in 0% and 80% w/w glycerol (Figure 7.4a, blue symbols, and Table F.2), and effective *AR* values are estimated using the fit to Eq. 7.7 for λ_{res} in 0% glycerol (Figure 7.1b). Experimental values of $d\lambda_{res}/dn_M$ fall well below MG predictions, to a greater extent than measured index sensitivities for Au nanorods,[231–233] as might be expected due to the much smaller sizes of the clusters. However, for Ag_N-DNA, even the lowest values of $d\lambda_{res}/dn_M$ are easily detectable because Ag_N-DNA excitation linewidths (~40 – 90 nm) are much narrower than Au nanorod linewidths (~ 100 – 200 nm).[83]

To illustrate the range of behaviors we observed, Figure 7.4b shows $\Delta\lambda_{res}$ *versus* n_M for DNA1 (N_0 = 4), DNA8 (N_0 = 6), and DNA9 (N_0 = 6) in glycerol-water mixtures. All three Ag_N-DNA exhibit smaller $\Delta\lambda_{res}$ than predicted by MG theory (Figure F.12). As in the case of larger Au nanorods, λ_{res} may be less sensitive to changes in bulk n_M due to local refractive index values near Ag_N-DNA that do not scale with bulk index. In contrast to the nearly linear behavior predicted by MG theory and observed for larger Au nanorods,[231–233] DNA9 shows a superlinear rise, possibly suggestive of dielectric variations local to the Ag_N-DNA that do not reflect bulk conditions. Also, we note that because of this superlinear behavior, the value of $d\lambda_{res}/dn_M$ in Figure 7.4a for DNA9 would be 75% greater if $d\lambda_{res}/dn_M$ were estimated at higher

refractive index. Below, we comment on the negligible response of DNA1, which is slightly negative (Figure 7.4b).

For sufficiently small metal clusters, the dipole moment of the electronic excitation will be too small to produce a response to changes in surrounding dielectric properties. To understand if clusters of ~ 10 atoms could exhibit index sensitivity arising from non-negligible near-fields, we turn to recent TDDFT calculations for ellipsoidal Ag particles with 19 to > 2000 atoms.[209] This work found that replacing the sharp interfaces of the MG model with more realistic electron spill-out led to substantially suppressed near-fields at distances less than ~ 0.5 nm from the particle surface. However, even for the smallest 19-atom particle, field enhancement was non-negligible (a factor of ~3 at 0.5 nm from the surface).[209] These results suggest that it is reasonable to expect index sensitivity to changes within ~ 0.1 – 1 nm of the surface of ~ 10 – 20 atom Ag clusters. The negligible index sensitivity we find for Ag_N-DNA with N_0 = 4 (Figure 7.4; $AR \approx 1 - 2$) may indicate that this cluster size is simply too small to produce index sensitivity.

Although larger clusters should produce larger near-field enhancements, the effects of inhomogeneous dielectric surroundings on index sensitivity are difficult to predict due to the strong shape-dependence of the spatial variation of near-field enhancements.[103,235] While larger *AR* produces higher local field enhancement, these fields also become more confined near the tips of elongated nanoparticles.[209] Thus, as *AR* increases for a fixed size, index sensitivity is likely dominated by increasingly small volumes near the ends of elongated metal particles. In the cluster regime, this could lead to loss of index sensitivity if the sensing volume shrinks to atomic scales over which solvent is excluded. These factors may contribute to our observation of maximum index sensitivity at intermediate $AR \sim 3$ (Figure 7.4a). For ligand-stabilized

nanocluster rods, solvent accessibility to the areas of highest near-field enhancement near the ends of the rods is also dependent on the arrangement of the surrounding ligands. Thus, we might expect variations in index sensitivity for Ag_N-DNA stabilized by different DNA templates, even for Ag_N-DNA of similar *AR*, due to differences in the arrangement of DNA bases surrounding and stabilizing the silver clusters.

7.3.5 Alternate approaches

Prior studies of Ag_N-DNA in alcohol cosolvents employed a different approach to model solvent-induced Ag_N-DNA wavelength shifts in terms of the Onsager-based Lippert-Mataga (LM) model.[74,75] In qualitative contrast to the MG model, the LM model treats a chromophore as a point dipole in an otherwise empty cavity and assumes that solvent-induced wavelength shifts arise from changes in the *static* dipole moment between the chromophore's ground and excited states. The LM model additionally assumes that the chromophore interacts with surrounding solvent molecules *via* only "nonspecific" dipolar interactions (without specific interactions including hydrogen bonding). However, the measured behavior of Ag_N-DNA in alcohol-aqueous solvent mixtures was found to be inconsistent with the LM model, perhaps because specific solvent interactions exist between alcohol molecules and DNA.[59,74] (Previous studies suggest that glycerol is unlikely to interact specifically with Ag_N-DNA,[236] although further studies are necessary to confirm this.) The qualitatively different interpretation taken here in terms of *AR* and index sensitivity is instead based on the collective nature of Ag_N-DNA excitation. Such an interpretation can capture hydrogen bonding effects on local solvation if these effects produce changes in the dielectric surroundings that are local enough to be sensed by cluster near-fields. Subtle shape changes would be captured by changes to the parameter *w*,

although drastic geometric changes could, of course, be outside of the scope of the ellipsoidal model.

7.4 Conclusions

The classical MG model can describe the wavelength of longitudinal collective excitations for atomic silver chains, even in the limit of just a few silver atoms and in the case of ligand-stabilized chains. The applicability of this model to Ag_N-DNA (Figure 7.1) provides further evidence for the existence of a collective excitation process in these ligand-stabilized silver clusters and suggests cluster aspect ratios of ~ $N_0/2$, where N_0 is the neutral silver content. The clusters respond to changes in bulk solvent composition, with index sensitivities that are smaller than reported for much larger Au nanorods but still easily detected due to narrower linewidths. While we present these results in the context of sensitivity to medium dielectric properties, solvent sensitivity may instead arise through distinct mechanisms such as perturbations to cluster structure arising from solvation-induced changes of DNA structure. In either scenario, sensitivity to local dielectric variations is especially interesting in the context of DNA, which is known to have sequence-sensitive hydration patterns that affect conformational preference and function, such as DNA-protein interactions.[215] The specific hydration patterns of DNA are still not well understood[201] and are currently explored largely by molecular dynamics simulations.[200,237,238] Thus, a better understanding of the fluorescence-reported wavelength sensitivities of DNA-stabilized metal clusters may ultimately serve to illuminate an important issue for biomedical science.

8. Concluding Remarks

Whenever possible, always try to use your science to make the world a better place.

- Prof. Mildred Dresselhauss

UCSB Institute for Energy Efficiency Seminar, 2013

The discovery of the transistor in 1947 revolutionized modern society.[239] Now a multi-billion dollar industry, semiconductor-based computing materials are the cornerstone of modern technology and are in nearly every electronic device we own. Yet these technological advances come at a cost. The manufacture of semiconductor devices requires large amounts of energy and resources and uses a number of hazardous chemicals, posing significant environmental concerns.[240] Self-assembly, particularly of soft matter systems, may be a key alternative to traditional silicon-based lithography methods.[241] This dissertation has focused on one such self-assembling type of soft matter, DNA, and the unique advantages that it affords for assembling metals with atomic precision on the nanoscale.

We showed in Chapter 2 and Chapter 3 that the structure and sequence of DNA selects the unique properties of fluorescent Ag_N-DNA. Chapter 2 discusses how DNA selects certain "magic" fluorescence colors of silver clusters more frequently than others; these extra-stable clusters have magic numbers of neutral silver atoms that are consistent with a rod-like cluster shape,[58] as proposed by other studies.[53,59,107] In Chapter 3, we investigate the role of DNA base sequence in selecting Ag_N-DNA optical properties. Using techniques from machine learning and bioinformatics, we discover certain base motifs that are predictors of whether a

DNA template strand will stabilize fluorescent Ag_N-DNA, and we use these motifs to design new template strands for brightly fluorescent Ag_N-DNA, improving the chance of selecting a "bright" template threefold. All discovered base motifs contain 3 – 5 bases, and mass spectrometry suggests that, for Ag_N-DNA with fluorescence in the 450 – 800 nm range, two 3 – 5 base DNA motifs are required to stabilize a single cluster.[70] More recent studies on Ag^+-mediated base pairing[76] rationalize the high cytosine and guanine content of the discovered bright motifs. Swasey, *et al.*, showed that Ag^+ mediates base pairing between homopolymers of cytosine and also between homopolymers of guanine (notably, this was the first demonstration of Ag^+-mediated guanine-guanine pairing).[76] Because Ag_N-DNA are formed by reduction of Ag^+-DNA precursors, inclusion of cytosine and guanine in silver cluster template strands may ensure sufficient Ag^+ are present to form a cluster upon reduction. Further, Swasey and Gwinn found that duplexes formed by C_{11} or G_{11} homopolymers with heterobase mutations contained different numbers of Ag^+ depending on the mutation(s) made. This discovery may shed light on the mechanisms behind the sequence specificity of Ag_N-DNA fluorescence. Much work remains to be done on this topic, but it is clear that DNA plays a key role in dictating the properties of fluorescent silver clusters, making DNA a powerful tool for tunable arrangement of metal atoms.

Chapter 4 and Chapter 5 extend the utility of DNA for nanoscale metal arrangement by demonstrating DNA-mediated assembly of multi-Ag_N-DNA constructs. In Chapter 4, we probe whether two distinct Ag_N-DNA can remain stable in nanoscale proximity by developing dual-color silver cluster pairs that exhibit FRET. By careful choice of DNA template sequence, two Ag_N-DNA are brought together by Watson-Crick pairing of AT-rich tails appended to DNA template strands. These pairs exhibit FRET that can be thermally cycled by cyclic

melting and reforming of AT-rich tail pairing, demonstrating the thermal stability of the dual cluster pair.[71] In Chapter 5, we then show that DNA sequence engineering can be used to arrange many atomically precise Ag_N-DNA onto a prototypical DNA breadboard, a DNA nanotube. The modular design and assembly method for these multi-Ag_N-DNA arrays exploits the "dark" sequences discovered in Chapter 3 to design template strands hosting a silver cluster in one region and containing a second short linker region that can bind to a complementary docker region on the nanotube. The success of this method hinges on short linker length to avoid steric hindrance and on high melting temperature of the linker-docker duplex. Design of such multifunctional strands are only feasible through the informed design enabled by Chapter 3. Both Chapter 4 and Chapter 5 rely on purification methods to isolate monodisperse Ag_N-DNA solutions, which are a necessity for nanophotonic applications of Ag_N-DNA.

Motivated by a desire to understand the nature of the excited state that leads to Ag_N-DNA fluorescence and to explore their utility for local sensing, Chapter 6 and Chapter 7 investigate the sensitivity of Ag_N-DNA to local solvent environment. Chapter 6 investigates previous claims that Ag_N-DNA excitation is characterized by significant charge transfer to the bases[75] by studying the solvatochromism of Ag_N-DNA in alcohols. We show that the Lippert-Mataga model used to infer such charge transfer does not universally apply to Ag_N-DNA due to specific interactions between Ag_N-DNA and solvent and/or changes in DNA template hydration. Instead, spectral shifts result from cluster shape changes and/or dielectric changes local to the cluster.[74] Chapter 7 explores the effects of such dielectric changes on the excitations of fluorescent Ag_N-DNA. Comparing with simulations of Ag atom chains,[56] we find that the classical Mie-Gans theory used to predict the plasmonics resonances of much larger metal nanoparticles can also be applied to silver clusters of just a few atoms. Applying Mie-Gans

theory to Ag_N-DNA suggests that these silver clusters are characterized by a collective excitation process, with aspect ratios of ~ 1.5 – 5 (characteristic of rods) and thicknesses of ~2 atoms. We then test if such cluster plasmonics can be used to sense local changes in dielectric. Wavelength shifts produced by addition of glycerol suggest that Ag_N-DNA have potential for dielectric sensing on 0.1 – 1 nm scales, much finer scale than metal nanoparticles.[206]

The focus of much of this dissertation has been to understand Ag_N-DNA on a fundamental level, but many of the discoveries described here have exciting implications for applications. We believe that a better fundamental understanding of these materials is crucial to realizing useful applications with well-understood mechanisms. Already, several groups are moving towards more informed sensing applications. Careful work has been done by Yeh's group to further develop the class of NanoCluster Beacons (NCB) that utilize fluorometric changes in Ag_N-DNA to for sensitive nucleic acid detection,[66] including systematic study of sequence-dependence of the NCB probes[242] and development of single methylation site sensing.[243] Del Bonis-O'Donnell and coauthors developed a universal Ag_N-DNA-based probe for sensing DNA target strands, which can be used for any DNA target, regardless of sequence.[244] It is likely that future sensing applications may benefit from our work in Chapter 3. While nanophotonics applications of Ag_N-DNA still remain limited, the potential of these clusters for very local sensing, as well as their highly polarization dependent emission, may allow for exciting applications in the future. From a broader perspective, these studies demonstrate the power of DNA for self-assembling nanomaterials with a "genome," whose properties are determined by information encoded in DNA sequence. As we learn more about how we can control nanomaterials through DNA sequence, we may also learn more about how the complexity of life can be encoded in a sequence of just four bases.

Appendices

Appendix A. Supporting Information for Chapter 2

A.1 Generation of random DNA oligomer sequences

To create a library of 10-base DNA oligomers with random sequences, we used the MATLAB function `randi`, with default `rng` settings, to generate a large set of vectors of length 10 with elements $x_i: i = 1,2,\dots,10\,;\ x_i \in \mathbb{Z}\,;\ 1 \leq x_i \leq 4$, where $\{x_i\}$ is a set of uniformly distributed integers 1, 2, 3, 4. The nucleobases adenine, cytosine, guanine, and thymine (A, C, G, T) each correspond to an integer: A ≙ 1, C ≙ 2, G ≙ 3, T ≙ 4. To increase the probability of producing fluorescent Ag_N-DNA solutions using a give oligomer, we excluded all oligomers with sequences low in C and G bases. Specifically, let N_C be the number of C bases and N_G be the number of G bases in an oligomer. Then, if $N_C + N_G \leq 3$, the oligomer was excluded from the library of sequences.

This specific exclusion of sequences having 3 or fewer combined C's and G's has a relatively small effect on the randomness of the base content of the 10-base sequences we investigate because these sequences are a small subset of the total possible sequences. To be more quantitative, for 100 such randomly generated libraries of 10,000 strands, each with $N_C + N_G \leq 3$ excluded, the average number of C and G bases per strand was 2.587 ± 0.004 and 2.589 ± 0.003, respectively, while the average number of A and T bases per strand was 2.410 ± 0.004 and 2.413 ± 0.004, respectively. Figure A.1 shows the similarity between N_C , N_G and N_A , N_T for one such library. Since these average base numbers are sufficiently close to 2.5, exclusion of strands with $N_C + N_G \leq 3$ does not greatly shift average base count numbers from those for the completely random set.

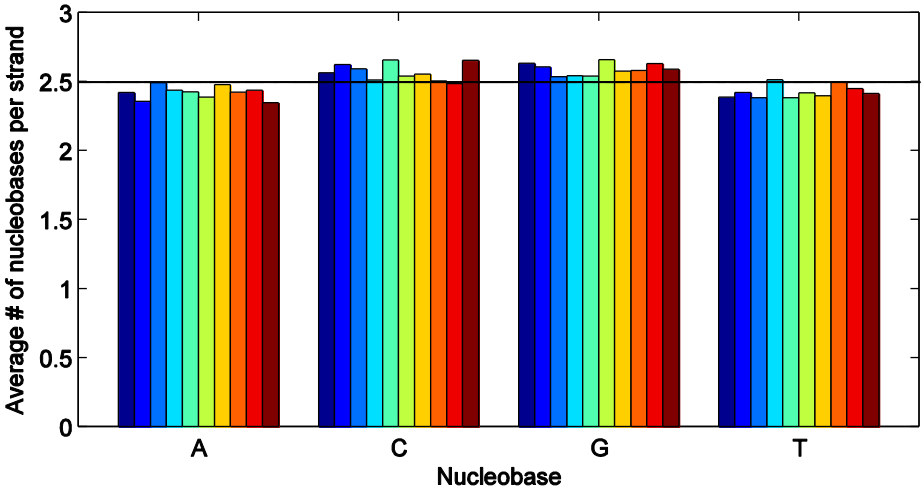

Figure A.1: Average number of bases per randomly generated sequence for a given example library. A library of 10,000 10-base DNA sequences was generated as described above. The average number of bases of each type are shown in this bar graph; color distinguishes each base position in the sequence, with dark blue indicating the first base (at the 5' end) and dark red representing the last base (at the 3' end). The horizontal black line marks 2.5, the expected average number of a given nucleobase per sequence for a perfectly uniformly distributed set of random oligomers. A slight increase in average C, G values, as well as a slight decrease in average A, T values is apparent for the case of excluding all strands with each with $N_C + N_G \leq 3$.

A.2 Robotic parallel synthesis and characterization of Ag_N-DNA

DNA was ordered in 384 well-plate format from Integrated DNA Technologies (IDT), with standard desalting. Each oligomer was pre-suspended in water at a concentration of 40 μM by IDT. Prior to robotic synthesis, plates were thawed by placing them in a shallow water bath at 40 °C. DNA was cooled to room temperature by the time synthesis was performed.

A Beckman Coulter Biomek® 2000 Laboratory Automation Workstation was used for all robotic Ag_N-DNA synthesis. Low retention pipette tips were used to minimize cross-contamination of adjacent wells and to improve pipetting accuracy (MAXYMum Recovery™ Robotic Pipet Tips, Axygen Scientific). Ag_N-DNA synthesis was performed in untreated, clear, flat-bottomed, low volume polystyrene well-plates (Corning®).

To obtain results over a range of possible Ag_N-DNA synthesis conditions, we performed preliminary robotic synthesis on about 300 of the strands to identify the DNA and $AgNO_3$ concentrations that produced the greatest number of brightly fluorescent Ag_N-DNA solutions.

After identifying 10 of the brightest Ag_N-DNA solutions from these trial runs, the DNA and $AgNO_3$ concentrations were optimized for each DNA oligomer based on solution brightness. Four synthesis conditions that bracket the optimal conditions were chosen for robotic synthesis:

(a) [DNA] = 10 μM, [$AgNO_3$] = 5 × [DNA] = 50 μM

(b) [DNA] = 10 μM, [$AgNO_3$] = 10 × [DNA] = 100 μM

(c) [DNA] = 20 μM, [$AgNO_3$] = 5 × [DNA] = 100 μM

(d) [DNA] = 20 μM, [$AgNO_3$] = 10 × [DNA] = 200 μM

All synthesis was performed in 10 mM NH_4OAc, pH 7, and [$NaBH_4$] = 0.5 × [$AgNO_3$]. DNase-free H_2O was used for solution preparation (IDT).

Solutions of 40 mM NH_4OAc with 4X concentration of $AgNO_3$ were mixed on the day of each experiment. Using the robotic pipettor, 10 μL of the buffer-silver solution was deposited into each well on the plate. Then, for synthesis conditions **(a)** and **(b)**, 10 μL of DNase-free H_2O was added to the entire plate, followed by 10 μL of 40 μM DNA from the IDT-shipped well-plate. For conditions **(c)** and **(d)**, 20 μL of 40 μM DNA were added to each well. The robot was programmed to mix by pipetting up and down twice after adding the DNA. During addition of DNA, fresh solutions of $NaBH_4$ were prepared. 10 μL of the reducing agent was then added to each well, followed by the aforementioned mixing. The process of adding DNA and then mixing the DNA-silver solution took 18-19 minutes; therefore no incubation step was necessary between addition of DNA and reduction by $NaBH_4$. Also, due to this time constraint, each plate was synthesized individually.

A well-plate centrifuge was used to gently spin each plate after robotic synthesis to remove any remaining air bubbles from the sides of the wells. Plates were covered and stored at 4 °C

until measurement. To be certain that solutions were reduced uniformly across the plate, a number of wells contained a control strand known to produce a very brightly fluorescent solution at all synthesis conditions used. This control strand, with sequence 5'-TTCCCACCCACCCCGGCCCGTT-3', produces a solution of clusters with a distinct spectrum characterized by a dominant red peak at ~636 nm and a green shoulder at ~540 nm. Emitters produced by this cluster were characterized in previous work.[53]

Each plate was measured 1 day after synthesis, 1 week after synthesis, and 4 weeks after synthesis. Generally, solution brightness peaked at 1 week and then decayed after 4 weeks. Plates were stored at 4 °C between measurements. A Tecan Infinite® 200 PRO was used to excite each well at 280 nm and collect fluorescent emission from 400-850 nm. The integration time was 20 μs.

A.3 Gaussian fitting of emission spectra

The emission spectrum from each individual well, corresponding to the Ag_N-DNA species formed by the 10-base oligomer in that well, was fitted to a single Gaussian lineshape, $f(x)$, as a function of energy, x:

$$f(x) = A_0 + a \cdot \exp\left[\frac{-(x-b)^2}{c^2}\right] \qquad (A.1)$$

From these fits, one can extract the constant offset A_0, which is due to the uniform background signal measured by the plate reader, the emission intensity a, the peak emission energy b, and the peak width c. Each fit parameter has estimated standard deviation σ_{A_0}, σ_a, σ_b, and σ_c respectively. Because some excess excitation light was collected by the instrument detector near 400 nm, emission data from 3.10 – 2.76 eV (corresponding to 400 – 450 nm) were excluded from the fit. This ensured the integrity of the Gaussian fit for Ag_N-DNA

solutions containing only dimly fluorescent emitters. Fits were performed using Igor Pro Curve Fitting software.

We chose to consider only spectra from the solutions that produced one dominant fluorescent peak (see Section 2.2). In fact, solutions characterized by a single dominant emission peak made up the majority of fluorescent Ag_N-DNA solutions; these either had a single emission peak or a dominant emission peak with a small shoulder to one side, indicating that an additional fluorescent species of Ag_N-DNA was also formed in smaller chemical yield and/or with lower quantum yield. To be specific, in the case of 10 μM DNA and 50 μM $AgNO_3$ measured one week after synthesis, all spectra were scrutinized by eye. From this scrutiny, about 240 of the 684 emitters were deemed to have sufficiently bright spectra, of which 116 were above 500 detector counts. Only spectra with > 500 detector counts were included in histograms to ensure that spectra were well above the noise signal at ~100-150 counts. Additionally, there were only 19 spectra that were both above 500 counts and contained two peaks of comparable intensity. The remaining 549 spectra either contained no fluorescent peaks or very dim fluorescence < 500 counts. We excluded all such spectra, regardless of the quality of the single Gaussian fit to one of the peaks, from the histograms.

Because such individual scrutiny is infeasible for the entire data set of > 8,000 spectra, the spectra were numerically sorted for quality of fit by a subset of their fitting parameters. This subset was chosen such that, for the case of 10 μM DNA and 50 μM $AgNO_3$ measured one week after synthesis (the case discussed above), the number of Gaussian fits identified by eye as "good fits" most closely matched the fits that were chosen numerically based on these parameters. Referring to the fit parameters in Eq. A.1, fits deemed as sufficient for histograms have the following criteria:

1. $a > 0$
2. $1.4 < b < 3.0$ (corresponds to peaks centered at 413 - 886 nm)
3. $0.05 < 2\sqrt{ln(2)} * c < 0.5$ ($2\sqrt{ln(2)} * c$ is the full width at half-maximum)
4. $\sigma_b < 0.01$
5. $\sigma_c < 0.008$

Condition (1) specifies the logical necessity that all Gaussian fits should have a maximum, not a minimum. Condition (2) requires that the spectral peak be only at most only a small distance outside the fitting range, which is 450-850 nm or 1.46-2.76 eV. Condition (3) constrains the full width at half-maximum (FWHM) to be within a given limit in order to remove all spectra resulting from two or more single Gaussians that are superimposed to create a single, broader Gaussian. This occurs in the case where two or more species of Ag_N-DNA form with equal brightness and are not sufficiently spectrally separated to resolve individual peaks. We also impose the condition that the FWHM may not be too small to remove cases where noise was fitted to narrow Gaussians. Finally, conditions (4) and (5) are imposed to remove cases where a sufficiently large amount of uncertainty exists in fitting parameter estimates. As specified, these conditions were tuned slightly to minimize the difference between the number of Gaussian fits numerically selected as "good" and those identified by eye as "good" for one out of the 12 data sets (10 μM DNA and 50 μM $AgNO_3$ measured one week after synthesis).

A.4 Color histograms

The complete set of histograms for all synthesis conditions and time points is displayed in Figure A.2. In addition to histograms, the distributions were also fitted by maximum likelihood estimation to a sum of two normal distributions (black curves, discussed in the next section).

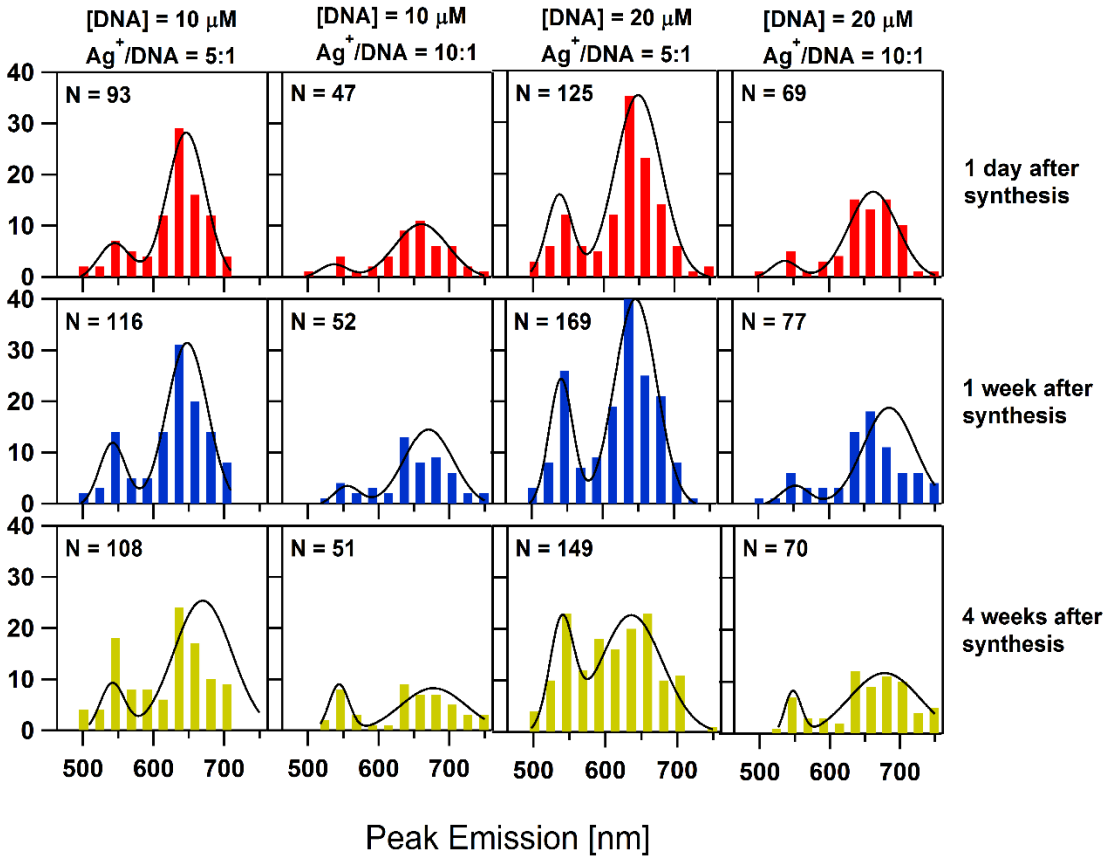

Figure A.2: Histograms of peak emission for Ag_N-DNA at different synthesis conditions and times after synthesis. Ag_N-DNA were synthesized using 10 μM or 20 μM DNA and 5:1 or 10:1 Ag^+:DNA. Measurements of UV-excited resulting solutions were taken 1 day (red), 1 week (blue), and 4 weeks (yellow) after synthesis. As an addition to histograms displayed here, maximum likelihood estimates for fits to a sum of two normal distributions are shown in black. Values for *N* indicate the number of Ag_N-DNA histogrammed in each plot, corresponding to criteria for brightness described in the previous section.

Four different synthesis conditions were employed, and three time points were chosen for measurement to establish the time stability of the clusters. For the higher Ag^+/DNA ratio of 10, the relative height of the ~550 nm histogram peak was diminished in comparison to the red peak, indicating the influence of silver concentration on the dominant cluster products formed.

The number of histogram bins, 12, was selected to be large enough to sufficiently demonstrate the presence of two dominant populations but small enough to avoid overemphasizing any other histogram structures that may be artifacts of bin size and position choice. Many different rules for selecting histogram bin size exist, but nearly all are intended

for normal data distributions. We intend these histograms to aid the reader in recognizing population abundances but also encourage scrutiny of the fits to the bimodal distributions for quantitative information.

A.5 Maximum likelihood estimation fits to histogram distributions

A normal distribution, with mean μ and standard deviation σ is defined as such:

$$normPDF(\lambda, \mu, \sigma) = \frac{1}{\sigma\sqrt{2\pi}} * \exp\left({-(\lambda-\mu)^2}/{2\sigma^2}\right) \qquad A.2$$

We used MATLAB software to fit data distributions to a custom defined bimodal distribution, $f(\lambda, p, \mu_1, \sigma_1, \mu_2, \sigma_2)$, using maximum likelihood estimation:

$$f(\lambda, p, \mu_1, \sigma_1, \mu_2, \sigma_2) = p * normPDF(\lambda, \mu_1, \sigma_1) + (1-p) * normPDF(\lambda, \mu_2, \sigma_2) \qquad A.3$$

where the mixing parameter p is measure of the relative sizes of the two modes. A maximum number of 400 iterations and 800 objective function evaluations were used to ensure convergence of the fits. Fit parameters for all data sets from Figure A.2 are in Table A.1.

	[DNA]	**[Ag^+]/[DNA]**	**p**	**μ_1 [nm]**	**μ_2 [nm]**	**σ_1 [nm]**	**σ_2 [nm]**
1 day	10	5	0.175	545	646	22.8	27.3
1 day	10	10	0.125	536	661	20.5	37.7
1 day	20	5	0.200	537	649	18.1	32.9
1 day	20	10	0.101	537	663	19.0	34.4
1 week	10	5	0.201	542	648	18.6	28.8
1 week	10	10	0.123	543	661	14.9	39.7
1 week	20	5	0.258	541	646	16.7	29.5
1 week	20	10	0.135	542	670	17.4	41.5
4 weeks	10	5	0.313	542	648	20.2	31.2
4 weeks	10	10	0.247	544	678	14.3	46.7
4 weeks	20	5	0.264	539	636	16.7	43.0
4 weeks	20	10	0.140	547	678	12.0	51.1

Table A.1: Fit parameters from maximum likelihood estimation fits to bimodal distributions.

In the case of all DNA and silver concentrations and for all time points, the first mode μ_1 is clearly more invariant than the second mode μ_2, which depends more strongly on the value of $[Ag^+]/[DNA]$. Specifically, for $[Ag^+]/[DNA] = 5$, the average values of the modes are $\mu_1 = 541 \pm 3$ nm and $\mu_2 = 646 \pm 5$ nm, while for $[Ag^+]/[DNA] = 10$, the average values are $\mu_1 = 542 \pm 4$ nm and $\mu_2 = 668 \pm 8$ nm. Thus, within statistical significance, the silver-to-DNA ratio during synthesis shifts only the redder portion of the bimodal distribution. Additionally, the mixing parameter p depends on the silver-to-DNA ratio, with $p = 0.235 \pm 0.052$ for the lower silver-to-DNA ratio and $p = 0.145 \pm 0.052$ for the higher ratio

A.6 HPLC-MS size measurements

The protocol used to determine cluster size and charge by tandem high-performance liquid chromatography-mass spectrometry (HPLC-MS) with in-line spectroscopy is described in detail elsewhere[52]. Specific Ag_N-DNA species were injected into 50 mm x 4.6 mm Kinetex C18 core-shell column with 2.6 µm particle size and 100 Å pore size (Phenomenex) and separated by one round of ion-pair reversed-phase HPLC (Waters 2695 Separations Module) with 35mM ion-pairing (IP) buffer triethylamine acetate (TEAA) in HPLC grade water and methanol at pH 7. All samples were separated with linear gradients from 5-25% methanol at ambient temperature, except for Sample 355, which was separated at 40ºC under the same gradient. A Waters 2487 absorbance detector was used to detect all DNA products, and an Ocean Optics QE65000 thermoelectrically cooled array detector was used to monitor all fluorescent products excited by a 270 nm LED source. Thus the spectral properties of each eluted plug of material collected from the HPLC can be matched to its mass composition and charge, determined by negative-ion mode MS (Micromass QTOF2) with electrospray

ionization. Prior to MS, purified samples were solvent exchanged from the HPLC eluent back into 10 mM ammonium acetate in water. Each sample was then directly injected at 10 μL/min into the MS, and the signal was averaged over 15 minutes. The MS was operated at 120ºC source temperature, 150ºC desolvation temperature, 45 V cone voltage, and 10 eV collision energy.

Three of the 684 random DNA oligomers, 356, 355, and 49, were chosen to inspect clusters stabilized by these strands using HPLC. Strand 356 forms a 630 nm emitting cluster, Strand 355 forms a 530 nm emitting cluster, and Strand 49 forms a 690 nm emitting cluster (Table A.2). Neutral silver atom numbers, N_0, are determined for each of these by subtracting the charge of the cluster in units of the electron charge, Q_{cl}/e (the number of cations N_+), from the total silver atom number, N_{Ag} (in Chapter 2, $N_{Ag} = N$; we append a subscript here for clarity):

$$N_0 = N_{Ag} - {}^{Q_{cl}}/_{e} = N_{Ag} - N_+ \qquad A.4$$

The number of DNA oligomers associated with each product, N_s, was also determined. In cases with $N_s = 1$, the Ag_N-DNA contains one DNA strand. We established previously[53] that silver clusters can "glue" together 2 DNA strands. That is what $N_s = 2$ means: the Ag_N-DNA contains 2 copies of the same DNA strand.

In the figures that follow, the ionization state is represented as Z.

The charge of the negative Ag_N-DNA ions formed by negative ion electrospray is

$$-eZ = -en_{pr} + eN_+ \qquad A.5$$

where n_{pr} is the number of protons removed from the DNA and N_+ is the number of silver cations.

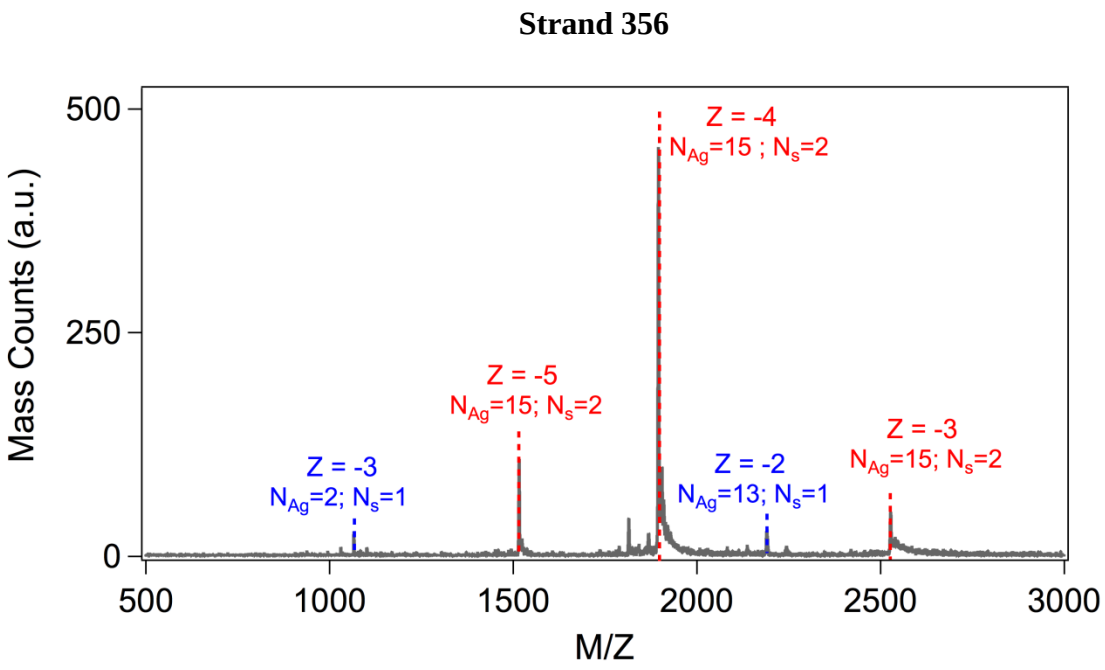

Figure A.3: Mass spectrum of cluster species stabilized by Strand 356, collected by direct injection into an electrospray ionization source following one round of TEAA-based HPLC purification. Red dashed lines indicate the ladder of ionization states, *Z*, of products containing 2 strands, $N_s = 2$, and the given number of bound silver atoms, N_{Ag}. Blue dashed lines indicate the ladder of ionization states, *Z*, of fragmentation products containing 1 strand, $N_s = 1$, and the given number of bound silver atoms, N_{Ag}.

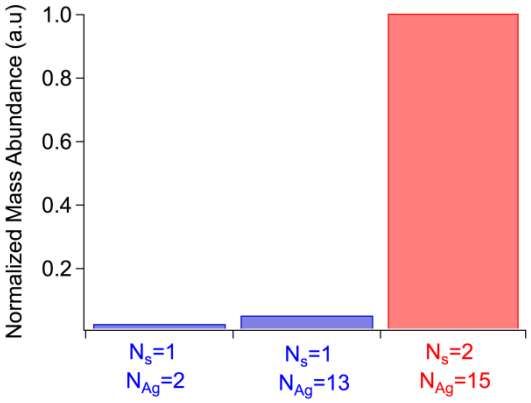

Figure A.4: Relative mass abundances of complexes with $N_{Ag} = 15$ and $N_s = 2$ (red) and with $N_{Ag} = 2,13$ and $N_s = 1$ (blue).

Integrated mass counts over the $N_{Ag} = 15$, $N_s = 2$ peak are ~20x more abundant than the $N_s = 1$ peaks. We conclude that the composition of the fluorescent Ag_N-DNA is $N_{Ag} = 15$, $N_s = 2$: a strand dimer species containing a total of 15 silver atoms. The peaks for the strand

monomer, N_s = 1, species are fragments produced during MS because 1) the sum of their N_{Ag} values equals 15 and the sum of their N_s values equals 2, consistent with fragmentation of the N_{Ag} = 15, N_s = 2 strand dimer species, 2) the relative abundances of the N_s = 1, N_{Ag} = 2 and N_s = 1, N_{Ag} = 13 peaks are comparable, as expected for two pieces of a whole, and 3) if these N_s = 1 species had been present *before* MS, they should have eluted the HPLC column at different times compared to the N_s = 2, N_{Ag} = 13 species. We thus identify the fluorescent Ag_N-DNA as containing 15 Ag atoms and 2 DNA strands.

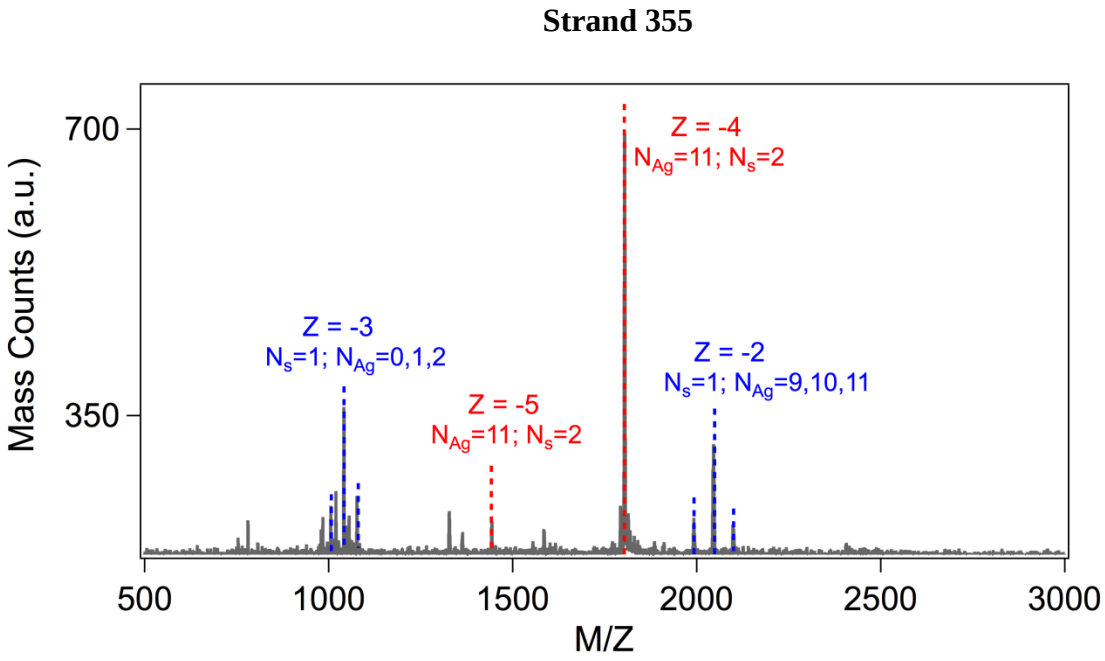

Figure A.5: Mass spectrum of cluster species stabilized by Strand 355, collected by direct injection into an electrospray ionization source following one round of TEAA-based HPLC purification. Red dashed lines indicate the ladder of ionization states, *Z*, of products containing 2 strands, N_s = 2, and the given number of bound silver atoms, N_{Ag}. Blue dashed lines indicate the ladder of ionization states, *Z*, of fragmentation products containing 1 strand, N_s = 1, and given bound silver atom number, N_{Ag}.

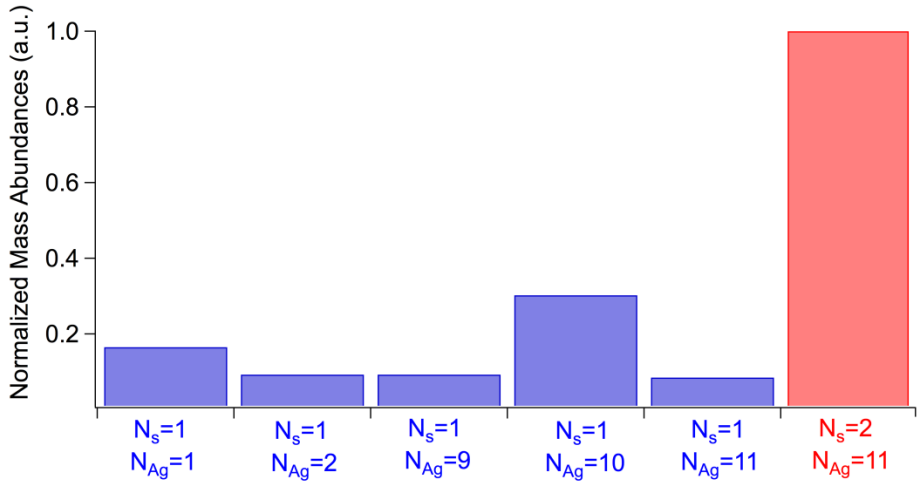

Figure A.6. Relative mass abundances of complexes with N_{Ag} = 11 and N_s = 2 (red) and with N_{Ag} = 1, 2, 9, 10 and N_s = 1 (blue).

Integrated mass counts over the N_{Ag} = 11 species are ~3x more abundant than the most abundant N_s = 1 species. We conclude that the N_s = 1 species are fragments of the 11 Ag atom strand dimer species because the sum of the monomer N_{Ag} and N_s values equal 11 and 2, respectively, because they are present in relatively equal abundances, as expected for two pieces of a whole, and because we expect species containing N_s = 1, present *before* MS, to elute the HPLC column at different times compared to N_s = 2 species. We thus identify the species containing 11 Ag atoms and 2 DNA strands as the fluorescent species.

Integrated mass counts over the N_s = 2, N_{Ag} = 16, 17 species are ~5x more abundant than the most abundant N_s = 1 species. We conclude that N_s = 1 species are fragments of the 16, 17, 18 Ag-atom dimers because these strand monomer products combine to yield summed values of N_{Ag} = 16,17, 18 and N_s = 2 (i.e. N_{Ag} = 13; N_s = 1 and N_{Ag} = 3, N_s = 1 together contain the same number of DNA strand and silver atoms as N_{Ag} = 15; N_s = 2); because they are present in relatively equal abundances (Figure A.8b), as expected for two pieces of a whole, and because we expect species containing N_s=1 to elute the HPLC column at different times compared to N_s = 2 complexes. We thus conclude that the fluorescent species is one of the 3

dimer complexes. Although the N_{Ag} = 16 species is the most abundant product, the fluorophore may instead be the 17 or 18 atom species, given their comparably high abundances.

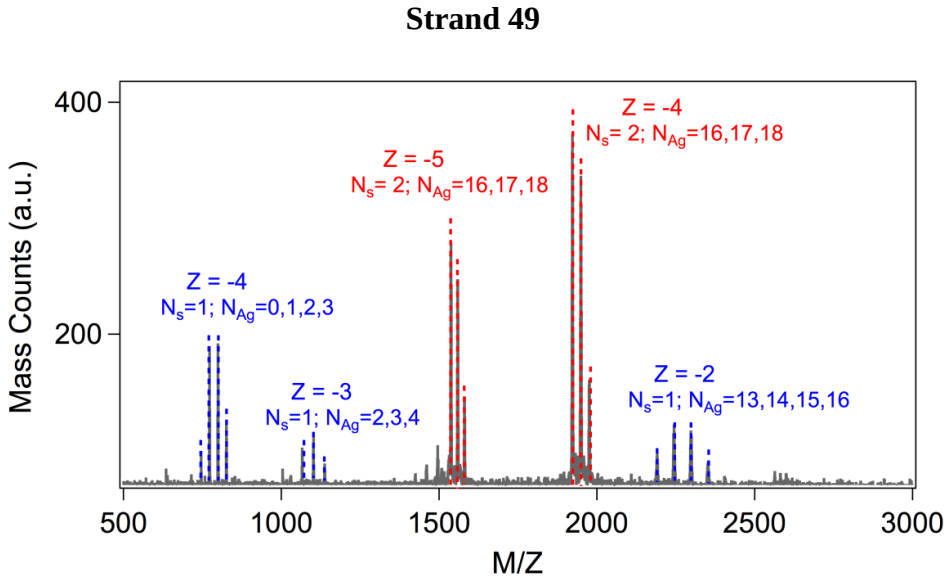

Figure A.7: Mass spectrum of cluster species stabilized by Strand 49, collected by direct injection into an electrospray ionization source following one round of TEAA-based HPLC purification. Red dashed lines indicate the ladder of ionization states, Z, of products containing 2 strands, N_s = 2, and the given number of bound silver atoms, N_{Ag}. Blue dashed lines indicate the ladder of ionization states, Z, of fragmentation products with N_s = 1, and the given number of bound silver atoms, N_{Ag}.

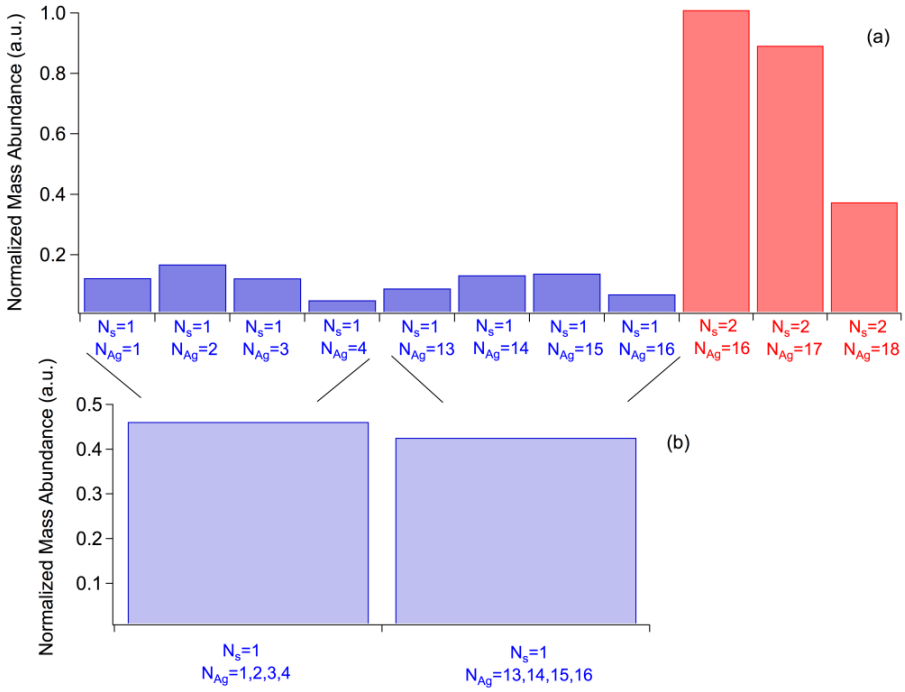

Figure A.8: Relative mass abundances of complexes with N_{Ag}=16, 17, 18 and N_s = 2 (red) and with $N_{A\,g}$= 1-4, 13-16 and N_s = 1 (blue). (b) Summed relative abundances of the N_{Ag} = 1-4, 13-16 and N_s = 1 complexes.

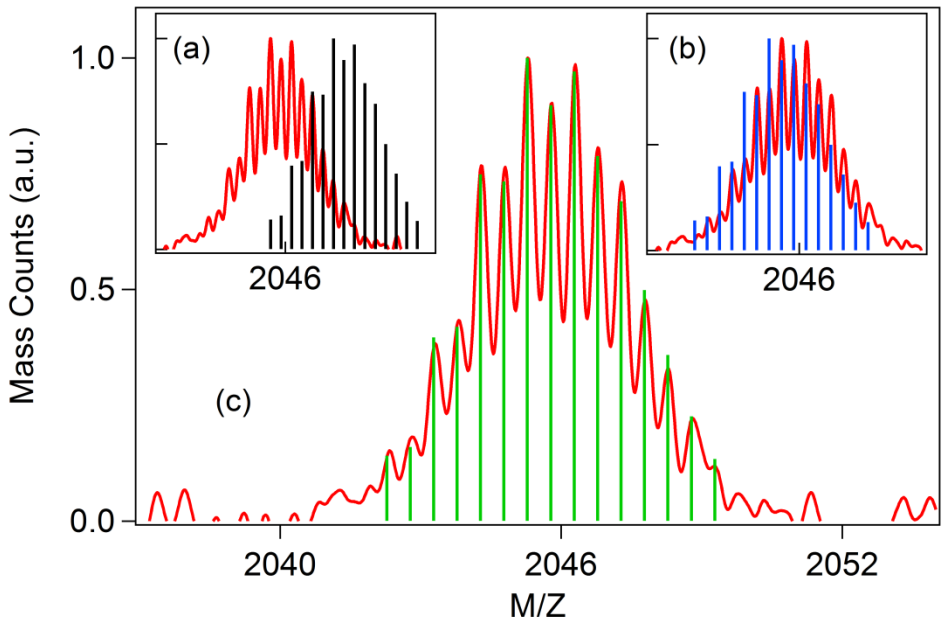

Figure A.9: Mass spectrum (red) of a N_{Ag} = 10 cluster stabilized by Strand 355, (TCCACGAGAA), with a Z = - 2e ionization charge state. Calculated mass distributions for the cases of a) a neutral cluster (Q_{cl} = 0) (black bars) and b) a cluster with charge Q_{cl} = +5e (blue bars) display offsets in M/Z with respect to the measured data. The calculated mass distribution for c) a cluster with charge Q_{cl} = +6e (green bars), however, shows excellent agreement with the data.

Calculated mass distributions for Ag_N-DNA, assuming entirely *neutral* silver content, consistently display shifts in M/Z relative to the measured mass spectra (Figure A.9a). We rationalize these apparent offsets by assuming that the silver content is comprised of N_0 neutral atoms and N_+ silver cations. For bare DNA, the electrospray ionization source sets the total ionization charge, $-eZ$, by removing Z protons. For DNA with attached silver cations, the electrospray process must remove additional protons to compensate for the net positive charge of the silver cations, N_+, in order to reach a given ionization charge, $-e$Z. Thus for Ag_N-DNA, the mass of the ionized complex is $M = M_{DNA} + m_{Ag}N_{Ag} - (Z + N_+/e)$, where M_{DNA} is the mass of the DNA strand, m_{Ag} is the mass of silver and N_{Ag} is the number of bound Ag atoms. We can then relate the observed shifts in M/Z to cluster charge by $\Delta M/Z = -N_+/eZ$. We determine $\Delta M/Z$ from the center values of Gaussian fits to both the data and calculated mass distributions

for different values of Q_{cl}. Figure A.9 displays calculated distributions for a 10 Ag atom cluster with $N_+ = 0$, $+6e$ and $+7e$, identifying $N_+ = +6e$ as the best fit for this cluster.

Sample #	λ_{ex}, max (nm)	λ_{em}, max (nm)	N_s	N_{Ag}	N_0	N_+
356	550	630	2	15	6	9
			1	2	0	2
			1	13	6.3	6.7
355	470	530	2	11	4	7
			1	1	0	1
			1	2	0	2
			1	9	4	5
			1	10	4	6
			1	11	*N/A*	*N/A*
49	540	690	2	16	6	10
			2	17	6	11
			2	18	7	11
			1	1	0	1
			1	2	0	2
			1	3	0	3
			1	4	*N/A*	*N/A*
			1	13	6.3	6.7
			1	14	5.6	8.4
			1	15	6.3	8.7
			1	16	7	9

Table A.2: Number of DNA strands (N_s) and number of Ag atoms (N_{Ag}) comprising identified Ag_N-DNA for given sample numbers. The number of neutral Ag atoms (N_0) contained within the cluster as well as the cluster charge (Q_{cl}) are additionally specified.

Table A.2 tabulates size and charge results for identified Ag_N-DNA species stabilized by strands 356, 355 and 49. N_s and N_{Ag} are determined directly from mass spectra (Figure C.3 – A.8). N_+ is determined by fitting calculated mass distributions to the mass spectral data (Figure A.9). As previously stated, N_0 is determined by subtracting the number of charged atoms from the total number of atoms ($N_{Ag} - N_+$). Instances of non-integer values of N_+ are observed in

fragmentation products, which arise when species comprising 2 DNA strands (dimer products) split into 2 distinct Ag species, each bound to 1 DNA strand (monomer products). For a given dimer product, fragmentation may yield several monomer products. For example, for Strand 49, the 16 Ag dimer species can split into 1 strand bound to 13 and 3 Ag atoms; 14 and 2 Ag atoms; 15 and 1 Ag atoms or 16 and 0 Ag atoms. Because fragmentation can produce different monomer products with the same total silver content, N_{Ag}, but different values of N_0 and N_+, the fitting process can return non-integer values for the neutral and cationic silver atom numbers.

A.7 Details of molecular dynamics simulations

We used the AMBER 12 molecular dynamics package[108] to generate the Ag_N-DNA structures shown in Figure 2.3. The Ag_N clusters were built with AMBER using LEaP, and DNA strands were built with AMBER using NAB (Nucleic Acid Builder). The AMBER 12 software package was used to combine the Ag cluster and DNA strands together into an Ag_N-DNA and to run molecular dynamics simulations.[108] Ag clusters were implemented as custom residues using the method by Walker,[109] and VMD was used to analyze structural distances.[110]

Based on the known affinity for Ag^+ ions to bind to conjugated ring nitrogens[111], we chose to attach the measured number of silver cations, N_+, to these sites, and to build the clusters by bonding neutral silver atoms to the Ag^+. Because prior work indicated a rod-like structure for the neutral cluster core,[53] and because base stacking energies set a preferred base-base separation, we initialized the cluster in an accordion-like rod form with an angle θ set at 79º between Ag-Ag bonds of length L_1 = 2.53 Å and with stretching force constant f = 143.96 kcal/mol Å^2 and an equal bending force constant[112]. This produces a distance of L_2 = 3.2 Å between the terminal Ag atoms in Ag-Ag-Ag triads of the accordion rod, equal to the base

separation in B form DNA (see Figure A.10 for a schematic). Each neutral Ag atom in this accordion-like rod structure is bound to a silver cation, which in turn attaches to the conjugated ring nitrogen of a base, chosen as cytosine (C) for simplicity. These reasonable choices are dictated by the known composition of Ag_N-DNA (N_0 and N_+) and geometrical constraints, which may be improved upon when more is known about the details of silver interactions with DNA.

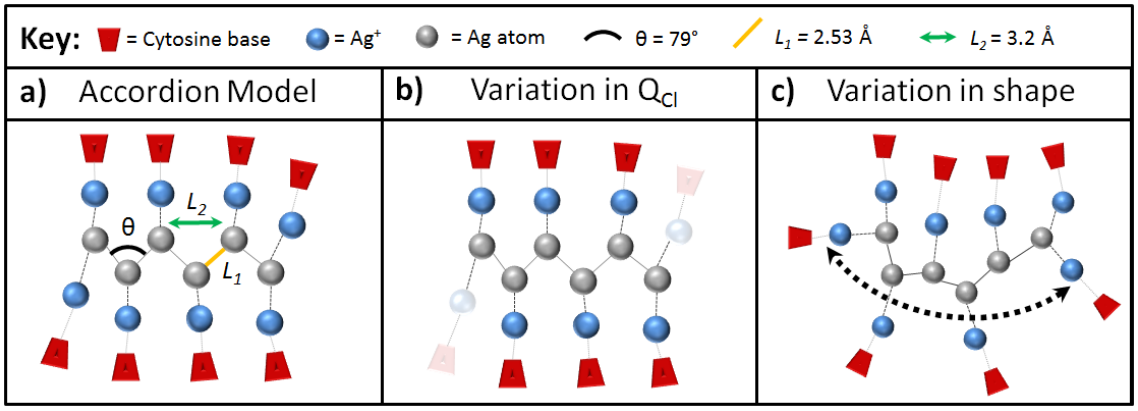

Figure A.10: Cartoon schematics of cluster diagrams, *not to scale*. **a)** Cluster initialization geometry and bond parameters for an accordion-like neutral core (grey spheres) surrounded by Ag^+ (blue) associated with cytosine bases (red). The silver-silver bond angle is set to 79º (black arc), and bond length is 2.53 Å (yellow). **b)** The accordion model allows for variations in cluster charge Q_{cl} for a given number of neutral silver atoms N_0, as seen in HPLC-MS measurements. Such changes in N_+ could also lead to cluster shape changes, as evidenced by the shape differences between clusters in Figure 2.3c and 2.3d. **d)** Bending or stretching of the zig-zag cluster backbone could explain the width of magic color peaks observed in Figure 2.1.

Because the AMBER force fields do not contain parameters for bonding Ag atoms to cytosine bases or for bonding Ag atoms to other Ag atoms, we used results from Refs 13-15 to estimate these parameters. Previous work on silver cations bound to DNA indicate that Ag^+ bind most strongly to the conjugated ring nitrogen in cytosine.[111] Because the bonding structure of Ag^+ to this nitrogen in the cytosine base resembles that of silver to the nitrogen in pyridine, we set the bond length L_1 and stretching force constant f in an Ag^+-N bond for cytosine to the previously studied bond length and stretching force constant in an Ag-N bond for pyridine.

The bond distance in an Ag-N bond for pyridine has been shown to be 2.38 Å, and the stretching force constant for Ag-N bonds for pyridine has been shown to be 71.98 kcal/mol·Å^2.[112] To model the bending force constant, results from Lin and Wang on zinc force field parameters for AMBER were used[113]. The bending force constant for Ag-N bonds was assumed to scale with the stretching force bond the same way as in Zn-N bonds; thus the ratio of stretching force constant to bending force constant in Zn-N bonds was used to determine the bending force constants for Ag-N bonds from the stretching force constant.

For MD simulations, we used implicit solvent in the Born solvation model. After initializing the structure as described above, simulations were run for 20,000,000 steps, with each step equal to 1 fs. The non-bonded interaction cut-off was 110 Å for minimization and simulations. Images were rendered in VMD with the Tachyon ray tracer. The images in Figure 2.3 are taken after 1 ns of simulation time. Figure 2.2 shows that for neutral clusters with N_0 = 6, the number of silver cations varies from N_+ = 6 to 10. To test effects of varying the locations and numbers of silver cations, we examined N_0 = 6 clusters with a single Ag^+ cation bound to each interior atom in the neutral cluster and two Ag^+ to each of the terminal atoms. We compared results for this N_+ = 8 structure (Figure 2.3c) to results for adding additional Ag^+ that join two C bases at either end of the cluster (N_+ = 10; Figure 2.3d). Figure A.11 and Figure 2.3 show that after brief initial transients, the different interactions of the ions with the phosphate backbone result in clusters with different degrees of curvature along the long axis of the rod. We expect higher degrees of curvature to correspond to increasing blue-shifts of the longitudinal collective mode. Thus clusters with different detailed arrangements of the silver cations should exhibit different wavelengths, qualitatively accounting for the widths of the magic color peaks that correspond to a cluster with a given magic number size, N_0.

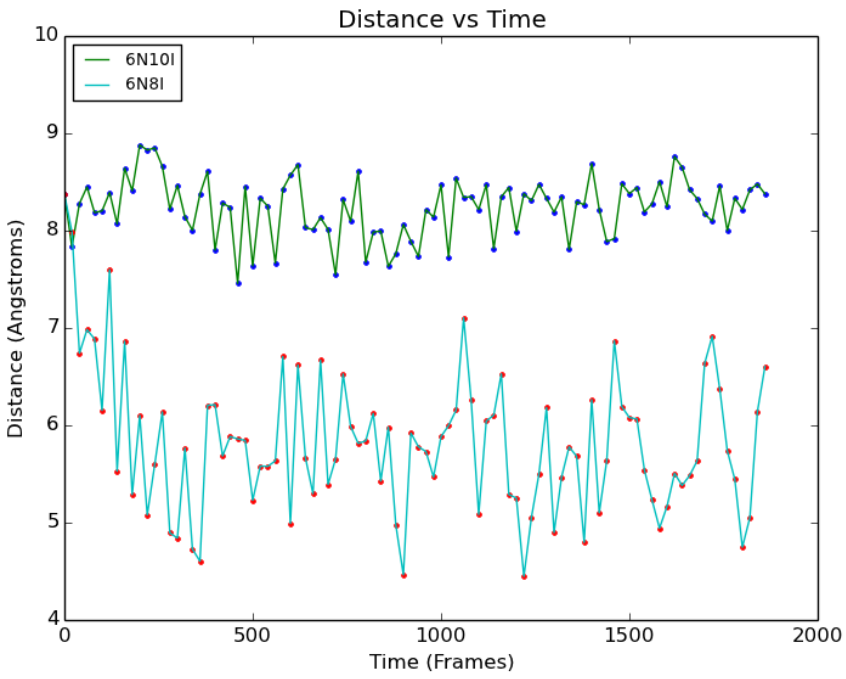

Figure A.11: Computed separation between the end atoms in an $N_0 = 6$ cluster with $N_+ = 8$ (blue trace, 6N8I) and $N_+ = 10$ (green trace, 6N10I). 2000 frames corresponds to 2 nanoseconds. Simulations are performed in implicit solvent at 300 K.

A.8 Color-sequence degeneracy in Ag_N-DNA

Section 2.3.5 states that 26 distinct 10-base DNA strands stabilize emitters with wavelengths that fall within the same 10 nm window. For the case of 20 μM DNA and $[AgNO_3] = 5 \times [DNA] = 100$ μM, Table A.3 lists oligomer sequences and corresponding peak cluster emission wavelength, as extracted by a single Gaussian fit. Many of the sequences in Table A.3 contain C- and G-rich regions, but variation exists in the exact 10-base sequences that stabilize clusters with very similar wavelengths. We emphasize that although sequence certainly controls cluster color, sequences with distinctly different base composition can stabilize clusters of the same color. This challenges base-recognition assays that have been proposed, where synthesis of Ag_N-DNA on a target strand is used as a distinguishing marker between different DNA sequences.

DNA sequence	Peak Emission [nm]
CGCCGAGGCT	630.2 ± 0.2
ACCGCGACCG	630.3 ± 0.2
AAGTGGCGTC	631.1 ± 0.4
CGGCCTCTAG	631.2 ± 0.5
TGGCGGCACT	631.8 ± 1.1
GCGCCAGTCC	631.9 ± 0.3
GGACGGCTCA	632.1 ± 0.3
GCTCTTGAGA	632.3 ± 0.4
TCTCTACTCG	633.6 ± 0.1
TAACTATGGT	633.8 ± 0.2
CCCACGCAAA	634.5 ± 0.4
TCCTCCGGCC	635.2 ± 0.4
CGGACCATCG	635.3 ± 0.4

DNA sequence	Peak Emission [nm]
GCCACCTCGA	635.3 ± 0.4
AACCCCTACG	635.7 ± 1.2
TGCCCTGTCG	636.0 ± 0.4
CGCGGAGGAT	636.0 ± 0.4
CCGCAGCTGG	637.0 ± 0.2
TAGTTGCCGT	637.0 ± 0.3
TTACGACCCA	637.1 ± 0.2
GGACTATCTC	638.7 ± 0.3
GAGCCTCAGC	638.8 ± 0.4
GGGCGGTACT	639.4 ± 0.2
TGTCAACAAA	639.6 ± 0.1
GCTCGCCGGG	639.8 ± 0.5
CACGGGCAGA	639.8 ± 0.2

Table A.3: DNA sequences and corresponding cluster color for Ag_N-DNA with peak emission wavelength between 630 nm and 640 nm. Peak wavelengths and standard deviations are extracted by Gaussian fitting, previously described.

Appendix B. Supporting Information for Chapter 3

B.1 Average bright/dark ratios for 3-base motifs

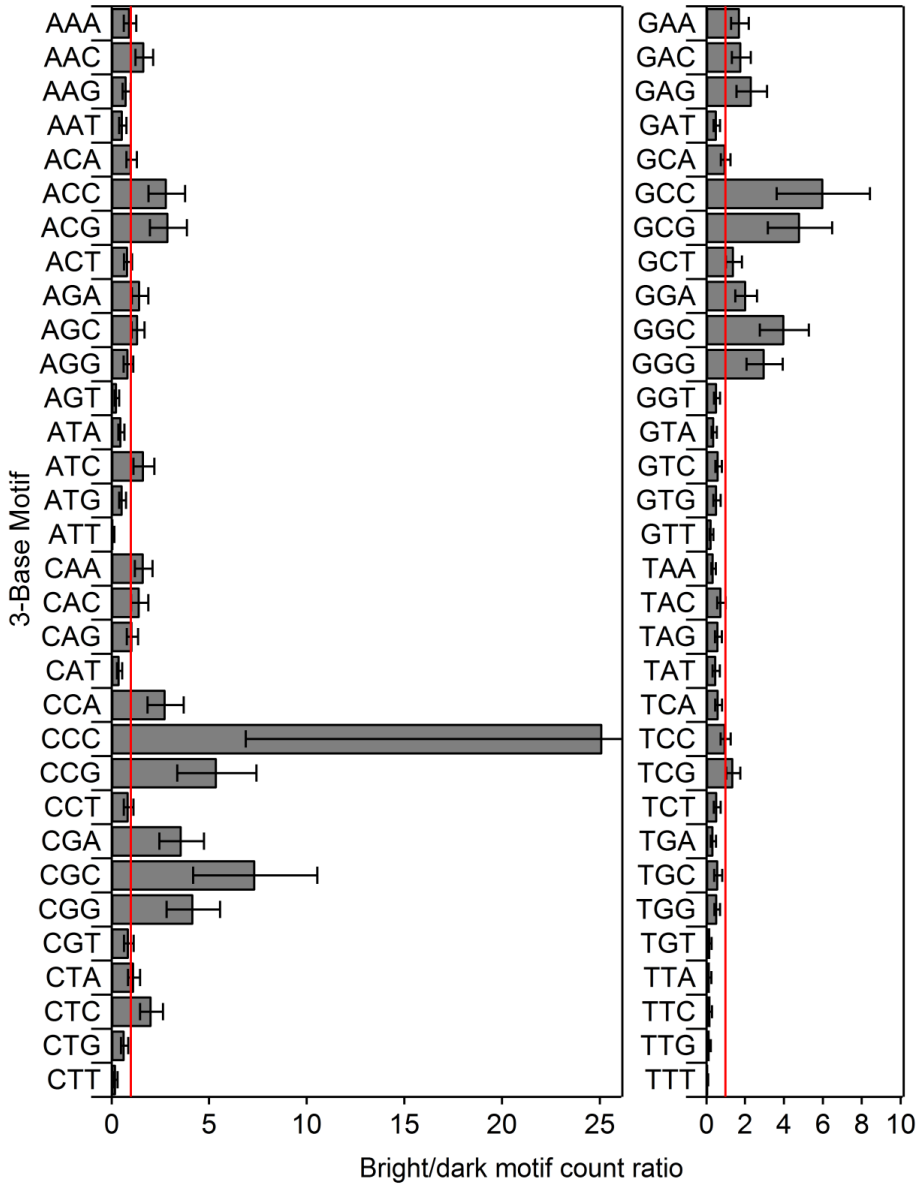

Figure B.1: Ratios of average 3-base motif counts per strand for DNA templates capable of producing brightly fluorescent Ag_N-DNA solutions to templates producing dark solutions (see text above for specifics). Error bars represent standard error, and the red line marks a ratio of one.

Figure B.1 displays average bright/dark ratios, $R_{B/D}$, for 3-base motifs, as measured in the set of 684 random template strands. These ratios are calculated by choosing the templates

corresponding to the top 30% of integrated intensity values, I_{int}, as "bright" and the bottom 30% as "dark." The average number of motif m_i per template is calculated for both bright and dark classes, and the ratio of these averages is taken, using standard error propagation. Averages that lie near unity correspond to motifs that do not, on average, select for I_{int}, while motifs with averages well above or well below 1 may be good discriminators of template brightness.

B.2 Positional features: base size and stickiness

To provide the SVM with information about the relative sizes of the four canonical bases, a qualitative "base size" parameter is assigned to each nucleobase. Because the size parameter is only qualitative, binary values, {0, 1}, are used to indicate size in a simple manner. The double-ringed purines, adenine (A) and guanine (G), are each assigned a "1" to indicate their larger size as compared to the single-ringed pyrimidines, cytosine (C) and thymine (T), which are assigned a "0."

Base	Base Size	Stickiness
A	1	0.5
C	0	1
G	1	1
T	0	0

Table B.1: Relative base size and "stickiness" to silver, as deduced from Figure 3.2a, for positional feature calculations for regions 1, 2, and 3 of the templates (Figure 3.2b).

In addition to a parameter describing relative base size, we also introduced a "stickiness" parameter to describe each base's affinity for fluorescent silver clusters, as summarized by ratios of average motif counts, $R_{B/D}$, per strand in bright to dark templates (Figure 3.2a). C and G assigned "1" for $R_{B/D} > 1$, A assigned "0.5" for $R_{B/D} \sim 1$, and T assigned "0" for $R_{B/D} < 1$. As

stated in Section 3.3.2, inclusion of these qualitative parameters describing base size and average base affinity for fluorescent silver clusters in the feature vectors representing DNA templates did not result in any significant gains in accuracy.

B.3 Top 10 brightest 10-base DNA templates

#	Sequence	I_{int}	R/D
1	ACGGCAACCA	7.5×10^6	D
2	ATCCCCAAAC	4.0×10^6	R
3	ACGGCAACCG	3.5×10^6	D
4	GGCCGAACGG	3.3×10^6	D
5	CCAGCCCGGA	3.0×10^6	D
6	ACGGGGCAAA	2.9×10^6	D
7	TCCAACCCGG	2.9×10^6	D
8	CTAGGGCCCT	2.6×10^6	R
9	CCCCCGAAAA	2.6×10^6	D
10	GATCCCCAAC	2.5×10^6	D

Table B.2: Sequences for templates producing Ag_N-DNA with the top 10 I_{int} values. Sequences are indicated as random (R) or designed by motif selection (D). Of the top 10 bright template sequences, all but one contain at least one set of consecutive cytosine bases, an important feature noted in many other studies. Use of 80 repeat instances of the same control template within one plate indicate an uncertainty of roughly 12% in I_{int}.

B.4 Tabulated training data set: sequence and I_{int}

#	Template Sequence	I_{int}
1	GGATCTGTCA	4.1E+04
2	AAATGACGTC	6.6E+04
3	ACCCAGTTTA	2.2E+04
4	GGGGTAATGT	3.5E+04
5	TTAACCAGAA	3.0E+04
6	TACCAATGGG	8.3E+04
7	GTTAACAAGA	1.8E+04
8	TTGGGCCTGG	1.7E+04
9	GCATCGGTCC	3.7E+04
10	CCATGGTGAC	4.0E+04
11	AAAGCAAGAG	5.0E+04
12	GCGAGTTCTG	3.7E+04

#	Template Sequence	I_{int}
13	GGACGCGTAT	9.4E+04
14	GTCCTCTATG	1.6E+04
15	CCTCTATGCA	4.3E+04
16	TGACTAAGAG	2.4E+04
17	GCGACAGTTG	2.9E+04
18	TTGCTTGGCT	1.1E+04
19	GAAGTTCATG	4.6E+04
20	AAAGAGCAAG	3.2E+04
21	TGGGCAGACT	4.2E+04
22	ATTCAGCTTC	1.5E+04
23	TTTCCAAACT	3.4E+04
24	GAAAGGTGCG	1.3E+06

#	Template Sequence	I_{int}
25	AGCTTCGGAA	7.2E+04
26	GACGGCGGTA	5.2E+04
27	ATACCATGCT	3.8E+04
28	CATGAGGTAA	3.5E+04
29	ATAATCCCTG	7.7E+05
30	GCGGTATCTG	5.6E+04
31	CACTCTCAGC	1.7E+04
32	CTCCTTGGCG	1.3E+05
33	TATCCCACTC	4.2E+04
34	CAAGACTTAT	4.8E+04
35	GTGGTCCCAT	4.0E+04
36	ACTGTTTGCA	1.7E+04
37	GCAATACACA	3.5E+04
38	GCCGCTACAA	3.2E+05
39	ACGACATCAG	4.6E+04
40	TGAAGAAGTG	6.5E+04
41	GTCCAGTGTG	1.1E+04
42	ACAATGAAGG	4.1E+04
43	GCATGGAAAT	3.5E+04
44	TGCGGCGGTT	5.4E+04
45	TTCGGAAGCA	3.4E+04
46	TACTTTGAGG	8.9E+03
47	CGGGGGGGTC	6.5E+04
48	GCCACCTCGA	2.1E+05
49	GCCAGTCCCG	7.0E+05
50	GCATGTGAGA	1.3E+04
51	TGCCTTTATA	1.2E+04
52	TATTTCGGCG	3.7E+04
53	TGATTCAAGT	2.1E+04
54	GGGGGTTAAA	2.2E+05
55	TGCCGCGTCA	3.4E+04
56	GAAGTGTAAT	1.1E+04
57	ATAAGCTTAG	1.4E+04
58	GCCTCGAGAT	1.1E+05
59	CCATTTTCGG	1.7E+04
60	CTATGCATGA	3.4E+04
61	ACAACTAAGT	5.2E+04
62	AGCACTGACT	1.7E+05
63	GCTCGCCGGG	1.7E+05
64	GGGAAACGTT	2.0E+04

#	Template Sequence	I_{int}
65	ATTAAGGCCG	4.4E+04
66	TTGACTAAGC	1.4E+04
67	TTGATGCACG	1.8E+04
68	TACGTAAGGT	1.5E+04
69	GGTCCGACAT	4.0E+04
70	GTAGCGATGC	2.0E+05
71	ACCGCGACCG	1.7E+05
72	GGGTCATATC	2.6E+04
73	CTCCCTTACG	6.1E+04
74	GGTGCCTTCG	3.9E+04
75	GTCAAAGTGC	6.7E+04
76	TCGATACAAT	1.2E+04
77	GAAACCTAAA	3.4E+04
78	CGAATAAGGG	7.9E+04
79	CGGTTAATTT	6.6E+03
80	TTTTCCGTTC	8.2E+03
81	TCGACACCGA	3.1E+05
82	AGTCACCACT	3.0E+04
83	AGTAACACGC	3.9E+04
84	GATGTGAACA	3.1E+04
85	TCCTGACTTC	1.2E+04
86	CTCTACATAA	4.4E+04
87	GGTTTAGCCT	6.9E+03
88	TCCGGCGTCT	5.9E+04
89	CTCATAGACC	2.5E+05
90	CTCTCATCTC	4.6E+04
91	GCTCAGAATG	7.6E+04
92	CATGCACCAG	3.6E+04
93	CTTTTGCTAC	1.6E+04
94	TGAGATAATG	1.4E+04
95	TAAGCGAATC	3.3E+04
96	AAGGGAATAA	2.8E+04
97	GGTACATACT	2.7E+04
98	ACACACTTCA	1.6E+04
99	CTAGGTCCTA	4.1E+04
100	ATCCCACGAG	9.2E+04
101	GTTGCCCATT	4.2E+04
102	TCCAATTTGT	2.1E+04
103	ATTACACCAG	2.5E+04
104	GCATTTGGGT	1.0E+04

#	Template Sequence	I_{int}
105	ACTGTTCGGA	1.7E+04
106	AACGCACATT	5.3E+04
107	ACTTCGCTGG	1.1E+04
108	GTGACCTACG	3.3E+04
109	CGAAGCGCGG	1.8E+05
110	GTACGTTGGG	2.4E+04
111	CAGGTCCTGG	2.7E+04
112	GACGGGCGTG	7.4E+04
113	ACTCGTAGCC	3.4E+04
114	GTTAATGTCT	7.7E+03
115	TAGATCGGGA	8.4E+04
116	TTTCGTCTCC	3.3E+04
117	GGGACTCTCA	1.7E+05
118	CGCCGAGGCT	1.2E+05
119	TCCGCTCAGT	1.4E+04
120	ATAGCTCACC	1.3E+05
121	AACATCTGTA	1.4E+04
122	CCGCGCAAAT	3.0E+05
123	CTAGGAAAGT	2.5E+04
124	GCGGGAGCGG	7.9E+04
125	CTGACTAAGT	3.0E+04
126	GTATCCTCGC	1.0E+05
127	TGCGAAGTAT	1.0E+04
128	CAATCCGTGA	4.3E+04
129	TGACAAGGTA	2.7E+04
130	AATAGACTGG	1.3E+04
131	GGGCGAACAT	1.4E+05
132	CCGCAGCTGG	3.7E+05
133	TAAGGTGAAA	1.5E+04
134	AAGATGTTCT	1.7E+04
135	TGTGAAGGAC	1.7E+04
136	GACCCTAAAG	5.0E+04
137	ACCGCAAATA	3.6E+04
138	TCGCCGGCGC	9.2E+04
139	CCAAGCCCAG	5.5E+05
140	GCGCCAGTCC	6.3E+04
141	GCCTAGAAGG	3.2E+04
142	AAGCACTCAC	1.1E+04
143	ACGGGCGAGG	4.9E+04
144	GTCGCGGGAA	4.5E+04

#	Template Sequence	I_{int}
145	GGTATTGACC	1.6E+04
146	AGTGCCGATC	3.2E+04
147	TAGTGTTTCT	4.2E+04
148	GAGACCTTGT	1.4E+04
149	GAATATTTCC	1.0E+04
150	TGGTCTTGAG	1.4E+04
151	GAGCGCACGG	3.1E+04
152	AACCATTCGC	5.7E+04
153	TGCATACTCC	3.9E+04
154	TAGCCACCAA	5.8E+04
155	TAATTCGCAA	6.1E+04
156	TTGGCTCCCG	1.2E+05
157	GAGCGTTATC	2.8E+04
158	GTCCCTGCGA	5.5E+04
159	CGGGCACTGG	1.1E+05
160	GGTATAGGTC	5.5E+04
161	CAGCAGTTAG	9.5E+03
162	GGCCCGGACA	1.9E+05
163	CCCATGCCCG	8.8E+04
164	CCCAGGACTT	1.0E+06
165	TTAACAAGCC	4.1E+04
166	TAATAGGATT	1.0E+04
167	AGCGACATAT	3.0E+04
168	TGTTTATGTC	1.4E+04
169	GACACTGCAG	9.1E+03
170	ACCTTGGCGT	2.8E+04
171	CCGAGCTCGT	2.3E+05
172	GTACGGGTAA	4.5E+04
173	TCTCCGACCA	2.8E+04
174	AACCTTTCTA	5.6E+04
175	TCTCTACTCG	2.1E+05
176	ACGTATTCGA	1.9E+04
177	ACGGACTGCA	5.0E+04
178	AATGGAGGGA	2.7E+05
179	GTGTCCTGGA	1.8E+04
180	TTGGGATCAA	1.8E+04
181	TCTCACGTCT	2.1E+04
182	GACTGCGACC	2.5E+05
183	TGACTCACGC	1.8E+05
184	CCAGGCAACT	1.1E+05

#	Template Sequence	I_{int}
185	CGAGCTAGCG	4.1E+04
186	GGACTATCTC	1.0E+05
187	CGCAGGCAAT	4.7E+04
188	TGCTATCCGT	5.9E+04
189	AAGGAATTCG	5.8E+04
190	TATCTGAGGC	3.9E+04
191	TCACAAGAAT	9.1E+04
192	CGGCACTTAC	1.2E+05
193	CAGATGGGTT	1.3E+04
194	CGTTAAATAC	6.1E+03
195	CGAGAAAGAG	7.5E+04
196	ACCGGACACA	2.6E+05
197	TTTACAATCC	1.5E+04
198	GGGAGCGTAA	7.9E+04
199	TCTGGGGTCA	3.9E+04
200	AGTTTCCCCA	5.7E+04
201	AACTAACCTA	7.2E+04
202	AGCGAAAAAT	2.3E+04
203	TCCCCTCCTG	3.8E+04
204	CCAAGACCGT	1.4E+04
205	GACATACGTG	3.3E+04
206	TTAGGTCCTC	2.9E+04
207	CCTTCACGCT	1.3E+04
208	TTCGGCGTCT	3.2E+04
209	GTACCTGGAG	2.8E+04
210	CAGATTGGTA	2.6E+04
211	CCTAGTCCTC	1.9E+04
212	TAGGTGAAAG	1.6E+04
213	AGGACAACTG	1.4E+04
214	GTGACCAACG	4.2E+04
215	CGGCCTCTAG	1.1E+05
216	CGTCAGCGTT	3.1E+04
217	CGTACTTGGC	4.8E+04
218	GATCAAAGGC	2.7E+04
219	CCCACGCAAA	1.8E+05
220	CCCCGATATC	1.4E+05
221	ATCATCGCCT	4.7E+04
222	TCGTTCAAGG	1.9E+04
223	GCGGTGAAGC	3.5E+04
224	TCTCGGGTTA	5.3E+04

#	Template Sequence	I_{int}
225	CGGATCAAGC	2.8E+04
226	CTAACTGCTG	1.3E+04
227	CTCTAAAGAG	4.5E+04
228	AATACATGGC	1.5E+04
229	AACATGGCTC	7.3E+04
230	TCCAGGCTAG	1.1E+05
231	TCCGTTGTAT	7.4E+03
232	TCGTACAGCT	1.5E+04
233	CGAACGGGTC	1.7E+05
234	GGGCGCTACA	4.7E+04
235	TAAAGCGGGG	9.1E+04
236	GCCGCTCTAC	6.7E+04
237	GCTTGCTCTA	1.7E+04
238	CATACAGATA	4.5E+04
239	GTCAGAGTGT	2.5E+04
240	CGCACTGTTT	3.4E+04
241	CGGCAGTAAG	3.2E+04
242	ACAGAAAAAG	1.4E+04
243	TCCCAATTTC	4.4E+04
244	AAAGCTCCTT	2.3E+04
245	CACGGGCAGA	1.5E+05
246	GGGTTCTTAG	8.4E+05
247	AGAACATTCG	2.2E+04
248	TGAGTATGCA	2.2E+04
249	TGAAGGGTCG	2.8E+04
250	ACGAGCGCTC	6.3E+04
251	CCTACGGCGT	6.6E+04
252	TGCATGGCCT	1.8E+04
253	GTGGTACATG	2.0E+04
254	GGGTCCGTCT	9.7E+04
255	AGGCGTGCTG	1.5E+05
256	GACGACTAGA	3.6E+04
257	GAGAGGTGCG	2.9E+04
258	GTAGCCTATA	2.2E+04
259	GCAAGCGGGA	2.1E+05
260	ATCTCCTACT	3.8E+04
261	GCTACACAGT	1.7E+04
262	TATCCGGCAC	4.4E+04
263	TTTGATCCTC	9.6E+03
264	TTCTCCCCTG	1.3E+05

#	Template Sequence	I_{int}
265	TCACTAGTTT	1.0E+04
266	GGGGAATACA	2.6E+05
267	TTAGCATTGG	1.4E+04
268	GCGGAGTAAG	4.5E+04
269	TTTACCATCG	1.1E+04
270	AAAGATACGG	2.4E+04
271	CTCTCCGAAC	1.6E+05
272	GGGCGGTACT	8.9E+04
273	ACACCGTTAA	4.1E+04
274	TTTAGGAGCC	2.3E+04
275	CCACCTTTTC	2.2E+06
276	AAGTGGCGTC	7.5E+04
277	ACAAGACCTT	3.1E+04
278	TATGAGCCTC	5.4E+04
279	AGTTAGCAAT	1.0E+04
280	GAAGGACCCT	3.3E+04
281	GTACTACACA	1.3E+05
282	ACAACCTAGA	4.9E+04
283	GGCAGCGTCG	1.2E+05
284	ATCGTTCATT	1.0E+04
285	ACGTGCACTA	4.0E+05
286	CCCCAGTTAC	4.0E+04
287	CGCTGCAATC	2.7E+04
288	CGGATAAAGC	3.4E+04
289	GCCCGTTTCG	2.8E+04
290	AGGGAAAGAG	2.1E+06
291	GTAACCTGCA	1.2E+04
292	TTGCAGGAAT	1.6E+04
293	AGTACTCGGC	4.1E+04
294	CGGGCGGCTA	7.3E+04
295	CGACTGGCGA	3.5E+05
296	ATTGGACCGC	4.2E+04
297	ATGTCGATAC	1.1E+04
298	GATCGCTGTA	1.4E+04
299	GAGCCTCAGC	6.7E+04
300	GAACTAAATG	1.7E+04
301	CAATTCGGGG	3.3E+04
302	CACTCCACGG	9.0E+04
303	CTTCTGGATT	7.0E+03
304	CGCCCTATCC	4.4E+05

#	Template Sequence	I_{int}
305	TTGGCAGCAA	3.6E+04
306	CGCGCGACCA	1.6E+05
307	CTTACATCTA	2.5E+04
308	ATTAACGAGT	8.7E+03
309	GGTGTTTCGC	1.7E+04
310	ATGACAGAAG	1.8E+04
311	CTGCGTGTCT	4.3E+04
312	TGCAGCGAAT	1.9E+04
313	TGGCGGCACT	5.8E+05
314	AGGCGAACAG	1.3E+05
315	ACGTCAACGT	1.7E+06
316	CATGATCGCT	3.7E+04
317	GGAATCCGCC	1.9E+05
318	CCTCGTTTTT	6.8E+03
319	GTATGGTTGG	1.2E+04
320	CTGATGACCT	3.5E+04
321	GGCGTCTCAG	8.5E+04
322	TCCAGCCCGC	5.8E+05
323	TTACTGGGTC	1.7E+04
324	CTTGGCTTTG	1.1E+04
325	TGCCCTGTCG	1.8E+05
326	CTAATATCGG	5.2E+04
327	TTGGAACCTA	4.5E+04
328	GGGATTTACC	1.4E+05
329	CACCCCCAGT	3.4E+05
330	GCACTTCTTT	5.7E+04
331	TTCAAAAGCA	2.3E+04
332	GTCCATTTAT	1.7E+04
333	GTACGTCCTT	2.6E+04
334	TATCTATCCA	9.0E+04
335	CGTCCGTGTT	1.6E+05
336	AACTCGCAAA	2.5E+05
337	AGGATAGGAA	6.9E+04
338	ATGGGGAAAC	5.8E+05
339	TAAAGCGGTA	7.8E+04
340	AACAACCGAA	1.8E+06
341	AGAAGATCCA	6.7E+04
342	CGTTCGGATC	4.0E+04
343	GCTCGTCTAT	1.7E+05
344	TGAGATATCG	2.5E+04

#	Template Sequence	I_{int}
345	GGCGATTGCT	5.0E+04
346	AGTGGCTAGT	3.6E+04
347	GGAATCGACA	7.5E+04
348	CACGGCATGG	2.3E+05
349	TTGATCTAAG	6.7E+03
350	GCTGTATTAA	2.5E+04
351	AATCGTGGCG	6.1E+04
352	GCCTACGCAA	1.9E+05
353	ACCTTTATGA	2.7E+04
354	ATCGCTGTCA	4.4E+05
355	TCCACGAGAA	1.9E+06
356	GCCGACCTAT	1.7E+06
357	TGTTTGCGTG	1.3E+04
358	GTCAACCGCT	3.8E+05
359	CACTTCCGTG	4.9E+04
360	GGACAGAACG	3.0E+05
361	CAAGATCGCG	1.5E+05
362	TTGATTGTCA	8.7E+03
363	TCTCATCTTT	1.4E+04
364	TTCCCGCCGA	3.7E+04
365	TGAGGCGAAG	1.1E+05
366	CAACTAGTTA	1.7E+04
367	CCGTCCATTA	1.4E+04
368	TAACCGCGAG	1.4E+05
369	TACAGACGTC	1.3E+05
370	ACTGCCCCGA	3.6E+05
371	CGCGGAGGAT	7.5E+04
372	CCTAGATACT	2.3E+04
373	GCTGGATATT	2.1E+04
374	TACAGAGCCG	9.8E+04
375	ATCACAGGGC	3.6E+05
376	ATCCCCAAAC	4.0E+06
377	TACTGTAGGG	1.0E+04
378	GCTACAAATA	4.4E+04
379	ACACCCGTCT	4.2E+04
380	TAAACTGAAC	9.4E+03
381	AGAGTCCAAC	4.6E+05
382	GACAAGTGCA	4.3E+04
383	ACCTCGGAAA	4.5E+05
384	GGGGCCAGGC	5.3E+04

#	Template Sequence	I_{int}
385	GCAGACCAGT	2.5E+04
386	CCTACACTGT	7.1E+04
387	ATCCTTAATG	1.6E+04
388	GAGTTAAGAT	1.2E+04
389	TTGCCGTGCC	4.0E+04
390	AGCCAACTGG	1.4E+05
391	GTTTAGCGAT	1.0E+04
392	TTACGACCCA	2.0E+06
393	GGTTAACACT	8.4E+03
394	CATAGATGTC	4.4E+04
395	GCTCTTGAGA	8.4E+04
396	ACGTATTTCC	1.5E+04
397	TCTACTCTCA	6.5E+04
398	CAACCTGCAG	3.4E+04
399	TGGGTCAGGA	2.2E+04
400	GGACAGCTCT	2.4E+05
401	CTATACGAAG	2.5E+04
402	TAAGCAAGAG	1.6E+05
403	AAAGAAACAC	2.5E+04
404	ATCATGTACC	1.6E+04
405	TCGTGCCGGT	3.4E+04
406	TTTGGGAGGG	1.7E+04
407	AGCAGCCGGT	1.1E+05
408	AGTACCACAG	3.1E+04
409	CTCGTCCGCT	5.0E+04
410	GTCTCGAGTT	3.0E+04
411	CGGGTGTGGC	1.5E+04
412	GGACTTCAGG	2.0E+04
413	GGACGGCTCA	8.6E+04
414	TTCAAATAGC	4.9E+04
415	AACAGAAACC	4.2E+04
416	TCCTATCGGG	1.7E+04
417	CTCAGATTTA	3.3E+04
418	AGACCACTCT	3.8E+04
419	ACCTGGACCG	3.0E+05
420	GCAAGATTGA	8.6E+04
421	TCTATACAAC	1.8E+04
422	AACACGATTG	3.4E+04
423	CCTATTAAAC	1.7E+04
424	CATACTAAGT	1.8E+04

#	Template Sequence	I_{int}
425	TTCTTGAAGT	1.1E+04
426	TAAGGCCCCA	1.7E+05
427	CTGGACTACG	1.7E+05
428	ATGTAGTGTC	1.9E+04
429	GTCCTTCATC	1.8E+04
430	CGAACGGGTT	9.4E+04
431	GCGGAGCCAA	2.4E+04
432	CTAGGGCCCT	2.6E+06
433	CAGTGCGTCT	1.9E+04
434	CGGGGGGAGC	1.6E+05
435	GTCGACGCCC	1.7E+05
436	GCCAACTCGT	5.2E+05
437	GGAAGGCAGC	4.8E+04
438	TTTAGCGATA	2.1E+04
439	CCTGGCTAGC	1.7E+06
440	CACCCTTAGA	6.1E+04
441	CGTTGGTACA	1.6E+04
442	AGATTGGTAT	5.3E+04
443	ACCAGGATCG	4.9E+04
444	GGCTCTACAA	1.9E+05
445	AAGAATCGGT	1.0E+05
446	GAGCTAGTGG	8.8E+04
447	ACTGCCTGTA	2.2E+04
448	GATTTCAAGG	1.2E+04
449	CGTCAATAAT	1.8E+04
450	GTGATTGTGT	1.4E+04
451	ATCTATCGGT	5.1E+04
452	GGTCATAACT	1.1E+05
453	GTCCACCACA	1.9E+04
454	CTTTATCACC	3.3E+04
455	ACGAATTGGA	5.2E+04
456	ACAAGCCCCA	1.1E+06
457	GGTGGACGGC	3.7E+04
458	CGGTCGTAGT	1.9E+04
459	GAAATCGCAC	3.0E+05
460	CTCCGACGAG	4.4E+04
461	TTCCCTGGTT	4.5E+04
462	TGCATGTGGT	1.1E+04
463	CTGTCTGGAC	2.3E+04
464	GGCGTGCAGG	5.3E+04

#	Template Sequence	I_{int}
465	TTCTAAACGT	1.4E+04
466	GCCTACCGTA	9.0E+04
467	CTGGTAGCAG	2.1E+04
468	ACAGAGCGGA	7.5E+04
469	AAAAATCCCA	1.9E+05
470	ATGGTCCCGC	3.5E+05
471	GCAAAGCAAA	2.7E+04
472	TGACGCTGTG	6.4E+05
473	TTCGTCCAGT	1.6E+04
474	TGGCATGGAA	1.8E+04
475	GGCACGAGTT	1.0E+05
476	AGGACGATCG	2.5E+05
477	TTTAGAGTGC	5.0E+04
478	GGGCCGCAAG	1.0E+05
479	GGGTGGGGTA	2.5E+05
480	ACTGCGTTGG	3.7E+04
481	TAATTTGTGG	1.3E+04
482	AGAATACGCC	6.9E+04
483	CTCGGCGGCA	2.8E+05
484	GTGCTTATGG	1.3E+04
485	GTCTGCGGCT	3.3E+04
486	GACGAGGAAC	3.0E+04
487	GGCACAGGCT	1.3E+05
488	TTTGTTACAG	1.2E+04
489	TGAGTTGCCG	5.3E+04
490	GATTATACCC	2.8E+04
491	GGCTAGCGCG	7.4E+05
492	GCATCCAGAT	9.7E+04
493	GAGACTAGCC	1.0E+05
494	GCATAGCGGT	2.4E+04
495	GACTAGGGTC	1.5E+04
496	CTTTATAGAC	1.3E+04
497	CTTTACCTCT	2.7E+04
498	TGTAGTCCTT	1.8E+04
499	TGTCTTGTGT	1.2E+04
500	TTGATTTCCC	1.4E+04
501	AGCGAATAAA	6.3E+04
502	TTAGTGCTTC	5.6E+04
503	TGTGAACGTG	1.6E+05
504	TACTGTCTCC	3.7E+04

#	Template Sequence	I_{int}
505	AGACAAGTAC	5.3E+04
506	AACGTTCTGT	3.6E+04
507	CTTGGTAATA	1.9E+04
508	TAGAACCATC	3.1E+04
509	AATGCACGAG	4.2E+04
510	GCCGTAGCGA	1.3E+05
511	CTACGAGATG	4.5E+04
512	CGGAGCTACT	3.9E+04
513	AGGGGAACAA	9.0E+05
514	AGCCGCGATA	5.3E+04
515	GTGGAGAATG	6.0E+05
516	ATACGGGTTA	7.4E+05
517	AAGTCAAAGT	1.5E+04
518	GAAAAGCCCA	7.0E+04
519	TTCGGCTTCA	1.1E+05
520	CGACTGCCGC	4.8E+04
521	CGGTTTGGCC	2.2E+05
522	CCTAATACAT	1.4E+04
523	TGGCACAATT	1.7E+04
524	TAACTATGGT	1.0E+05
525	AACCACCCCA	3.9E+05
526	CGTCTAACTT	1.6E+04
527	CGGACCATCG	1.4E+05
528	GGGAGGCAGT	3.2E+04
529	TTAGCGAAGA	2.4E+04
530	ACGCTGGTGA	4.2E+04
531	CGTCTGCGCA	5.3E+04
532	TTTTACTCAC	1.6E+04
533	CAGCTGCGCG	7.1E+04
534	GGGGTGCAGT	2.5E+04
535	TAGGGTGTAC	1.8E+04
536	AGGTTTGTTG	1.2E+04
537	TTCAATTTGG	1.3E+04
538	CAGTCAGCAC	1.7E+04
539	CCGCAAAGTA	4.1E+04
540	AGCTTGGTAA	5.4E+04
541	CGAAGGGATC	4.2E+04
542	ATATCCCCGT	6.4E+04
543	TCTGATTCGG	1.6E+04
544	TGTCGACGGG	3.2E+04

#	Template Sequence	I_{int}
545	TGGATTAAGA	1.7E+04
546	CAACCATGTA	8.9E+04
547	ACCGTTCTAT	1.8E+04
548	TCCTCCGGCC	2.4E+05
549	CACAGCGGAG	4.9E+04
550	CCAACAGCCT	3.5E+04
551	GCTAACCTAC	5.3E+04
552	GCGGGGTGTG	5.5E+04
553	ACCATAACGT	3.1E+04
554	GCGTTGGCCC	1.2E+06
555	TAGCGAGCGG	1.0E+05
556	TTGTCGCGAT	5.2E+04
557	GCTGATCACA	3.2E+04
558	TCAGAGACTT	3.6E+04
559	CACCGCGGAG	7.6E+04
560	CAGGGTCGAA	4.5E+04
561	TCTCAAGTAG	3.3E+04
562	ATGCGCTCAT	4.3E+04
563	CTGTAGGTCC	2.0E+04
564	TTCGTTGCGC	6.5E+04
565	ACATGATACC	2.2E+04
566	ATGAACAGAA	1.9E+04
567	CTACCGAAGA	4.0E+04
568	ACTCTTGTAC	1.7E+04
569	ACTCGGGCAG	2.2E+05
570	TGGCGTGTAG	2.6E+04
571	TGTCATTCTC	2.0E+04
572	ATTCTTCTTG	2.0E+04
573	TCTCACATAT	2.1E+04
574	CTTGACTCAT	1.7E+04
575	GTTGGCTCGC	5.4E+04
576	CTGCGCTTTG	4.3E+04
577	ACGGTCCGAT	2.1E+04
578	TCTACTCATT	4.2E+04
579	TCGTATTCAA	1.0E+05
580	CTGAATAAGC	2.0E+04
581	AGGACTGGCC	6.0E+04
582	ATGGGCACTT	1.9E+04
583	CGAAAGGGAA	1.4E+05
584	CCAAACATTC	1.5E+05

#	Template Sequence	I_{int}
585	GGACTCGATC	3.8E+04
586	CGTTTCGACT	2.1E+04
587	CGACTCATAG	7.1E+04
588	GACTAGTACA	5.2E+04
589	GCCGATACCC	3.0E+05
590	CGTGAAGCGG	5.0E+04
591	AGATTAACCT	2.8E+04
592	GCATAGAACG	2.0E+05
593	ATCCTGCTTG	4.7E+04
594	GAAGTGATAT	6.0E+04
595	TTTCGTCCGT	1.3E+04
596	CATAGAGGCG	2.1E+04
597	AGCTGAGGTC	2.0E+04
598	CGGGACAGAC	2.1E+05
599	TGGAACTCGT	2.9E+04
600	ATTTTGTGTT	1.2E+04
601	GTATCAAAGC	1.5E+05
602	AGGCGATCAT	6.8E+04
603	GTGGACGGTC	3.9E+04
604	GTGCGGGCGG	5.7E+04
605	GTTTAGCATT	1.2E+04
606	AGACCATTTC	3.4E+04
607	ACCGTCGGCC	1.5E+05
608	CTCATGTCCC	2.6E+04
609	CGAGCTGAAC	1.0E+05
610	TCGCCGGGAA	6.6E+04
611	AGTCCATTTA	2.0E+04
612	TGAGTCACGC	6.7E+04
613	AAAACCATTG	1.8E+04
614	ACCGATGCAA	8.8E+05
615	GGAACTAAAG	1.3E+05
616	GGGCTTGCTG	3.7E+04
617	TAGTTGCCGT	5.7E+04
618	GACCCCGAAG	3.8E+05
619	AAGCTCACTG	1.3E+04
620	GACGGGTCCC	9.8E+05
621	GCTTAACGCC	3.7E+05
622	GACTGTGGTA	1.7E+04
623	GTCTAAAAAC	3.2E+04
624	TCCGGACAAT	3.3E+04

#	Template Sequence	I_{int}
625	TGTTGGTAAC	1.2E+04
626	TTGCCAAGTG	7.2E+04
627	AGCCTCCAGG	6.0E+04
628	TCTTTGATTC	1.3E+04
629	CGTTTTGGCA	1.6E+04
630	TGTCAACAAA	1.1E+06
631	TGTTCAAGGA	1.9E+04
632	CCTCTAGCAC	3.4E+04
633	AAACTTCCGT	3.8E+04
634	ATTATAGGAC	3.8E+04
635	CTCTCGCCCG	1.2E+05
636	ATGTCTACCA	4.3E+04
637	GTGATCCCGC	6.4E+05
638	TGTTCCACGT	2.8E+04
639	AATACAGCTG	1.6E+04
640	GCCAGCCGTT	2.6E+04
641	ATCTCACGCG	7.1E+04
642	TCATTGGCAC	2.9E+04
643	CAAAGCGCAT	3.5E+04
644	CTTGTTAAAG	1.5E+04
645	AACCCCTACG	1.3E+06
646	GTTAAACGCA	1.4E+04
647	TCAGATATGC	4.2E+04
648	CGAGTTCTCG	3.9E+04
649	TCTAAAACGT	4.1E+04
650	CATGTGGGTC	1.7E+04
651	GAAAAGGTCT	5.1E+04
652	CGAGATAAGT	3.5E+04
653	CCTCCTTTAA	2.4E+04
654	TTCTTGTCGT	1.6E+04
655	TTACGCCGGG	3.4E+04
656	GGTTCCGGGC	8.8E+05
657	CGCGCCTGAG	1.8E+05
658	CGCTCGTGAA	4.1E+05
659	ACTAAGAACC	2.0E+04
660	TGTTCGTGAC	1.5E+04
661	CAGATGTCCA	2.9E+05
662	GTAGAACGTT	4.0E+04
663	AGTTTTTGTG	1.2E+04
664	CAGGGATAGA	3.5E+04

#	Template Sequence	I_{int}
665	GGCTAGTTCG	3.8E+04
666	CTAGCGTCGC	2.4E+05
667	TATCCTTATC	2.7E+04
668	CTAATTCAGG	3.2E+04
669	AAACCCCTGT	2.2E+05
670	TTTTCGGAAA	2.0E+04
671	ATAGCAACGC	7.6E+04
672	GACTAGGTAG	1.9E+04
673	GGATACACTG	3.5E+04
674	GCGTCACGAG	4.8E+04

#	Template Sequence	I_{int}
675	AGTTGCCCAG	7.2E+04
676	GGTATTGCAA	2.0E+04
677	GAAATTAGCG	2.8E+04
678	ATTGCATACA	1.8E+04
679	GACATATCTT	1.6E+04
680	CCCCGTTGTT	1.7E+05
681	ACGAACATGC	1.4E+05
682	AATACAGACG	9.0E+04
683	CTAGCCTTAA	3.6E+04
684	TAAAGCAGGT	1.6E+04

Table B.3: Tabulation of the 684 randomly generated template sequences, with their corresponding integrated intensity values, as used to develop the SVM- and MERCI-assisted, motif-based design method. I_{int} values correspond to measurements taken 1 week after synthesis for Ag_N-DNA synthesized with the following conditions: [DNA] = 20 μM, 10 mM NH_4OAc, pH 7, [$AgNO_3$] = 100 μM, and [$NaBH_4$] = 0.5 × [$AgNO_3$]. Use of 80 repeat instances of the same control template within one plate indicate an uncertainty of roughly 12% in I_{int}. Templates with I_{int} values within the top 30% ($I_{int} > 6.76 \times 10^4$) are classified as "bright," and templates in the bottom 30% of I_{int} values ($I_{int} < 2.4 \times 10^4$) are classified as dark.

B.5 Discriminative motifs identified by MERCI for bright templates

MERCI identifies motifs occurring with frequency ≥ F_P in the positive (P) class and ≤ F_N in the negative (N) class. "Bright" motifs were found by defining bright templates as class P and dark templates as class N, with F_P = 10 and F_N = 10, and by searching for all motifs with length up to 10 bases (the total length of each sequence) and up to one gap (wildcard acting as any base A, C, G, T or no base) that satisfy these criteria. Table B.4 lists all bright motifs in order of the total number of occurrences in both bright and dark templates.

Motif	#Bright	#Dark	Avg. I_{int}
CC_C	54	9	4.7 ± 0.9E+5
C_CC	52	5	4.8 ± 0.9E+5
GCG	42	9	1.8 ± 0.3E+5
CCG	42	8	2.9 ± 0.5E+5
GCC	42	7	3.0 ± 0.6E+5
CGC	40	6	2.2 ± 0.2E+5
CCC	36	2	5.9 ± 1.3E+5
GG_AC	22	8	2.0 ± 0.4E+5

Motif	#Bright	#Dark	Avg. I_{int}
G_GAA	19	10	3.0 ± 0.9E+5
AGC_G	18	10	1.2 ± 0.3E+5
AG_CG	21	6	1.2 ± 0.2E+5
CA_AG	17	10	1.5 ± 0.4E+5
CA_GA	18	9	1.9 ± 0.7E+5
GC_TC	21	6	1.1 ± 0.1E+5
AC_GC	19	7	1.6 ± 0.3E+5
C_GAA	17	9	1.8 ± 0.7E+5

Motif	#Bright	#Dark	Avg. I_{int}
GC_GA	20	6	1.8 ± 0.6E+5
G_GCG	24	2	2.0 ± 0.5E+5
A_GCG	19	6	1.2 ± 0.3E+5
CA_GC	17	8	1.8 ± 0.4E+5
CC_CG	24	1	3.0 ± 0.7E+5
CGA_A	19	6	2.6 ± 0.9E+5
CG_AA	20	5	2.1 ± 0.7E+5
CT_AC	15	10	1.4 ± 0.5E+5
GAA_A	15	10	2.8 ± 0.9E+5
GC_CT	16	9	2.4 ± 1.0E+5
GGA_C	19	6	2.0 ± 0.5E+5
GG_GA	20	5	2.7 ± 0.8E+5
C_AAC	19	5	4.8 ± 1.7E+5
C_AGA	17	7	1.7 ± 0.7E+5
CG_GC	24	0	2.1 ± 0.4E+5
CTC_T	15	9	1.3 ± 0.2E+5
CT_CG	22	2	2.5 ± 0.5E+5
GA_CG	22	2	1.9 ± 0.4E+5
GGC_A	20	4	2.3 ± 0.7E+5
G_GAC	18	6	1.8 ± 0.4E+5
TC_AC	15	9	2.9 ± 1.0E+5
C_AGC	16	7	2.9 ± 0.8E+5
C_CGC	21	2	2.2 ± 0.3E+5
CGG_G	21	2	2.2 ± 0.5E+5
CG_GG	21	2	2.2 ± 0.5E+5
C_GGA	15	8	1.6 ± 0.4E+5
C_TAG	13	10	3.2 ± 1.2E+5
GAA_C	17	6	1.7 ± 0.4E+5
G_AAC	15	8	1.5 ± 0.4E+5
GC_CG	22	1	2.7 ± 0.7E+5
GCG_A	18	5	1.2 ± 0.2E+5
GCT_C	16	7	1.2 ± 0.2E+5
G_CGA	17	6	2.0 ± 0.7E+5
G_CTC	18	5	1.2 ± 0.2E+5
GGA_A	17	6	3.0 ± 0.9E+5
GGC_C	19	4	2.9 ± 1.1E+5
GG_CA	17	6	1.5 ± 0.2E+5
AAC_A	13	9	2.5 ± 0.9E+5
AA_CG	18	4	2.9 ± 1.0E+5
AC_CA	12	10	1.8 ± 0.8E+5

Motif	#Bright	#Dark	Avg. I_{int}
A_CGC	19	3	2.1 ± 0.4E+5
A_CGG	18	4	1.7 ± 0.5E+5
A_CTC	15	7	1.5 ± 0.2E+5
AG_CT	12	10	8.8 ± 1.6E+4
A_TGG	12	10	1.2 ± 0.3E+5
CAC_G	16	6	1.9 ± 0.8E+5
CGA_C	21	1	3.1 ± 1.0E+5
CG_AC	20	2	3.2 ± 1.0E+5
CG_CC	19	3	3.1 ± 1.0E+5
CG_CT	14	8	1.6 ± 0.3E+5
CG_GA	19	3	2.2 ± 0.8E+5
CTA_C	17	5	2.8 ± 0.9E+5
CTC_C	14	8	1.0 ± 0.1E+5
C_TCG	19	3	1.9 ± 0.2E+5
GAC_C	17	5	3.3 ± 1.0E+5
G_ACA	12	10	1.5 ± 0.4E+5
GC_AA	17	5	1.7 ± 0.4E+5
GC_AC	15	7	1.5 ± 0.3E+5
GC_AG	16	6	2.3 ± 0.7E+5
GC_GG	17	5	1.3 ± 0.3E+5
GCT_G	14	8	2.5 ± 0.7E+5
G_CAA	17	5	3.0 ± 0.8E+5
GGC_T	17	5	1.9 ± 0.7E+5
GG_CT	16	6	2.3 ± 0.8E+5
GGG_A	18	4	2.8 ± 0.9E+5
GGG_C	16	6	3.0 ± 1.2E+5
TCC_G	13	9	2.0 ± 0.5E+5
TCG_C	16	6	1.5 ± 0.2E+5
T_GGC	12	10	2.3 ± 0.8E+5
AAC_G	13	8	2.7 ± 1.0E+5
AA_GC	12	9	1.6 ± 0.5E+5
AC_AA	11	10	2.9 ± 1.0E+5
AC_GA	16	5	4.1 ± 1.3E+5
A_CAG	11	10	9.7 ± 1.8E+4
AGC_C	14	7	2.2 ± 0.6E+5
AG_GG	15	6	3.5 ± 1.4E+5
A_GGG	15	6	4.5 ± 1.4E+5
CA_AC	15	6	5.3 ± 1.9E+5
CCC_G	20	1	3.4 ± 0.6E+5
CC_GT	11	10	1.2 ± 0.3E+5

Motif	#Bright	#Dark	Avg. I_{int}
CCT_G	12	9	2.2 ± 0.8E+5
C_CTA	12	9	2.5 ± 0.9E+5
C_CTG	12	9	2.4 ± 0.8E+5
CGC_G	19	2	2.0 ± 0.4E+5
CG_CG	21	0	1.8 ± 0.3E+5
CGG_C	19	2	2.0 ± 0.4E+5
C_GGC	21	0	2.8 ± 0.8E+5
C_GGG	18	3	2.3 ± 0.6E+5
CTC_G	18	3	1.9 ± 0.3E+5
GA_CA	14	7	1.6 ± 0.4E+5
GCG_G	19	2	1.6 ± 0.4E+5
G_CCG	18	3	2.3 ± 0.7E+5
G_CGG	20	1	1.7 ± 0.5E+5
GG_CG	19	2	1.4 ± 0.3E+5
GG_GT	12	9	1.9 ± 0.6E+5
GG_TC	11	10	1.9 ± 0.6E+5
G_GGA	18	3	3.0 ± 1.0E+5
TCA_A	11	10	2.2 ± 0.8E+5
TCC_C	15	6	5.0 ± 1.9E+5
TC_CG	14	7	2.0 ± 0.5E+5
AA_CA	11	9	2.6 ± 1.0E+5
AAG_C	10	10	1.5 ± 0.5E+5
AAG_G	13	7	2.4 ± 1.1E+5
A_CTA	11	9	1.6 ± 0.8E+5
AGA_T	13	7	1.2 ± 0.3E+5
AG_AC	10	10	1.5 ± 0.5E+5
AG_CC	12	8	2.2 ± 0.6E+5
AGG_G	12	8	4.2 ± 1.5E+5
A_GCT	12	8	1.2 ± 0.3E+5
ATC_C	16	4	4.0 ± 1.9E+5
AT_GG	10	10	1.0 ± 0.3E+5
CAA_G	13	7	2.3 ± 0.9E+5
CA_CG	15	5	2.7 ± 1.1E+5
CAG_C	13	7	1.5 ± 0.4E+5
CCA_G	16	4	3.1 ± 1.0E+5
CCC_A	19	1	6.5 ± 2.0E+5
CCG_T	12	8	1.5 ± 0.4E+5
C_CAG	14	6	2.4 ± 0.6E+5
C_CGA	19	1	4.6 ± 1.3E+5
CG_AG	17	3	2.1 ± 0.9E+5

Motif	#Bright	#Dark	Avg. I_{int}
CGG_A	18	2	1.7 ± 0.3E+5
GAA_G	14	6	3.0 ± 1.1E+5
GAC_A	13	7	1.3 ± 0.2E+5
GAC_G	16	4	2.2 ± 0.5E+5
GA_GC	17	3	1.7 ± 0.4E+5
GA_TC	12	8	1.3 ± 0.3E+5
GCA_C	14	6	1.4 ± 0.3E+5
GCC_C	20	0	4.4 ± 1.3E+5
G_CCC	20	0	6.1 ± 1.5E+5
GGC_G	19	1	1.5 ± 0.3E+5
G_GGC	16	4	3.0 ± 1.2E+5
TA_CG	13	7	3.2 ± 1.0E+5
TCC_A	11	9	2.1 ± 0.9E+5
TC_GC	13	7	1.4 ± 0.2E+5
TC_TA	10	10	1.2 ± 0.4E+5
T_CAC	10	10	1.8 ± 0.9E+5
T_CCA	12	8	2.1 ± 0.9E+5
T_CTC	10	10	7.8 ± 1.3E+4
TG_GC	10	10	2.3 ± 0.9E+5
AAA_C	10	9	3.1 ± 2.0E+5
AC_CG	17	2	3.2 ± 0.9E+5
ACG_G	16	3	2.9 ± 1.0E+5
AC_GG	15	4	2.1 ± 0.5E+5
A_CAA	11	8	3.2 ± 1.1E+5
AG_AA	12	7	2.0 ± 0.9E+5
AT_CG	11	8	1.4 ± 0.4E+5
A_TCC	13	6	4.2 ± 1.9E+5
A_TCG	12	7	1.5 ± 0.3E+5
CAA_C	15	4	6.6 ± 2.1E+5
CAG_A	11	8	1.4 ± 0.5E+5
CCG_C	17	2	3.1 ± 0.8E+5
C_CCG	19	0	2.6 ± 0.4E+5
C_CGT	11	8	1.2 ± 0.3E+5
C_CTC	11	8	1.2 ± 0.2E+5
CGGG	17	2	2.4 ± 0.6E+5
CG_TA	10	9	8.2 ± 1.7E+4
C_GAC	17	2	3.4 ± 1.2E+5
C_GCT	11	8	1.7 ± 0.4E+5
GAA_T	11	8	1.1 ± 0.3E+5
GA_AT	12	7	1.2 ± 0.3E+5

Motif	#Bright	#Dark	Avg. I_{int}
GACT	10	9	1.5 ± 0.5E+5
G_AGC	15	4	1.2 ± 0.2E+5
GCA_A	14	5	1.6 ± 0.4E+5
GC_GT	14	5	1.9 ± 0.6E+5
GC_TA	12	7	2.2 ± 0.8E+5
G_CTA	12	7	2.1 ± 0.8E+5
GG_GC	16	3	3.5 ± 1.4E+5
TC_GG	10	9	1.4 ± 0.4E+5
T_GCG	13	6	2.3 ± 0.7E+5
AA_CC	14	4	4.1 ± 1.1E+5
ACG_C	15	3	3.4 ± 1.2E+5
A_CGA	13	5	4.5 ± 1.5E+5
AGCG	13	5	1.3 ± 0.4E+5
AGG_C	13	5	3.0 ± 1.4E+5
AT_GC	10	8	1.5 ± 0.5E+5
C_ACG	15	3	3.7 ± 1.3E+5
CC_AG	12	6	2.3 ± 0.6E+5
CC_CA	16	2	6.0 ± 2.2E+5
CC_CC	16	2	6.5 ± 2.2E+5
CCG_A	17	1	4.2 ± 1.2E+5
CCT_C	10	8	1.7 ± 0.7E+5
C_CAC	11	7	3.2 ± 1.4E+5
CGA_G	16	2	2.7 ± 1.0E+5
CGA_T	10	8	1.4 ± 0.4E+5
CG_GT	12	6	1.7 ± 0.6E+5
CG_TG	12	6	2.8 ± 0.7E+5
C_GCG	17	1	1.8 ± 0.4E+5
GA_AA	10	8	4.2 ± 1.4E+5
G_AAG	11	7	2.7 ± 1.2E+5
GCC_G	16	2	2.8 ± 0.9E+5
GC_CC	17	1	4.6 ± 1.4E+5
GCG_T	13	5	1.5 ± 0.6E+5
GCT_A	11	7	2.2 ± 0.9E+5
G_CCA	12	6	1.9 ± 0.4E+5
GGAC	14	4	2.0 ± 0.5E+5
GG_AA	12	6	2.9 ± 1.1E+5
GG_CC	14	4	3.8 ± 1.4E+5
G_GCT	15	3	2.2 ± 0.9E+5
G_TCG	12	6	1.3 ± 0.2E+5
TCG_A	10	8	1.2 ± 0.3E+5

Motif	#Bright	#Dark	Avg. I_{int}
AAC_C	12	5	3.4 ± 1.1E+5
A_ACC	11	6	3.2 ± 1.1E+5
A_ACG	12	5	2.4 ± 0.9E+5
ACAG	10	7	1.1 ± 0.2E+5
A_CCC	16	1	7.6 ± 2.3E+5
AGA_C	11	6	1.1 ± 0.2E+5
AG_GC	15	2	3.1 ± 1.4E+5
A_GAA	11	6	2.2 ± 1.0E+5
A_GGC	14	3	2.6 ± 1.4E+5
CA_AA	11	6	4.0 ± 2.2E+5
C_ACC	16	1	6.1 ± 1.8E+5
CCC_C	17	0	6.2 ± 2.2E+5
CC_GA	15	2	4.2 ± 1.2E+5
CC_TG	11	6	2.4 ± 0.9E+5
C_CAA	14	3	4.2 ± 2.2E+5
C_CCA	15	2	6.1 ± 2.3E+5
CGG_T	12	5	1.7 ± 0.6E+5
CGTC	10	7	1.8 ± 0.9E+5
CGT_G	12	5	2.0 ± 0.6E+5
C_GAG	15	2	2.0 ± 1.0E+5
C_GCC	16	1	2.1 ± 0.3E+5
CT_GC	12	5	2.7 ± 0.9E+5
GAAC	12	5	1.6 ± 0.4E+5
GA_AG	11	6	3.0 ± 1.2E+5
GA_CC	11	6	3.6 ± 1.3E+5
G_AAA	11	6	3.4 ± 1.2E+5
G_AAT	10	7	1.1 ± 0.3E+5
GCGA	12	5	1.2 ± 0.2E+5
GCG_C	16	1	2.1 ± 0.4E+5
G_CAC	11	6	1.6 ± 0.3E+5
GGA_T	10	7	1.4 ± 0.5E+5
GGGA	14	3	3.2 ± 1.1E+5
G_GCA	13	4	1.7 ± 0.3E+5
TAC_G	10	7	2.9 ± 1.2E+5
TCG_G	11	6	1.3 ± 0.3E+5
T_CGC	13	4	1.4 ± 0.2E+5
T_CGG	11	6	2.0 ± 0.5E+5
ACC_T	10	6	3.4 ± 1.5E+5
A_CCG	14	2	3.1 ± 1.1E+5
A_GCC	13	3	2.3 ± 0.7E+5

Motif	#Bright	#Dark	Avg. I_{int}
AT_CC	12	4	4.4 ± 2.3E+5
CAA_A	11	5	4.2 ± 2.3E+5
CAC_C	11	5	2.7 ± 1.2E+5
C_ACA	11	5	2.0 ± 0.6E+5
CC_AC	15	1	6.0 ± 1.7E+5
CC_GC	14	2	2.5 ± 0.4E+5
C_CCC	16	0	6.0 ± 2.4E+5
C_CGG	16	0	2.3 ± 0.5E+5
CG_CA	14	2	3.1 ± 0.9E+5
C_GCA	11	5	1.9 ± 0.3E+5
GAG_C	13	3	1.2 ± 0.2E+5
G_ACG	15	1	2.2 ± 0.6E+5
GC_CA	13	3	1.9 ± 0.5E+5
GC_GC	15	1	2.3 ± 0.5E+5
GCTC	12	4	1.3 ± 0.2E+5
GGCG	15	1	1.5 ± 0.3E+5
GGG_G	13	3	1.9 ± 0.5E+5
TA_CC	10	6	1.0 ± 0.2E+5
TC_CC	15	1	5.4 ± 2.3E+5
T_CCC	15	1	5.6 ± 2.3E+5
T_CCG	11	5	2.3 ± 0.6E+5
T_GCC	11	5	1.7 ± 0.7E+5
ACC_A	11	4	5.1 ± 1.7E+5
ACC_C	13	2	4.3 ± 1.3E+5
CCCA	14	1	6.8 ± 2.6E+5
CGAA	12	3	2.4 ± 1.1E+5
CGC_C	14	1	2.1 ± 0.3E+5
CTCG	14	1	2.3 ± 0.3E+5
C_TAC	10	5	1.9 ± 0.8E+5
G_ATC	11	4	1.3 ± 0.4E+5
GCCC	15	0	5.3 ± 1.7E+5
G_CGT	11	4	1.6 ± 0.7E+5
GGAA	11	4	3.3 ± 1.3E+5
GGCA	11	4	1.5 ± 0.3E+5
T_ACG	10	5	3.9 ± 1.3E+5
ACC_G	11	3	3.3 ± 1.2E+5

Motif	#Bright	#Dark	Avg. I_{int}
CA_CC	13	1	4.8 ± 1.7E+5
CAGA	10	4	1.1 ± 0.2E+5
CCA_C	12	2	4.9 ± 1.7E+5
CC_AA	11	3	6.0 ± 2.7E+5
CCG_G	14	0	2.2 ± 0.5E+5
CC_GG	12	2	3.7 ± 1.2E+5
GCC_A	13	1	3.4 ± 1.1E+5
GCGG	13	1	1.4 ± 0.4E+5
GG_AG	10	4	1.4 ± 0.4E+5
GG_GG	13	1	2.8 ± 0.6E+5
G_GCC	11	3	3.8 ± 1.8E+5
ACCG	11	2	3.6 ± 1.3E+5
AC_CC	12	1	4.6 ± 1.5E+5
ATCC	10	3	5.1 ± 2.8E+5
CAAC	10	3	4.9 ± 1.6E+5
CCGC	12	1	2.8 ± 0.5E+5
C_CCT	11	2	6.5 ± 2.2E+5
CGCG	13	0	1.9 ± 0.5E+5
GCAA	11	2	2.0 ± 0.6E+5
G_CGC	13	0	2.5 ± 0.6E+5
GGCT	11	2	2.6 ± 1.2E+5
GGGC	11	2	3.7 ± 1.8E+5
ACGC	10	2	1.7 ± 0.4E+5
CCCC	12	0	7.3 ± 3.0E+5
CCCG	12	0	3.2 ± 0.6E+5
CC_CT	10	2	5.4 ± 2.0E+5
CCGA	11	1	5.4 ± 1.7E+5
CGC_A	11	1	2.1 ± 0.2E+5
GGA_G	10	2	1.5 ± 0.4E+5
G_GGG	10	2	2.5 ± 0.6E+5
CGAC	10	1	4.8 ± 1.9E+5
CGAG	10	1	2.7 ± 1.5E+5
CGGC	11	0	1.9 ± 0.4E+5
TCCC	10	1	7.2 ± 3.2E+5
CGCC	10	0	1.9 ± 0.4E+5
GCCG	10	0	3.1 ± 1.5E+5

Table B.4: Tabulation of motifs identified as discriminative of bright sequences in the 684 random templates by MERCI, in order of the number of times each motif occurs, with the number of occurrences of each motif in bright and dark strands, respectively. The average I_{int} with its standard error for templates associated with the motifs is also tabulated.

B.6 Discriminative motifs identified by MERCI for dark templates

"Dark" motifs were found by defining bright templates as class N and dark templates as class P, with F_P = 10 and F_N = 10, and by searching for all motifs with length up to 10 bases (the total length of each sequence) and up to one gap (wildcard acting as any base A, C, G, T or no base) that satisfy these criteria. Table B.5 lists all dark motifs in order of the total number of occurrences in both bright and dark templates. Note that seven of these listed motifs occur in each list (Tables B.4 and B.5). These "degenerate" motifs occur in each list because each motif occurs 10 times in bright templates and 10 times in dark templates. When forming feature vectors for each template sequence, this degeneracy is removed by counting these motifs only once. We also note that the three identified 6-base motifs listed below occur in sequences where the gap in each motif represents no base- thus all 6-base gapped motifs represent 5-base motifs occurring in sequences associated with darkness.

Motif	**#Bright**	**#Dark**	**Avg. I_{int}**
T_TT	8	64	6.8 ±3.3E+4
TT_T	6	62	6.7 ±3.4E+4
AT_T	10	52	3.3 ±0.6E+4
A_TT	8	52	4.3 ±1.7E+4
TTG	9	47	5.0 ±2.2E+4
TTT	3	46	6.6 ±4.5E+4
TTC	8	38	1.1 ±0.5E+5
CTT	9	36	1.2 ±0.6E+5
TTA	7	36	1.1 ±0.5E+5
ATT	4	38	2.5 ±0.5E+4
AGT	8	26	6.8 ±2.5E+4
CT_GT	10	19	1.1 ±0.3E+5
TTT_G	1	27	2.2 ±0.7E+4
T_TTG	2	26	2.4 ±0.8E+4
GT_CA	8	18	2.0 ±0.8E+5
G_TCC	10	16	1.9 ±0.6E+5
TA_AG	9	17	4.9 ±1.0E+4
T_ACA	10	16	7.7 ±2.0E+4
TTG_G	5	21	7.8 ±4.6E+4

Motif	**#Bright**	**#Dark**	**Avg. I_{int}**
TTG_T	1	25	2.0 ±0.6E+4
T_TCA	8	18	9.8 ±4.4E+4
T_TGG	5	21	8.0 ±4.6E+4
C_TGG	10	15	1.5 ±0.7E+5
C_TGT	7	18	8.3 ±3.0E+4
GT_AA	7	18	1.7 ±0.8E+5
T_AGC	10	15	1.5 ±0.7E+5
CA_TG	9	15	5.4 ±1.2E+4
CGT_T	8	16	9.7 ±4.9E+4
GA_TA	9	15	6.5 ±1.6E+4
GC_TG	9	15	1.0 ±0.3E+5
GT_TT	3	21	3.2 ±1.1E+4
TAC_A	10	14	1.5 ±0.8E+5
T_AAG	6	18	4.1 ±1.0E+4
TGG_T	5	19	1.1 ±0.7E+5
TG_TC	6	18	1.4 ±0.5E+5
TG_TT	2	22	2.7 ±0.9E+4
TT_GC	6	18	8.6 ±5.0E+4
TT_GG	6	18	8.9 ±4.9E+4

Motif	#Bright	#Dark	Avg. I_{int}
AC_TA	10	13	1.4 ±0.7E+5
ATA_C	9	14	9.3 ±3.4E+4
CAT_G	9	14	6.6 ±1.6E+4
C_TTG	4	19	8.1 ±5.2E+4
G_GGT	10	13	1.6 ±0.6E+5
GTC_A	9	14	2.2 ±0.8E+5
GTC_C	9	14	1.6 ±0.5E+5
GT_CC	8	15	1.8 ±0.6E+5
GT_TA	3	20	6.0 ±3.3E+4
G_TTA	3	20	6.8 ±3.5E+4
TAA_G	7	16	5.7 ±1.8E+4
TA_AC	8	15	6.3 ±1.9E+4
TAG_C	10	13	1.7 ±0.8E+5
TCC_T	6	17	7.7 ±3.4E+4
T_CAA	9	14	2.4 ±0.9E+5
TGT_G	3	20	5.5 ±2.8E+4
TG_TA	1	22	1.9 ±0.3E+4
T_GCA	5	18	9.6 ±4.2E+4
TT_AA	3	20	4.3 ±1.8E+4
TT_TG	1	22	2.2 ±0.9E+4
A_ACT	10	12	8.1 ±2.5E+4
AC_AT	9	13	6.4 ±1.4E+4
AGC_A	9	13	6.3 ±1.3E+4
AT_TC	6	16	5.0 ±1.5E+4
CT_TC	10	12	9.5 ±2.7E+4
GG_TA	10	12	1.9 ±0.8E+5
G_GTC	10	12	1.3 ±0.5E+5
GT_CT	7	15	8.2 ±3.8E+4
GTT_A	2	20	5.5 ±3.4E+4
T_AAC	10	12	2.0 ±0.9E+5
TC_AT	6	16	4.6 ±1.3E+4
T_CAG	8	14	6.7 ±2.6E+4
TG_CA	5	17	1.5 ±0.6E+5
TG_GT	2	20	3.5 ±1.6E+4
TGT_A	4	18	9.4 ±5.2E+4
T_GTA	2	20	2.4 ±0.5E+4
AAA_G	9	12	2.0 ±1.1E+5
AC_GT	7	14	1.4 ±0.8E+5
AG_GA	10	11	2.2 ±1.0E+5
AT_CA	9	12	1.1 ±0.4E+5

Motif	#Bright	#Dark	Avg. I_{int}
CAT_T	2	19	2.5 ±0.7E+4
CTG_A	5	16	5.6 ±1.8E+4
CT_GA	8	13	7.3 ±1.9E+4
CTT_G	4	17	6.5 ±3.9E+4
CT_TA	6	15	9.9 ±4.2E+4
CT_TG	4	17	5.7 ±3.0E+4
GAT_C	8	13	1.3 ±0.5E+5
GCA_T	8	13	1.0 ±0.3E+5
G_CCT	9	12	2.8 ±1.4E+5
GTCC	7	14	1.6 ±0.6E+5
G_TCA	9	12	2.0 ±0.9E+5
TAA_C	7	14	9.1 ±3.9E+4
TAG_G	8	13	2.1 ±1.2E+5
TC_CT	6	15	1.0 ±0.4E+5
TC_GT	8	13	9.4 ±3.1E+4
TCT_A	9	12	1.0 ±0.4E+5
TC_TT	3	18	6.4 ±3.9E+4
T_CGT	7	14	9.0 ±3.1E+4
TG_AC	8	13	1.1 ±0.4E+5
TGT_C	4	17	1.1 ±0.6E+5
T_GTC	6	15	1.3 ±0.6E+5
T_GTT	2	19	2.8 ±1.0E+4
TTG_C	6	15	9.7 ±5.6E+4
TT_GT	1	20	2.1 ±0.8E+4
AAG_A	7	13	1.5 ±1.0E+5
AA_TA	7	13	4.9 ±1.4E+4
ACA_T	5	15	4.1 ±1.1E+4
A_CAT	7	13	5.0 ±1.1E+4
A_GCA	8	12	1.0 ±0.4E+5
ATA_A	7	13	9.8 ±4.0E+4
AT_AC	7	13	1.1 ±0.4E+5
A_TGT	3	17	3.4 ±1.4E+4
CAG_T	7	13	1.2 ±0.4E+5
CA_TT	2	18	2.8 ±0.8E+4
CC_AT	9	11	2.0 ±0.9E+5
CCT_T	7	13	2.6 ±1.3E+5
G_ATT	3	17	2.8 ±0.8E+4
G_CTG	9	11	1.4 ±0.4E+5
GGT_A	6	14	8.6 ±3.8E+4
GGT_C	9	11	2.5 ±0.9E+5

Motif	#Bright	#Dark	Avg. I_{int}
GTT_T	3	17	7.3 ±4.2E+4
TAA_A	4	16	3.7 ±1.2E+4
TACA	8	12	7.4 ±2.0E+4
T_ACT	7	13	5.9 ±1.5E+4
TCA_C	8	12	2.1 ±1.0E+5
TCG_T	7	13	1.1 ±0.4E+5
T_CTT	3	17	6.6 ±4.1E+4
TG_AG	5	15	7.3 ±3.1E+4
TG_CT	6	14	1.3 ±0.8E+5
TGG_A	4	16	8.1 ±3.4E+4
TGT_T	2	18	2.9 ±1.0E+4
T_GGT	3	17	4.2 ±1.7E+4
TT_CA	2	18	2.6 ±0.6E+4
TTG_A	2	18	2.1 ±0.5E+4
TTT_A	1	19	2.1 ±0.6E+4
TT_TA	1	19	2.1 ±0.6E+4
T_TTA	2	18	6.3 ±4.2E+4
AAG_C	10	10	1.5 ±0.6E+5
AG_AC	10	10	1.5 ±0.5E+5
AT_GG	10	10	1.0 ±0.3E+5
TC_TA	10	10	1.2 ±0.4E+5
T_CAC	10	10	1.8 ±0.9E+5
T_CTC	10	10	7.8 ±1.6E+4
TG_GC	10	10	2.3 ±1.0E+5
AA_AC	7	12	2.9 ±2.1E+5
AAG_T	5	14	1.0 ±0.7E+5
A_ATA	4	15	3.9 ±1.4E+4
ACTG	7	12	8.6 ±2.7E+4
ACT_T	6	13	9.5 ±5.4E+4
AG_TG	9	10	1.4 ±0.7E+5
A_TAC	7	12	1.0 ±0.4E+5
CAC_T	9	10	2.2 ±1.2E+5
CA_GG	9	10	1.3 ±0.5E+5
CA_GT	4	15	7.6 ±3.9E+4
C_ATG	9	10	1.1 ±0.5E+5
CC_TT	3	16	1.5 ±1.2E+5
C_GTT	3	16	9.5 ±6.3E+4
CTA_A	6	13	5.9 ±1.9E+4
CT_AT	8	11	1.6 ±0.9E+5
C_TAT	8	11	1.6 ±0.9E+5

Motif	#Bright	#Dark	Avg. I_{int}
G_ATA	7	12	7.0 ±2.0E+4
GTA_T	6	13	4.6 ±1.1E+4
GTC_T	4	15	3.8 ±1.0E+4
GT_GT	2	17	3.1 ±1.1E+4
G_TTT	2	17	3.1 ±1.2E+4
TA_GG	6	13	2.1 ±1.4E+5
T_AGG	5	14	1.7 ±1.3E+5
TC_AA	6	13	2.1 ±1.0E+5
TC_AG	7	12	7.2 ±2.9E+4
T_CAT	4	15	3.9 ±1.3E+4
TG_AT	1	18	4.7 ±3.3E+4
TG_GA	7	12	1.1 ±0.4E+5
TG_GG	4	15	6.6 ±3.2E+4
TG_TG	3	16	6.1 ±3.4E+4
T_GAC	9	10	1.3 ±0.4E+5
T_GGA	7	12	1.1 ±0.4E+5
T_GGG	6	13	2.1 ±1.4E+5
TTA_A	2	17	4.3 ±2.1E+4
TTC_G	3	16	6.9 ±4.5E+4
T_TAA	2	17	4.2 ±2.1E+4
T_TCG	4	15	3.8 ±1.1E+4
AA_CT	8	10	8.8 ±3.0E+4
A_AAC	8	10	4.2 ±2.3E+5
AG_GT	5	13	1.3 ±0.7E+5
ATT_T	1	17	2.1 ±0.7E+4
AT_TT	1	17	2.1 ±0.7E+4
A_TTC	2	16	2.8 ±0.9E+4
A_TTT	1	17	2.1 ±0.7E+4
C_AGT	5	13	8.3 ±4.1E+4
C_ATA	6	12	7.1 ±2.1E+4
CTA_T	8	10	1.7 ±0.9E+5
CTT_A	5	13	9.6 ±4.8E+4
C_TTC	3	15	3.1 ±0.9E+4
GGT_T	6	12	1.7 ±0.7E+5
GG_TT	8	10	1.9 ±0.7E+5
GT_AT	6	12	7.7 ±3.5E+4
G_TAC	4	14	6.0 ±2.2E+4
G_TCT	7	11	1.0 ±0.5E+5
G_TGG	6	12	1.5 ±0.7E+5
G_TGT	5	13	1.0 ±0.4E+5

Motif	#Bright	#Dark	Avg. I_{int}
G_TTC	4	14	1.2 ±0.6E+5
TAA_T	3	15	6.6 ±4.2E+4
TA_AA	7	11	7.6 ±2.2E+4
T_ATT	1	17	2.0 ±0.5E+4
TCT_T	5	13	8.9 ±4.6E+4
TGA_T	3	15	6.8 ±3.6E+4
T_GAT	2	16	5.3 ±3.5E+4
T_GTG	4	14	8.3 ±4.0E+4
TTA_C	4	14	1.5 ±1.1E+5
TTC_A	2	16	2.7 ±0.7E+4
TT_CG	4	14	1.8 ±1.2E+5
TTT_C	2	16	1.4 ±1.2E+5
TTTG	1	17	2.5 ±1.1E+4
TTT_T	1	17	1.4 ±1.2E+5
TT_TT	3	15	1.9 ±1.3E+5
T_TGA	3	15	2.9 ±0.9E+4
T_TTC	2	16	1.4 ±1.2E+5
T_TTT	1	17	1.4 ±1.2E+5
AA_GA	7	10	1.7 ±1.2E+5
AGG_T	6	11	1.2 ±0.8E+5
ATAC	5	12	9.7 ±4.5E+4
ATG_G	7	10	1.1 ±0.4E+5
AT_GT	4	13	5.9 ±2.5E+4
C_GTA	7	10	4.9 ±1.0E+4
CTG_T	5	12	1.0 ±0.4E+5
CTT_T	1	16	1.4 ±1.3E+5
GAT_T	4	13	4.9 ±1.9E+4
GA_TT	4	13	9.1 ±6.0E+4
GC_AT	5	12	5.7 ±1.8E+4
G_GTA	5	12	4.7 ±1.5E+4
GTG_T	3	14	6.8 ±3.7E+4
GT_GG	6	11	1.5 ±0.7E+5
GT_TC	5	12	1.3 ±0.7E+5
G_TAG	7	10	1.9 ±1.0E+5
TA_AT	2	15	6.2 ±4.4E+4
T_AAA	5	12	4.9 ±1.5E+4
TCA_G	4	13	3.7 ±1.0E+4
T_CCT	4	13	8.6 ±4.5E+4
TGC_A	4	13	1.1 ±0.6E+5
TT_AG	2	15	6.7 ±4.9E+4

Motif	#Bright	#Dark	Avg. I_{int}
TTGG	4	13	1.1 ±0.7E+5
T_TCT	5	12	9.1 ±4.9E+4
T_TGT	1	16	2.3 ±0.9E+4
AA_GT	5	11	2.1 ±1.3E+5
A_CTT	4	12	2.3 ±1.5E+5
AG_CA	6	10	5.7 ±1.5E+4
A_GTC	5	11	2.1 ±1.1E+5
ATT_C	2	14	3.0 ±0.9E+4
AT_TG	1	15	1.9 ±0.5E+4
A_TAA	5	11	8.3 ±4.6E+4
CAA_T	6	10	8.7 ±3.5E+4
C_ATT	1	15	2.4 ±0.8E+4
CCA_T	6	10	10.0 ±4.5E+4
CT_AA	4	12	5.3 ±2.3E+4
C_TAA	5	11	5.8 ±2.3E+4
C_TTT	1	15	1.5 ±1.4E+5
GTA_C	6	10	6.0 ±1.5E+4
GT_AG	2	14	3.5 ±1.3E+4
G_TAA	2	14	3.0 ±1.4E+4
G_TTG	5	11	1.2 ±0.7E+5
TC_TG	2	14	4.4 ±2.5E+4
T_CTA	6	10	6.6 ±1.8E+4
TGA_C	6	10	1.3 ±0.5E+5
TT_AC	4	12	1.7 ±1.2E+5
TT_AT	0	16	1.2 ±0.1E+4
TT_GA	2	14	2.3 ±0.6E+4
TTTA	1	15	2.3 ±0.8E+4
T_TAG	2	14	7.2 ±5.2E+4
A_GGT	3	12	1.3 ±0.9E+5
ATG_T	4	11	6.6 ±2.8E+4
ATT_G	1	14	2.1 ±0.5E+4
CA_TC	5	10	8.9 ±4.5E+4
C_CTT	4	11	1.8 ±1.5E+5
CG_TT	3	12	1.2 ±0.8E+5
CTTG	2	13	2.8 ±0.9E+4
C_TGA	5	10	7.4 ±2.8E+4
G_CAT	4	11	5.4 ±1.9E+4
G_CTT	4	11	1.2 ±0.7E+5
GTT_G	4	11	1.2 ±0.8E+5
GTTT	1	14	2.7 ±1.4E+4

Motif	#Bright	#Dark	Avg. I_{int}
GT_TG	4	11	1.2 ±0.8E+5
TAG_A	5	10	5.6 ±1.9E+4
TA_TG	2	13	2.6 ±0.7E+4
T_AAT	1	14	6.3 ±5.0E+4
TCA_T	4	11	4.4 ±1.7E+4
TGA_A	4	11	6.2 ±2.7E+4
TGTT	2	13	3.5 ±1.4E+4
TTAA	2	13	5.1 ±2.7E+4
TTA_G	2	13	2.0 ±1.4E+5
TTC_T	2	13	7.8 ±5.5E+4
TT_CT	2	13	7.8 ±5.5E+4
TTGT	1	14	2.4 ±1.1E+4
TT_TC	2	13	1.7 ±1.5E+5
AATA	4	10	4.6 ±1.8E+4
AAT_A	4	10	4.6 ±1.8E+4
AC_TT	4	10	2.6 ±1.7E+5
AGT_T	2	12	2.4 ±0.7E+4
AG_TT	4	10	3.3 ±0.9E+4
AT_CT	4	10	3.7 ±1.0E+4
ATTT	1	13	2.3 ±0.9E+4
CA_AT	4	10	6.7 ±2.7E+4
CT_TT	2	12	1.8 ±1.6E+5
GAT_A	4	10	5.4 ±2.1E+4
GC_TT	4	10	1.3 ±0.9E+5
GTTA	2	12	7.8 ±5.3E+4
GTT_C	3	11	1.4 ±0.8E+5
TCCT	3	11	4.8 ±1.8E+4
TG_AA	4	10	1.2 ±0.7E+5
TGTC	4	10	1.6 ±0.8E+5
TGTG	2	12	6.8 ±4.5E+4
TTCA	2	12	3.0 ±0.9E+4

Motif	#Bright	#Dark	Avg. I_{int}
TTCG	2	12	2.7 ±0.7E+4
TTGA	2	12	2.3 ±0.7E+4
A_TTG	2	11	2.5 ±0.7E+4
CGTT	2	11	1.2 ±0.9E+5
CTT_C	3	10	3.5 ±1.1E+4
GTA_G	2	11	4.1 ±1.6E+4
TAAG	3	10	4.3 ±1.6E+4
TAC_T	3	10	4.5 ±1.7E+4
TAG_T	3	10	3.7 ±1.0E+4
TA_GT	1	12	2.2 ±0.5E+4
TA_TT	1	12	2.1 ±0.7E+4
TCT_G	3	10	3.6 ±1.2E+4
TGCA	2	11	1.1 ±0.7E+5
TGC_T	1	12	2.6 ±1.1E+4
TGTA	1	12	2.1 ±0.6E+4
A_GTT	2	10	2.6 ±0.8E+4
A_TTA	2	10	3.4 ±1.3E+4
CATT	1	11	2.7 ±1.1E+4
GATT	2	10	3.0 ±1.2E+4
G_AGT	2	10	5.8 ±3.7E+4
GT_AC	2	10	3.1 ±1.1E+4
AG_TA	1	10	2.3 ±0.7E+4
GTGT	1	10	2.8 ±1.3E+4
GTT_AA	1	10	3.2 ±1.9E+4
GT_TAA	1	10	3.1 ±1.9E+4
TAAT	1	10	8.1 ±6.8E+4
T_ATG	1	10	2.3 ±0.8E+4
TCC_TT	1	10	2.7 ±1.1E+4
TGAT	1	10	7.1 ±5.7E+4
TTTC	1	10	2.1 ±2.0E+5
TTA_T	0	10	1.3 ±0.1E+4

Table B.5: Tabulation of motifs identified as discriminative of dark sequences in the 684 random templates by MERCI, in order of the number of times each motif occurs, with the number of occurrences of each motif in bright and dark strands, respectively. The average I_{int} with its standard error for templates associated with the motifs is also tabulated.

B.7 Sequences generated by intensity-weighted motif selection

#	Sequence	I_{int}
1	ACGGCAACCA	7.5E+06
2	ACGGCAACCG	3.5E+06
3	GGCCGAACGG	3.3E+06
4	CCAGCCCGGA	3.0E+06
5	ACGGGGCAAA	2.9E+06
6	TCCAACCCGG	2.9E+06
7	CCCCCGAAAA	2.6E+06
8	GATCCCCAAC	2.5E+06
9	GCCGCCCGCC	2.4E+06
10	GGACCCCCGT	2.4E+06
11	ACGCACCCAG	2.4E+06
12	CCTCGCGGCG	2.4E+06
13	AACCCCCAGC	1.8E+06
14	CCAGCTCCCG	1.7E+06
15	CCCGGCCGAA	1.7E+06
16	AATCCCCCCA	1.7E+06
17	AACCCCCGGT	1.6E+06
18	AATCCCCCAA	1.4E+06
19	ACCCCGGAGA	1.4E+06
20	CCGCCGAATA	1.4E+06
21	ATCCCCCGCG	1.4E+06
22	ACACAGCCGA	1.4E+06
23	GCCCCCCTAG	1.4E+06
24	CCACGACCGG	1.3E+06
25	ACCCCACCTA	1.3E+06
26	ACCGCCGGGA	1.3E+06
27	GCGACCCCAG	1.3E+06
28	GGCCCTGCGA	1.3E+06
29	CGCCCCCACC	1.3E+06
30	TGCCCCTCCG	1.2E+06
31	CACAAACCCA	1.2E+06
32	ATCGCGCAAA	1.2E+06
33	ACCAACCCGC	1.1E+06
34	CCCAACCCGA	1.0E+06
35	CCCGGACGAC	9.9E+05
36	TCGACGCGGC	9.8E+05
37	ACCTCCCCAA	9.5E+05
38	CCGAGAGAAG	9.2E+05
39	GCCGGCTCCC	8.7E+05
40	GGACCCCCGC	8.2E+05
41	TCGATCCCGC	8.0E+05
42	ATCCCCCCCG	7.8E+05
43	GCCGACCGCG	7.6E+05
44	ACCCGGAAAG	7.6E+05
45	ACCCCACCCG	7.6E+05
46	CCCCCGGACG	7.5E+05
47	CCCACACGCC	7.4E+05
48	ATCCCGAGCG	7.3E+05
49	CCCCCGGGCG	7.0E+05
50	AACAGCGCCC	6.9E+05
51	TCAACCCCCG	6.8E+05
52	GGCCGACCCA	6.7E+05
53	CGGCCCACCT	6.6E+05
54	GCCGTCCCCA	6.4E+05
55	ATCCCACCTC	6.4E+05
56	CCACCCCTGC	6.3E+05
57	CACAAGCCCC	6.3E+05
58	CCACGGCTAG	6.2E+05
59	CCCCCGCATA	6.2E+05
60	ATCCCCCAAA	6.1E+05
61	TGCCCCCAAC	6.0E+05
62	GCCGCCCAGG	5.9E+05
63	ACCCATCCCG	5.9E+05
64	ACCCGAGCCG	5.7E+05
65	ACGCCCATGC	5.7E+05
66	ACCGACCCCC	5.5E+05
67	GCTCCCGGCT	5.3E+05
68	CGACCCACCC	5.2E+05
69	CCGCCCCGAG	5.1E+05
70	CCCCGCGAGT	5.1E+05
71	CCGCCCGCCC	5.1E+05
72	CCGACGCCCT	5.0E+05
73	GCCAGAACGC	4.9E+05
74	CCGACCCCGA	4.7E+05
75	GGACGACACT	4.6E+05
76	TCCGACCCCC	4.6E+05

#	Sequence	I_{int}
77	CAAGGGACCC	4.6E+05
78	AACACCCCCG	4.6E+05
79	ATCGCAGCGG	4.3E+05
80	CCCCAGCCCT	4.1E+05
81	GCTACGCGCC	4.1E+05
82	GTATCGCCCG	4.0E+05
83	ACGAGGGCCC	4.0E+05
84	GGGAGACCCT	4.0E+05
85	GATCCCCAAA	3.8E+05
86	GAACAGCCGA	3.8E+05
87	CTGCCCCCGC	3.8E+05
88	CCAGCACCGA	3.7E+05
89	CCGCCCCTGG	3.7E+05
90	GAAAGCGCGA	3.7E+05
91	TGCGCCCCGC	3.6E+05
92	GCCTCTCGCG	3.6E+05
93	ACTCCGGCCG	3.6E+05
94	CCACGGGCAA	3.5E+05
95	ATCCCGCCCA	3.5E+05
96	GCCATCCCGC	3.5E+05
97	CCCACCGGCC	3.4E+05
98	CCGAACCCGC	3.4E+05
99	GCCGGGCCGG	3.4E+05
100	CCAGCGGGTT	3.3E+05
101	GGGGAACAAA	3.3E+05
102	GGCAACGAAC	3.3E+05
103	CCGCCCCTTC	3.2E+05
104	CCCCCCCCAT	3.2E+05
105	CCCCAGCTCG	3.2E+05
106	GGCTCGCCAA	3.2E+05
107	GGAACCCCGC	3.2E+05
108	ACCGGCCCTC	3.2E+05
109	ACCCGGCGCG	3.1E+05
110	GGAGAGCCCC	3.1E+05
111	GCCCCCGACA	3.0E+05
112	AGAAACCCAC	2.9E+05
113	GCCGATCCCG	2.9E+05
114	GCCGAGCCCG	2.9E+05
115	CCAGCCGCGC	2.9E+05
116	GGCGACGCCA	2.9E+05

#	Sequence	I_{int}
117	GCCGCCCGAA	2.9E+05
118	AGCGAGCCCA	2.8E+05
119	GTCCCCAACG	2.8E+05
120	CCGCCCGGAT	2.8E+05
121	GGACACCCCT	2.7E+05
122	CCGAGCGTCC	2.7E+05
123	GCCCACACAA	2.7E+05
124	GACGCGGCCC	2.7E+05
125	GGCAGCGCAC	2.6E+05
126	GGCAACCTCG	2.6E+05
127	GGAGCGCCCT	2.5E+05
128	GGCGCGAGGG	2.4E+05
129	AGGGCCCAAC	2.4E+05
130	CCGGGGCCCA	2.4E+05
131	TCCCACGGAT	2.4E+05
132	GCCGCGCCGA	2.4E+05
133	CCCGGACCCC	2.3E+05
134	CCAGGCCGAC	2.3E+05
135	GATCCGCGGG	2.3E+05
136	GCGGAGAACA	2.3E+05
137	ATCCGGGCAC	2.3E+05
138	CCGCGAGCAT	2.2E+05
139	GCAAGCCCGC	2.2E+05
140	GCGATGCCCA	2.2E+05
141	GGAAGGACCG	2.2E+05
142	GGCGGGCAAA	2.2E+05
143	CCGACGGGGT	2.2E+05
144	CCTAGCCCCG	2.2E+05
145	AACAGACCCC	2.2E+05
146	CCGGAATCCG	2.2E+05
147	GACGACGGAT	2.2E+05
148	ATCCCACCGA	2.1E+05
149	TAGGGCTCCG	2.1E+05
150	ATCCCTCCCA	2.0E+05
151	AGGGCAACGC	2.0E+05
152	ACCGACCTAC	2.0E+05
153	CCGCCCCCAT	1.9E+05
154	GCTCGCGGCG	1.9E+05
155	CACCCCCCGA	1.9E+05
156	CCCAGCGCGG	1.9E+05

#	Sequence	I_{int}
157	TCGGGCAGAC	1.9E+05
158	CCTCCCCAAA	1.9E+05
159	TCGCCCAAAC	1.9E+05
160	CCGACAACGC	1.9E+05
161	TTCCCCACCC	1.9E+05
162	AGCCCTCCCC	1.8E+05
163	GAACTCGCCC	1.8E+05
164	CAAGACCCCG	1.8E+05
165	CCGCCCGAAA	1.8E+05
166	GAGGGCGGCA	1.8E+05
167	GACACGGACC	1.8E+05
168	CACCCCGAGC	1.8E+05
169	CCGAGCCGGG	1.7E+05
170	CCACCCCAAT	1.7E+05
171	TCCCTCGGGA	1.7E+05
172	CCCACCAACA	1.7E+05
173	GCCGGCCCCG	1.7E+05
174	CACCCGGCTA	1.7E+05
175	AGAGCCCTAC	1.7E+05
176	GCGAATCCCC	1.7E+05
177	GCGTCCCCCT	1.7E+05
178	CCACTCCCCG	1.6E+05
179	AGGACCCGAA	1.6E+05
180	ATCCGGGGGA	1.6E+05
181	ATCCACCGAC	1.6E+05
182	GCCAACCAAA	1.6E+05
183	GATCCGGGAG	1.6E+05
184	GCTCCCCGAC	1.6E+05
185	CGCAAGCCCG	1.6E+05
186	GGGCCCAAAC	1.6E+05
187	CCCAAGCCGC	1.5E+05
188	CCGAAGCGCG	1.5E+05
189	GCAAGGGGCC	1.5E+05
190	GCTCCGGACT	1.5E+05
191	CCCAAGCTCG	1.5E+05
192	AACGACCCGG	1.5E+05
193	ACAACCGCCT	1.5E+05
194	AGGGGCCCAG	1.5E+05
195	GAGAGCCCGA	1.5E+05
196	ACAGCCCGCA	1.5E+05

#	Sequence	I_{int}
197	CCCGCCCCAT	1.5E+05
198	CCCCCCCCCA	1.5E+05
199	CCAGGGCGCC	1.5E+05
200	AGGGTGCCCC	1.4E+05
201	TCAAGGCCCA	1.4E+05
202	GCGGCGCCTA	1.4E+05
203	ACGCGCGCAA	1.4E+05
204	AGGGCGCCGC	1.4E+05
205	ACGCCCCCCA	1.4E+05
206	CCACGCGGGA	1.3E+05
207	TCCGACGCCC	1.3E+05
208	ACCAACGCCC	1.3E+05
209	ACCACGCCGA	1.3E+05
210	CCAAGACCCA	1.3E+05
211	GAAGCGCCCC	1.3E+05
212	ACGGGCCTCG	1.3E+05
213	GAGGCCGTCA	1.2E+05
214	ACCCGAAACG	1.2E+05
215	CGGCTGGGCG	1.2E+05
216	CCCTCCCCCT	1.2E+05
217	CCCAGGAAAA	1.2E+05
218	CCTGGCCCCC	1.2E+05
219	CGCGAGAGAA	1.2E+05
220	CCCGAAGGCC	1.2E+05
221	CTACGCGAAG	1.2E+05
222	TCCCGGCCCC	1.2E+05
223	CCGCCACGCG	1.2E+05
224	AGGACACCGA	1.1E+05
225	CCGCCCTAGT	1.1E+05
226	AGCCGAAACT	1.1E+05
227	GAGGCACCGG	1.1E+05
228	AGGCTACCCC	1.1E+05
229	GCCAAAGCGC	1.1E+05
230	ATCCGAGCGG	1.1E+05
231	ACCGATCCCG	1.1E+05
232	GGGCCACGAA	1.1E+05
233	GAGATCCGGC	1.1E+05
234	GGCGAACCGA	1.1E+05
235	GCCCATGCCC	1.1E+05
236	CGACGGCAAA	1.1E+05

#	Sequence	I_{int}
237	AACGAACCCA	1.1E+05
238	CCCACCGCGC	1.1E+05
239	GACCCCCCCG	1.0E+05
240	CCGCGACCAG	1.0E+05
241	GACAGACCGG	1.0E+05
242	GCCGCGAGGG	1.0E+05
243	TGGGACCGAA	1.0E+05
244	AGGGGCCGAA	1.0E+05
245	CGGGAACGCG	9.9E+04
246	GGCAACCGCG	9.5E+04
247	GACGAAACCC	9.5E+04
248	AGCCGCAAAC	9.5E+04
249	GCGCCCAAAC	9.5E+04
250	ATCCCAAGCT	9.4E+04
251	GCGATCGCCC	9.4E+04
252	GGGACGCGTA	9.3E+04
253	GCGCCCATCG	9.2E+04
254	CCTGCGCAGA	9.1E+04
255	CGGTCCGGCA	8.9E+04
256	ACCTACGCGC	8.9E+04
257	TCCGCGCCAA	8.8E+04
258	CCGGGTCCGC	8.8E+04
259	GTCCACGAAC	8.7E+04
260	CGAACCGGGC	8.6E+04
261	GACCCGGTGG	8.6E+04
262	GGGCTCCCGA	8.6E+04
263	CACCTCCCCG	8.5E+04
264	AATCCGCACG	8.4E+04
265	GGACGACGGG	8.3E+04
266	ATCCCGTCGT	8.2E+04
267	CGGGAAGAAT	8.1E+04
268	CGAGAAGCCG	8.1E+04
269	AACCCGCCAC	8.1E+04
270	CCACCGCTGT	8.0E+04
271	AGCGACGCCC	8.0E+04
272	CGTGGCCCTG	7.9E+04
273	CTCCGCAAGT	7.9E+04
274	CGACAGGACG	7.8E+04
275	CTCCGATCGC	7.8E+04
276	GACAGGGGCG	7.8E+04

#	Sequence	I_{int}
277	CGCGCGCCTA	7.7E+04
278	GCCTCGCCCC	7.7E+04
279	GGCGCCGCCT	7.6E+04
280	CCGCAACCGA	7.6E+04
281	CGCCAGCGCT	7.6E+04
282	CCGACCAATC	7.5E+04
283	TACGAGGCCC	7.4E+04
284	CGGGCCAAAC	7.4E+04
285	GACCAGAGCG	7.4E+04
286	GTCACGCCCC	7.3E+04
287	GGGCAGGAGA	7.3E+04
288	GGGCTGCCCG	7.2E+04
289	AGCCCGAACA	7.1E+04
290	GAACGGCGGT	7.1E+04
291	CGTCTCCGCG	7.1E+04
292	GCGACGAGAC	6.9E+04
293	ACAACAGGCC	6.8E+04
294	CAAGGCGGGG	6.7E+04
295	CACCACCAAA	6.7E+04
296	TAACGAGCGC	6.6E+04
297	CCTCGCAAAC	6.6E+04
298	AGCCGACAGT	6.6E+04
299	CCAGGCGTCA	6.5E+04
300	GACGGAACCC	6.3E+04
301	CACCCGGCGG	6.3E+04
302	GGCGACTCCA	6.3E+04
303	CTCGCAGAAC	6.1E+04
304	GCACGTCCCA	6.0E+04
305	CGCCGATCCG	6.0E+04
306	CACGATCCGA	5.9E+04
307	CACCCGACGT	5.9E+04
308	GGGGCCAACG	5.9E+04
309	CCACTCCCGC	5.8E+04
310	CACCGACCCG	5.8E+04
311	ACCGGAACCA	5.8E+04
312	CCGTCCCGCC	5.8E+04
313	ACGAACCGGG	5.8E+04
314	GCACGCCCCA	5.6E+04
315	GCTCCGCTAG	5.6E+04
316	CCGCGACTCG	5.6E+04

#	Sequence	I_{int}
317	CCGGAACCGA	5.5E+04
318	AGGCGGGATA	5.5E+04
319	TCGAACGCGC	5.5E+04
320	GCCACCCCCG	5.4E+04
321	CCACGCGCCG	5.3E+04
322	GACGAGGCAA	5.3E+04
323	GCACCCACCT	5.2E+04
324	CCGGTCACGC	5.2E+04
325	CCCAGAGAGT	5.1E+04
326	TTCGCCGCAC	5.0E+04
327	TCACTCCCGC	5.0E+04
328	ACGTCCCGGG	4.8E+04
329	ATGCGGAATG	4.8E+04
330	GCCGCAGCAA	4.7E+04
331	ATCCCTGGCA	4.6E+04
332	CCCGCCACGT	4.6E+04
333	ATCGGCCCTC	4.6E+04
334	CCGAAACAAC	4.6E+04
335	GGCCGCCTGT	4.6E+04
336	TACGCCCAAA	4.5E+04
337	GCTCGTCGCC	4.5E+04
338	CCAGGCCCCC	4.3E+04
339	GCTACTCCCC	4.3E+04
340	TCGGCTCCAA	4.3E+04
341	GACGTGCGAG	4.1E+04
342	GGCCGCTAGT	4.1E+04
343	AACCCGCGGT	4.0E+04
344	TACGACTCCC	3.9E+04
345	TGCTCGCCCT	3.9E+04
346	AAGCCCGCAT	3.9E+04
347	CGCCGGGAGT	3.8E+04
348	TACCGAACCA	3.8E+04
349	CCACGCCCGC	3.7E+04
350	ATCCGCGAAT	3.7E+04
351	AACAGATCCC	3.6E+04
352	ACCGGGGCTC	3.5E+04
353	GGGCTCGCGA	3.4E+04
354	AGGCCCGCTT	3.3E+04
355	TCCCGACGCG	3.2E+04
356	TCCGCCGTCT	3.2E+04
357	TCCCGGTCCC	3.2E+04
358	CCACGTCCCG	3.1E+04
359	TGACCGACCC	3.1E+04
360	TCCGCAACGT	3.1E+04
361	GCGTGCCCAG	3.0E+04
362	GCCGACCCTT	2.9E+04
363	GACGGAAGCC	2.8E+04
364	ACCGACACTA	2.8E+04
365	CTCCGCCGCC	2.7E+04
366	CCGCGCTCCA	2.7E+04
367	CCGATCCCTT	2.6E+04
368	TCGGACCGCT	2.5E+04
369	CCAGCCTCCT	2.5E+04
370	CCACCGTGAA	2.5E+04
371	CGACGCCCCG	2.4E+04
372	CACAGACCCG	2.3E+04
373	GAACAGGGAC	2.3E+04
374	ATCCGAAGGG	2.3E+04

Table B.6: Sequences generated by the intensity-weighted motif distribution model presented in Section 3.3.2, as ordered by the measured integrated intensity, I_{int}, of Ag_N-DNA synthesized with each template. I_{int} values correspond to measurements taken 1 week after synthesis for Ag_N-DNA synthesized with the following conditions: [DNA] = 20 μM, 10 mM NH_4OAc, pH 7, [$AgNO_3$] = 100 μM, and [$NaBH_4$] = 0.5 × [$AgNO_3$]. As for Table B.3, use of 80 repeat instances of the same control template within one plate indicate an uncertainty of roughly 12% in I_{int}. By the intensity thresholds for "bright" and "dark" templates used to classify the random template sequences (Table B.1), 293 of the 374 generated templates are "bright" while only 3 of the 374 are "dark."

Appendix C. Supporting Information for Chapter 4

C.1 Overlap of spectra for D-A2 SC pair

Figure C.1 shows the normalized absorbance (dashed) and emission (solid) spectra for D (green) and A2 (red). These FRET pair candidates have well resolved absorbance spectra. Thus donor excitation can be achieved without directly exciting A2. The emission spectra of these clusters are not as spectrally resolved as D and A1, however a red fluorescence signal beyond 650 nm is expected to be produced under 490 nm excitation in the presence of FRET.

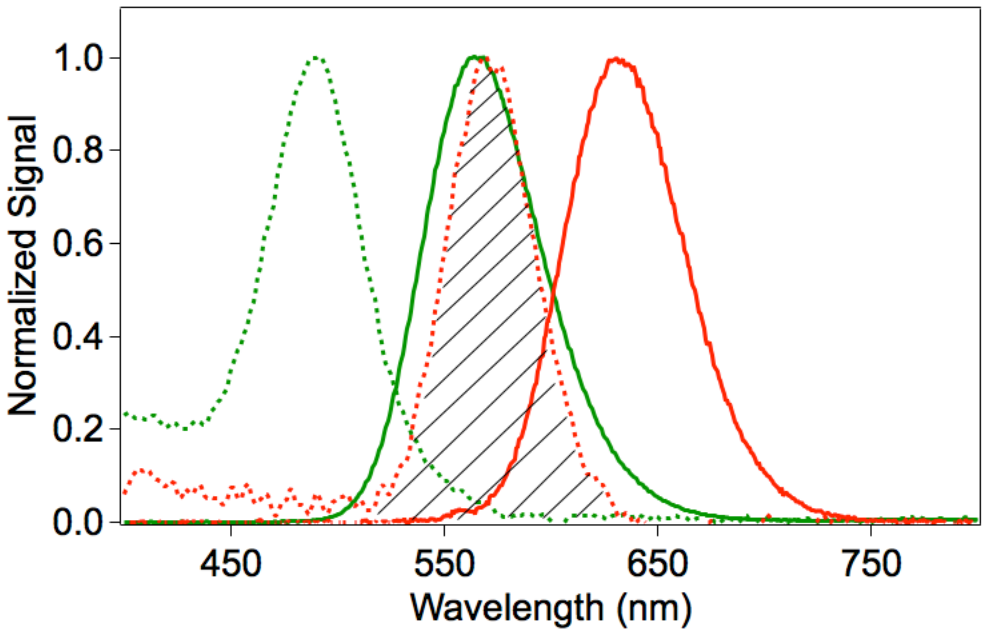

Figure C.1: Normalized absorbance and emission spectra of the donor cluster (green) are compared to those of acceptor cluster A2 (red). Dashed lines: absorbance. Solid lines: emission. Shaded region marks the range of spectral overlap between donor emission and acceptor absorbance.

C.2 Chromatograms and absorbance spectra for estimates of ε_{vis}

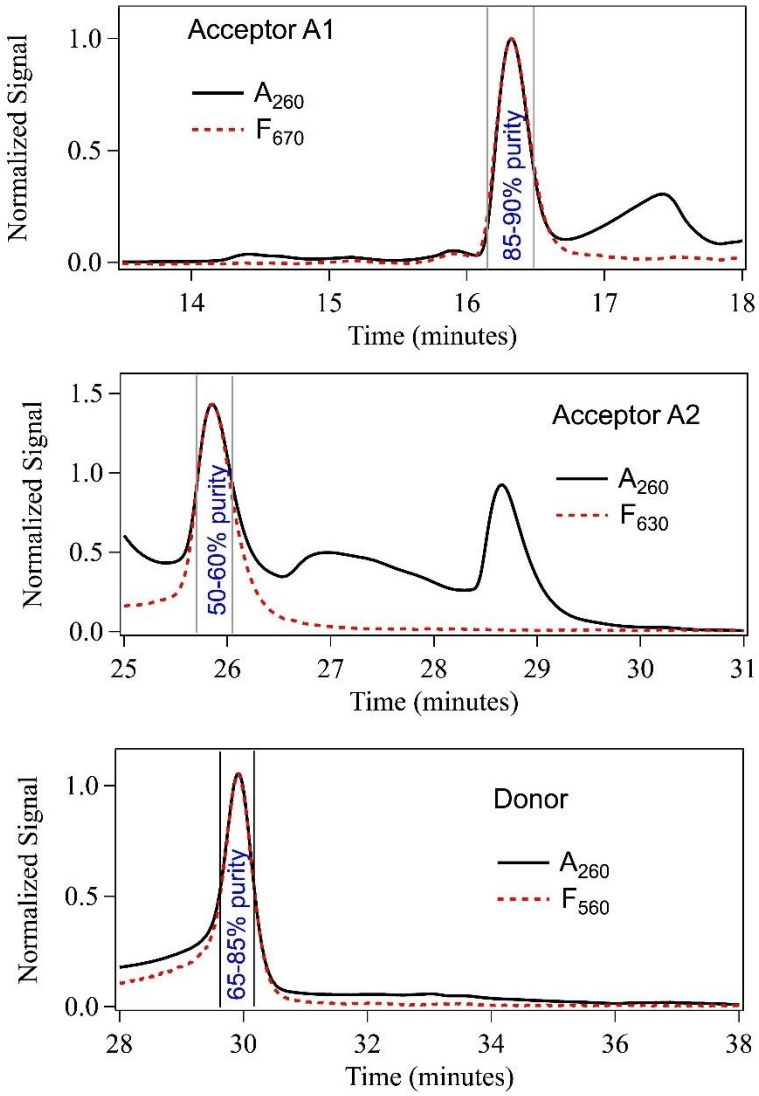

Figure C.2: UV absorbance (260 nm) and visible fluorescence chromatograms of donor and acceptor clusters in their template strands. Gray lines indicate the time window over which aliquots were collected. The estimated purity for each interval is noted within.

During HPLC, we collected purified aliquots only during elution of the fluorescent, DNA-bound clusters, as detected by the fluorescence chromatogram, F_{vis}, measured at the peak emission wavelength of the D, A1 and A2 clusters. To estimate the purity of the collected fluorescent product, we fit the lineshape of the fluorescence (F_{vis}) chromatogram to a Gaussian and then fit the A_{260} chromatogram to a Gaussian with the same lineshape, with an additional

constant offset to account for co-eluting byproducts. The ratio of the F_{vis} contribution to the total A_{260} area over the collection time then gives the fraction, f_{pure}, of the pure fluorescent product in the collected aliquot. We use the ~10% uncertainty in the collection time to estimate the uncertainty in the purity (Figure C.2).

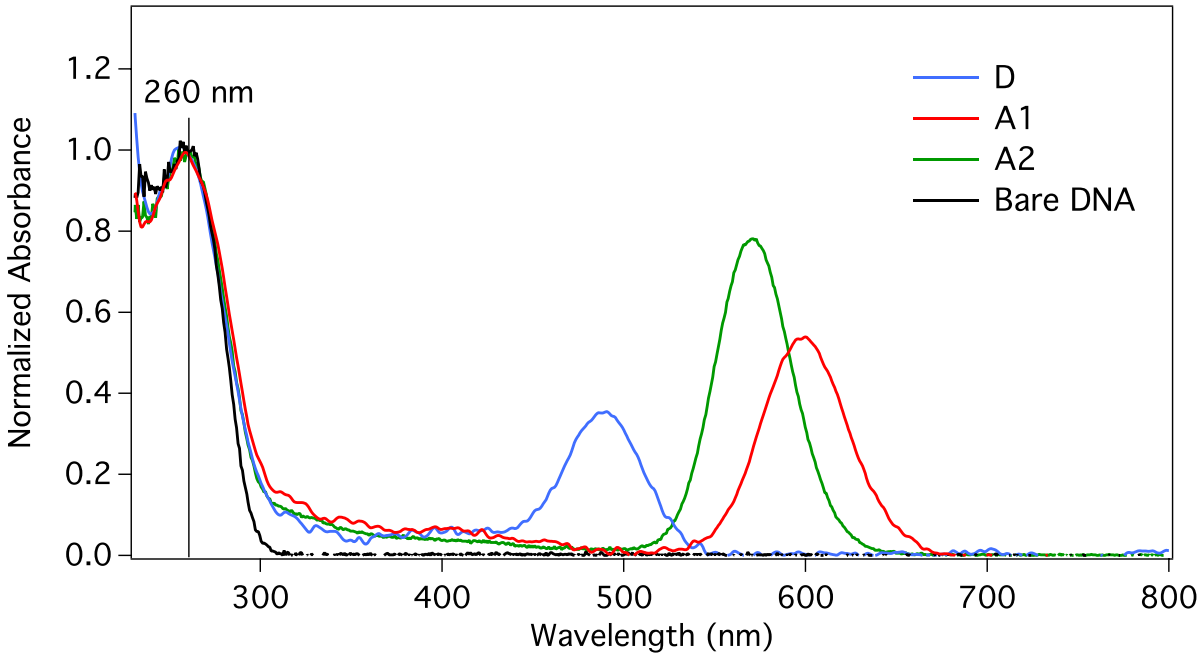

Figure C.3: Absorbance spectra of the purified donor and acceptor clusters together with the bare A2-stabilizing DNA strand. The blue line represents the donor; the green line, A2; the red line, A1 and the black line, bare DNA. All spectra are normalized to absorbance at 260 nm.

Absorbance spectra of the purified, DNA-bound fluorescent clusters and bare DNA have similar shapes near 260 nm (Figure C.3). Thus, the UV transitions of the clusters themselves apparently do not contribute greatly at 260 nm. Assuming that the DNA bases dominate absorbance at 260 nm, we use the known ε_{260} of the DNA to find the visible extinction coefficient, ε_{vis}, of the silver clusters. Specifically, we find the UV absorbance of the pure silver-DNA fluorophore as $A_{pure,260} = f_{pure} * A_{260}$, where A_{260} is the measured 260 nm absorbance of the collected aliquot. The concentration of the pure product is then

$C_{pure} = A_{pure,260}/\varepsilon_{DNA,260}$, and the peak visible extinction coefficient is A_{vis}/ C_{pure}, where A_{vis} is the visible peak absorbance of the purified aliquot.

C.3 Emission spectra with and without hybridization tails

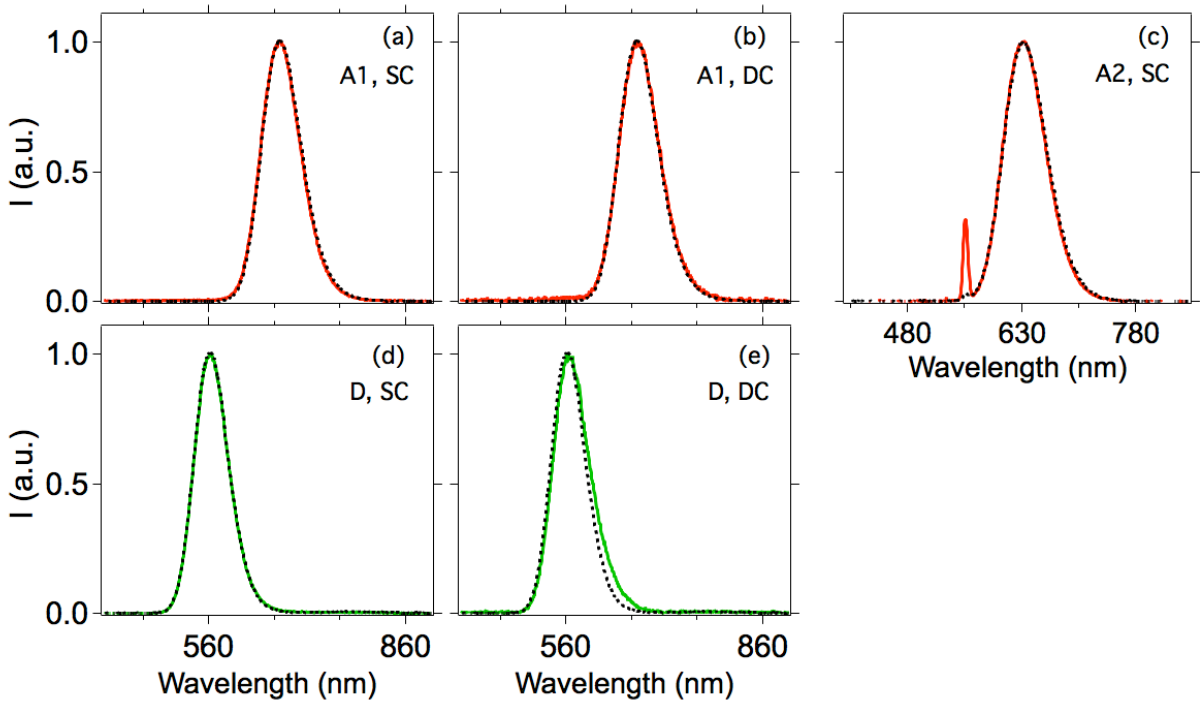

Figure C.4: Comparison of D, A1 and A2 emitters with and without hybridization tails. Black dashed lines represent D, A1 and A2 without tails. **(a,b)** Red traces: A1 with SC and DC tails, respectively. **(c)** Red trace: A2 with SC tail. The sharp peak at 560 nm is scattered excitation light. **(d,e)** Green traces: D with SC and DC tails, respectively. All traces, except those in (c), are taken using a 270 nm LED excitation source.

To ensure that hybridization tails were not altering the optical properties of the FRET pair emitters, we compare emission spectra of D, A1 and A2 emitters with and without tails. Figure C.4 shows that the addition of AT-rich tails do not produce significant changes in peak emission or spectral shape of the emitters.

C.4 UV melting curves

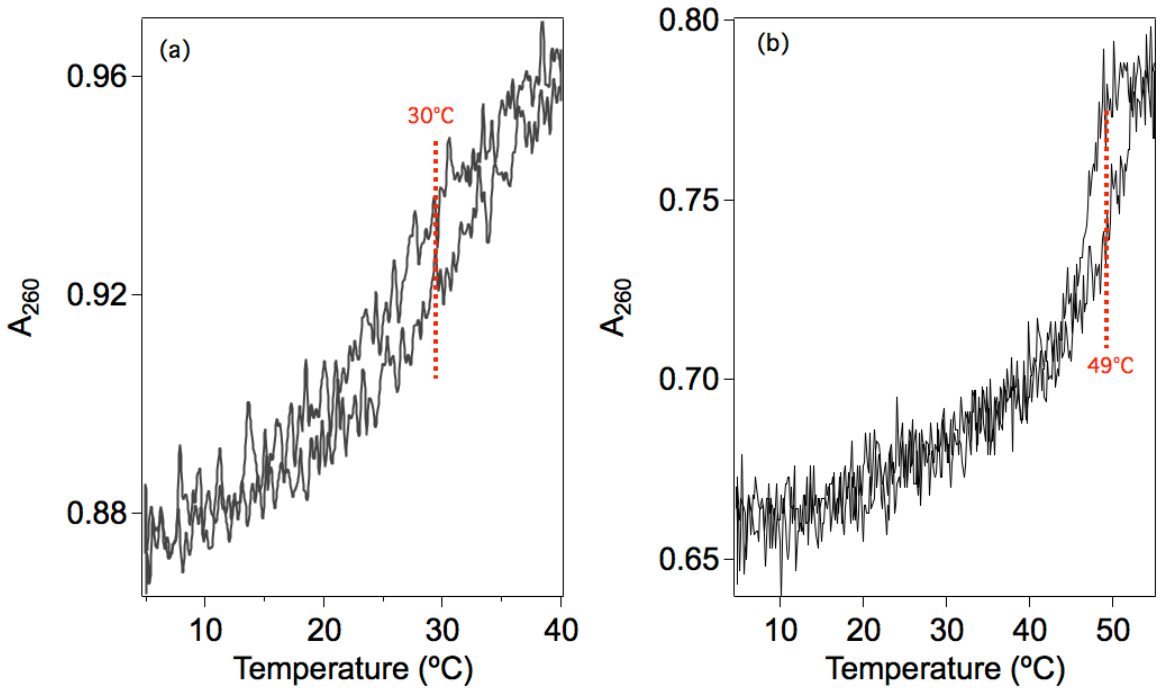

Figure C.5: Melting curves for the D-A1 **(a)** double clamp and **(b)** single clamp assemblies.

Figure C.5 shows the melting curves for the D-A1 (a) double clamp and (b) single clamp assemblies. Absorbance at 260 nm was monitored as a function of temperature, which was ramped at a rate of 2°C/min. This ramp rate was equivalent to the one used for monitoring FRET signal as temperature was thermally modulated (Figure 4.5). Vertical lines mark the approximate melting temperatures of the hybridized tails.

C.5 Emission spectra before and after centrifugal filtration

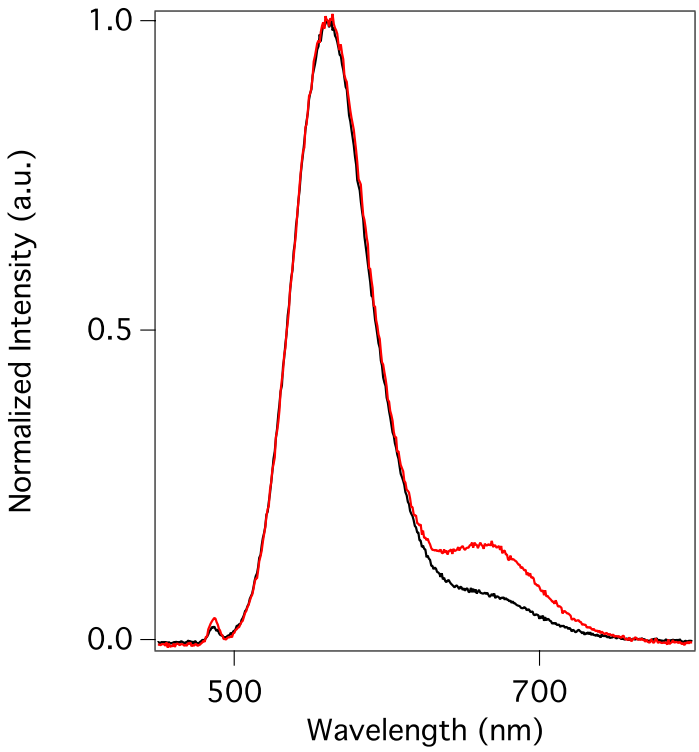

Figure C.6: Fluorescence spectra of D-A1 SC FRET pair solutions before (black) and after (red) centrifugal filtration. Excitation wavelength was 490 nm, at the donor absorbance peak.

Figure C.6 demonstrates the efficacy of centrifugal filtration for separating FRET pairs from excess donor monomers. Fluorescence is excited at the donor absorbance peak, 490 nm, and normalized by the donor emission peak intensity.

Samples were spun at 11,000 rpm using 30 kDa centrifugal filters (Millipore). Excess buffer was added following each spin such that the final concentration was at least 50 mM NH_4OAc, to maintain Watson-Crick pairing of the hybridization tails. Unhybridized donors present in the unfiltered pair solution (black curve) emit in the donor ("green") color channel but do not participate in FRET, generating no "red" photons from acceptors. Thus the presence of unhybridized donors reduces red acceptor emission relative to green donor emission. As shown, the ratio of acceptor to donor emission is significantly enhanced following 3 rounds of

spin filtration (red curve). Apparently unhybridized donors, present before spin filtration (black curve), were removed.

C.6 Absorbance spectra of D-A1 SC monomers and spin-filtered pair

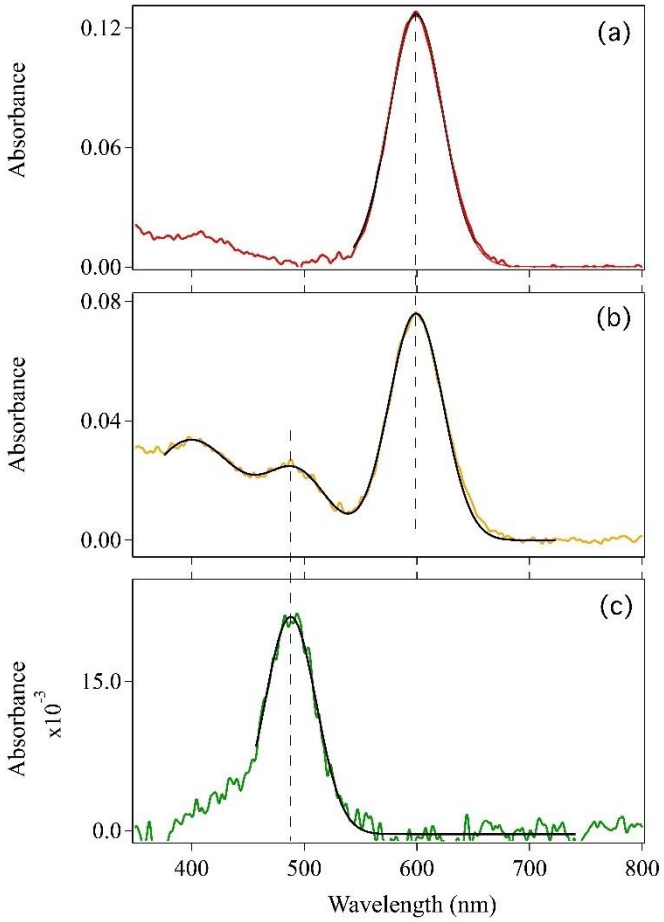

Figure C.7: Absorbance spectra of the single-clamp (SC) acceptor, A1 **(a)**, the D-A1 SC pair **(b)**, and the SC donor D **(c)**, used to normalize the emission spectra in Figure 4.4 and to estimate E_{FRET}. Black traces represent Gaussian fits to the data. Black dashed lines indicate the peak absorbance wavelengths of the donor and acceptor. Absorbance at shorter wavelengths arises from residual non-fluorescent products associated with the hybridization tails.

The emission spectra in Figure 4.4 were first normalized to the intensity of the Xe arc lamp used for excitation. Emission spectra of the donor and acceptor monomers were then normalized to their respective ***visible*** absorbance maxima in the solution of hybridized pairs, which were determined from Gaussian fits to the data (black traces, Figure C.7). In Eq. 4.3 for

E_{FRET}, we correct for concentration differences using $I_D = I_{D,measured}*(A_{490,Pair}/A_{490,D})$, where $I_{D,measured}$ is the emission intensity from the D solution. Normalizing to A_{490} ensures that the *relative* concentrations of D in the monomer SC solution, and in the D-A1 pair solution, are accurately determined. (It is only the relative concentrations that affect E_{FRET}). Lastly, each spectrum was normalized again, such that the integrated emission intensity of the donor alone was unity.

C.7 FRET data for the D-A1 DC pair

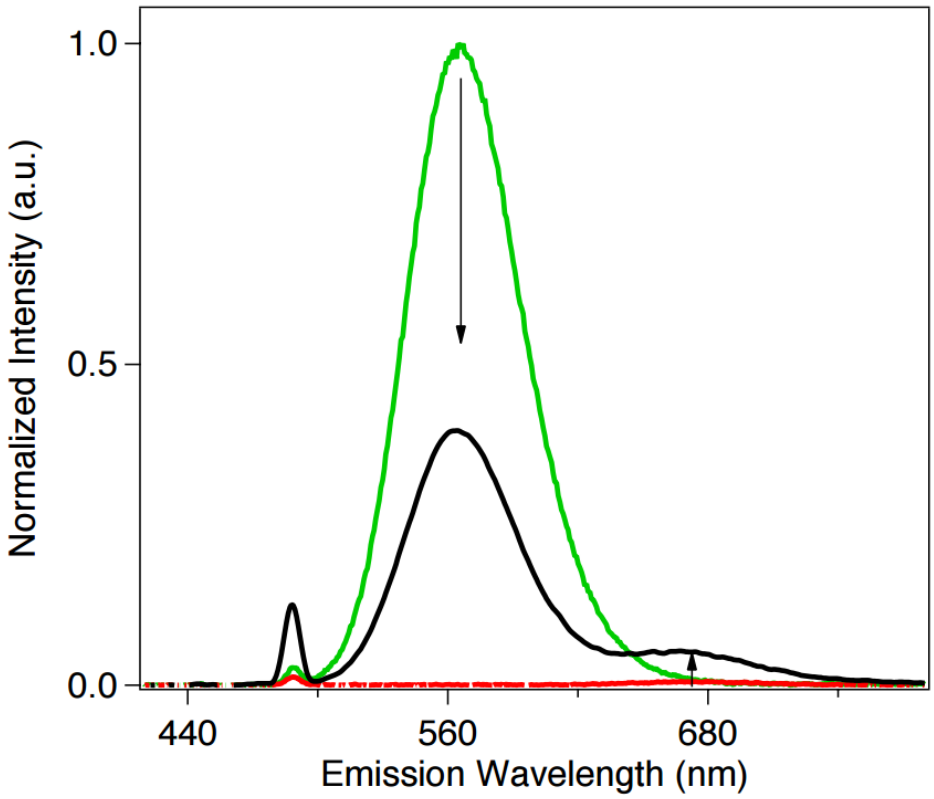

Figure C.8: Data for 490 nm excitation of the D-A1 double clamp (DC) assembly. Black Line: Emission from the D-A1 pair. Green line: Emission from D alone. Red line: Emission from A1 alone. The peak at 490 nm is scattered excitation light.

Normalized emission spectra of the D-A1 double clamp (DC) pair together with monomer components demonstrates the same signatures of FRET seen in the D-A1 (SC) pair. Green emission intensity drops while, simultaneously, emission from A1 rises dramatically. The efficiency estimated for the D-A1 (DC) pair was calculated using, $E_{FRET} = 1\text{-}I_{DA}/I_D$, where I_{DA} is the intensity from the pair and I_D is intensity from donor alone, yielding $E_{FRET} = 0.6$.

C.8 FRET data for the D-A2 SC pair

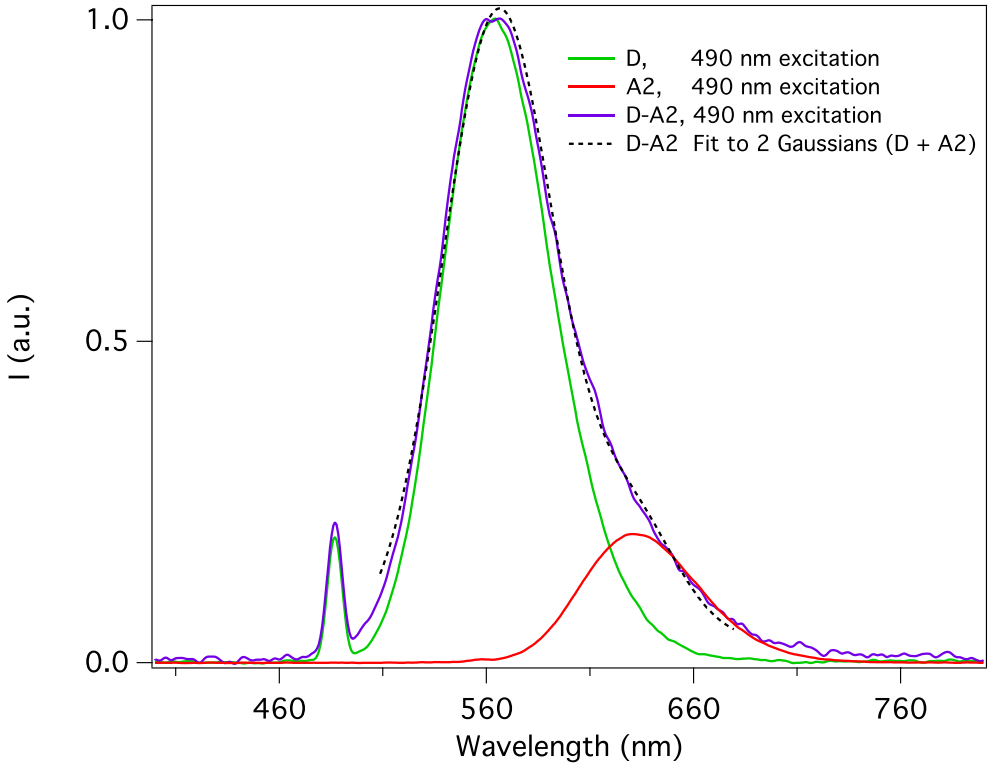

Figure C.9: Data for the D-A2 single clamp (SC) pair. Green Trace: Emission from D alone, using 490 nm excitation. Red Trace: Emission from A2 alone, using 560 nm excitation. Purple trace: Emission for the D-A2 pair, using 490 nm excitation. Black dashed trace: Fit to the sum of 2 Gaussians (D + A2), using parameters determined from separate fits to D and A2.

Figure C.9 shows emission data for the D-A2 single clamp (SC) pair (purple trace). Although a distinct red peak is not observed from the pair, D-A2 emission is significantly broadened to longer wavelengths. The sum of 2 Gaussians (black dashed trace), whose

parameters were determined from separate fits of D and A2, fits well over the D-A2 spectrum. We thus conclude that donor excitation is producing red emission from the A2 cluster in the D-A2 pair due to FRET.

C.9 Raw fluorescence data for thermally modulated D-A1 DC pair

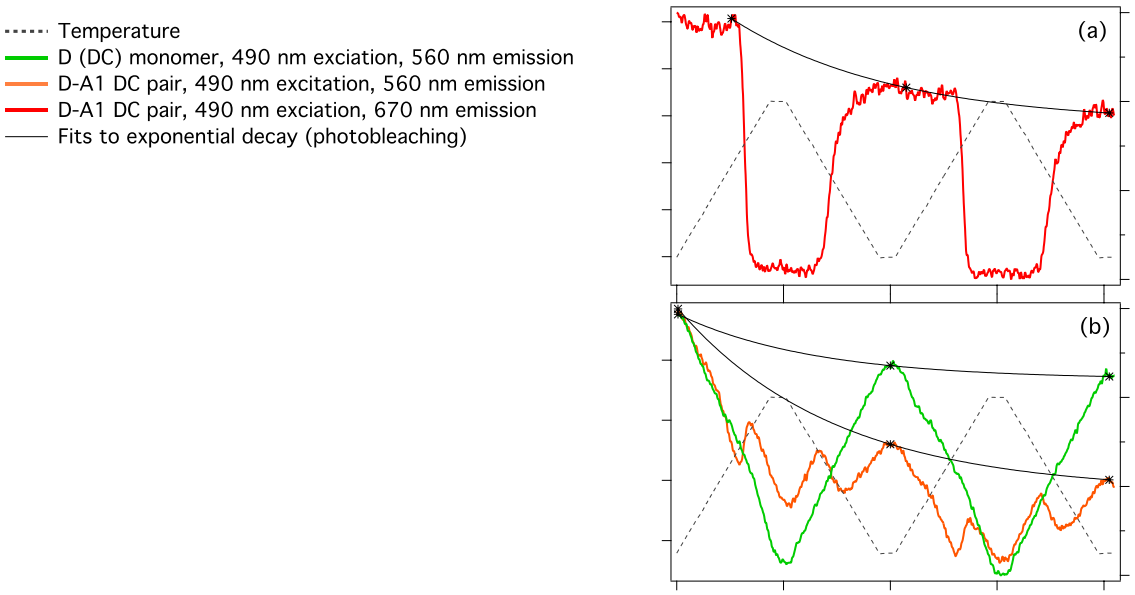

Figure C.10: Raw data for the fluorescence signals from the acceptor A1 **(a)** and donor D **(b**, orange**)** in the spin-filtered D-A1 pair, and fluorescence signal from D alone **(b**, green**)**. Excitation was at the peak absorbance of D, 490 nm, and the temperature was cycled twice from 5 to 40°C over 80 minutes. Acceptor emission (a) is monitored at 670 nm and donor emission (b) at 560 nm. The combination of heating and long light exposure resulted in some decay of donor emission and of FRET-induced acceptor emission.

Figure C.10 shows fluorescence intensity during thermal cycling for the spin-filtered D-A1 pair, *without* normalization for i) photobleaching over time and ii) temperature (T)-dependent emission from the donor. Steps in brightness in Figure C.10 occur where T crosses T_M, the melting T of the pair assembly. The orange trace in Figure C.10b is the *donor* emission (560 nm) from D-A1 and also shows abrupt steps as T crosses T_M, shutting off (heating) or turning on (cooling) the FRET-quenching of D emission. The triangular shape of the orange curve at intermediate temperatures arises from the temperature dependence of emission from

the D cluster alone. This is shown by the green trace (Figure C.10b), which shows the emission from the donor *monomer*, under the same thermal cycling.

In Figure 4.5, effects of photobleaching were removed by dividing by a fitted exponential time-dependence (black curves, Figure C.10). We also normalize for the T-dependence of the D monomer in a similary way for the D-A pair curve in Figure 4.5b.

C.10 Intensity normalization for D-A1 SC thermal data

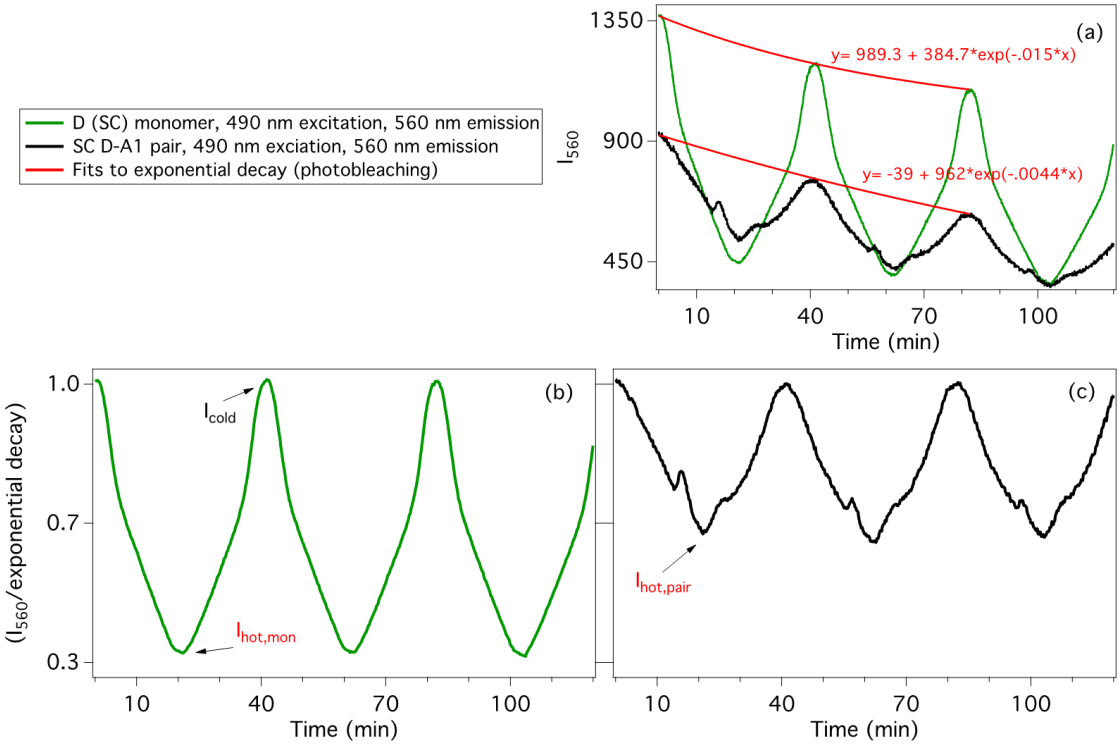

Figure C.11: (a) Raw data for the fluorescence signals from the SC donor monomer (green) and D-A1 pair (black) solutions. Excitation was at D peak absorbance, 490 nm, and the temperature was cycled three times from 20 to 55°C over 120 minutes. Red lines represent the exponential functions describing the intensity decay (photobleaching) over time. Each intensity curve was normalized to its respective decay **(b,c)**. The intensities at temperatures above T_m, indicated with arrows as I_{hot} for the donor alone **(b)** and donor in the pair solution **(c)** were used to normalize the relative concentrations of D for estimates of E_{FRET}.

Well above the melting temperature, T_M, all D and A pair components exist as monomers, and there is no FRET quenching of emission for hybridized pairs. Thus, for equal

concentrations of D (C_D), the intensity at 560 nm for the *pair* solution should equal the intensity at 560 nm for D alone, *i.e.* $I_{hot,pair} = I_{hot,mon}$ for $C_{D,pair} = C_{D,mon}$. To normalize the relative concentration of D_{pair} to $D_{monomer}$ for estimates of E_{FRET}, the 560 nm emission intensity measured for the pair was multiplied by the correction factor, $I_{hot,mon}/I_{hot,pair}$. Estimates obtained this way agreed well with the correction factor determined directly from the visible absorbance (Figure C.8).

C.11 Experiments with impure cluster solutions

To simplify synthesis procedures, we attempted to form D-A1 FRET pairs using unpurified emitters. For "one-pot" syntheses of DC, SC, and EE configurations, DNA oligomers stabilizing clusters D and A1, with complementary A-T rich tails, were annealed by heating to 95°C for 3 minutes and then slowly cooling the mixture to room temperature overnight. Cluster synthesis was performed on annealed DNA using several $AgNO_3$ and $NaBH_4$ concentrations. Absorbance and fluorescence emission were measured one day after synthesis. For "two-pot" syntheses, D and A1 were synthesized separately and then mixed 1 day after synthesis, without a purification step. Because D does not retain fluorescence when heated above ~50°C, the "two-pot" D-A1 solutions were not annealed. We measured absorbance and fluorescence one day and, in the case of EE and SC configurations, two days after mixing. Mixtures were left at room temperature between measurements on day 1 and day 2 to promote D-A1 binding.

We ran 10% native PAGE gels to compare D-A1 with their respective monomer components for both one-pot and two-pot synthesis methods. All DNA in the gel was made visible using SYBR Gold stain. Figure C.12 shows the relative shifts of products formed on

the D (lane 1) and A1 (lane 2) monomers compared to one-pot synthesis (lane 3) and two-pot synthesis (lane 4) of the SC (Figure C.12a) and DC (Figure C.12d) assembly. The presence of lower mobility bands indicates that hybridization occurred. Bands are less well-resolved than for the purified case (Figure 4.3) due to the presence of products other than D and A1 in the unpurified solutions, particularly in the case of the one-pot synthesis method, and additional products from synthesis are also visible in the gels. The two-pot method appears to produce a less heterogeneous range of products than the one-pot method.

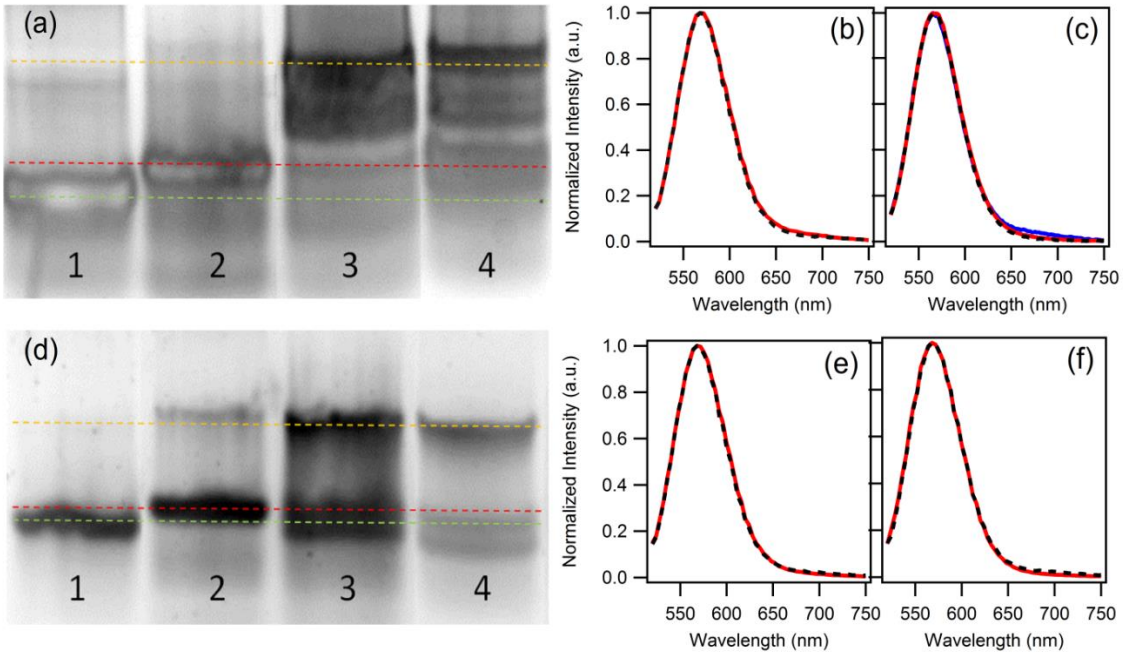

Figure C.12: One- and two-pot attempts to form D-A1 assemblies in the DC configuration.
a) Gel image for one- and two-pot attempts to form D-A1 in the SC configuration. Lanes 1 and 2 contain products formed on the individual strands stabilizing D (green) and A1 (red) clusters, respectively. Green and red lines mark monomer products corresponding to the desired D and A clusters and other silver-DNA products formed on these strands. Lane 3 contains one-pot synthesized D-A1, and lane 4 contains two-pot synthesized D-A1. Duplex DNA formation is evident in both lanes 3 and 4 (yellow dashed line). **b)** One-pot normalized emission spectra of EE (dashed black) and SC (red) configurations, excited at 490 nm. No FRET signal is apparent for the SC as compared to the EE configuration. **c)** Two-pot normalized emission spectra of EE (dashed black) and SC, excited at 490 nm. No FRET signal is evident for D-A1 in the SC configuration 1 day after mixing (red). When the mixture was then left at room temperature for 24 hours, a small enhancement of A1 excited at 490 nm is present (blue), but the small chemical yield of D-A1 structures results in a much smaller FRET signal than in the case of purified clusters (Figure 4.4). **d)** Gel image for one- and two-pot attempts to form D-A1 in the DC configuration. Lanes 1-4 are analogous to (a). **e)** One-pot and **f)** two-pot normalized emission spectra of EE (dashed black) and DC (red) configurations, excited at 490 nm. FRET signal is also not detectable for the DC configuration.

We compared spectra of SC and DC to EE configurations, excited at 490 nm, to search for evidence of FRET. As discussed in the text, the EE configuration holds clusters apart at a distance of about twice the Förster radius, R_0, so FRET efficiency of the D-A1 EE configuration is expected to be quite small. SC and DC configurations, however, bring clusters within R_0, making FRET much more efficient. Thus, relative shape differences between emission spectra from SC/DC and from EE are good metrics to investigate chemical yield of D-A1 FRET pairs. Figures C.12b and C.12e show spectra for one-pot synthesis of D-A1 for SC and DC, respectively. Normalized spectra for EE (dashed black) and SC/DC (red) are quite similar, suggesting that one-pot synthesis does not form D-A1 FRET pairs in high enough chemical yields to produce measureable FRET signal for SC/DC configurations. These spectra, combined with the poorly resolved bands in lane 3 of the gel (Figure C.12a and d), show that a one-pot method is not a successful way to form D-A1 FRET pairs. The two-pot method produced a similarly low chemical yield of FRET pairs: EE (dashed black) and SC/DC (red) spectra are similar in shape. In the case of SC, when the mixture of D and A1 was allowed to sit at room temperature for an additional 24 hours, as opposed to keeping the mixture at 4°C, a small enhancement of A1 emission became visible when D was excited at 490 nm (blue). This enhancement is still quite small as compared to the enhancement observed for purified materials (Figure 4.4). Thus, unless strands can be selected that form desired clusters as the major synthesis product, use of purified silver cluster materials is crucial for assembly of multi-emitter structures.

Appendix D. Supporting Information for Chapter 5

D.1 DNA sequences

Name	Sequence (5' – 3')
U1	GGCGATTAGG-ACGCTAAGCCA-CCTTTAGATCC-TGTATCTGGT
U2	GGATCTAAAGG-ACCAGATACA-CCACTCTTCC-TGACATCTTGT
U3	GGAAGAGTGG-ACAAGATGTCA-CCGTGAGAACC-TGCAATGCGT
U4	GGTTCTCACGG-ACGCATTGCA-CCGCACGACC-TGTTCGACAGT
U5	GGTCGTGCGG-ACTGTCGAACA-CCAACGATGCC-TGATAGAAGT
U6	GGCATCGTTGG-ACTTCTATCA-ATGCACCTCC-AGCTTTGAATG
U7	GGAGGTGCAT-CATTCAAAGCT-AACGGTAACTA-TGACTTGGGA
U8	TAGTTACCGTT-TCCCAAGTCA-AACACTAGAC-ACATGCTCCTA
U9	GTCTAGTGTT-TAGGAGCATGT-CGAGACTACAC-CCTTGCCACC
T10	GTGTAGTCTCG-GGTGGCAAGG-CCTAATCGCC-TGGCTTAGCGT
U6-docker	GGCATCGTTGG-ACTTCTATCA-ATGCACCTCC-AGCTTTGAATG-TTTT-ATTTATACAACGGA
U9-docker	GTCTAGTGTT-TAGGAGCATGT-CGAGACTACAC-CCTTGCCACC-TTTT-ATTAACACAAGACA
Ag_{14}-DNA host, U9	TTCCCACCCACCCCGGCCCGTT-TTTT- TGTCTTGTGT
Ag_{15}-DNA host, U6	CACCGCTTTTGCCTTTTGGGGACGGATA-TTTT-TCCGTTGTATAAAT

Table D.1: Sequences of DNA oligomers. 10-helix DNA nanotube (NT) construction oligomers (U1 – U9, T10),[26] modified NT oligomers with docking sites (U6-docker, U9-docker), and Ag_N-DNA host strands (template – TTTT – linker).

D.2 Attachment of Cy5 to NT via AT-rich tail

As described in Section 4.3.2, AT-rich tails can prove unsuitable to use for attachment of decorating elements to DNA nanotubes (NT) due to the limited sequence space, which challenges choice of sequences without self-complementary. Here, a 30-base A,T tail developed elsewhere[65] was appended to the 3' end of U6, and its complement was labeled with Cy5 dye. Attachment of this Cy5-labeled oligomer to FAM-labeled nanotubes annealed with

the modified U6 strand was only observable for a select few images – the image below is *not* a representative image but is a "*best case*" image showing colocalization of DNA nanotubes (green) with incomplete Cy5 labeling on a fraction of the nanotubes. Due to the AT-rich tail's high degree of self-complementarity, the strands often aggregate instead of labeling the nanotubes, and the nanotubes themselves also aggregate.

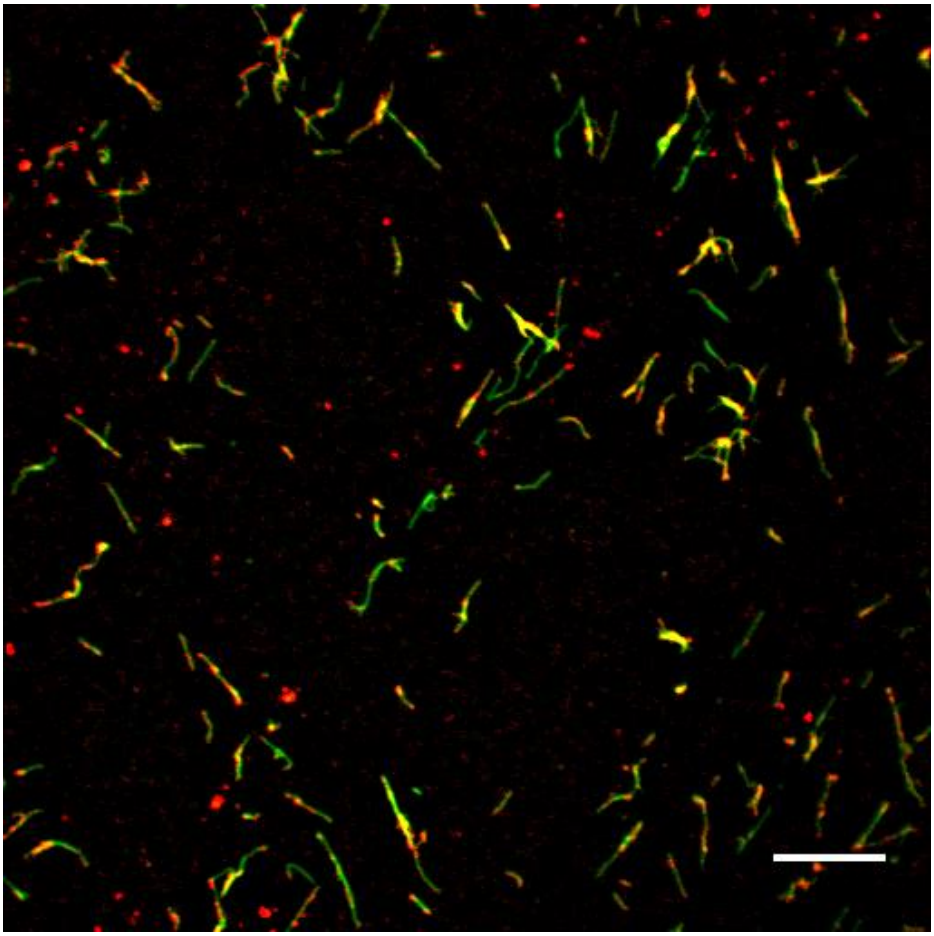

Figure D.1: Confocal images of fluorescein (FAM) labeled NT with 100% U6 AT-rich docking sites, decorated with Cy5-labeled AT-rich complements after tube formation. Samples are in aqueous buffer on clean glass coverslips. Scale bar is 10 μm. Overlap of red (Cy5) and green (FAM) channels shows some colocalization, indicating that a fraction of the Cy-AT oligomers dock onto the nanotubes, while large red aggregates also form due to self-complementarity of the AT-rich tail.

D.3 Ag_{15}-DNA host strand selection

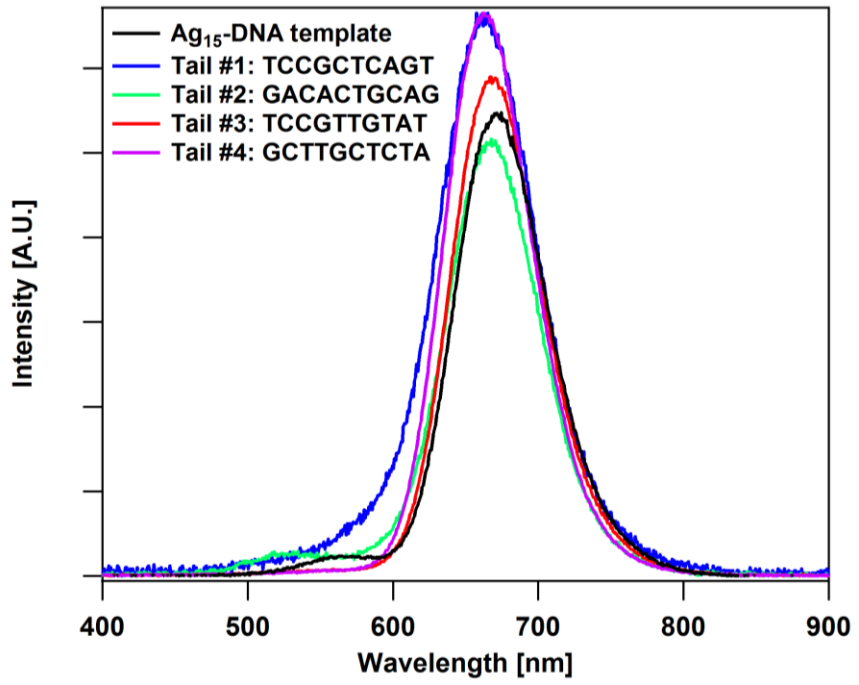

Figure D.2: UV-excited fluorescence spectra of unpurified Ag_N-DNA stabilized by the template strand for Ag_{15}-DNA (black) and with appended candidate linker regions at the 3' end of that template (blue, green, red, magenta). All syntheses were performed with 15.0 μM DNA, 188 μM AgNO3, 93.8 μM NaBH4, and 10 mM NH4OAc (corresponding to 12.5 Ag atoms per host strand; Ag/base ratios vary with host strand length). Spectra are normalized to the absorbance peak corresponding to the dominant fluorescent product (~ 600 nm peak absorbance). Tail #3 was selected for a linker region because spectra of Ag_N-DNA stabilized by this template most closely resemble those stabilized by the Ag_{15}-DNA template alone, indicating highest yield of the desired cluster product. Subsequent purification isolates the Ag_{15}-DNA.

D.4 Ag_{14}-DNA host strand selection

Host strands for Ag_{14}-DNA were selected using the same methods described for Ag_{15}-DNA in Section 4.3.2. The Ag_{14}-DNA used here has peak fluorescence excitation and emission at ~ 570 nm and ~ 637 nm, respectively, and a 93% quantum yield. Its size and quantum yield were previously determined elsewhere.[53] This silver cluster is templated by the DNA oligomer TCCCACCCACCCCGGCCCGTT. To discover appropriate sequences for linking regions appended to the 3' end of this sequence, 6 candidate 10-base sequences previously found to be unfavorable for formation of fluorescent silver clusters[58,70] were appended to the 3' end of

Ag_{14}-DNA's template sequence, separated by 4 thymines. Candidate host strands thus had the sequence: TCCCACCCACCCCGGCCCGTT-TTTT-'10 base oligomer'.

Emission spectra of Ag_N-DNA products formed on these candidate host strands were compared to the spectrum of Ag_{14}-DNA (Figure D.3). The similarity of the spectra in Figure D.3 strongly suggest that Ag_N-DNA formed by the modified host strands also contain N = 14 Ag atoms. Tail #5 was selected for HPLC purification because Ag_N-DNA stabilized by this template closely resemble those stabilized by the Ag_{14}-DNA template alone and because its complement has low complementarity with the oligomers composing the NT. The complement of Tail #5 was appended to the 3' end of the U9 oligomer.

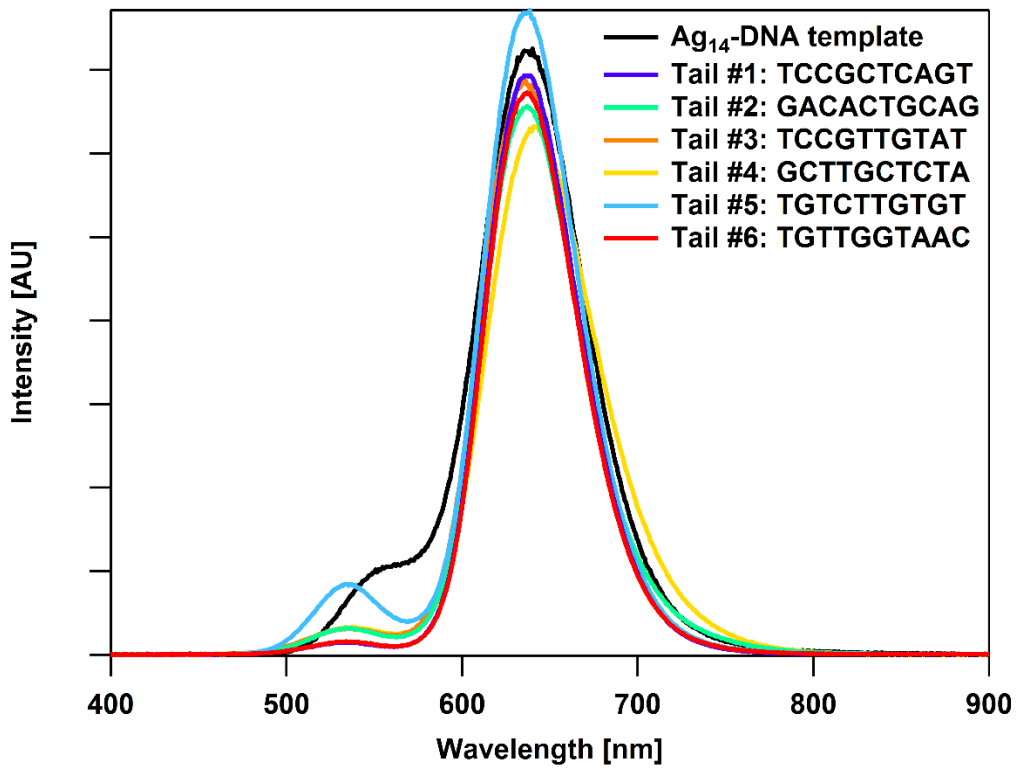

Figure D.3: UV-excited fluorescence spectra of unpurified Ag_N-DNA stabilized by the template strand for Ag_{14}-DNA (black) and with appended candidate linker regions at the 3' end of that template. All syntheses were performed with 15.0 µM DNA, 188 µM AgNO3, 93.8 µM NaBH4, and 10 mM NH4OAc (corresponding to 12.5 Ag atoms per host strand; Ag/base ratios vary with host strand length). Spectra are normalized to the absorbance peak corresponding to the dominant fluorescent product (~ 570 nm peak absorbance).

D.5 Chromatograms and mass spectra

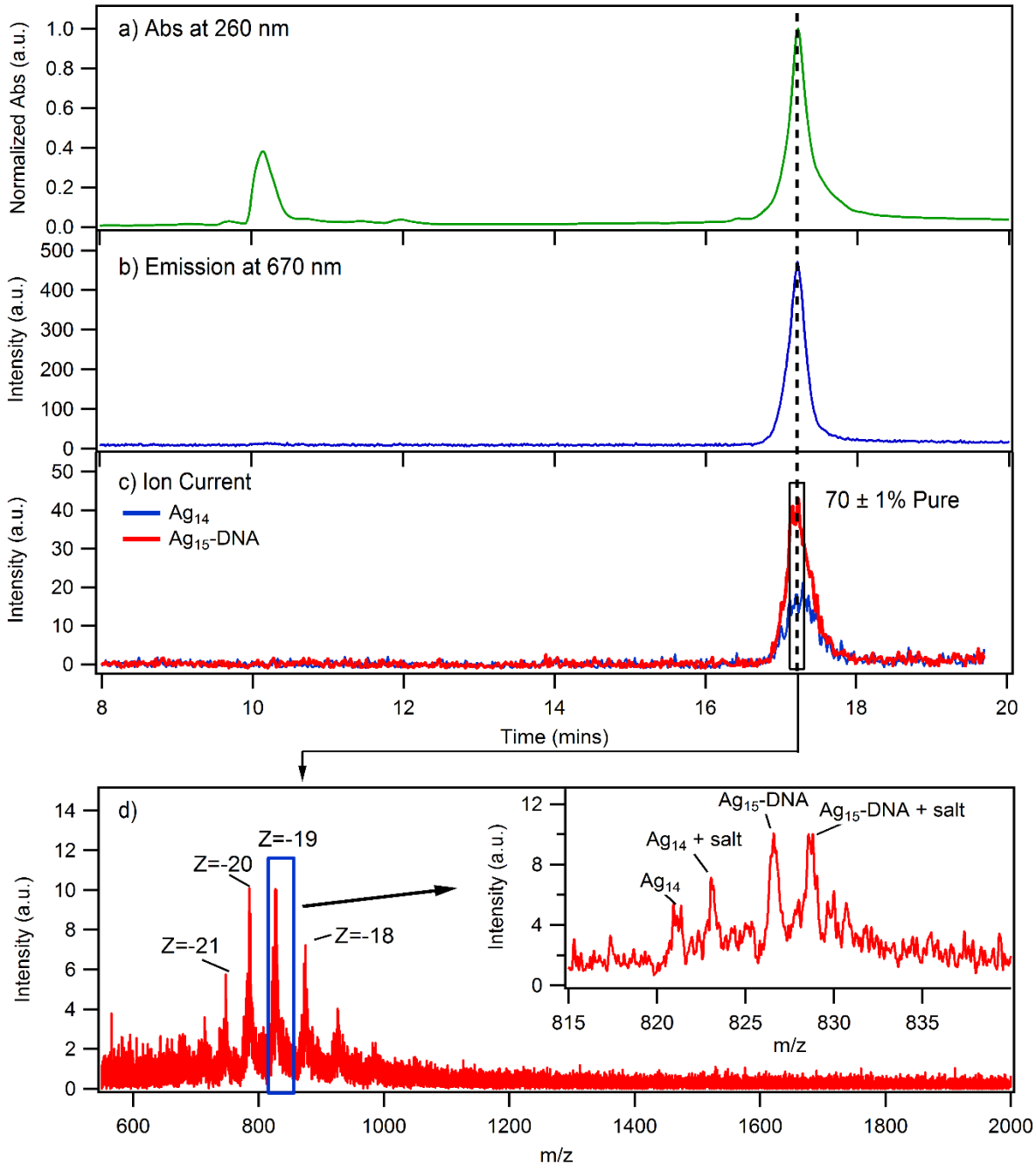

Figure D.4: Second round HFIP purification chromatograms of Ag_{15}-DNA for a) absorbance at 260 nm, b) emission at 670 nm, the peak fluorescemce wavelength of the Ag_{15}-DNA in the running buffer; and c) the ion current of the major species in the elution window over which the sample for nanotube attachment was caught (black, boxed area). The 70 ± 1% purity estimate is based on the integrated ion current of Ag_{15}-DNA relative to all other silver species attached to DNA present in the catch window. The same window was used to compile the mass spectrum in (d), showing a range of major charge states (Z = -18 to -21) with the inset representing the blue, boxed area of the mass spectrum which displays all prominent species present at one charge state (Z = -19).

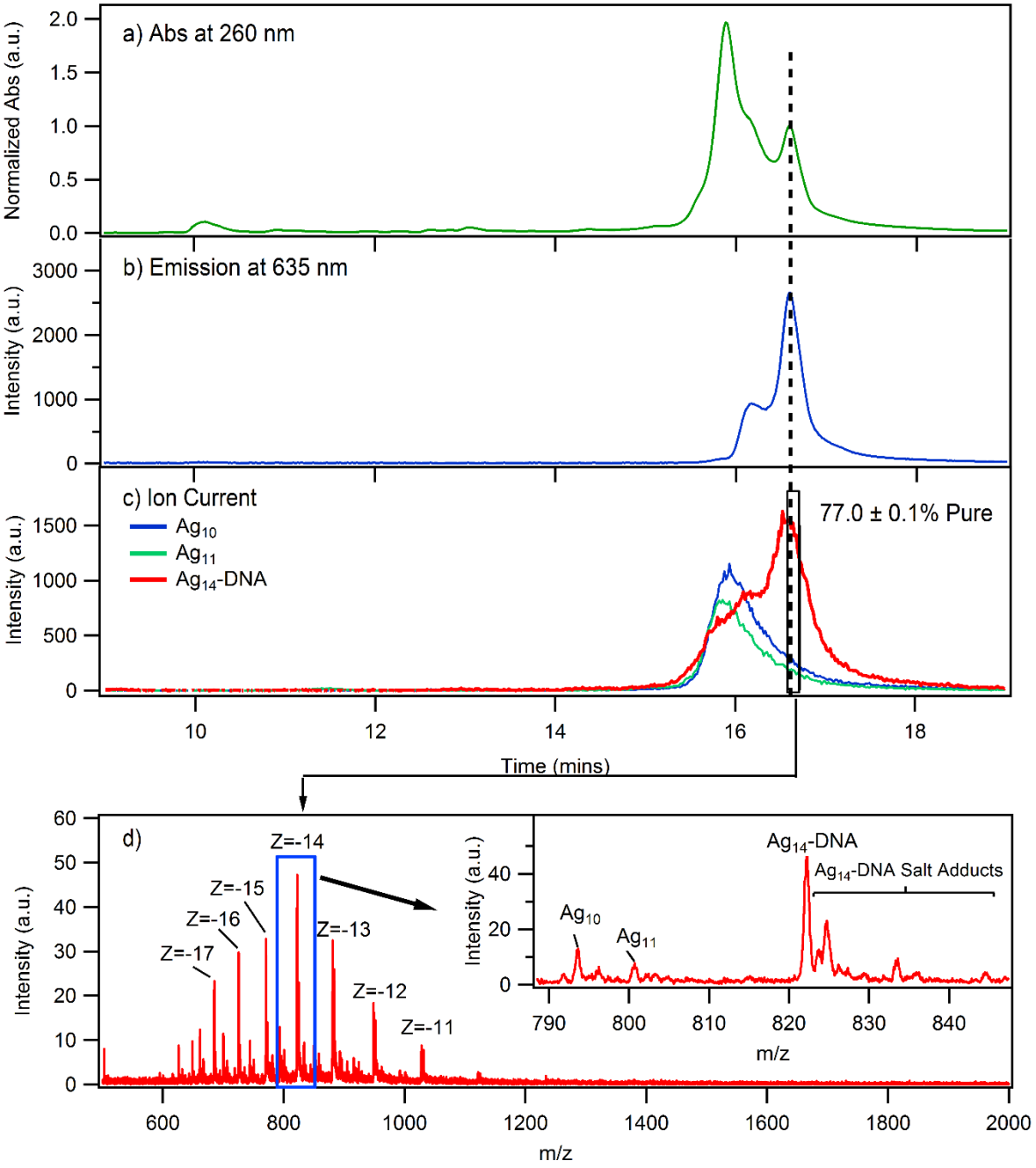

Figure D.5: Second round HFIP purification chromatograms of Ag_{14}-DNA for a) absorbance at 260 nm, b) emission at Ag_{14}-DNA's fluorescence peak wavelength in running buffer, 635 nm; and c) the ion current of the major species in the window that the sample was caught (black, boxed area) for nanotube attachment. The 77.0 ± 0.1% purity estimate is based on the integrated ion current of Ag_{14}-DNA relative to all other silver species attached to DNA present in the catch window. The same window was used to compile the mass spectrum in (d), showing a range of major charge states (Z = -11 to -17) with the inset representing the blue, boxed area of the mass spectrum which displays all prominent species present at one charge state (Z = -14).

D.6 Microscopy of NT with docker sites

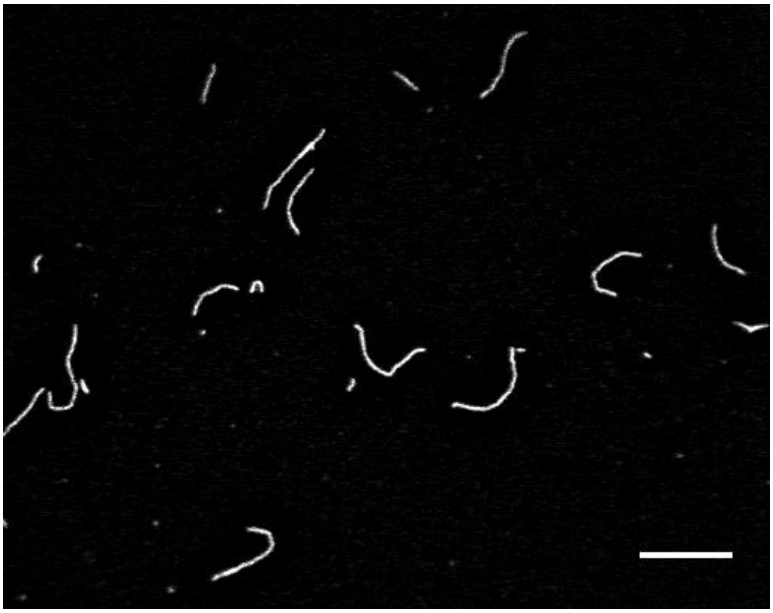

Figure D.6: Spinning disc confocal image of fluorescein-labeled 10-helix DNA nanotubes[26] (NT) in a polyvinyl alcohol (PVA) film. Proper nanotube formation with an appended 14-base docker site on the 3' end of the 100% of the U6 NT oligomers is evident in this representative image. Scale bar: 10 μm.

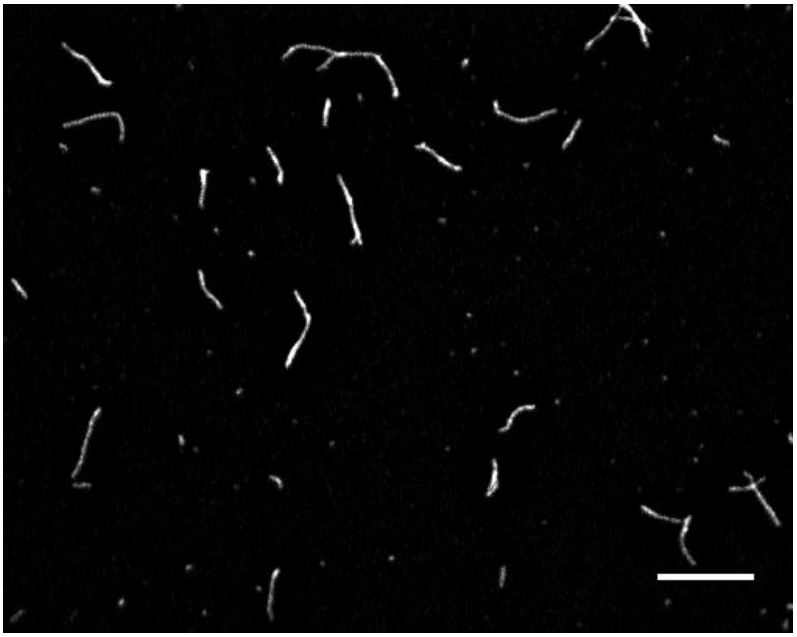

Figure D.7: Spinning disc confocal image of fluorescein-labeled 10-helix DNA nanotubes[26] (NT) in a polyvinyl alcohol (PVA) film. Proper nanotube formation with an appended 14-base docker site on the 3' end of the 100% of the U9 NT oligomers is evident in this representative image, albeit with more defects visible than for NT with different docking sites appended to the U6 oligomers (Figure D.6). Scale bar: 10 μm.

D.7 NT contour intensity mapping and simulations

DNA nanotube (NT) contours were traced using a MATLAB script from the Paul Wiggins group at the University of Washington,[176] with 2 pixel step size between points along a single NT trace. The EMCCD camera used here for microscopy has a pixel size of 0.16 μm. To investigate intensity fluctuations along NT, the extracted NT contours are imported into a custom MATLAB script that calculates the peak intensity at each point along the NT contour, using 10-pixel cross-sections perpendicular to a NT contour trace and averaging intensity over a 5-pixel window centered on the NT. Local background correction is achieved by subtracting the average intensity of the ends of the cross-sections, which extend far from the NT contour (Figure D.6). Then, the standard deviation of the intensity along the NT contour is calculated for each NT, normalized to the average intensity of all points along the NT contour, as a quantitative measure of intensity fluctuations along NT that is invariant to variations in intensity among different NT. The average of this standard deviation over the population of all tubes is called *M*.

While *M* allows relative comparison of intensity fluctuations between different species of NT, it is necessary to perform simulations of NT with certain labeling percentages and emitter dipole orientations in order to understand what values of *M* might be expected for various labeling scenarios. Using MATLAB, we simulated microscope images of NT with decorating emitters randomly arranged on docking sites with 7.1 nm spacing, using the specifics of the microscope objective and camera used for microscopy, described in Section 5.2.4, for various % labeling. For each point in Figure D.9, the average value and standard deviation of *M* was calculated from 100 such simulated NT. In the case of emitters with no dipolar dependence (yellow), that is, all emitters couple equally to the microscope objective, $M = 0$ for NT with

100% of docking sites labeled, as would be expected for ~32 emitters within the point spread function of the objective. Even for emitters with randomly assigned fixed dipoles with respect to the microscope objective (blue), M = 0.08 for NT with 100% labeling.

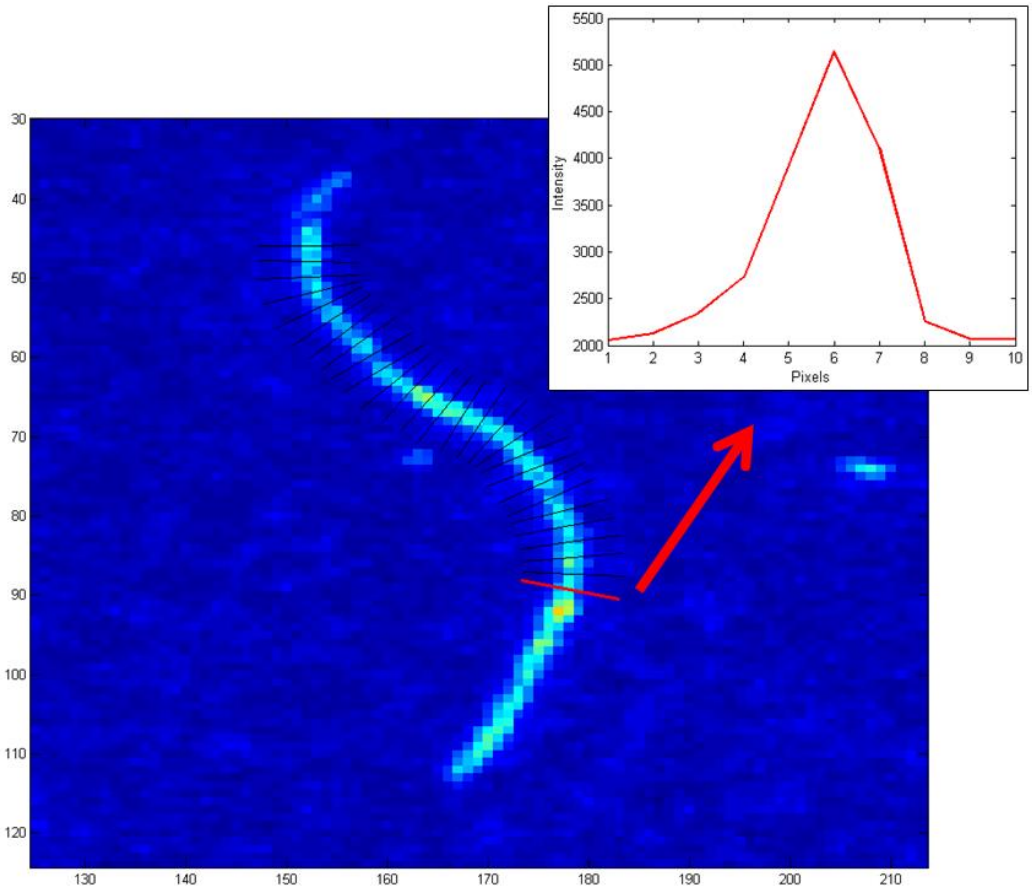

Figure D.8: Example image of cross-sections on an Ag_{15}-DNA-labeled NT, with 100% U6 docking sites, as produced by the custom MATLAB script. The intensity profile of the red cross-section is plotted in the upper right. Local background correction is achieved by subtracting the average of the endpoints of this intensity profile, and the average intensity of the NT at this point along the NT contour is calculated by taking the 5-pixel-wide average of the intensity, centered at the maximum intensity of the intensity profile.

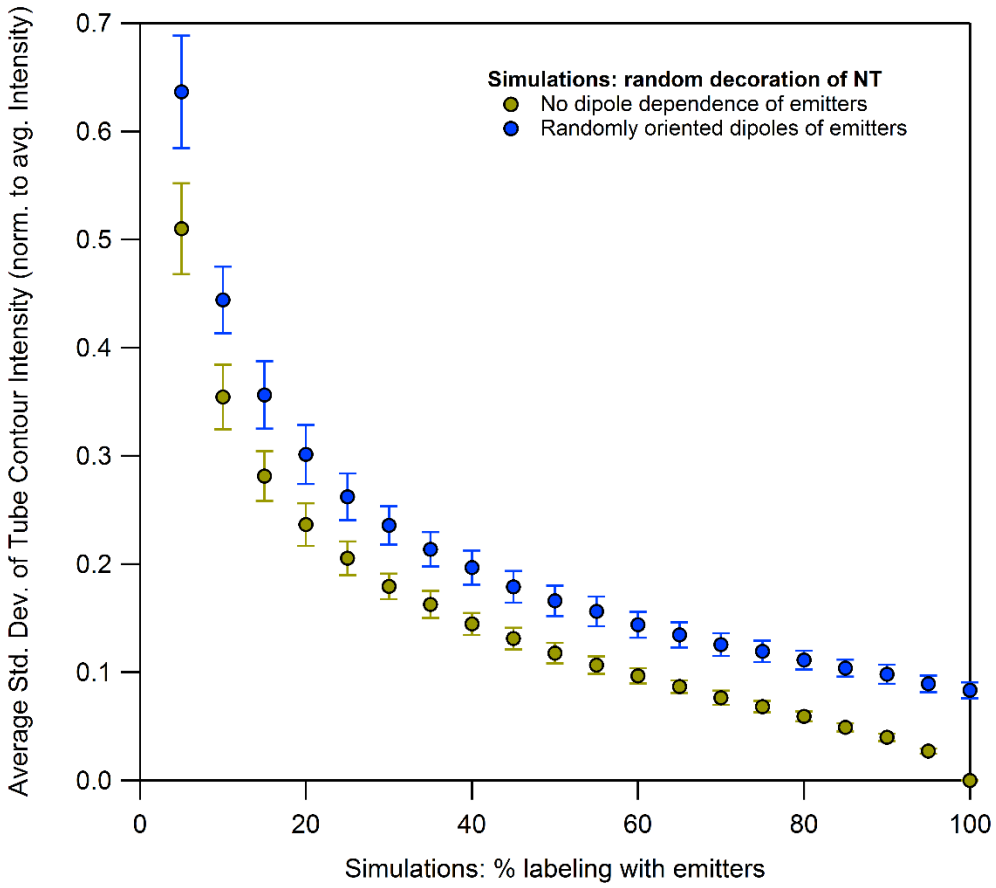

Figure D.9: Simulated values for *M*, the average standard deviation of intensity along NT contours, normalized to average intensity, as a function of %-labeling with emissive decorating elements for two cases: NT with randomly placed decorating emitters, each having the same dipolar angle with respect to the microscope objective (yellow), and NT with randomly placed decorating elements, each having a random fixed dipolar angle with respect to the microscope objective (blue).

D.8 Microscopy of Ag_{14}-DNA-decorated NT

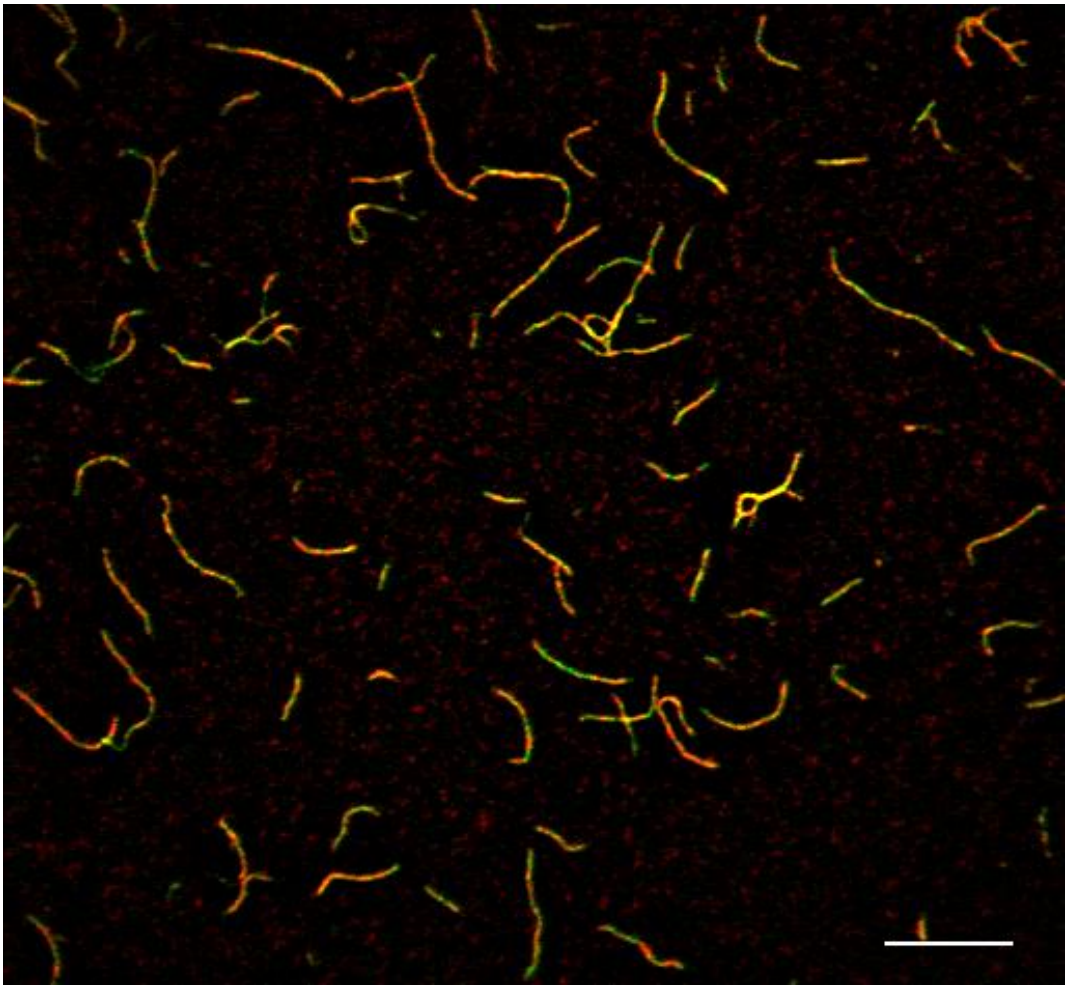

Figure D.10: FAM-labeled NT decorated with Ag_{14} clusters. Overlap of confocal images of fluorescein-labeled NT with 100% U9 docking sites (green) decorated with purified Ag_{14}-DNA (red) after tube formation and embedded in PVA film on clean glass coverslips. Scale bar is 10 μm. Red and green fluorescence clear colocalize, indicating successful labeling of NT with Ag_{14}-DNA. (Intensities of red and green channels in overlap are adjusted to best illustrate each color to the eye and are not representative of actual intensities.)

D.9 Individual Ag_{15}-DNA blinking on NT with 10% docker sites

Movie D.1 can be found free of charge at http://pubs.acs.org/doi/suppl/10.1021/nn506322q

Movie D.1: Widefield microscopy image of 10H tubes, with 10% of U6 strands labeled with docking sites, decorated by Ag15-DNA and embedded in PVA film. Widefield microscopy was used for imaging, as opposed to spinning disc confocal microscopy, to increase the intensity of light per each 1 second exposure window and therefore increase the probabilities of blinking and bleaching events. Three individual diffraction-limited spots, labeled 1, 2, and 3, are identified as single Ag15-DNA by their "on-off" blinking and bleaching characteristics. The circle around each emitter changes from red, when the emitter is fluorescing, to blue, when the emitter is either bleached or in a long-lived dark state (a "blinking" state). Figure D.11 shows intensity profiles for these three emitters.

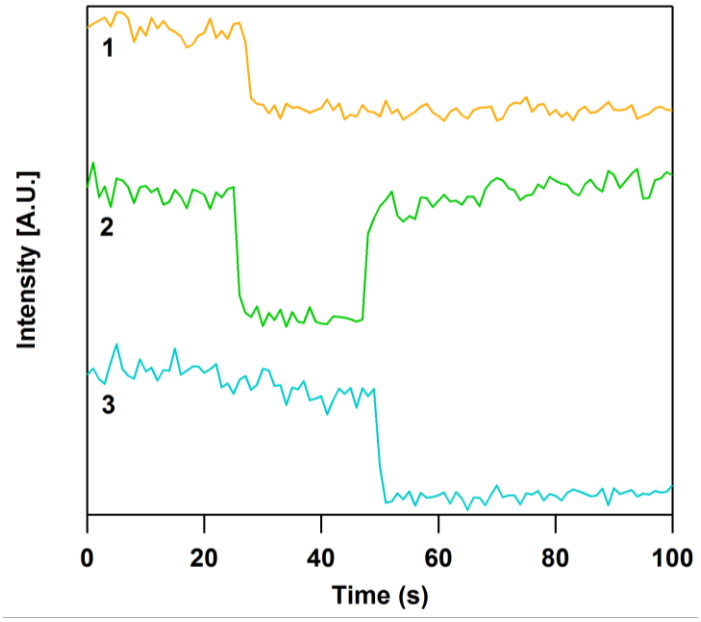

Figure D.11: Intensity traces for three selected Ag_{15}-DNA emitters, as labeled in Movie D.1. The intensity values plotted here are calculated by summing up all pixel values in a 7x7 pixel square, centered on each emitter. Each trace has two states: an "on" state marked by high intensity, and an "off" state marked by low intensity. The "off" states for all three traces have intensity values comparable to background noise – thus "off" states indicate that no fluorescent emitter is located within the 7x7 pixel square. Traces 1 and 3 show bleaching events for Ag_{15}-DNA, and trace 2 shows a blinking event, indicating that only one Ag_{15}-DNA is imaged at a time because the fluorescence states are binary.

D.10 Comparing NT labeled with once- and twice-purified Ag_{15}-DNA

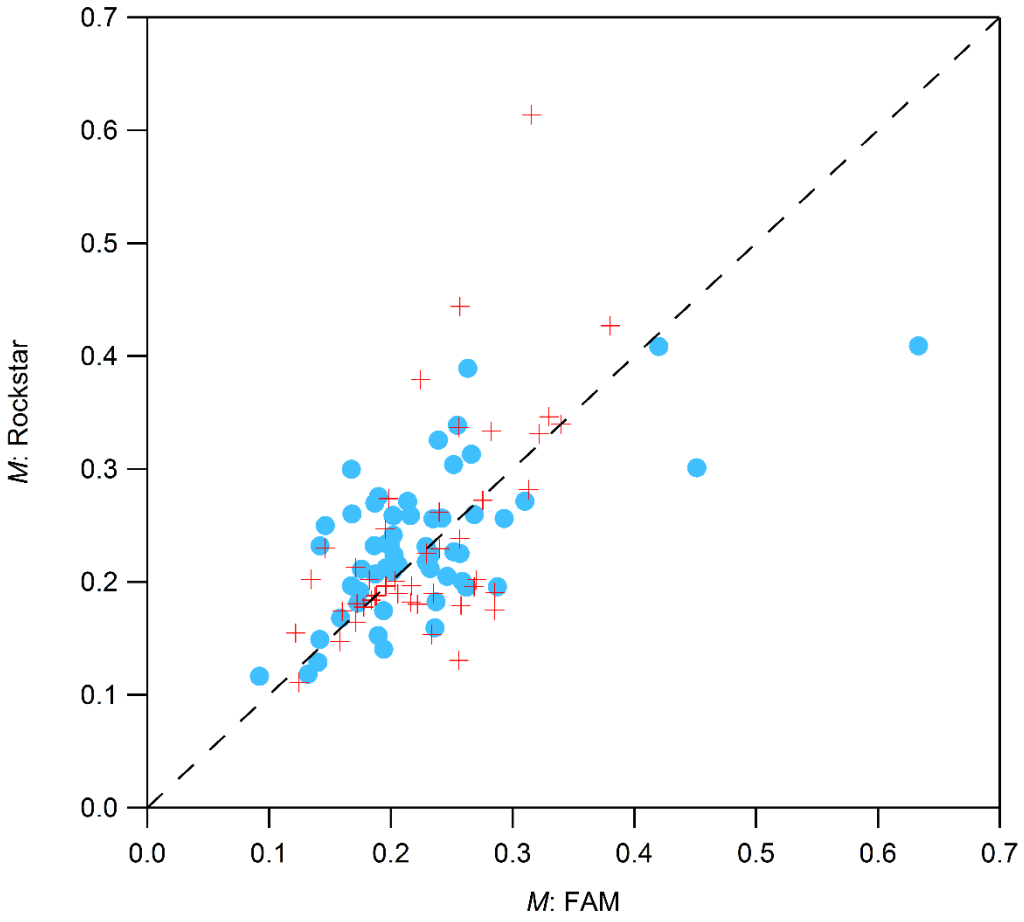

Figure D.12: *M* values for NT labeled with once-purified and twice-purified Ag_{15}-DNA. *M*, the average standard deviation of the background-corrected intensity along each contour, normalized to the contour's average intensity, calculated for emission from FAM (x-axis) and from Ag_{15}-DNA (y-axis). NT have 100% U6 strands with dockers, FAM labels on U1 strands, and are labeled with red crosses for TEAA as the ion-pairing agent in the HPLC running buffer and with blue dots for purification with a second stage of HPLC using HFIP/TEA as the ion-pairing agent. The similarity between the distributions for NT decorated with clusters purified once and twice by HPLC indicates similar levels of purity in both cases. The second purification with HFIP/TEA was necessary for quantification of achieved purity by ESI-MS.

Appendix E. Supporting Information for Chapter 6

E.1 Assumptions of the Lippert-Mataga Model

Several considerable assumptions are made in Eq. 6.1. First, it is assumed that the cavity occupied by the fluorophore is a sphere with radius *a* in *both* the ground and excited states. Solutions of Maxwell's equations can be modified for nonspherical cavities, but shape changes of the fluorophore with solvent composition are beyond the scope of the LM model, which presumes that the fluorophore structure is unchanged by solvent. Second, $\overrightarrow{\mu_G}$ and $\overrightarrow{\mu_E}$ are assumed to be identical in both initial Franck-Condon and solvent-relaxed states and are often assumed to be either parallel or antiparallel; proper modifications must otherwise be made to Eq. 6.1 to appropriately account for the relative angle between the dipole moments.[191] Eq 6.1 also neglects the polarizability of the fluorophore and assumes that both solute-solvent and solvent-solvent intermolecular distances are large enough to allow dipolar field approximations. Eq. 6.1 additionally presumes that reorientation of solvent molecules occurs on times well below the fluorescence lifetime. The LM model is invalid when specific solvent interactions, including hydrogen bonding, are present (except for a very few special cases) because these interactions nullify dipolar assumptions.[186] Such interactions can result in nonlinear LM plots. Finally, the LM model does not apply to cases where the emissive state is not reached directly by excitation, e.g. when the emissive state is a charge transfer state; in such cases the absorbance spectrum of the fluorophore does not represent the emissive state.[245] (Note that there is an overall sign error in Eq. 5.4 in [239]).

E.2 Purity estimates for Ag_N-DNA

For details on Ag_N-DNA purification, see Section 6.2.1. Ag_N-DNA purities are estimated from the overlap of UV and visible absorbance chromatograms. Emission spectra of purified samples at varying excitation wavelengths were compared to confirm that one dominant fluorescent product was isolated, based on small shifts in peak emission wavelength as a function of excitation wavelength compared to studies of heterogeneous mixtures of silver clusters studied elsewhere.[188]

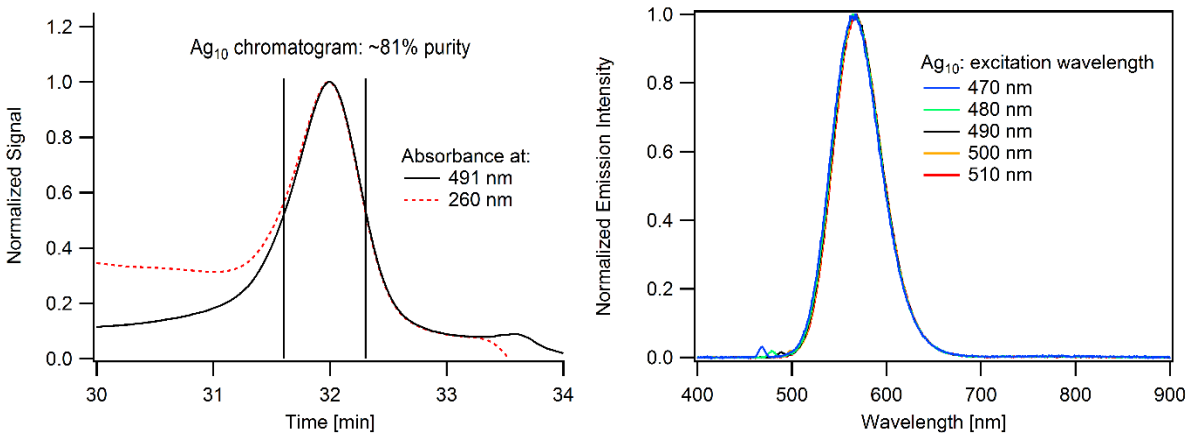

Figure E.1: **Left:** The overlap of HPLC absorbance chromatograms at 260 nm and at 491 nm, the peak excitation wavelength for Ag_{10}, indicate that the purified sample contains at least ~81% Ag_{10} (data used with permission from the authors[59]). Absorbance at 260 nm results from all DNA products, while absorbance at 491 nm is dominated by Ag_{10}. Remaining impurities after HPLC purification are non-fluorescent, as indicated by the emission spectra to the right. **Right:** Emission spectra of purified Ag_{10} for various excitation wavelengths. Small peaks at shorter wavelengths result from scattered excitation light. Spectral peaks and linewidths do not shift significantly for varying excitation wavelength, indicating that only one fluorescent product is present in solution.

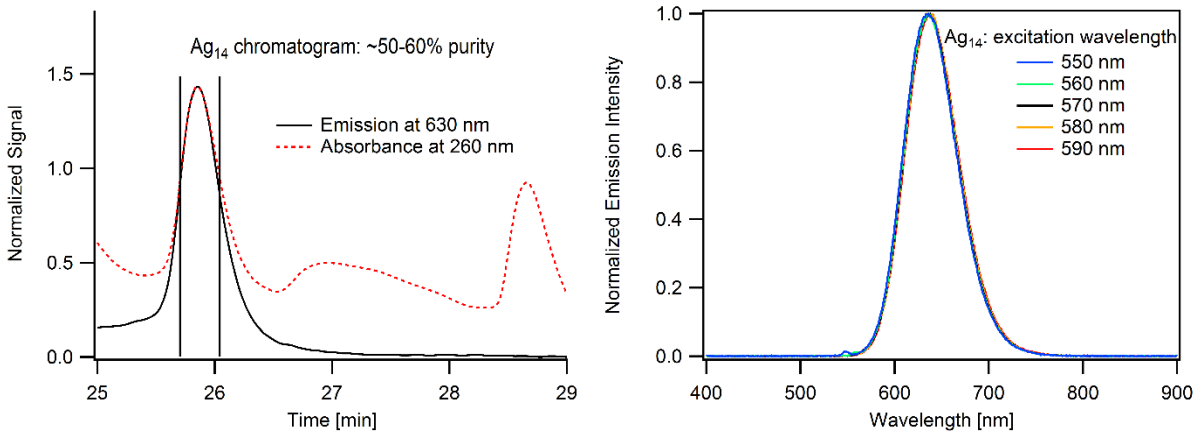

Figure E.2: **Left:** The overlap of the HPLC absorbance chromatogram at 260 nm and emission chromatogram at 630 nm for Ag_{14} indicate that the purified sample contains at least 50-60% Ag_{14} (data used with permission from the authors[71]). Absorbance at 260 nm results from all DNA products, while emission at 630 nm results from Ag_{14}. Despite the lower purity of Ag_{14} as compared to other Ag_N studied here, all remaining impurities are non-fluorescent, as indicated by the constant linewidths and peaks of emission spectra to the right. **Right:** Emission spectra of purified Ag_{14} for various excitation wavelengths. Small peaks at shorter wavelengths result from scattered excitation light. Spectral peaks and linewidths do not shift significantly for varying excitation wavelength, indicating that only one fluorescent product is present in solution.

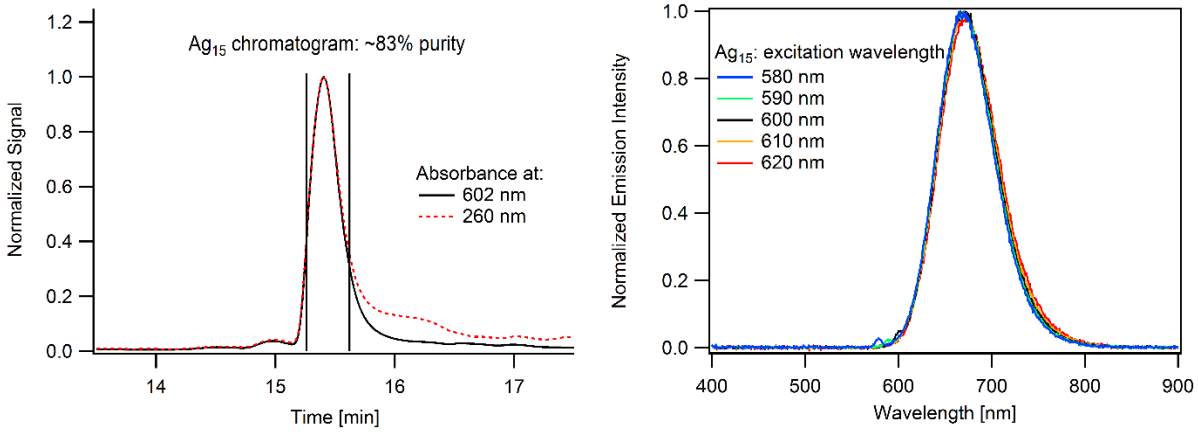

Figure E.3: **Left:** The overlap of HPLC absorbance chromatograms at 260 nm and 602 nm, the peak excitation wavelength for Ag_{15}, indicate that the purified sample contains at least ~83% Ag_{15} (data used with permission from the authors[59]). Absorbance at 260 nm results from all DNA products, while absorbance at 602 nm is dominated by Ag_{15}. Other impurities are almost entirely non-fluorescent, as indicated by the emission spectra to the right. **Right:** Emission spectra of purified Ag_{15} for various excitation wavelengths. Small peaks at shorter wavelengths result from scattered excitation light. Spectral peaks and linewidths shift only slightly for varying excitation wavelength, indicating that one dominant fluorescent product is present in solution. The slight shifts are an order of magnitude smaller than those observed for more heterogeneous samples.[188] Numerical analysis of the effects of these small shifts for Ag_{15} found negligible changes to the Stokes shift behavior discussed in Section 6.3.

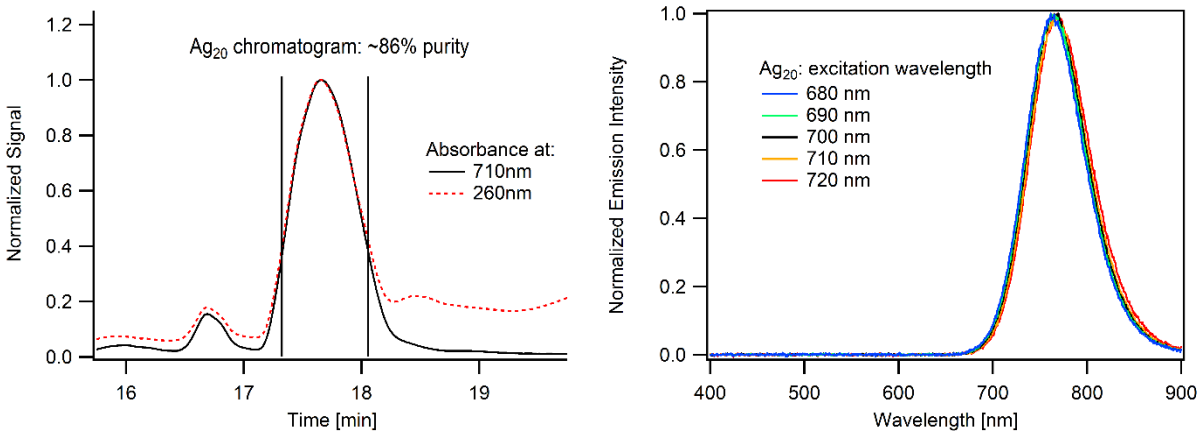

Figure E.4: **Left:** The overlap of HPLC absorbance chromatograms at 260 nm and 710 nm, the peak excitation wavelength for Ag_{20}, indicate that the purified sample contains at least ~86% Ag_{20} (data used with permission from the authors[59]). Absorbance at 260 nm results from DNA products, while absorbance at 602 nm is dominated by Ag_{20}. Other impurities are almost entirely non-fluorescent, as indicated by the emission spectra to the right. **Right:** Emission spectra of purified Ag_{20} for various excitation wavelengths. Spectral peaks and linewidths do not shift significantly for varying excitation wavelength, indicating that one dominant fluorescent product is present in solution. The slight shifts are an order of magnitude smaller than those observed for more heterogeneous samples.[188] Numerical analysis of the effects of these small shifts for Ag_{20} found changes that are small compared to the Stokes shift behavior in MeOH (Figure 2d). The small shifts are ~50% less than the changes in Stokes shift for Ag_{20} in EtOH, and thus we do not discuss the implications of the EtOH data in Figure 2d with respect to the LM model, as this spectral heterogeneity may contribute somewhat to the observations for this single case.

E.3 Measurements on impure Ag_N-DNA solutions

Different pure Ag_N-DNA exhibit distinct solvatochromic responses. Purity is important because measurements on impure mixtures containing multiple emissive species are a superposition of the individual species' distinct solvatochromic behaviors. Especially for impure mixtures of different Ag_N-DNA species that have overlapping emission peaks, this superposition can result in solvent composition trends that are not characteristic of any of the individual species and, consequently, not meaningful for relating the observed solvatochromism to a particular Ag_N-DNA species.

The DNA templates used in our experiments (Table 6.1) were selected because they form one dominant, spectrally well separated fluorescent species that is stable under ambient conditions for weeks or longer, and stable enough to isolate using HPLC. In contrast, most other previously studied templates form multiple fluorescent species, in many cases with overlapping spectral peaks, which are unstable over times of hours. Figures E.5 and E.6 (below) display the solvatochromic behavior of the initial, unpurified solutions, before HPLC purification.

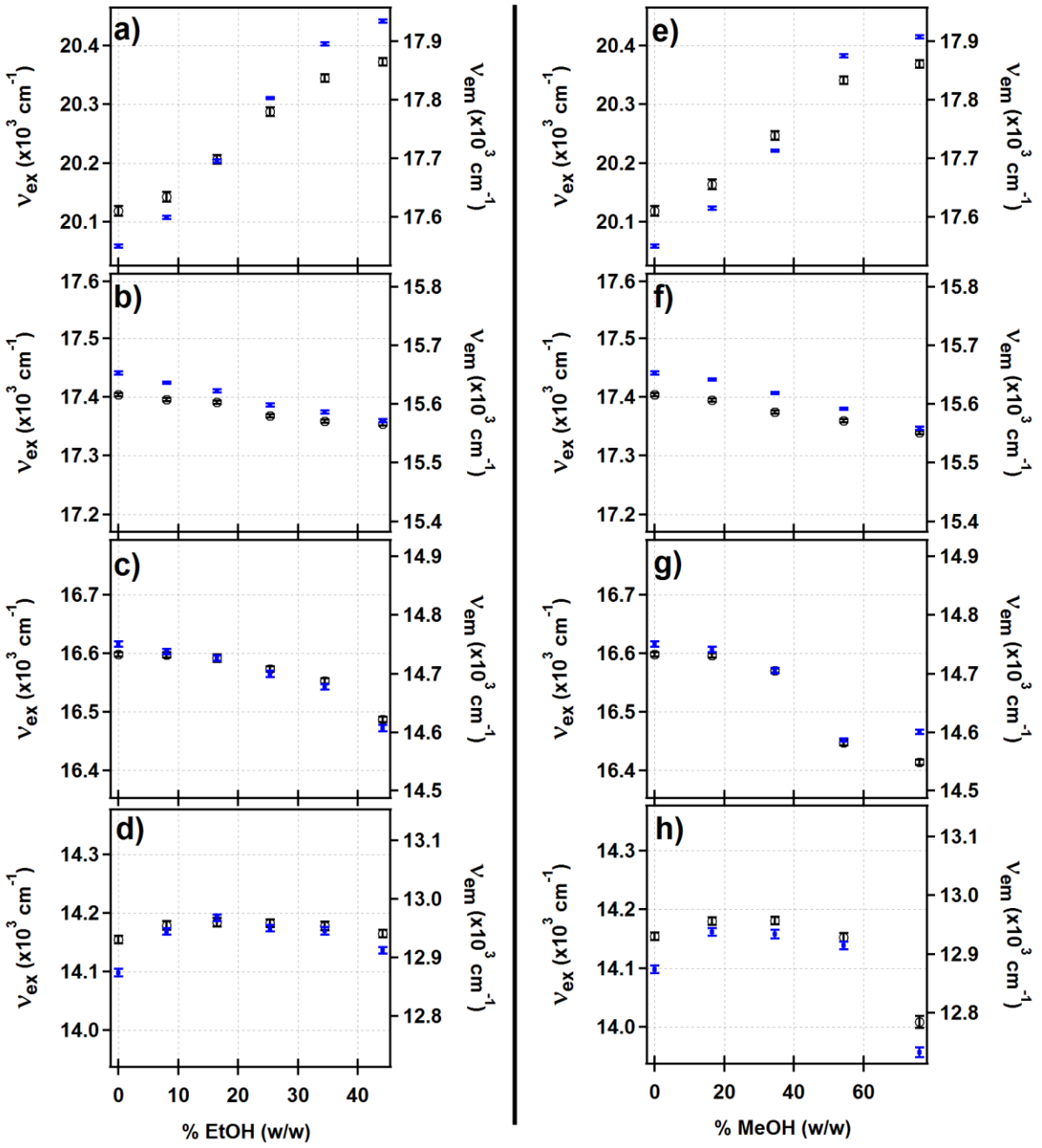

Figure E.5: Peak excitation (ν_{ex}, black circles, left axes) and emission (ν_{em}, blue dots, right axes) wavenumbers in **(a-d)** EtOH- and **(e-h)** MeOH-buffer mixtures for unpurified **a)**, **e)** Ag_{10}, **b)**, **f)** Ag_{14}, **c)**, **g)** Ag_{15}, and **d)**, **h)** Ag_{20} (analogous to Figure 6.1 for purified Ag_N-DNA). Y-axis ranges are equal for all plots to enable comparisons. Arrows in **a)** indicate axes for ν_{ex} (black) and ν_{em} (blue). Error bars represent standard deviations determined from Gaussian fits. (Note: error bars for Ag_{14}, Ag_{15}, and Ag_{20} in Figure 6.1 represent standard deviation from multiple duplicate experiments, not simply error from Gaussian fits to spectral lines. Thus, error bars in Figure 6.1 cannot be compared quantitatively to error bars in Figure E.1).

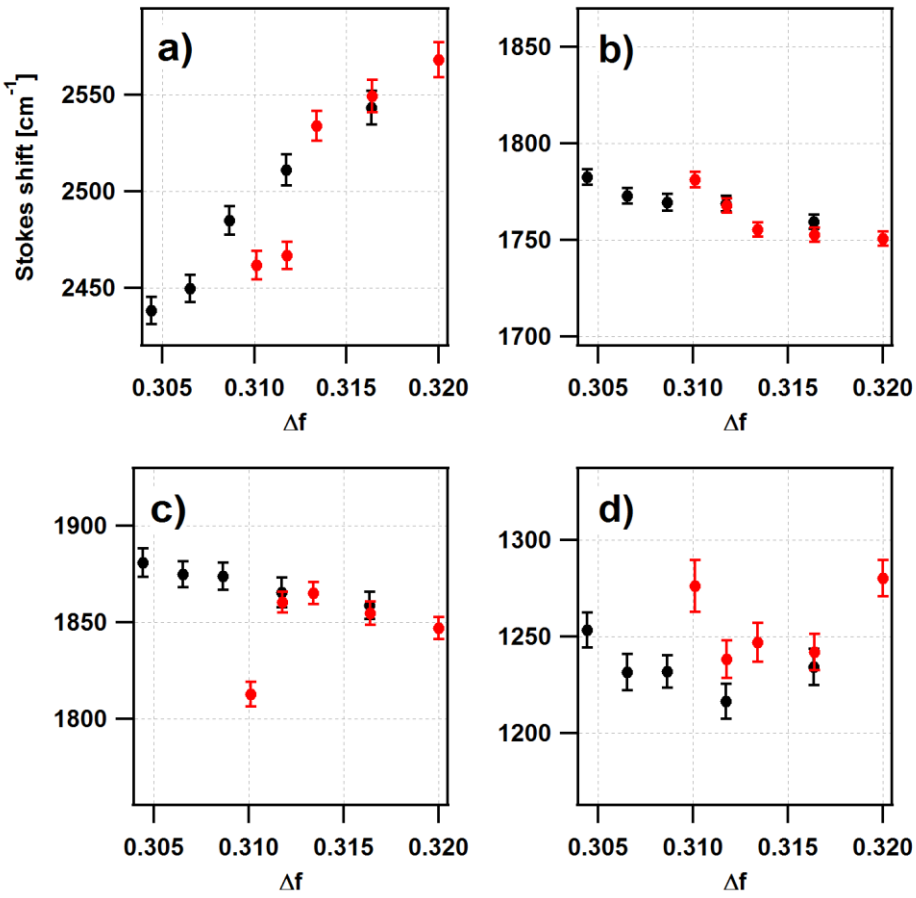

Figure E.6: Lippert-Mataga plots for impure **a)** Ag_{10}, **b)** Ag_{14}, **c)** Ag_{15}, and **d)** Ag_{20} in EtOH-buffer mixtures (black) and MeOH-water mixtures (red) (analogous to Figure 6.2 for purified Ag_N-DNA). Y-axis ranges are equal for all plots to enable comparison. Error bars represent standard deviation, as determined by error propagation.

E.4 Ag_{10} excitation and absorbance spectra with and without MeOH

To test the fidelity of fluorescence excitation peaks to emissive cluster absorbance peaks, we select the "worst case" scenario of Ag_{10}, the only one of the clusters studied to exhibit a reversible, solvent-controlled equilibrium between fluorescent and dark states, with the absorbance peak for the emissive form near 2.5 eV and for the non-emissive form, near 3 eV.[59] It has been shown that the solvent-tuned equilibrium is between the emissive Ag_{10} studied here and a conformationally distinct, nonemissive form with peak absorbance > 3 eV (see Figure E.7a inset).[59] Thus, for low % MeOH, a small blue-shift is expected for the absorbance peak

relative to the excitation peak at ~2.5 eV due to overlap of the visible and UV absorbance peaks. This is clear in Figure E.7a, as compared to Figure E.7b. Such non-emissive species were not detected for Ag_{14}, Ag_{15}, or Ag_{20}, but we use excitation rather than absorbance spectra in all cases to avoid any nonfluorescent species that coelute with the fluorescent product during HPLC.

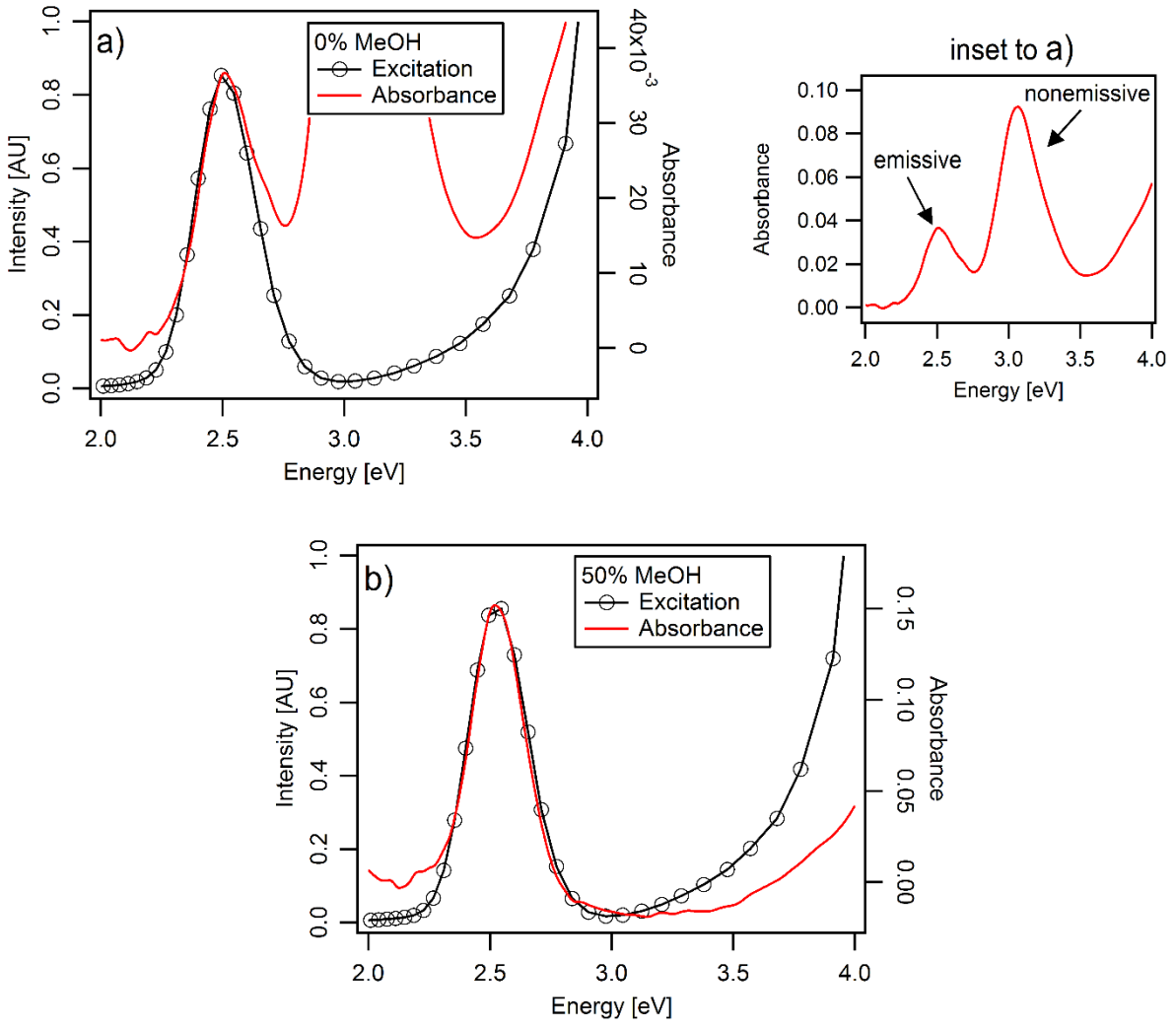

Figure E.7: Excitation (black, left axes) and absorbance (red, right axes) spectra for purified Ag_{10} **a)** without MeOH and **b)** in 50% MeOH. Excitation spectra were collected at 10 nm resolution. The visible absorbance and excitation peaks near 2.5 eV do not shift significantly with respect to one another as a function of solvent concentration.

Appendix F. Supporting Information for Chapter 7

F.1 Properties of Ag_N-DNA

Name	Sequence	N_0	λ_{res}
DNA1	TATCCGTCCCCCCCCCACGGATA †	3.9±0.2	405.97±0.03
DNA2	TCCACGAGAA *	3.8±0.1	470.53±0.04
DNA3	TGCCTTTTGGGGACGGATA †	4.0±0.1	489.82±0.07
DNA4	TTCCCCACCACCCAGGCCCCGTT ‡	5.9±0.2	527.2±0.2
DNA5	GCCGACCTAT *	6.0±0.1	540.92±0.03
DNA6	GCCAGTCCCG *	6.0±0.2	548.0±0.1
DNA7	TTCGCCCCCCGCCCCAGGCGTT †	6.1±0.1	563.3±0.1
DNA8	TTCCCACCCACCCCGGCCCGTT †	5.9±0.2	572.36±0.03
DNA9	CACCGCTTTTGCCTTTTGGGGACGGATA †	5.7±0.2	600.67±0.03
DNA10	GGCAGGTTGGGGTGACTAAAAACCCTTAA TCCCC †	5.9±0.2	600.8±0.2
DNA11	CCCACCCACCCGCCCA †	11.8±0.1	707.71 ±0.04
DNA12	CCCACCCACCCTCCCA †	9.8±0.2	754.99±0.03
DNA13	CCCACCCACCCACCCG †	10.8±0.3	850.26±0.03

Table F.1: DNA was purchased with standard desalting from Integrated DNA Technologies. All Ag_N-DNA are synthesized in 10 mM NH_4OAc, and synthesis conditions are indicated below:
† Synthesis conditions listed elsewhere.[53]
* Final concentrations for synthesis are [DNA] = 20 μM, [$AgNO_3$] = 100 μM, and [$NaBH_4$]/[$AgNO_3$] = 0.5.[58]
‡ Final concentrations for synthesis are [DNA] = 25 μM, [$AgNO_3$] = 300 μM, and [$NaBH_4$]/[$AgNO_3$] = 0.5.

The number of neutral silver atoms, N_0, is determined by mass spectrometry of Ag_N-DNA purified by high performance liquid chromatography (HPLC).[52,53,58] Values for DNA2, DNA5, and DNA6 are listed in Ref. 58; all others are listed in Ref. 53. To determine λ_{res}, absorbance spectra of purified Ag_N-DNA were fit to a single Gaussian as a function of energy, and the peak energy and associated standard deviation were extracted from the fit. Values were then converted to wavelength. Because the peak absorbance and peak excitation of a pure solution containing only one form of Ag_N-DNA coincide in the visible and near-infrared spectrum,[50] peak absorbance and peak excitation may be used interchangeably.

F.2 Fits to the dielectric functions of Ag and Au

Figure F.1 plots the real part of the dielectric function[223] function for silver (we neglect the small imaginary part). For sufficiently long wavelengths, the expected form (Eq. 7.6) is:

$$\varepsilon(\lambda) = a\lambda^2 + c \qquad (7.6)$$

with a negative and c positive. The published data closely follow Eq. 7.6 for λ greater than about 470 nm. Error-weighted fits over this wavelength range give $a = -5.55 \pm 0.02 \times 10^{-5}$ nm^{-2} and $c = 4.00 \pm 0.06$ (Figure F.1), where uncertainties are standard fit errors. (Fit parameters vary somewhat with wavelength range; for example, fitting for $\lambda > 520$ nm gives $a = -5.47 \pm 0.03 \times 10^{-5}$ nm^{-2} and $c = 3.67 \pm 0.09$, but with almost no change to $\varepsilon(\lambda)$).

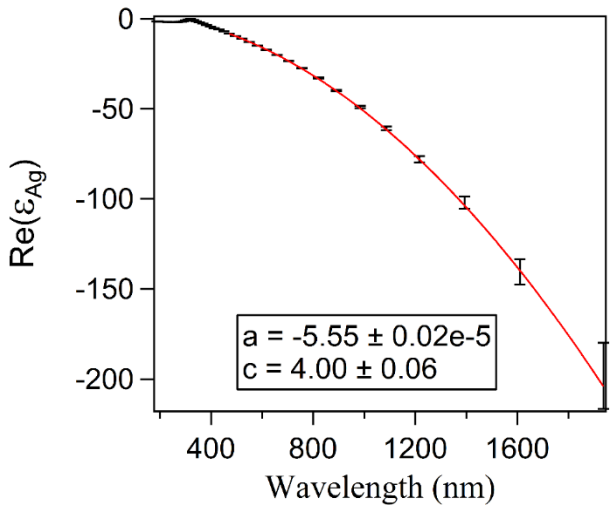

Figure F.1: Error-weighted fit of Eq. 7.6 (red) to the data of Johnson and Christy[223] for silver (black).

We perform the same fit for gold and find $a = -5.09 \pm 0.02 \times 10^{-5}$ nm^{-2} and $c = 8.83 \pm 0.06$ (Figure F.2). These values for silver and gold are used to produce the expected index sensitivity, $d\lambda_{res}/dn_M$, as a function of AR in Figure 7.2.

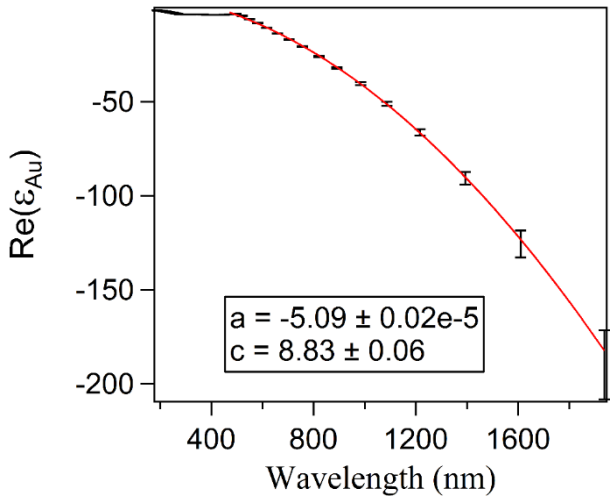

Figure F.2: Error-weighted fit of Eq. 7.6 (red) to the data of Johnson and Christy[223] for gold (black).

F.3 Extinction coefficients

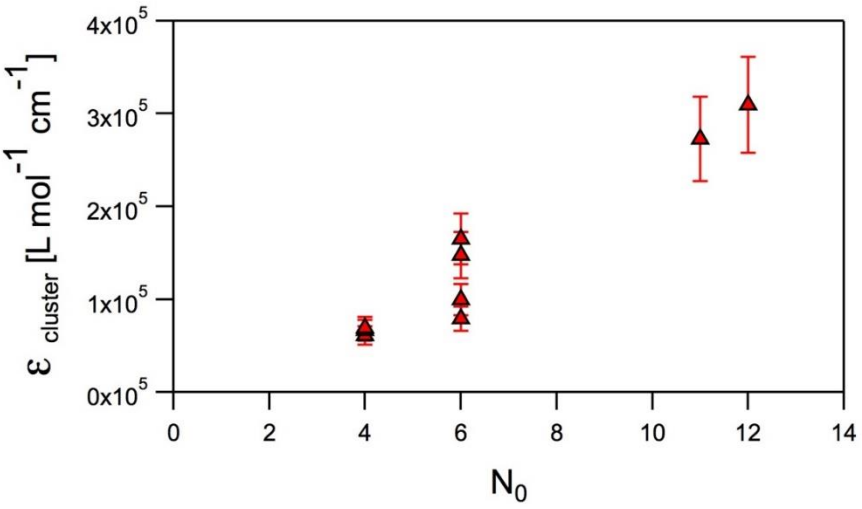

Figure F.3: Cluster extinction coefficient at the main visible-NIR absorbance peak, ε_{cl}, *versus* N_0 for various purified Ag_N-DNA solutions. As expected for rod-like clusters that are described by MG theory, ε_{cl} increases with N_0. The error bars are rough estimates of systematic effects from variation in the DNA absorbance that may arise from cluster-induced changes in base stacking.

To find $\varepsilon_{cluster}$ from absorbance data, we use Beer's Law, $A_{cl} = C_{cl}\,\varepsilon_{cl}\,L$, where L is the light path length and C_{cl} is the concentration of silver clusters in a given solution with absorbance A_{cl} at the peak visible/NIR cluster excitation wavelength. The cluster concentration C_{cl} depends on the purity p of the solution (p = 1 for a perfectly pure Ag_N-DNA solution), the

DNA concentration, C_{DNA}, and the number of DNA strands attached to the cluster, n_s, as $C_{cl} = p\, C_{DNA}/n_s$. The strand number n_s is one or two, depending on the specific Ag_N-DNA, and is determined by mass spectrometry. C_{DNA} is measured using the absorbance at 260 nm, A_{260}, because the DNA extinction coefficient, ε_{260}, is specified at this wavelength by the manufacturer, as $C_{DNA} = A_{260}/(\varepsilon_{260}\, L)$. Solving for $\varepsilon_{cluster}$ as a function of these measureable quantities, we find the values displayed in Figure F.3: $\varepsilon_{cluster} = (A_{cluster}/A_{260})\,(n_s/p)\,\varepsilon_{260}$.

DNA extinction coefficients, ε_{260}, were calculated by the nearest neighbor model using Integrated DNA Technologies' OligoAnalyzer tool. Cluster purities, *p*, were estimated from emission and absorbance chromatograms measured during HPLC purification. Additional error may be introduced from hypochromic effects of single stranded DNA association, commonly observed in Watson-Crick paired duplex DNA formation.[23] This can alter ε_{260} for DNA by some tens of percent, as represented by the rough systematic error bars in Figure F.3.

F.4 Shift in λ_{res} with increasing w/w % glycerol

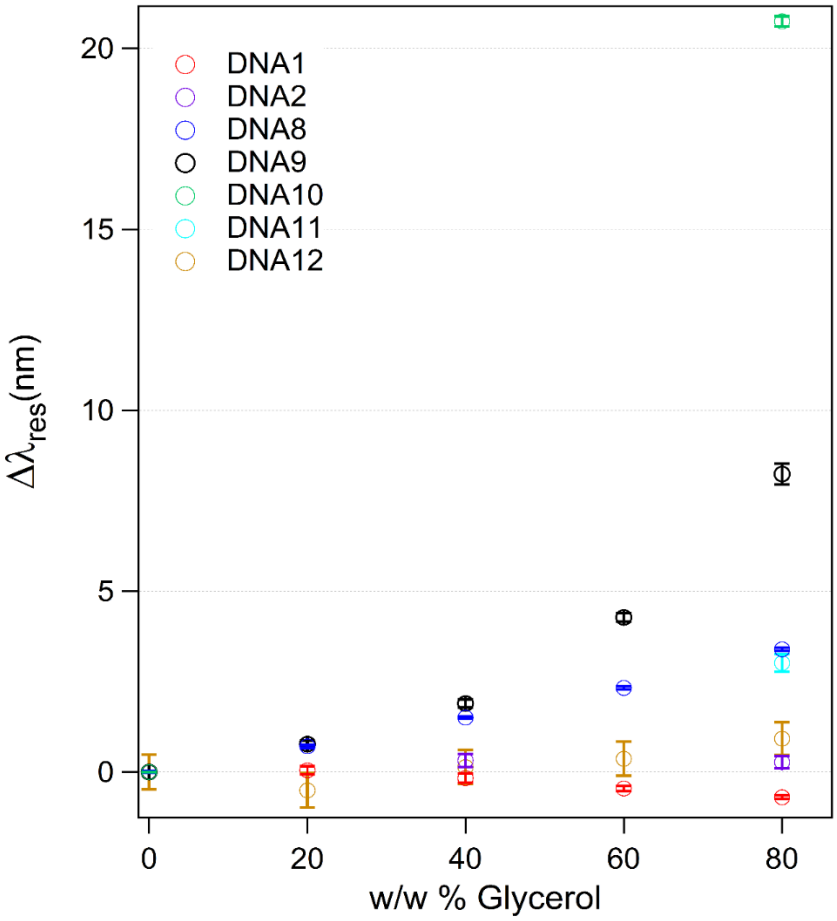

Figure F.4: Shift in Ag_N-DNA excitation wavelength, λ_{res}, with increasing w/w % glycerol, for all data points in Figure 3b.

Name:	DNA1	DNA2	DNA8	DNA9	DNA10	DNA11	DNA12
$\Delta\lambda_{res}/\Delta n_M$	-6.3±0.5	2 ±2	30.8±0.5	75±3	188±1	27±2	8±4

Table F.2: $\Delta\lambda_{res}/\Delta n_M$ values from Figure 7.4a for Ag_N-DNA, calculated in nm from λ_{res} in 0% and 80% glycerol.

F.5 Individual excitation spectra

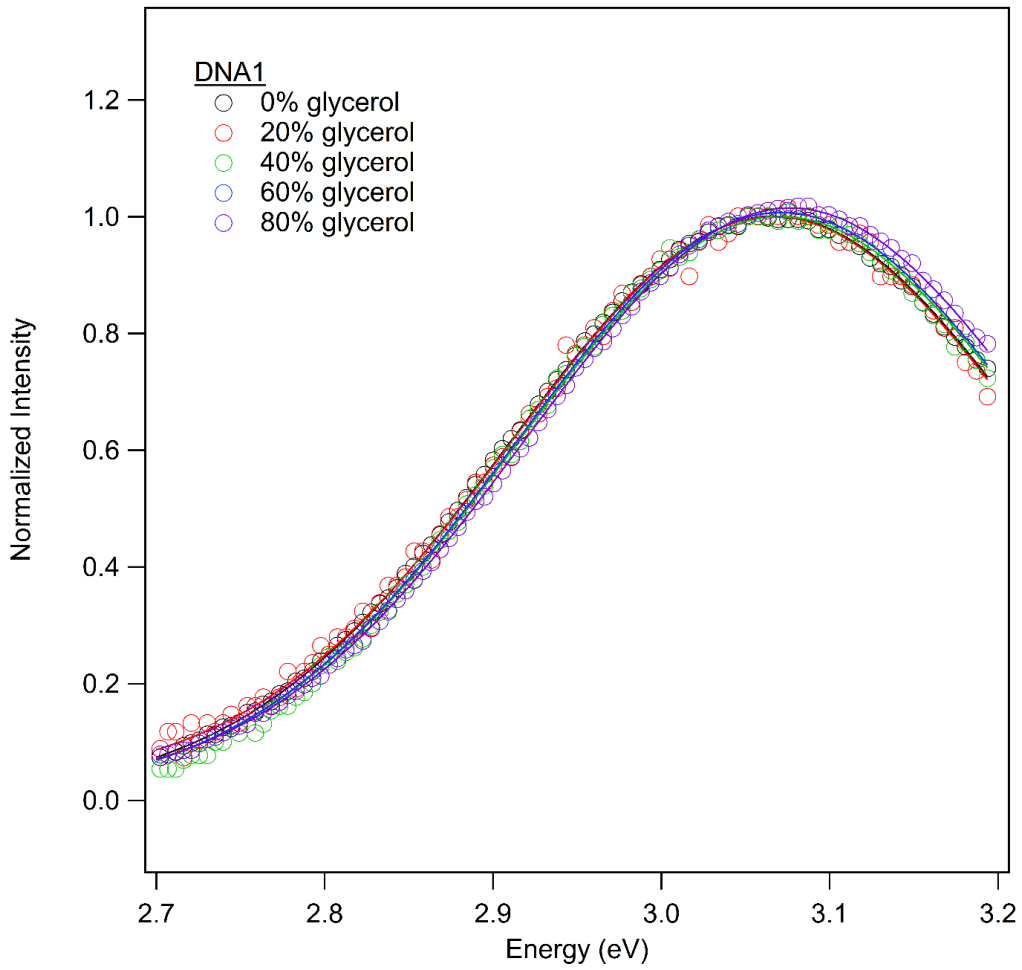

Figure F.5: Excitation spectra for DNA1 in varying w/w % glycerol. Solid lines indicate Gaussian fits as a function of energy.

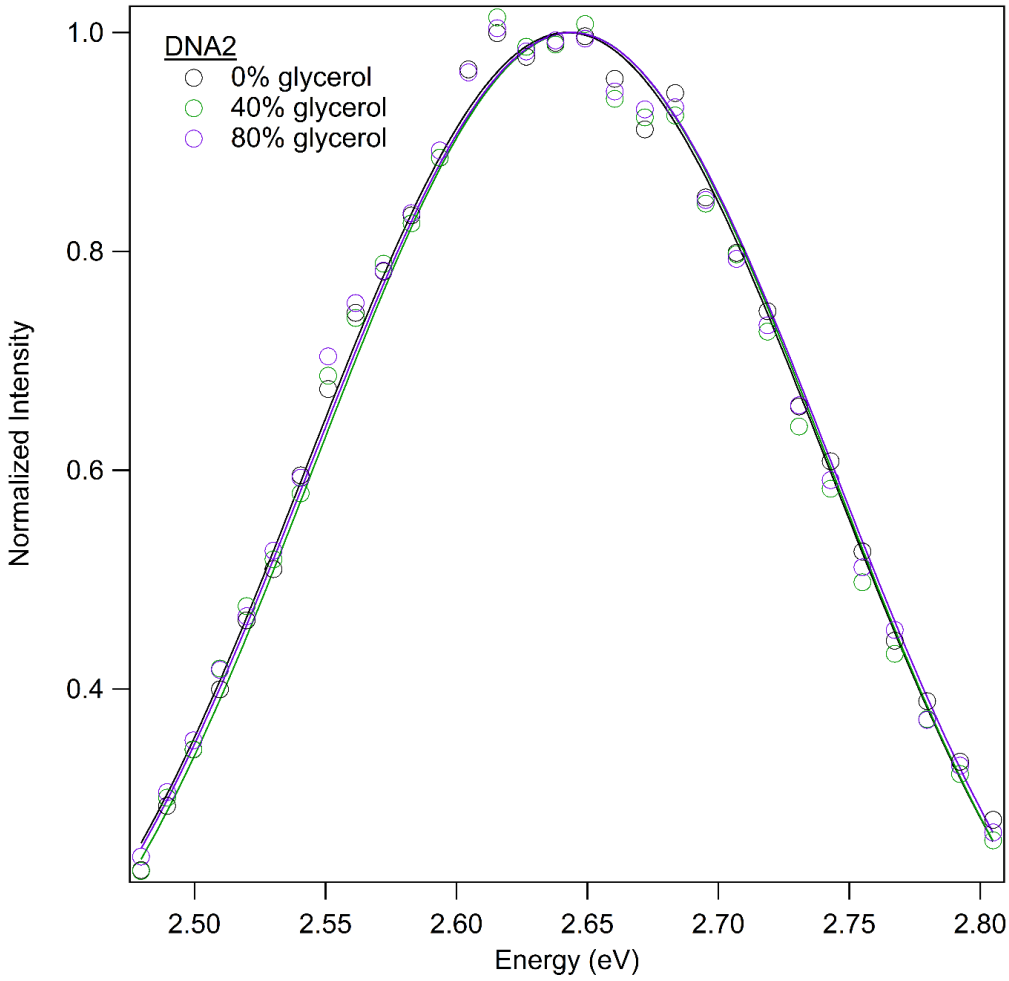

Figure F.6: Excitation spectra for DNA2 in varying w/w % glycerol. Solid lines indicate Gaussian fits as a function of energy.

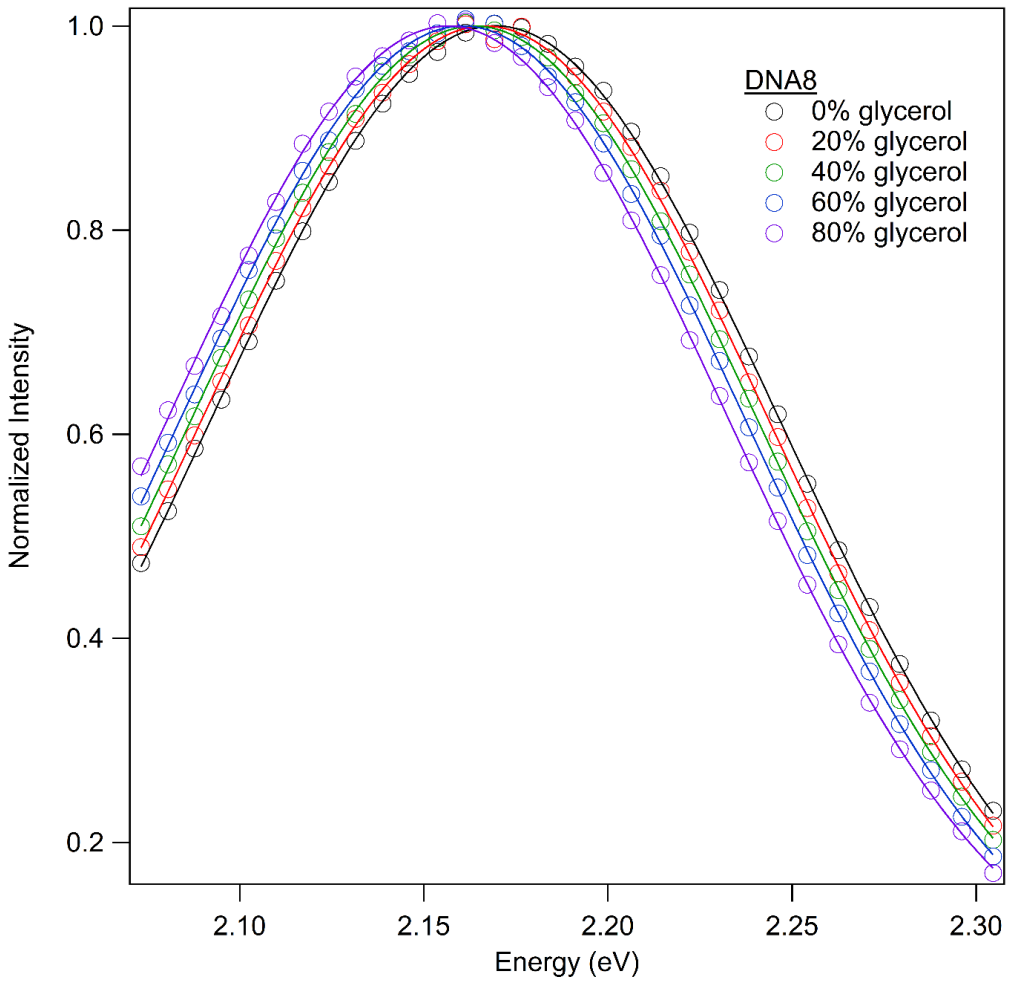

Figure F.7: Excitation spectra for DNA8 in varying w/w % glycerol. Solid lines indicate Gaussian fits as a function of energy.

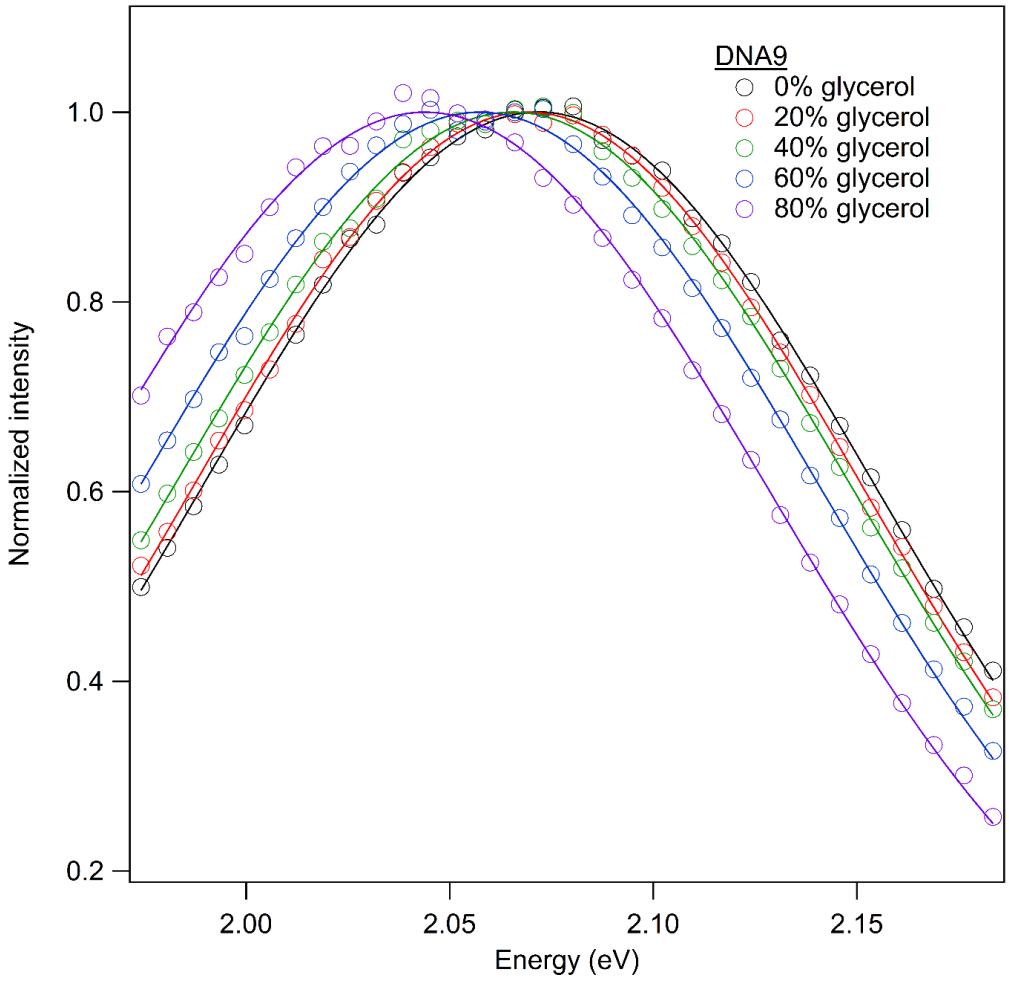

Figure F.8: Excitation spectra for DNA9 in varying w/w % glycerol. Solid lines indicate Gaussian fits as a function of energy.

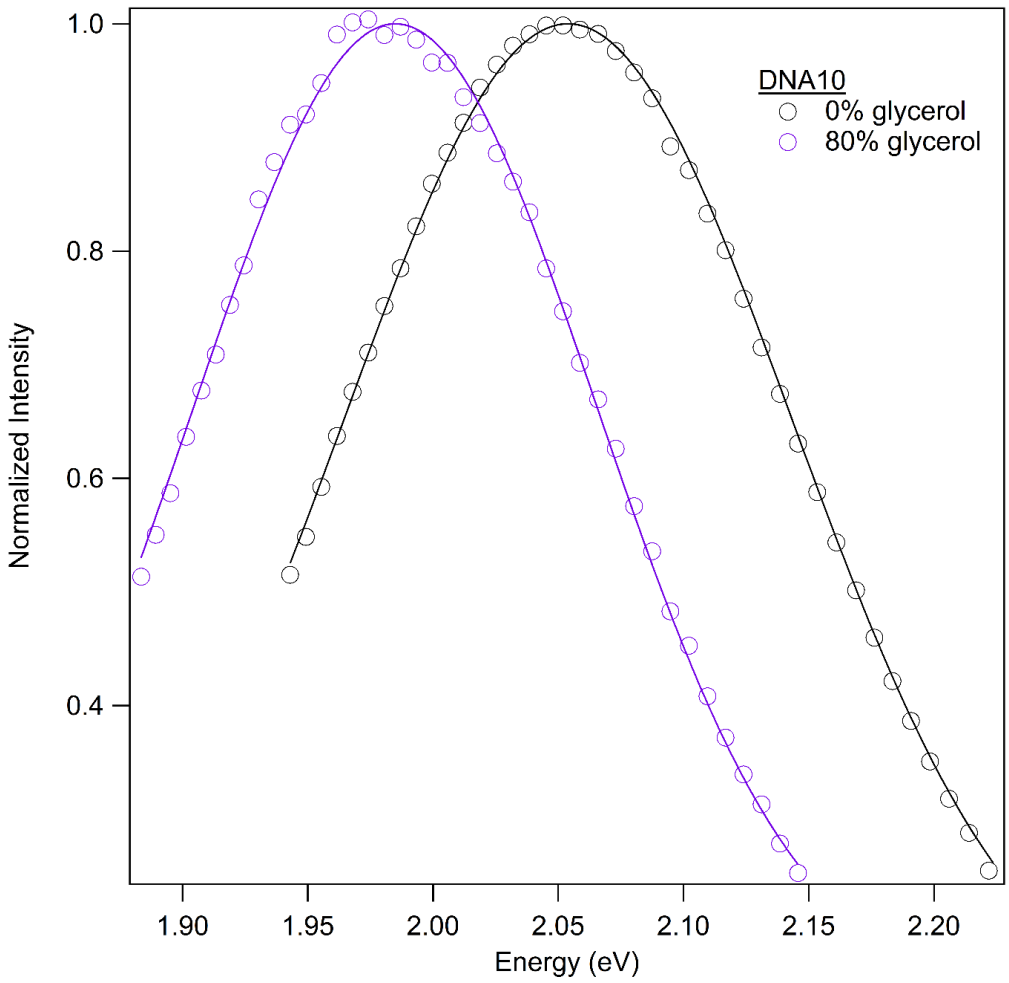

Figure F.9: Excitation spectra for DNA10 in varying w/w % glycerol. Solid lines indicate Gaussian fits as a function of energy.

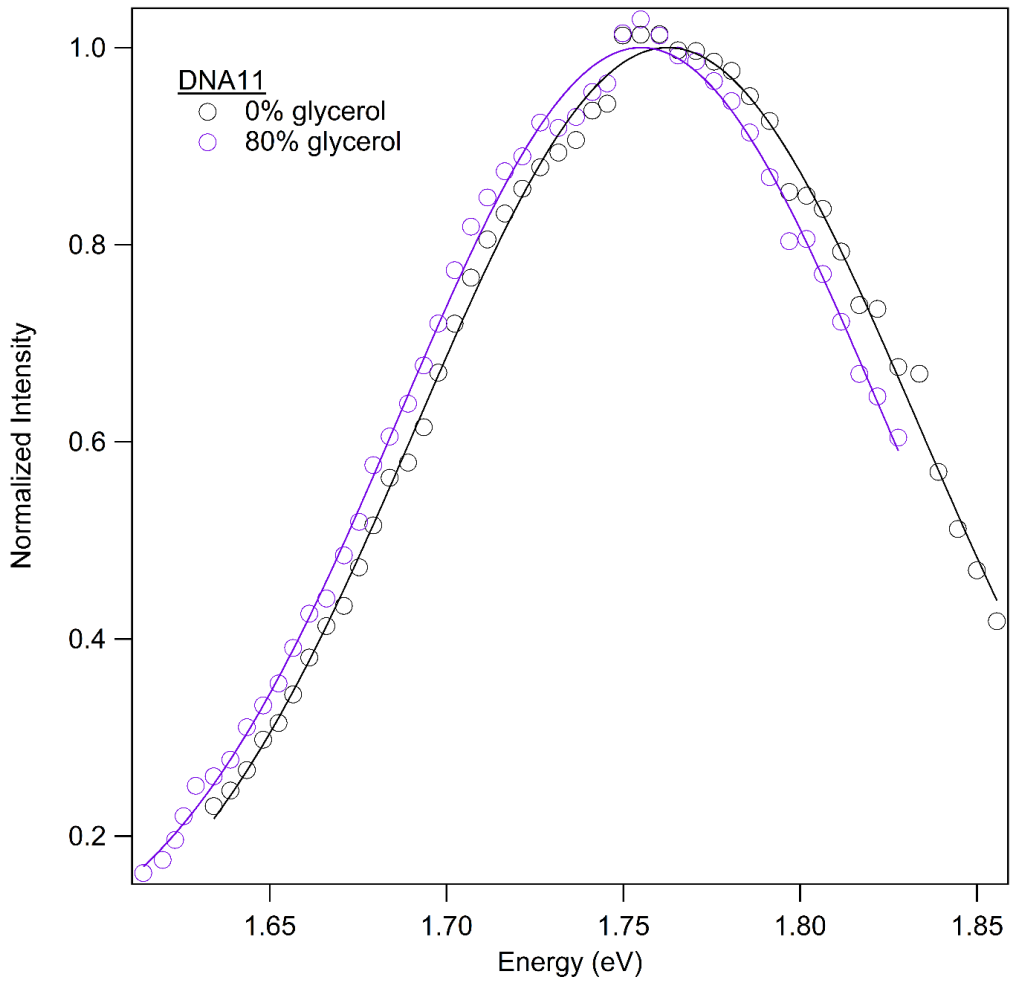

Figure F.10: Excitation spectra for DNA11 in varying w/w % glycerol. Solid lines indicate Gaussian fits as a function of energy.

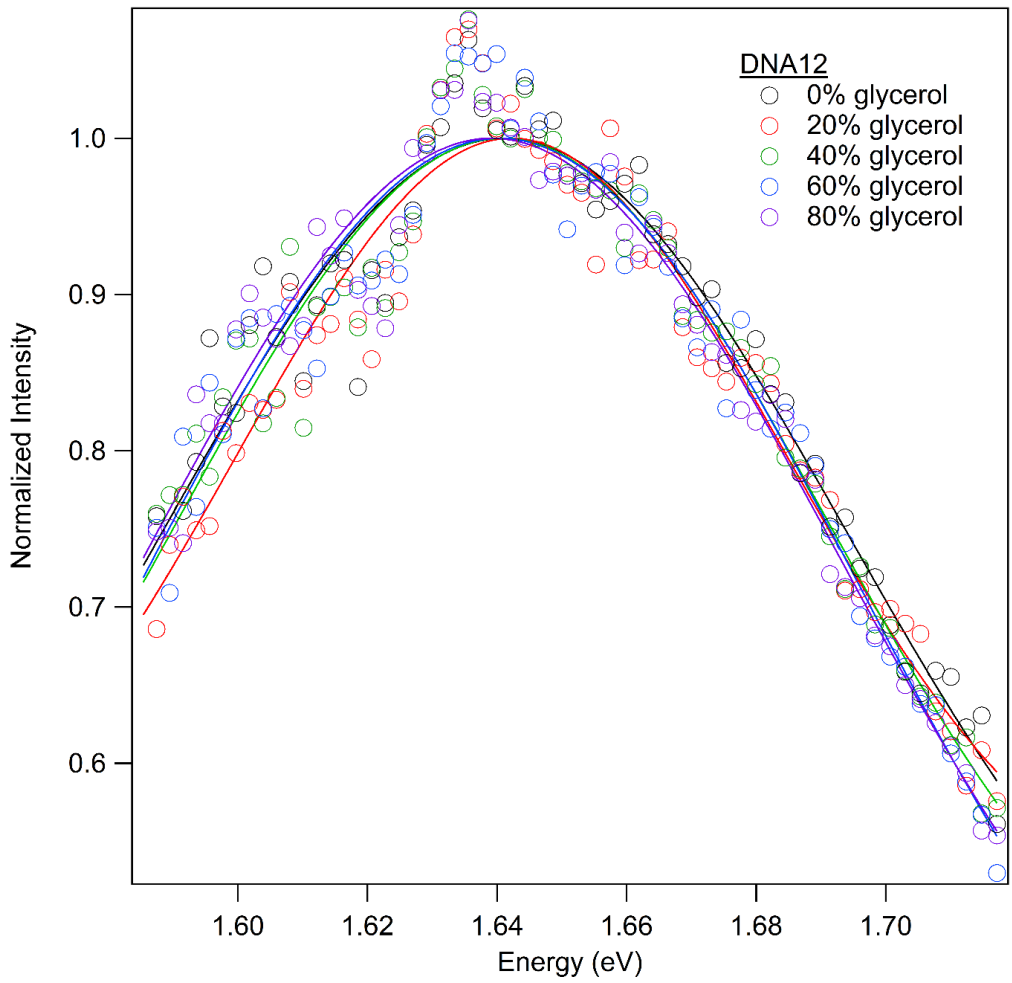

Figure F.11: Excitation spectra for DNA12 in varying w/w % glycerol. Solid lines indicate Gaussian fits as a function of energy.

F.6 MG predictions for $\lambda_{res}(n_M)$

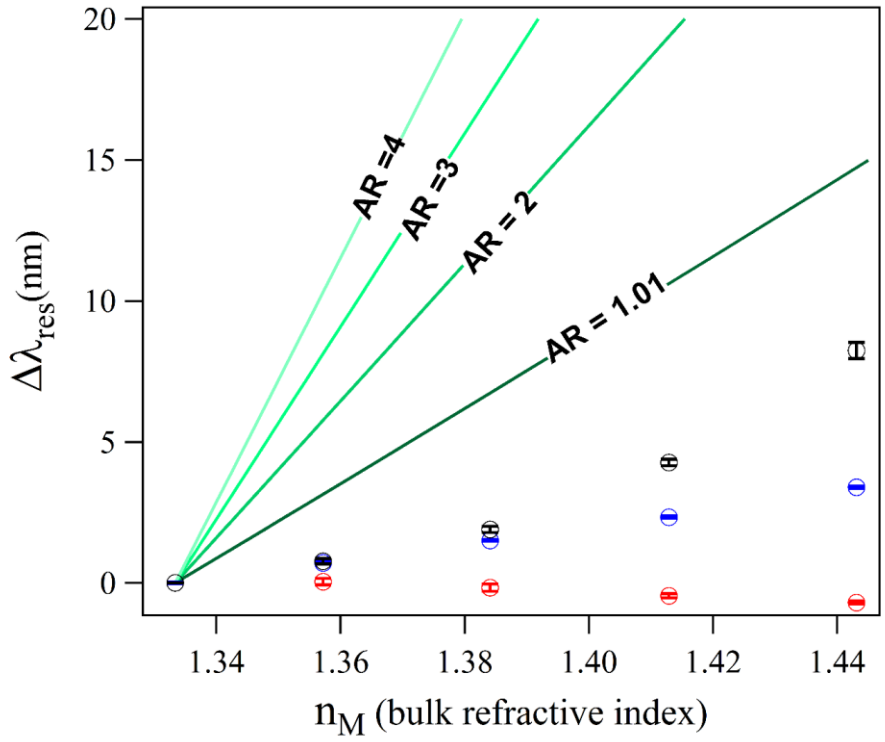

Figure F.12: Shift in λ_{res} as a function of bulk refractive index, n_M, as predicted by MG theory for Ag nanorods of various *AR* (green lines) and measured for Ag_N-DNA: DNA1 (red), DNA8 (blue), and DNA9 (black). Fit values from Figures F.1 and F.2 are used for MG theory calculations.

Appendix G. Custom Igor Pro software

G.1 Multipeak fitting for well plate format emission spectra

To extract the spectral features of fluorescence emission from a well plate of (up to) 384 different solutions of Ag_N-DNA, we use a custom Igor Pro routine that fits each emission spectrum to a set of one, two, or three Gaussian peaks. The form of the Gaussian, as given by Eq. A.1, is:

$$f(x) = A_0 + a \cdot \exp\left[\frac{-(x-b)^2}{c^2}\right] \qquad (G.1)$$

We edit the Igor Pro MyAutomaticallyFindPeaks routine, which can be found here, to identify the number of peaks in a spectrum. The maximum number of peaks to search for is set to three, and peaks with amplitude less than 5% of the main identified peak are ignored. We found that constraining the fitting parameters too stringently resulted in poor fits in some cases. Thus, the only contraints used are $a > 0$ (peaks with negative amplitude are not permitted) and $c > 0.05$ (peaks whose widths are sufficiently narrow are not permitted). To allow the user to check each fit for goodness, the program queries after each fit.

The main procedure is FitPlate_multipeak.ipf, which also requires Multigauss_fit.ipf and MyAutomaticallyFindPeaks.ipf. Routines are included below.

```
--------------------FitPlate_multipeak.ipf--------------------
#pragma rtGlobals=3
#include <Peak AutoFind>
Function FitPlate_multipeak()
```

```
//Uses the sub-procedure Multigauss_fit to fit individual spectra to
a sum of N Gaussians.  N is determined for each spectrum using a
modified version of Igor Pro's MyAutomaticallyFindPeaks.ipf

Wave Wavel_
Wave A1,A2,A3,A4,A5,A6,A7,A8,A9,A10,A11,A12,A13,A14,A15,A16,A17,A18,
A19,A20,A21,A22,A23,A24
Wave B1,C1,D1,E1,B2,C2,D2,E2,B3,C3,D3,E3,B4,C4,D4,E4,B5,C5,D5,E5,B6,
C6,D6,E6,B7,C7,D7,E7,B8,C8,D8,E8,B9,C9,D9,E9,B10,C10,D10,E10,B11,C11
,D11,E11,B12,C12,D12,E12,B13,C13,D13,E13,B14,C14,D14,E14,B15,C15,D15
,E15,B16,C16,D16,E16,B17,C17,D17,E17,B18,C18,D18,E18,B19,C19,D19,E19
,B20,C20,D20,E20,B21,C21,D21,E21,B22,C22,D22,E22,B23,C23,D23,E23,B24
,C24,D24,E24
Wave F1,G1,H1,I1,F2,G2,H2,I2,F3,G3,H3,I3,F4,G4,H4,I4,F5,G5,H5,I5,F6,
G6,H6,I6,F7,G7,H7,I7,F8,G8,H8,I8,F9,G9,H9,I9,F10,G10,H10,I10,F11,G11
,H11,I11,F12,G12,H12,I12,F13,G13,H13,I13,F14,G14,H14,I14,F15,G15,H15
,I15,F16,G16,H16,I16,F17,G17,H17,I17,F18,G18,H18,I18,F19,G19,H19,I19
,F20,G20,H20,I20,F21,G21,H21,I21,F22,G22,H22,I22,F23,G23,H23,I23,F24
,G24,H24,I24
Wave J1,K1W,L1,J2,K2W,L2,J3,K3W,L3,J4,K4W,L4,J5,K5W,L5,J6,K6W,L6,J7,
K7W,L7,J8,K8W,L8,J9,K9W,L9,J10,K10W,L10,J11,K11W,L11,J12,K12W,L12,J1
3,K13W,L13,J14,K14W,L14,J15,K15W,L15,J16,K16W,L16,J17,K17W,L17,J18,K
18W,L18,J19,K19W,L19,J20,K20,L20,J21,K21,L21,J22,K22,L22,J23,K23,L23
,J24,K24,L24
Wave    M1,N1,O1,P1,M2,N2,O2,P2,M3,N3,O3,P3,M4,N4,O4,P4,M5,N5,O5,P5,
M6,N6,O6,P6,M7,N7,O7,P7,M8,N8,O8,P8,M9,N9,O9,P9,M10,N10,O10,P10,M11,
```

```
N11,O11,P11,M12,N12,O12,P12,M13,N13,O13,P13,M14,N14,O14,P14,M15,N15,
O15,P15,M16,N16,O16,P16,M17,N17,O17,P17,M18,N18,O18,P18,M19,N19,O19,
P19,M20,N20,O20,P20,M21,N21,O21,P21,M22,N22,O22,P22,M23,N23,O23,P23,
M24,N24,O24,P24

Variable i, j, k, av=0.0, sdev=0.0;
String wave_index, fit_wave_index;

//Want to pause and compare each spectrum to its fit?  Then flag = 1
Variable flag = 0;

//GaussFit contains fit parameters from the procedure Multigauss_fit
Make/N=(384,12)/O GaussFit= 0.0;
Make/N=(384,12)/O FitError = 0.0;
Make/N=(384,3)/O GaussFWHM = 0.0;

//Convert wavelength in nm to energy in eV
//226 is the length of traces measured by Tecan, use 201 to cut out
everything above 800 nm
Wave Energy
If(WaveExists(Energy) == 0)
     Make/N=(numpnts(Wavel_))  Energy  =  (4.136e-15)*(2.998e8)/(1e-
9*Wavel_);
Else
     Energy = (4.136e-15)*(2.998e8)/(1e-9*Wavel_);
Endif
```

```
Make/N=12/O allgauss=0;
Make/N=12/O W_sigma=0;
Make/N=12/O errorgauss=0;

//GaussFit contains all W_coef values for all waves
//    fit_wave    =    W_coef[0]    +    W_coef[1]    *    exp(-((x    -
W_coef[2])/W_coef[3])^2)
// FWHM = 2 * sqrt(2 * ln(2)) * W_coef[3]

Display  //prevent fit waves appended to open graphs

//iterate over all waves
For (i=1;i<25;i+=1)
      //Waves starting with A
      j = (i-1) + 0*24
      wave_index = "A" + num2str(i);
      fit_wave_index = "fit_A" + num2str(i);
      if(WaveExists($wave_index))
            wave wave_temp = $wave_index
            wave fit_wave_temp = $fit_wave_index
            Multigauss_fit(Energy, wave_temp)
            For (k=0; k<12; k+=1)
                  GaussFit[j][k] =  allgauss[k]
                  FitError[j][k] = errorgauss[k]
            Endfor
            If(flag == 1)
```

```
            DoWindow/k graph0; Display;
            Appendtograph wave_temp vs Energy;
            Appendtograph fit_wave_temp
            NewPanel /K=2 /W=(187,368,437,531) as "Pause"
            // Set to an unlikely name
            DoWindow/C tmp_PauseforCursor
            AutoPositionWindow/E/M=1/R=Graph0
            // Put panel near the graph
            Button             button0,pos={80,58},size={92,20},
      title="Continue"
            Button button0,proc=UserCursorAdjust_ContButtonProc
            PauseForUser tmp_PauseforCursor,Graph0
      EndIf
EndIf
//Waves starting with B
j = (i-1) + 1*24
wave_index = "B" + num2str(i)
fit_wave_index = "fit_B" + num2str(i);
if(WaveExists($wave_index))
      wave wave_temp = $wave_index
      wave fit_wave_temp = $fit_wave_index
      Multigauss_fit(Energy, wave_temp)
      For (k=0; k<12; k+=1)
            GaussFit[j][k] =  allgauss[k]
            FitError[j][k] = errorgauss[k]
      Endfor
```

```
      If(flag == 1)
            DoWindow/k graph0; Display;
            Appendtograph wave_temp vs Energy;
            Appendtograph fit_wave_temp
            NewPanel /K=2 /W=(187,368,437,531) as "Pause"
            // Set to an unlikely name
            DoWindow/C tmp_PauseforCursor
            AutoPositionWindow/E/M=1/R=Graph0
            // Put panel near the graph
            Button             button0,pos={80,58},size={92,20},
      title="Continue"
            Button button0,proc=UserCursorAdjust_ContButtonProc
            PauseForUser tmp_PauseforCursor,Graph0
      EndIf
EndIf
//Waves starting with C
j = (i-1) + 2*24
wave_index = "C" + num2str(i)
fit_wave_index = "fit_C" + num2str(i);
if(WaveExists($wave_index))
      wave wave_temp = $wave_index
      wave fit_wave_temp = $fit_wave_index
      Multigauss_fit(Energy, wave_temp)
      For (k=0; k<12; k+=1)
            GaussFit[j][k] =  allgauss[k]
            FitError[j][k] = errorgauss[k]
```

```
      Endfor
      If(flag == 1)
            DoWindow/k graph0; Display;
            Appendtograph wave_temp vs Energy;
            Appendtograph fit_wave_temp
            NewPanel /K=2 /W=(187,368,437,531) as "Pause"
            // Set to an unlikely name
            DoWindow/C tmp_PauseforCursor
            AutoPositionWindow/E/M=1/R=Graph0
            // Put panel near the graph
            Button             button0,pos={80,58},size={92,20},
      title="Continue"
            Button button0,proc=UserCursorAdjust_ContButtonProc
            PauseForUser tmp_PauseforCursor,Graph0
      EndIf
EndIf
//Waves starting with D
j = (i-1) + 3*24
wave_index = "D" + num2str(i)
fit_wave_index = "fit_D" + num2str(i);
if(WaveExists($wave_index))
      wave wave_temp = $wave_index
      wave fit_wave_temp = $fit_wave_index
      Multigauss_fit(Energy, wave_temp)
      For (k=0; k<12; k+=1)
            GaussFit[j][k] =  allgauss[k]
```

```
            FitError[j][k] = errorgauss[k]
      Endfor
      If(flag == 1)
            DoWindow/k graph0; Display;
            Appendtograph wave_temp vs Energy;
            Appendtograph fit_wave_temp
            NewPanel /K=2 /W=(187,368,437,531) as "Pause"
            // Set to an unlikely name
            DoWindow/C tmp_PauseforCursor
            AutoPositionWindow/E/M=1/R=Graph0
            // Put panel near the graph
            Button             button0,pos={80,58},size={92,20},
      title="Continue"
            Button button0,proc=UserCursorAdjust_ContButtonProc
            PauseForUser tmp_PauseforCursor,Graph0
      EndIf
EndIf
//Waves starting with E
j = (i-1) + 4*24
wave_index = "E" + num2str(i)
fit_wave_index = "fit_E" + num2str(i);
if(WaveExists($wave_index))
      wave wave_temp = $wave_index
      wave fit_wave_temp = $fit_wave_index
      Multigauss_fit(Energy, wave_temp)
      For (k=0; k<12; k+=1)
```

```
            GaussFit[j][k] =  allgauss[k]
            FitError[j][k] = errorgauss[k]
      Endfor
      If(flag == 1)
            DoWindow/k graph0; Display;
            Appendtograph wave_temp vs Energy;
            Appendtograph fit_wave_temp
            NewPanel /K=2 /W=(187,368,437,531) as "Pause"
            // Set to an unlikely name
            DoWindow/C tmp_PauseforCursor
            AutoPositionWindow/E/M=1/R=Graph0
            // Put panel near the graph
            Button             button0,pos={80,58},size={92,20},
      title="Continue"
            Button button0,proc=UserCursorAdjust_ContButtonProc
            PauseForUser tmp_PauseforCursor,Graph0
      EndIf
EndIf
//Waves starting with F
j = (i-1) + 5*24
wave_index = "F" + num2str(i)
fit_wave_index = "fit_F" + num2str(i);
if(WaveExists($wave_index))
      wave wave_temp = $wave_index
      wave fit_wave_temp = $fit_wave_index
      Multigauss_fit(Energy, wave_temp)
```

```
      For (k=0; k<12; k+=1)
            GaussFit[j][k] =  allgauss[k]
            FitError[j][k] = errorgauss[k]
      Endfor
      If(flag == 1)
            DoWindow/k graph0; Display;
            Appendtograph wave_temp vs Energy;
            Appendtograph fit_wave_temp
            NewPanel /K=2 /W=(187,368,437,531) as "Pause"
            // Set to an unlikely name
            DoWindow/C tmp_PauseforCursor
            AutoPositionWindow/E/M=1/R=Graph0
            // Put panel near the graph
            Button             button0,pos={80,58},size={92,20},
      title="Continue"
            Button button0,proc=UserCursorAdjust_ContButtonProc
            PauseForUser tmp_PauseforCursor,Graph0
      EndIf
EndIf
//Waves starting with G
j = (i-1) + 6*24
wave_index = "G" + num2str(i)
fit_wave_index = "fit_G" + num2str(i);
if(WaveExists($wave_index))
      wave wave_temp = $wave_index
      wave fit_wave_temp = $fit_wave_index
```

```
      Multigauss_fit(Energy, wave_temp)
      For (k=0; k<12; k+=1)
            GaussFit[j][k] =  allgauss[k]
            FitError[j][k] = errorgauss[k]
      Endfor
      If(flag == 1)
            DoWindow/k graph0; Display;
            Appendtograph wave_temp vs Energy;
            Appendtograph fit_wave_temp
            NewPanel /K=2 /W=(187,368,437,531) as "Pause"
            // Set to an unlikely name
            DoWindow/C tmp_PauseforCursor
            AutoPositionWindow/E/M=1/R=Graph0
            // Put panel near the graph
            Button             button0,pos={80,58},size={92,20},
      title="Continue"
            Button button0,proc=UserCursorAdjust_ContButtonProc
            PauseForUser tmp_PauseforCursor,Graph0
      EndIf
EndIf
//Waves starting with H
j = (i-1) + 7*24
wave_index = "H" + num2str(i)
fit_wave_index = "fit_H" + num2str(i);
if(WaveExists($wave_index))
      wave wave_temp = $wave_index
```

```
      wave fit_wave_temp = $fit_wave_index
      Multigauss_fit(Energy, wave_temp)
      For (k=0; k<12; k+=1)
            GaussFit[j][k] =  allgauss[k]
            FitError[j][k] = errorgauss[k]
      Endfor
      If(flag == 1)
            DoWindow/k graph0; Display;
            Appendtograph wave_temp vs Energy;
            Appendtograph fit_wave_temp
            NewPanel /K=2 /W=(187,368,437,531) as "Pause"
            // Set to an unlikely name
            DoWindow/C tmp_PauseforCursor
            AutoPositionWindow/E/M=1/R=Graph0
            // Put panel near the graph
            Button             button0,pos={80,58},size={92,20},
      title="Continue"
            Button button0,proc=UserCursorAdjust_ContButtonProc
            PauseForUser tmp_PauseforCursor,Graph0
      EndIf
EndIf
//Waves starting with I
j = (i-1) + 8*24
wave_index = "I" + num2str(i)
fit_wave_index = "fit_I" + num2str(i);
if(WaveExists($wave_index))
```

```
	wave wave_temp = $wave_index
	wave fit_wave_temp = $fit_wave_index
	Multigauss_fit(Energy, wave_temp)
	For (k=0; k<12; k+=1)
		GaussFit[j][k] =  allgauss[k]
		FitError[j][k] = errorgauss[k]
	Endfor
	If(flag == 1)
		DoWindow/k graph0; Display;
		Appendtograph wave_temp vs Energy;
		Appendtograph fit_wave_temp
		NewPanel /K=2 /W=(187,368,437,531) as "Pause"
		// Set to an unlikely name
		DoWindow/C tmp_PauseforCursor
		AutoPositionWindow/E/M=1/R=Graph0
		// Put panel near the graph
		Button             button0,pos={80,58},size={92,20},
	title="Continue"
		Button button0,proc=UserCursorAdjust_ContButtonProc
		PauseForUser tmp_PauseforCursor,Graph0
	EndIf
EndIf
//Waves starting with J
j = (i-1) + 9*24
wave_index = "J" + num2str(i)
fit_wave_index = "fit_J" + num2str(i);
```

```
if(WaveExists($wave_index))
      wave wave_temp = $wave_index
      wave fit_wave_temp = $fit_wave_index
      Multigauss_fit(Energy, wave_temp)
      For (k=0; k<12; k+=1)
            GaussFit[j][k] =  allgauss[k]
            FitError[j][k] = errorgauss[k]
      Endfor
      If(flag == 1)
            DoWindow/k graph0; Display;
            Appendtograph wave_temp vs Energy;
            Appendtograph fit_wave_temp
            NewPanel /K=2 /W=(187,368,437,531) as "Pause"
            // Set to an unlikely name
            DoWindow/C tmp_PauseforCursor
            AutoPositionWindow/E/M=1/R=Graph0
            // Put panel near the graph
            Button             button0,pos={80,58},size={92,20},
      title="Continue"
            Button button0,proc=UserCursorAdjust_ContButtonProc
            PauseForUser tmp_PauseforCursor,Graph0
      EndIf
EndIf
//Waves starting with K
j = (i-1) + 10*24
If (i<20)
```

```
wave_index = "K" + num2str(i) + "W"
fit_wave_index = "fit_K" + num2str(i) + "W";
if(WaveExists($wave_index))
      wave wave_temp = $wave_index
      wave fit_wave_temp = $fit_wave_index
      Multigauss_fit(Energy, wave_temp)
      For (k=0; k<12; k+=1)
            GaussFit[j][k] =  allgauss[k]
            FitError[j][k] = errorgauss[k]
      Endfor
      If(flag == 1)
            DoWindow/k graph0; Display;
            Appendtograph wave_temp vs Energy;
            Appendtograph fit_wave_temp
            NewPanel /K=2 /W=(187,368,437,531) as "Pause"
            // Set to an unlikely name
            DoWindow/C tmp_PauseforCursor
            AutoPositionWindow/E/M=1/R=Graph0
            // Put panel near the graph
            Button             button0,pos={80,58},size={92,20},
      title="Continue"
            Button button0,proc=UserCursorAdjust_ContButtonProc
            PauseForUser tmp_PauseforCursor,Graph0
      EndIf
EndIf
```

```
ElseIf (i > 19)
wave_index = "K" + num2str(i)
fit_wave_index = "fit_K" + num2str(i);
if(WaveExists($wave_index))
      wave wave_temp = $wave_index
      wave fit_wave_temp = $fit_wave_index
      Multigauss_fit(Energy, wave_temp)
      For (k=0; k<12; k+=1)
            GaussFit[j][k] =  allgauss[k]
            FitError[j][k] = errorgauss[k]
      Endfor
      If(flag == 1)
            DoWindow/k graph0; Display;
            Appendtograph wave_temp vs Energy;
            Appendtograph fit_wave_temp
            NewPanel /K=2 /W=(187,368,437,531) as "Pause"
            // Set to an unlikely name
            DoWindow/C tmp_PauseforCursor
            AutoPositionWindow/E/M=1/R=Graph0
            // Put panel near the graph
            Button             button0,pos={80,58},size={92,20},
      title="Continue"
            Button button0,proc=UserCursorAdjust_ContButtonProc
            PauseForUser tmp_PauseforCursor,Graph0
      EndIf
EndIf
```

```
EndIf
//Waves starting with L
j =(i-1) + 11*24
wave_index = "L" + num2str(i)
fit_wave_index = "fit_L" + num2str(i);
if(WaveExists($wave_index))
      wave wave_temp = $wave_index
      wave fit_wave_temp = $fit_wave_index
      Multigauss_fit(Energy, wave_temp)
      For (k=0; k<12; k+=1)
            GaussFit[j][k] =  allgauss[k]
            FitError[j][k] = errorgauss[k]
      Endfor
      If(flag == 1)
            DoWindow/k graph0; Display;
            Appendtograph wave_temp vs Energy;
            Appendtograph fit_wave_temp
            NewPanel /K=2 /W=(187,368,437,531) as "Pause"
            // Set to an unlikely name
            DoWindow/C tmp_PauseforCursor
            AutoPositionWindow/E/M=1/R=Graph0
            // Put panel near the graph
            Button             button0,pos={80,58},size={92,20},
      title="Continue"
            Button button0,proc=UserCursorAdjust_ContButtonProc
            PauseForUser tmp_PauseforCursor,Graph0
```

```
      EndIf
EndIf
//Waves starting with M
j = (i-1) + 12*24
wave_index = "M" + num2str(i)
fit_wave_index = "fit_M" + num2str(i);
if(WaveExists($wave_index))
      wave wave_temp = $wave_index
      wave fit_wave_temp = $fit_wave_index
      Multigauss_fit(Energy, wave_temp)
      For (k=0; k<12; k+=1)
            GaussFit[j][k] =  allgauss[k]
            FitError[j][k] = errorgauss[k]
      Endfor
      If(flag == 1)
            DoWindow/k graph0; Display;
            Appendtograph wave_temp vs Energy;
            Appendtograph fit_wave_temp
            NewPanel /K=2 /W=(187,368,437,531) as "Pause"
            // Set to an unlikely name
            DoWindow/C tmp_PauseforCursor
            AutoPositionWindow/E/M=1/R=Graph0
            // Put panel near the graph
            Button             button0,pos={80,58},size={92,20},
      title="Continue"
            Button button0,proc=UserCursorAdjust_ContButtonProc
```

```
            PauseForUser tmp_PauseforCursor,Graph0
      EndIf
EndIf
//Waves starting with N
j = (i-1) + 13*24
wave_index = "N" + num2str(i)
fit_wave_index = "fit_N" + num2str(i);
if(WaveExists($wave_index))
      wave wave_temp = $wave_index
      wave fit_wave_temp = $fit_wave_index
      Multigauss_fit(Energy, wave_temp)
      For (k=0; k<12; k+=1)
            GaussFit[j][k] =  allgauss[k]
            FitError[j][k] = errorgauss[k]
      Endfor
      If(flag == 1)
            DoWindow/k graph0; Display;
            Appendtograph wave_temp vs Energy;
            Appendtograph fit_wave_temp
            NewPanel /K=2 /W=(187,368,437,531) as "Pause"
            // Set to an unlikely name
            DoWindow/C tmp_PauseforCursor
            AutoPositionWindow/E/M=1/R=Graph0
            // Put panel near the graph
            Button             button0,pos={80,58},size={92,20},
      title="Continue"
```

```
            Button button0,proc=UserCursorAdjust_ContButtonProc
            PauseForUser tmp_PauseforCursor,Graph0
      EndIf
EndIf
//Waves starting with O
j = (i-1) + 14*24
wave_index = "O" + num2str(i)
fit_wave_index = "fit_O" + num2str(i);
if(WaveExists($wave_index))
      wave wave_temp = $wave_index
      wave fit_wave_temp = $fit_wave_index
      Multigauss_fit(Energy, wave_temp)
      For (k=0; k<12; k+=1)
            GaussFit[j][k] =  allgauss[k]
            FitError[j][k] = errorgauss[k]
      Endfor
      If(flag == 1)
            DoWindow/k graph0; Display;
            Appendtograph wave_temp vs Energy;
            Appendtograph fit_wave_temp
            NewPanel /K=2 /W=(187,368,437,531) as "Pause"
            // Set to an unlikely name
            DoWindow/C tmp_PauseforCursor
            AutoPositionWindow/E/M=1/R=Graph0
            // Put panel near the graph
```

```
            Button              button0,pos={80,58},size={92,20},
      title="Continue"
            Button button0,proc=UserCursorAdjust_ContButtonProc
            PauseForUser tmp_PauseforCursor,Graph0
      EndIf
EndIf
//Waves starting with P
j = (i-1) + 15*24
wave_index = "P" + num2str(i)
fit_wave_index = "fit_P" + num2str(i);
if(WaveExists($wave_index))
      wave wave_temp = $wave_index
      wave fit_wave_temp = $fit_wave_index
      Multigauss_fit(Energy, wave_temp)
      For (k=0; k<12; k+=1)
            GaussFit[j][k] =  allgauss[k]
            FitError[j][k] = errorgauss[k]
      Endfor
      If(flag == 1)
            DoWindow/k graph0; Display;
            Appendtograph wave_temp vs Energy;
            Appendtograph fit_wave_temp
            NewPanel /K=2 /W=(187,368,437,531) as "Pause"
            // Set to an unlikely name
            DoWindow/C tmp_PauseforCursor
            AutoPositionWindow/E/M=1/R=Graph0
```

```
                // Put panel near the graph
                Button             button0,pos={80,58},size={92,20},
          title="Continue"
                Button button0,proc=UserCursorAdjust_ContButtonProc
                PauseForUser tmp_PauseforCursor,Graph0
          EndIf
     EndIf
Endfor
//Calculate the full width at half-maximum, FWHM, from W_coef[3]
For (i=0; i< 384; i += 1)
     For(j=0; j<3; j += 1)
          GaussFWHM[i][j] = 2*sqrt(ln(2))*GaussFit[i][3+4*j];
     EndFor
EndFor
Edit GaussFit
AppendtoTable FitError,  GaussFWHM
End



//Procedure for pausing functionality
Function UserCursorAdjust_ContButtonProc(ctrlName) : ButtonControl
     String ctrlName
     DoWindow/K tmp_PauseforCursor         // Kill self
End
```

```
--------------------Multigauss_fit.ipf--------------------
#pragma rtGlobals=3
#include <Peak AutoFind>

Function Multigauss_fit(xwave,ywave)
//This procedure creates the wave allgauss, which contains fit parameters for a sum of N Gaussians: allgauss = {K0_1,K1_1,K2_1,K3_1,K0_2,K1_2,K2_2,K3_2,K0_3,K1_3,K2_3,K3_3}
//For each Gaussian fit N, f(x) = K0_N + K1_N exp(-(x-K2_N)^2/K3_N^2)
//Flags: /M=2 calculates covariant matrix, /N=1 suppresses updates during fits, /Q=1 suppresses printing to history, /W=0 "do not wait" for user to click OK, /D default fit curve name "fit_wavename" /R calculates residuals

Wave xwave, ywave
Variable peak_number
//This procedure searches for the number of peaks occuring in a given (x,y) data set
MyAutomaticallyFindPeaks(ywave, xwave);
//Contains the results of the above procedure.  "peak_number" is the number N of identified peaks.
Wave W_AutoPeakInfo
peak_number = dimsize(W_autopeakinfo,0);

//Constrain all Gaussians to have maxima (no negative peaks)
Make/O/T/N=1 T_Constraints1
```

```
T_Constraints1[0] = {"K1 > 0", "K3 > 0.05"}
Make/O/T/N=2 T_Constraints2
T_Constraints2[0] = {"K1 > 0", "K5 > 0", "K7 > 0.05"}
Make/O/T/N=3 T_Constraints3
T_Constraints3[0] = {"K1 > 0", "K5 > 0", "K9 > 0", "K11 > 0.05"}

//Fits a spectrum to a sum of N Gaussians. N is identified above.
Wave W_sigma
If(real(peak_number) == 1)
     Make/D/O gauss1 = {0, wavemax(ywave), W_AutoPeakInfo[0][0],
0.15};
     Make/D/O gauss2 = {NaN,NaN,NaN,NaN};
     Make/D/O gauss3 = {NaN,NaN,NaN,NaN};
     FuncFit/N/Q {{gauss, gauss1}} ywave/D/X = xwave
/C=T_Constraints1
     Make/D/O errorgauss = {W_sigma[0],W_sigma[1],W_sigma[2],
W_sigma[3],NaN,NaN,NaN,NaN,NaN,NaN,NaN,NaN}
Elseif(real(peak_number) == 2)
     Make/D/O gauss1 = {0, wavemax(ywave), W_AutoPeakInfo[0][0],
0.15};
     Make/D/O gauss2 = {0, wavemax(ywave),W_AutoPeakInfo[1][0],
0.15};
     Make/D/O gauss3 = {NaN,NaN,NaN,NaN};
     FuncFit/N/Q {{gauss, gauss1},{gauss, gauss2, hold="1"}}
ywave/D/X = xwave /C=T_Constraints2
```

```
	Make/D/O errorgauss = {W_sigma[0],W_sigma[1],W_sigma[2],
W_sigma[3],W_sigma[4],W_sigma[5],W_sigma[6],W_sigma[7],NaN,NaN,NaN,N
aN}
Elseif(real(peak_number) == 3)
	Make/D/O gauss1 = {0, wavemax(ywave), W_AutoPeakInfo[0][0],
0.15};
	Make/D/O gauss2 = {0, wavemax(ywave), W_AutoPeakInfo[1][0],
0.15};
	Make/D/O gauss3 = {0, wavemax(ywave), W_AutoPeakInfo[2][0],
0.15};
	FuncFit/N/Q {{gauss, gauss1},{gauss, gauss2, hold="1"},{gauss,
gauss3, hold="1"}} ywave/D/X = xwave /C=T_Constraints3
	Make/D/O errorgauss = {W_sigma[0],W_sigma[1],W_sigma[2],
W_sigma[3],W_sigma[4],W_sigma[5],W_sigma[6],W_sigma[7],W_sigma[8],W_
sigma[9],W_sigma[10],W_sigma[11]}
Endif
//Get rid of bad fits, like infinite values, values outside of the
400 - 850 nm range, etc.
If(gauss1[2] > 3.1)
	gauss1 = {NaN,NaN,NaN,NaN};
Endif
If(gauss2[2] > 3.1)
	gauss2 = {NaN,NaN,NaN,NaN};
Endif
If(gauss3[2] > 3.1)
	gauss3 = {NaN,NaN,NaN,NaN};
```

```
Endif


If(gauss1[2] < 1.45)
      gauss1 = {NaN,NaN,NaN,NaN};
Endif
If(gauss2[2] < 1.45)
      gauss2 = {NaN,NaN,NaN,NaN};
Endif
If(gauss3[2] < 1.45)
      gauss3 = {NaN,NaN,NaN,NaN};
Endif


If(gauss1[3] < 0)
      gauss1 = {NaN,NaN,NaN,NaN};
Endif
If(gauss2[3] < 0)
      gauss2 = {NaN,NaN,NaN,NaN};
Endif
If(gauss3[3] < 0)
      gauss3 = {NaN,NaN,NaN,NaN};
Endif


//Sort the ordering of results based on peak areas (peak amplitude
times peak width
Make/D/O  gauss_areas  =  {gauss1[1]*gauss1[3],gauss2[1]*gauss2[3],
gauss3[1]*gauss3[3]}
```

```
Variable test1, test2, test3
//numtype(variable) = 0 for numerical value, 1 for +- inf, 2 for NaN
     test1      =      numtype(gauss_areas[0]);      test2      =
numtype(gauss_areas[1]); test3 = numtype(gauss_areas[2]);

//Concatenate/O {gauss1, gauss2, gauss3}, allgauss
//Make/D/O    errorgauss    =    {W_sigma[0],W_sigma[1],W_sigma[2],
W_sigma[3],W_sigma[4],W_sigma[5],W_sigma[6],W_sigma[7],W_sigma[8],W_
sigma[9],W_sigma[10],W_sigma[11]}

//If all three peaks exist
If(test1==0&&test2==0&&test3==0)
     If(Wavemax(gauss_areas)       ==       gauss_areas[0]       &&
Wavemin(gauss_areas) == gauss_areas[2])
     Concatenate/O {gauss1, gauss2, gauss3}, allgauss
          Make/D/O errorgauss = {W_sigma[0],W_sigma[1],W_sigma[2],
W_sigma[3],W_sigma[4],W_sigma[5],W_sigma[6],W_sigma[7],W_sigma[8],W_
sigma[9],W_sigma[10],W_sigma[11]}
     ElseIf(Wavemax(gauss_areas)         ==         gauss_areas[0]&&
Wavemin(gauss_areas) == gauss_areas[1])
          Concatenate/O {gauss1, gauss3, gauss2}, allgauss
          Make/D/O errorgauss = {W_sigma[0],W_sigma[1],W_sigma[2],
W_sigma[3],W_sigma[8],W_sigma[9],W_sigma[10],W_sigma[11],W_sigma[4],
W_sigma[5],W_sigma[6],W_sigma[7]}
```

```
      ElseIf(Wavemax(gauss_areas)        ==        gauss_areas[1]&&
Wavemin(gauss_areas) == gauss_areas[2])
            Concatenate/O {gauss2, gauss1, gauss3}, allgauss
            Make/D/O                  errorgauss                  =
{W_sigma[4],W_sigma[5],W_sigma[6],W_sigma[7],W_sigma[0],W_sigma[1],W
_sigma[2],W_sigma[3],W_sigma[8],W_sigma[9],W_sigma[10],W_sigma[11]}
      ElseIf(Wavemax(gauss_areas)        ==        gauss_areas[1]&&
Wavemin(gauss_areas) ==gauss_areas[0])
            Concatenate/O {gauss2, gauss3, gauss1}, allgauss
            Make/D/O errorgauss = {W_sigma[4],W_sigma[5],W_sigma[6],
W_sigma[7],W_sigma[8],W_sigma[9],W_sigma[10],W_sigma[11],W_sigma[0],
W_sigma[1],W_sigma[2],W_sigma[3]}

      ElseIf(Wavemax(gauss_areas)                                    ==
gauss_areas[2]&&Wavemin(gauss_areas) == gauss_areas[1])
            Concatenate/O {gauss3, gauss1, gauss2}, allgauss
            Make/D/O                  errorgauss                  =
{W_sigma[8],W_sigma[9],W_sigma[10],W_sigma[11],W_sigma[0],W_sigma[1]
,W_sigma[2],W_sigma[3],W_sigma[4],W_sigma[5],W_sigma[6],W_sigma[7]}
      ElseIf(Wavemax(gauss_areas)                                    ==
gauss_areas[2]&&Wavemin(gauss_areas) == gauss_areas[0])
            Concatenate/O {gauss3, gauss2, gauss1}, allgauss
            Make/D/O errorgauss = {W_sigma[8],W_sigma[9],W_sigma[10],
W_sigma[11],W_sigma[4],W_sigma[5],W_sigma[6],W_sigma[7],W_sigma[0],W
_sigma[1],W_sigma[2],W_sigma[3]}
      EndIf
```

```
EndIf

//If one peak does not exist
If(test1==0&&test2==0&&test3>0)
      If(Wavemax(gauss_areas) ==gauss_areas[0])
            Concatenate/O {gauss1, gauss2, gauss3}, allgauss
            Make/D/O errorgauss = {W_sigma[0],W_sigma[1],W_sigma[2],
W_sigma[3],W_sigma[4],W_sigma[5],W_sigma[6],W_sigma[7],NaN,NaN,NaN,N
aN}
      ElseIf(Wavemax(gauss_areas) == gauss_areas[1])
            Concatenate/O {gauss2, gauss1, gauss3}, allgauss
            Make/D/O errorgauss = {W_sigma[4],W_sigma[5],W_sigma[6],
W_sigma[7],W_sigma[0],W_sigma[1],W_sigma[2],W_sigma[3],NaN,NaN,NaN,N
aN}
EndIf
ElseIf(test1==0&&test2>0&&test3==0)
      If(Wavemax(gauss_areas) == gauss_areas[0])
            Concatenate/O {gauss1, gauss3, gauss2}, allgauss
            Make/D/O errorgauss = {W_sigma[0],W_sigma[1],W_sigma[2],
W_sigma[3],W_sigma[8],W_sigma[9],W_sigma[10],W_sigma[11],NaN,NaN,NaN
,NaN}
      ElseIf(Wavemax(gauss_areas) == gauss_areas[2])
      Concatenate/O {gauss3,gauss1, gauss2}, allgauss
            Make/D/O errorgauss = {W_sigma[8],W_sigma[9],W_sigma[10],
W_sigma[11],W_sigma[0],W_sigma[1],W_sigma[2],W_sigma[3],NaN,NaN,NaN,
NaN}
```

```
EndIf
ElseIf(test1>0&&test2==0&&test3==0)
      If(Wavemax(gauss_areas) == gauss_areas[1])
            Concatenate/O {gauss2, gauss3, gauss1}, allgauss
            Make/D/O errorgauss = {W_sigma[4],W_sigma[5],W_sigma[6],
W_sigma[7],W_sigma[8],W_sigma[9],W_sigma[10],W_sigma[11],NaN,NaN,NaN
,NaN}
      ElseIf(Wavemax(gauss_areas) == gauss_areas[2])
      Concatenate/O {gauss3,gauss2, gauss1}, allgauss
            Make/D/O errorgauss = {W_sigma[8],W_sigma[9],W_sigma[10],
W_sigma[11],W_sigma[4],W_sigma[5],W_sigma[6],W_sigma[7],NaN,NaN,NaN,
NaN}
      EndIf
      //if only one peak exists
ElseIf(test1==0&&test2>0&&test3>0)
      Concatenate/O {gauss1, gauss2, gauss3}, allgauss
      Make/D/O   errorgauss   =   {W_sigma[0],W_sigma[1],W_sigma[2],
W_sigma[3],NaN,NaN,NaN,NaN,NaN,NaN,NaN,NaN}
ElseIf(test1>0&&test2==0&&test3>0)
      Concatenate/O {gauss2,gauss1, gauss3}, allgauss
      Make/D/O   errorgauss   =   {W_sigma[4],W_sigma[5],W_sigma[6],
W_sigma[7],NaN,NaN,NaN,NaN,NaN,NaN,NaN,NaN}
ElseIf(test1>0&&test2>0&&test3==0)
      Concatenate/O {gauss3,gauss1, gauss2}, allgauss
      Make/D/O   errorgauss   =   {W_sigma[8],W_sigma[9],W_sigma[10],
W_sigma[11],NaN,NaN,NaN,NaN,NaN,NaN,NaN,NaN}
```

```
//If no peaks exist
ElseIf(test1>0&&test2>0&&test3>0)
      Concatenate/O {gauss1,gauss2,gauss3}, allgauss
      Make/D/O     errorgauss     =     {NaN,NaN,NaN,NaN,NaN,NaN,NaN,
NaN,NaN,NaN,NaN,NaN}
EndIf
End
```

----------MyAutomaticallyFindPeaks.ipf----------

```
Function/C MyAutomaticallyFindPeaks(w,wx)
WAVE/Z w//=$wname
WAVE/Z wx//=$xdata
Variable maxPeaks=3, minPeakPercent=5
Variable pBegin=0, pEnd= numpnts(w)-1
Variable/C estimates= EstPeakNoiseAndSmfact(w,pBegin, pEnd)
Variable noiselevel=real(estimates)
Variable smoothingFactor=imag(estimates)
Variable     peaksFound=     AutoFindPeaks(w,pBegin,pEnd,noiseLevel,
smoothingFactor,maxPeaks)
if( peaksFound > 0 )
    WAVE W_AutoPeakInfo
    // Remove too-small peaks
    peaksFound=                  TrimAmpAutoPeakInfo(W_AutoPeakInfo,
minPeakPercent/100);
    if( peaksFound > 0 )
```

```
        // Make waves to display in a graph
        // The x values in W_AutoPeakInfo are still actually points,
not X
        Make/O/N=(peaksFound)           WA_PeakCentersY           =
w[W_AutoPeakInfo[p][0]]
        AdjustAutoPeakInfoForX(W_AutoPeakInfo,w,wx)
        Make/O/N=(peaksFound) WA_PeakCentersX = W_AutoPeakInfo[p][0]
        // Show W_AutoPeakInfo in a table, with dimension labels
        SetDimLabel 1, 0, center, W_AutoPeakInfo
        SetDimLabel 1, 1, width, W_AutoPeakInfo
        SetDimLabel 1, 2, height, W_AutoPeakInfo
        CheckDisplayed/A W_AutoPeakInfo
      Endif
Endif
End
```

G.2 Fitting for well plate format excitation spectra

A set of excitation spectra collected for various wells on a 384 well plate can be fitted with the Igor Pro script ExSpectraFit_Gauss.ipf and supplementary Fit_ex_spectrum.ipf. This routine separately fits both the UV peak of the excitation spectrum (230 nm – 306 nm) and the visible – near IR peak (> 330 nm). The region from 306 nm – 330 nm is omitted in order to omit leaking light at 314 nm in the Tecan plate reader.

```
--------------------ExSpectraFit_Gauss.ipf--------------------
#pragma rtGlobals=3
```

```
#include <Peak AutoFind>
Function ExSpectraFit_Gauss()
Wave Wavel_
Wave/Z A1,A2,A3,A4,A5,A6,A7,A8,A9,A10,A11,A12,A13,A14,A15,A16,
A17,A18,A19,A20,A21,A22,A23,A24
Wave/Z B1,C1,D1,E1,B2,C2,D2,E2,B3,C3,D3,E3,B4,C4,D4,E4,B5,C5,D5,E5,
B6,C6,D6,E6,B7,C7,D7,E7,B8,C8,D8,E8,B9,C9,D9,E9,B10,C10,D10,E10,B11,
C11,D11,E11,B12,C12,D12,E12,B13,C13,D13,E13,B14,C14,D14,E14,B15,C15,
D15,E15,B16,C16,D16,E16,B17,C17,D17,E17,B18,C18,D18,E18,B19,C19,D19,
E19,B20,C20,D20,E20,B21,C21,D21,E21,B22,C22,D22,E22,B23,C23,D23,E23,
B24,C24,D24,E24
Wave/Z F1,G1,H1,I1,F2,G2,H2,I2,F3,G3,H3,I3,F4,G4,H4,I4,F5,G5,H5,I5,
F6,G6,H6,I6,F7,G7,H7,I7,F8,G8,H8,I8,F9,G9,H9,I9,F10,G10,H10,I10,F11,
G11,H11,I11,F12,G12,H12,I12,F13,G13,H13,I13,F14,G14,H14,I14,F15,G15,
H15,I15,F16,G16,H16,I16,F17,G17,H17,I17,F18,G18,H18,I18,F19,G19,H19,
I19,F20,G20,H20,I20,F21,G21,H21,I21,F22,G22,H22,I22,F23,G23,H23,I23,
F24,G24,H24,I24
Wave/Z J1,K1W,L1,J2,K2W,L2,J3,K3W,L3,J4,K4W,L4,J5,K5W,L5,J6,K6W,L6,
J7,K7W,L7,J8,K8W,L8,J9,K9W,L9,J10,K10W,L10,J11,K11W,L11,J12,K12W,L12
,J13,K13W,L13,J14,K14W,L14,J15,K15W,L15,J16,K16W,L16,J17,K17W,L17,J1
8,K18W,L18,J19,K19W,L19,J20,K20,L20,J21,K21,L21,J22,K22,L22,J23,K23,
L23,J24,K24,L24
Wave/Z M1,N1,O1,P1,M2,N2,O2,P2,M3,N3,O3,P3,M4,N4,O4,P4,M5,N5,O5,P5,
M6,N6,O6,P6,M7,N7,O7,P7,M8,N8,O8,P8,M9,N9,O9,P9,M10,N10,O10,P10,M11,
N11,O11,P11,M12,N12,O12,P12,M13,N13,O13,P13,M14,N14,O14,P14,M15,N15,
O15,P15,M16,N16,O16,P16,M17,N17,O17,P17,M18,N18,O18,P18,M19,N19,O19,
```

```
P19,M20,N20,O20,P20,M21,N21,O21,P21,M22,N22,O22,P22,M23,N23,O23,P23,
M24,N24,O24,P24


Variable i, j, k, flag     //flag denotes whether peak-finding
program looks for peak wavelength or peak intensity
String wave_index
Variable/C get_peaks
Wave/Z UV_peak, Vis_peak, Vis_error, Energy
//preallocate memory for waves, or set exisiting waves to zero
If(WaveExists(UV_peak) == 0)
      Make/N=(384,3) UV_peak = 0
Elseif((WaveExists(UV_peak) ==1))
       UV_peak = 0
EndIf
If(WaveExists(Vis_peak) == 0)
      Make/N=(384,3) Vis_peak = 0
Elseif((WaveExists(Vis_peak) ==1))
      Vis_peak = 0
EndIf
If(WaveExists(Vis_error) == 0)
      Make/N=(384,2) Vis_error = 0
Elseif((WaveExists(Vis_error) ==1))
      Vis_error = 0
EndIf
If(WaveExists(Energy) == 0)
      Make/N=(DimSize(Wavel_,0)) Energy =0;
```

```
Endif
Energy = (4.136e-15)*(2.998e8)/(1e-9*Wavel_);
For (i=1;i<25;i+=1)
      //Waves starting with A
      j = (i-1) + 0*24 //assigns number from 1-384 to all waves for
final data arrays
      wave_index = "A" + num2str(i)
      If(WaveExists($wave_index)) //check if this well was measured
            flag = 1   //look for peak intensities
            get_peaks = Fit_ex_spectrum($wave_index,Energy,flag)
            UV_peak[j][0] = real(get_peaks)
            Vis_peak[j][0] = imag(get_peaks)
            flag = 2   //look for peak wavelengths
            get_peaks = Fit_ex_spectrum($wave_index,Energy,flag)
            UV_peak[j][1] = real(get_peaks)
            Vis_peak[j][1] = imag(get_peaks)
            flag = 3   //look for linewidths
            get_peaks = Fit_ex_spectrum($wave_index,Energy,flag)
            UV_peak[j][2] = 2*sqrt(ln(2))*real(get_peaks)
            Vis_peak[j][2] = 2*sqrt(ln(2))*imag(get_peaks)
            flag = 4   //look for standard deviations in fits to
visible excitation spectra
            get_peaks = Fit_ex_spectrum($wave_index,Energy,flag)
            Vis_error[j][0] = real(get_peaks)
            Vis_error[j][1] = 2*sqrt(ln(2))*imag(get_peaks)
      Else
```

```
      UV_peak[j][] = NaN
      Vis_peak[j][] = NaN
      Vis_error[j][] = NaN
EndIf
//Waves starting with B
j = (i-1) + 1*24
wave_index = "B" + num2str(i)
If(WaveExists($wave_index))
      flag = 1
      get_peaks = Fit_ex_spectrum($wave_index,Energy,flag)
      UV_peak[j][0] = real(get_peaks)
      Vis_peak[j][0] = imag(get_peaks)
      flag = 2
      get_peaks = Fit_ex_spectrum($wave_index,Energy,flag)
      UV_peak[j][1] = real(get_peaks)
      Vis_peak[j][1] = imag(get_peaks)
      flag = 3
      get_peaks = Fit_ex_spectrum($wave_index,Energy,flag)
      UV_peak[j][2] = 2*sqrt(ln(2))*real(get_peaks)
      Vis_peak[j][2] = 2*sqrt(ln(2))*imag(get_peaks)
      flag = 4
      get_peaks = Fit_ex_spectrum($wave_index,Energy,flag)
      Vis_error[j][0] = real(get_peaks)
      Vis_error[j][1] = 2*sqrt(ln(2))*imag(get_peaks)
Else
      UV_peak[j][] = NaN
```

```
      Vis_peak[j][] = NaN
      Vis_error[j][] = NaN
EndIf
//Waves starting with C
j = (i-1) + 2*24
wave_index = "C" + num2str(i)
If(WaveExists($wave_index))
      flag = 1
      get_peaks = Fit_ex_spectrum($wave_index,Energy,flag)
      UV_peak[j][0] = real(get_peaks)
      Vis_peak[j][0] = imag(get_peaks)
      flag = 2
      get_peaks = Fit_ex_spectrum($wave_index,Energy,flag)
      UV_peak[j][1] = real(get_peaks)
      Vis_peak[j][1] = imag(get_peaks)
      flag = 3
      get_peaks = Fit_ex_spectrum($wave_index,Energy,flag)
      UV_peak[j][2] = 2*sqrt(ln(2))*real(get_peaks)
      Vis_peak[j][2] = 2*sqrt(ln(2))*imag(get_peaks)
      flag = 4
      get_peaks = Fit_ex_spectrum($wave_index,Energy,flag)
      Vis_error[j][0] = real(get_peaks)
      Vis_error[j][1] = 2*sqrt(ln(2))*imag(get_peaks)
Else
      UV_peak[j][] = NaN
      Vis_peak[j][] = NaN
```

```
      Vis_error[j][] = NaN
EndIf
//Waves starting with D
j = (i-1) + 3*24
wave_index = "D" + num2str(i)
If(WaveExists($wave_index))
      flag = 1
      get_peaks = Fit_ex_spectrum($wave_index,Energy,flag)
      UV_peak[j][0] = real(get_peaks)
      Vis_peak[j][0] = imag(get_peaks)
      flag = 2
      get_peaks = Fit_ex_spectrum($wave_index,Energy,flag)
      UV_peak[j][1] = real(get_peaks)
      Vis_peak[j][1] = imag(get_peaks)
      flag = 3
      get_peaks = Fit_ex_spectrum($wave_index,Energy,flag)
      UV_peak[j][2] = 2*sqrt(ln(2))*real(get_peaks)
      Vis_peak[j][2] = 2*sqrt(ln(2))*imag(get_peaks)
      flag = 4
      get_peaks = Fit_ex_spectrum($wave_index,Energy,flag)
      Vis_error[j][0] = real(get_peaks)
      Vis_error[j][1] = 2*sqrt(ln(2))*imag(get_peaks)
Else
      UV_peak[j][] = NaN
      Vis_peak[j][] = NaN
      Vis_error[j][] = NaN
```

```
EndIf
//Waves starting with E
j = (i-1) + 4*24
wave_index = "E" + num2str(i)
If(WaveExists($wave_index))
      flag = 1
      get_peaks = Fit_ex_spectrum($wave_index,Energy,flag)
      UV_peak[j][0] = real(get_peaks)
      Vis_peak[j][0] = imag(get_peaks)
      flag = 2
      get_peaks = Fit_ex_spectrum($wave_index,Energy,flag)
      UV_peak[j][1] = real(get_peaks)
      Vis_peak[j][1] = imag(get_peaks)
      flag = 3
      get_peaks = Fit_ex_spectrum($wave_index,Energy,flag)
      UV_peak[j][2] = 2*sqrt(ln(2))*real(get_peaks)
      Vis_peak[j][2] = 2*sqrt(ln(2))*imag(get_peaks)
      flag = 4
      get_peaks = Fit_ex_spectrum($wave_index,Energy,flag)
      Vis_error[j][0] = real(get_peaks)
      Vis_error[j][1] = 2*sqrt(ln(2))*imag(get_peaks)
Else
      UV_peak[j][] = NaN
      Vis_peak[j][] = NaN
      Vis_error[j][] = NaN
EndIf
```

```
//Waves starting with F
j = (i-1) + 5*24
wave_index = "F" + num2str(i)
If(WaveExists($wave_index))
      flag = 1
      get_peaks = Fit_ex_spectrum($wave_index,Energy,flag)
      UV_peak[j][0] = real(get_peaks)
      Vis_peak[j][0] = imag(get_peaks)
      flag = 2
      get_peaks = Fit_ex_spectrum($wave_index,Energy,flag)
      UV_peak[j][1] = real(get_peaks)
      Vis_peak[j][1] = imag(get_peaks)
      flag = 3
      get_peaks = Fit_ex_spectrum($wave_index,Energy,flag)
      UV_peak[j][2] = 2*sqrt(ln(2))*real(get_peaks)
      Vis_peak[j][2] = 2*sqrt(ln(2))*imag(get_peaks)
      flag = 4
      get_peaks = Fit_ex_spectrum($wave_index,Energy,flag)
      Vis_error[j][0] = real(get_peaks)
      Vis_error[j][1] = 2*sqrt(ln(2))*imag(get_peaks)
Else
      UV_peak[j][] = NaN
      Vis_peak[j][] = NaN
      Vis_error[j][] = NaN
EndIf
//Waves starting with G
```

```
j = (i-1) + 6*24
wave_index = "G" + num2str(i)
If(WaveExists($wave_index))
      flag = 1
      get_peaks = Fit_ex_spectrum($wave_index,Energy,flag)
      UV_peak[j][0] = real(get_peaks)
      Vis_peak[j][0] = imag(get_peaks)
      flag = 2
      get_peaks = Fit_ex_spectrum($wave_index,Energy,flag)
      UV_peak[j][1] = real(get_peaks)
      Vis_peak[j][1] = imag(get_peaks)
      flag = 3
      get_peaks = Fit_ex_spectrum($wave_index,Energy,flag)
      UV_peak[j][2] = 2*sqrt(ln(2))*real(get_peaks)
      Vis_peak[j][2] = 2*sqrt(ln(2))*imag(get_peaks)
      flag = 4
      get_peaks = Fit_ex_spectrum($wave_index,Energy,flag)
      Vis_error[j][0] = real(get_peaks)
      Vis_error[j][1] = 2*sqrt(ln(2))*imag(get_peaks)
Else
      UV_peak[j][] = NaN
      Vis_peak[j][] = NaN
      Vis_error[j][] = NaN
EndIf
//Waves starting with H
j = (i-1) + 7*24
```

```
wave_index = "H" + num2str(i)
If(WaveExists($wave_index))
      flag = 1
      get_peaks = Fit_ex_spectrum($wave_index,Energy,flag)
      UV_peak[j][0] = real(get_peaks)
      Vis_peak[j][0] = imag(get_peaks)
      flag = 2
      get_peaks = Fit_ex_spectrum($wave_index,Energy,flag)
      UV_peak[j][1] = real(get_peaks)
      Vis_peak[j][1] = imag(get_peaks)
      flag = 3
      get_peaks = Fit_ex_spectrum($wave_index,Energy,flag)
      UV_peak[j][2] = 2*sqrt(ln(2))*real(get_peaks)
      Vis_peak[j][2] = 2*sqrt(ln(2))*imag(get_peaks)
      flag = 4
      get_peaks = Fit_ex_spectrum($wave_index,Energy,flag)
      Vis_error[j][0] = real(get_peaks)
      Vis_error[j][1] = 2*sqrt(ln(2))*imag(get_peaks)
Else
      UV_peak[j][] = NaN
      Vis_peak[j][] = NaN
      Vis_error[j][] = NaN
EndIf
//Waves starting with I
j = (i-1) + 8*24
wave_index = "I" + num2str(i)
```

```
If(WaveExists($wave_index))
      flag = 1
      get_peaks = Fit_ex_spectrum($wave_index,Energy,flag)
      UV_peak[j][0] = real(get_peaks)
      Vis_peak[j][0] = imag(get_peaks)
      flag = 2
      get_peaks = Fit_ex_spectrum($wave_index,Energy,flag)
      UV_peak[j][1] = real(get_peaks)
      Vis_peak[j][1] = imag(get_peaks)
      flag = 3
      get_peaks = Fit_ex_spectrum($wave_index,Energy,flag)
      UV_peak[j][2] = 2*sqrt(ln(2))*real(get_peaks)
      Vis_peak[j][2] = 2*sqrt(ln(2))*imag(get_peaks)
      flag = 4
      get_peaks = Fit_ex_spectrum($wave_index,Energy,flag)
      Vis_error[j][0] = real(get_peaks)
      Vis_error[j][1] = 2*sqrt(ln(2))*imag(get_peaks)
Else
      UV_peak[j][] = NaN
      Vis_peak[j][] = NaN
      Vis_error[j][] = NaN
EndIf
//Waves starting with J
j = (i-1) + 9*24
wave_index = "J" + num2str(i)
If(WaveExists($wave_index))
```

```
      flag = 1
      get_peaks = Fit_ex_spectrum($wave_index,Energy,flag)
      UV_peak[j][0] = real(get_peaks)
      Vis_peak[j][0] = imag(get_peaks)
      flag = 2
      get_peaks = Fit_ex_spectrum($wave_index,Energy,flag)
      UV_peak[j][1] = real(get_peaks)
      Vis_peak[j][1] = imag(get_peaks)
      flag = 3
      get_peaks = Fit_ex_spectrum($wave_index,Energy,flag)
      UV_peak[j][2] = 2*sqrt(ln(2))*real(get_peaks)
      Vis_peak[j][2] = 2*sqrt(ln(2))*imag(get_peaks)
      flag = 4
      get_peaks = Fit_ex_spectrum($wave_index,Energy,flag)
      Vis_error[j][0] = real(get_peaks)
      Vis_error[j][1] = 2*sqrt(ln(2))*imag(get_peaks)
Else
      UV_peak[j][] = NaN
      Vis_peak[j][] = NaN
      Vis_error[j][] = NaN
EndIf
//Waves starting with K
j = (i-1) + 10*24
If(i<20)
wave_index = "K" + num2str(i) + "W"
If(WaveExists($wave_index))
```

```
	flag = 1
	get_peaks = Fit_ex_spectrum($wave_index,Energy,flag)
	UV_peak[j][0] = real(get_peaks)
	Vis_peak[j][0] = imag(get_peaks)
	flag = 2
	get_peaks = Fit_ex_spectrum($wave_index,Energy,flag)
	UV_peak[j][1] = real(get_peaks)
	Vis_peak[j][1] = imag(get_peaks)
	flag = 3
	get_peaks = Fit_ex_spectrum($wave_index,Energy,flag)
	UV_peak[j][2] = 2*sqrt(ln(2))*real(get_peaks)
	Vis_peak[j][2] = 2*sqrt(ln(2))*imag(get_peaks)
	flag = 4
	get_peaks = Fit_ex_spectrum($wave_index,Energy,flag)
	Vis_error[j][0] = real(get_peaks)
	Vis_error[j][1] = 2*sqrt(ln(2))*imag(get_peaks)
	Else
		UV_peak[j][] = NaN
		Vis_peak[j][] = NaN
		Vis_error[j][] = NaN
	EndIf
ElseIf(i>19)
wave_index = "K" + num2str(i)
If(WaveExists($wave_index))
	flag = 1
	get_peaks = Fit_ex_spectrum($wave_index,Energy,flag)
```

```
      UV_peak[j][0] = real(get_peaks)
      Vis_peak[j][0] = imag(get_peaks)
      flag = 2
      get_peaks = Fit_ex_spectrum($wave_index,Energy,flag)
      UV_peak[j][1] = real(get_peaks)
      Vis_peak[j][1] = imag(get_peaks)
      flag = 3
      get_peaks = Fit_ex_spectrum($wave_index,Energy,flag)
      UV_peak[j][2] = 2*sqrt(ln(2))*real(get_peaks)
      Vis_peak[j][2] = 2*sqrt(ln(2))*imag(get_peaks)
      flag = 4
      get_peaks = Fit_ex_spectrum($wave_index,Energy,flag)
      Vis_error[j][0] = real(get_peaks)
      Vis_error[j][1] = 2*sqrt(ln(2))*imag(get_peaks)
Else
      UV_peak[j][] = NaN
      Vis_peak[j][] = NaN
      Vis_error[j][] = NaN
EndIf
EndIf
//Waves starting with L
j = (i-1) + 11*24
wave_index = "L" + num2str(i)
If(WaveExists($wave_index))
      flag = 1
      get_peaks = Fit_ex_spectrum($wave_index,Energy,flag)
```

```
      UV_peak[j][0] = real(get_peaks)
      Vis_peak[j][0] = imag(get_peaks)
      flag = 2
      get_peaks = Fit_ex_spectrum($wave_index,Energy,flag)
      UV_peak[j][1] = real(get_peaks)
      Vis_peak[j][1] = imag(get_peaks)
      flag = 3
      get_peaks = Fit_ex_spectrum($wave_index,Energy,flag)
      UV_peak[j][2] = 2*sqrt(ln(2))*real(get_peaks)
      Vis_peak[j][2] = 2*sqrt(ln(2))*imag(get_peaks)
      flag = 4
      get_peaks = Fit_ex_spectrum($wave_index,Energy,flag)
      Vis_error[j][0] = real(get_peaks)
      Vis_error[j][1] = 2*sqrt(ln(2))*imag(get_peaks)
Else
      UV_peak[j][] = NaN
      Vis_peak[j][] = NaN
      Vis_error[j][] = NaN
EndIf
//Waves starting with M
j = (i-1) + 12*24
wave_index = "M" + num2str(i)
If(WaveExists($wave_index))
      flag = 1
      get_peaks = Fit_ex_spectrum($wave_index,Energy,flag)
      UV_peak[j][0] = real(get_peaks)
```

```
	Vis_peak[j][0] = imag(get_peaks)
	flag = 2
	get_peaks = Fit_ex_spectrum($wave_index,Energy,flag)
	UV_peak[j][1] = real(get_peaks)
	Vis_peak[j][1] = imag(get_peaks)
	flag = 3
	get_peaks = Fit_ex_spectrum($wave_index,Energy,flag)
	UV_peak[j][2] = 2*sqrt(ln(2))*real(get_peaks)
	Vis_peak[j][2] = 2*sqrt(ln(2))*imag(get_peaks)
	flag = 4
	get_peaks = Fit_ex_spectrum($wave_index,Energy,flag)
	Vis_error[j][0] = real(get_peaks)
	Vis_error[j][1] = 2*sqrt(ln(2))*imag(get_peaks)
Else
	UV_peak[j][] = NaN
	Vis_peak[j][] = NaN
	Vis_error[j][] = NaN
EndIf
//Waves starting with N
j = (i-1) + 13*24
wave_index = "N" + num2str(i)
If(WaveExists($wave_index))
	flag = 1
	get_peaks = Fit_ex_spectrum($wave_index,Energy,flag)
	UV_peak[j][0] = real(get_peaks)
	Vis_peak[j][0] = imag(get_peaks)
```

```
	flag = 2
	get_peaks = Fit_ex_spectrum($wave_index,Energy,flag)
	UV_peak[j][1] = real(get_peaks)
	Vis_peak[j][1] = imag(get_peaks)
	flag = 3
	get_peaks = Fit_ex_spectrum($wave_index,Energy,flag)
	UV_peak[j][2] = 2*sqrt(ln(2))*real(get_peaks)
	Vis_peak[j][2] = 2*sqrt(ln(2))*imag(get_peaks)
	flag = 4
	get_peaks = Fit_ex_spectrum($wave_index,Energy,flag)
	Vis_error[j][0] = real(get_peaks)
	Vis_error[j][1] = 2*sqrt(ln(2))*imag(get_peaks)
Else
	UV_peak[j][] = NaN
	Vis_peak[j][] = NaN
	Vis_error[j][] = NaN
EndIf
//Waves starting with O
j = (i-1) + 14*24
wave_index = "O" + num2str(i)
If(WaveExists($wave_index))
	flag = 1
	get_peaks = Fit_ex_spectrum($wave_index,Energy,flag)
	UV_peak[j][0] = real(get_peaks)
	Vis_peak[j][0] = imag(get_peaks)
	flag = 2
```

```
      get_peaks = Fit_ex_spectrum($wave_index,Energy,flag)
      UV_peak[j][1] = real(get_peaks)
      Vis_peak[j][1] = imag(get_peaks)
      flag = 3
      get_peaks = Fit_ex_spectrum($wave_index,Energy,flag)
      UV_peak[j][2] = 2*sqrt(ln(2))*real(get_peaks)
      Vis_peak[j][2] = 2*sqrt(ln(2))*imag(get_peaks)
      flag = 4
      get_peaks = Fit_ex_spectrum($wave_index,Energy,flag)
      Vis_error[j][0] = real(get_peaks)
      Vis_error[j][1] = 2*sqrt(ln(2))*imag(get_peaks)
Else
      UV_peak[j][] = NaN
      Vis_peak[j][] = NaN
      Vis_error[j][] = NaN
EndIf
//Waves starting with P
j = (i-1) + 15*24     wave_index = "P" + num2str(i)
If(WaveExists($wave_index))
      flag = 1
      get_peaks = Fit_ex_spectrum($wave_index,Energy,flag)
      UV_peak[j][0] = real(get_peaks)
      Vis_peak[j][0] = imag(get_peaks)
      flag = 2
      get_peaks = Fit_ex_spectrum($wave_index,Energy,flag)
      UV_peak[j][1] = real(get_peaks)
```

```
            Vis_peak[j][1] = imag(get_peaks)
            flag = 3
            get_peaks = Fit_ex_spectrum($wave_index,Energy,flag)
            UV_peak[j][2] = 2*sqrt(ln(2))*real(get_peaks)
            Vis_peak[j][2] = 2*sqrt(ln(2))*imag(get_peaks)
            flag = 4
            get_peaks = Fit_ex_spectrum($wave_index,Energy,flag)
            Vis_error[j][0] = real(get_peaks)
            Vis_error[j][1] = 2*sqrt(ln(2))*imag(get_peaks)
      Else
            UV_peak[j][] = NaN
            Vis_peak[j][] = NaN
            Vis_error[j][] = NaN
      EndIf
Endfor
Edit UV_peak, Vis_peak
End

Function/C Fit_ex_spectrum(w,wx,flag)
Wave/Z w, wx
Variable flag         //Denotes whether procedure returns UV and Vis
peak wavelength (2) or intensity (1) or linewidth (3)
Variable UV_peak, Vis_peak
Variable/C UV_Vis_peaks //This variable is returned.
Make/O/N=4 W_coef, W_sigma
Make/O/D/N = (dimsize(w,0)) wx_right = wx;
```

```
Duplicate/D/O w, fit_wUV;
CurveFit/Q/NTHR=0 gauss  w[0,38] /X=wx_right /D=fit_wUV;  //Fit from
230 nm to 306 nm to avoid 314 nm peak from Tecan
if(flag == 1)
   UV_peak = W_coef[0] + W_coef[1]  //peak intensities
elseif(flag == 2)
   UV_peak = W_coef[2] //peak wavelengths
elseif(flag == 3)
   UV_peak = W_coef[3] //FWHM (linewidths)
endif
Duplicate/D/O w, fit_wVis;
//Fit from 330 nm to end of wave: visible excitation spectrum
CurveFit/Q/NTHR=0 gauss  w[50,dimsize(w,0)] /X=wx_right /D=fit_wVis;
if(flag == 1)
   Vis_peak = W_coef[0] + W_coef[1]  //peak intensities
elseif(flag == 2)
   Vis_peak = W_coef[2]          //peak wavelengths
elseif(flag == 3)
      Vis_peak = W_coef[3]  //FWHM (linewidths)
elseif(flag == 4)
//for flag = 4, UV_peak set to error in Vis peak wavelength (not
UV!), and Vis_peak set to error in Vis linewidth
      UV_peak = W_sigma[2]
      Vis_peak = W_sigma[3]
endif
```

```
dowindow/k graph0
Display;AppendToGraph w,fit_wUV, fit_wVis vs wx_right;
If(flag == 1)
   NewPanel /K=2 /W=(187,368,437,531) as "Pause"
   DoWindow/C tmp_PauseforCursor // Set to an unlikely name
   AutoPositionWindow/E/M=1/R=Graph0 // Put panel near graph
   Button button0,pos={80,58},size={92,20},title="Continue"
   Button button0,proc=UserCursorAdjust_ContButtonProc
   PauseForUser tmp_PauseforCursor,Graph0
EndIf
UV_Vis_peaks = cmplx(UV_peak, Vis_peak)
return(UV_Vis_peaks)
End
//Procedure for pausing functionality
Function UserCursorAdjust_ContButtonProc(ctrlName) : ButtonControl
String ctrlName
DoWindow/K tmp_PauseforCursor
End
```

References

(1) Phillpotts, E. *A Shadow Passes*; Cecil Palmer and Hayward: London, 1918.
(2) Binnig, G.; Rohrer, H.; Gerber, C.; Weibel, E. Surface Studies by Scanning Tunneling Microscopy. *Phys. Rev. Lett.* **1982**, *49* (1), 57–61.
(3) Binnig, G.; Quate, C. F.; Gerber, C. Atomic Force Microscope. *Phys. Rev. Lett.* **1986**, *56* (9), 930–933.
(4) Whitesides, G. M. Nanoscience, Nanotechnology, and Chemistry. *Small* **2005**, *1* (2), 172–179.
(5) Kreibig, U.; Vollmer, M. *Optical Properties of Metal Clusters*; Springer Series in Materials Science; Springer Berlin Heidelberg: Berlin, Heidelberg, 1995; Vol. 25.
(6) Schmid, G. Large Clusters and Colloids. Metals in the Embryonic State. *Chem. Rev.* **1992**, *92* (8), 1709–1727.
(7) de Heer, W. The Physics of Simple Metal Clusters: Experimental Aspects and Simple Models. *Rev. Mod. Phys.* **1993**, *65* (3), 611–676.
(8) Knight, W. D.; Clemenger, K.; de Heer, W. A.; Saunders, W. A.; Chou, M. Y.; Cohen, M. L. Electronic Shell Structure and Abundances of Sodium Clusters. *Phys. Rev. Lett.* **1984**, *52* (24), 2141–2143.
(9) Brack, M. The Physics of Simple Metal Clusters: Self-Consistent Jellium Model and Semiclassical Approaches. *Rev. Mod. Phys.* **1993**, *65* (3), 677–732.
(10) Schmid, G. Large Clusters and Colloids. Metals in the Embryonic State. *Chem. Rev.* **1992**, *92* (8), 1709–1727.
(11) Schmid, G.; Maihack, V.; Lantermann, F.; Peschel, S. Ligand-Stabilized Metal Clusters and Colloids: Properties and Applications. *J. Chem. Soc. Dalt. Trans.* **1996**, *0* (5), 589.
(12) Lu, Y.; Chen, W. Sub-Nanometre Sized Metal Clusters: From Synthetic Challenges to the Unique Property Discoveries. *Chem. Soc. Rev.* **2012**, *41* (9), 3594–3623.
(13) Shang, L.; Dong, S.; Nienhaus, G. U. Ultra-Small Fluorescent Metal Nanoclusters: Synthesis and Biological Applications. *Nano Today*. 2011, pp 401–418.
(14) Jin, R.; Zeng, C.; Zhou, M.; Chen, Y. Atomically Precise Colloidal Metal Nanoclusters and Nanoparticles: Fundamentals and Opportunities. *Chem. Rev.* **2016**, *116* (18), 10346–10413.
(15) Aiken, J. D.; Finke, R. G. Polyoxoanion- and Tetrabutylammonium-Stabilized Rh(0)(n) Nanoclusters: Unprecedented Nanocluster Catalytic Lifetime in Solution. *J. Am. Chem. Soc.* **1999**, *121* (38), 8803–8810.
(16) Marjomäki, V.; Lahtinen, T.; Martikainen, M.; Koivisto, J.; Malola, S.; Salorinne, K.; Pettersson, M.; Häkkinen, H. Site-Specific Targeting of Enterovirus Capsid by Functionalized Monodisperse Gold Nanoclusters. *Proc. Natl. Acad. Sci. U. S. A.* **2014**, *111* (4), 1277–1281.
(17) Koh, T.-W.; Hiszpanski, A. M.; Sezen, M.; Naim, A.; Galfsky, T.; Trivedi, A.; Loo, Y.-L.; Menon, V.; Rand, B. P.; Wang, Z. B.; et al. Metal Nanocluster Light-Emitting Devices with Suppressed Parasitic Emission and Improved Efficiency: Exploring the Impact of Photophysical Properties. *Nanoscale* **2015**, *7* (20), 9140–9146.
(18) Jadzinsky, P. D.; Calero, G.; Ackerson, C. J.; Bushnell, D. a; Kornberg, R. D. Structure of a Thiol Monolayer-Protected Gold Nanoparticle at 1.1 A Resolution. *Science* **2007**, *318* (5849), 430–433.

(19) Häkkinen, H. The Gold–sulfur Interface at the Nanoscale. *Nat. Chem.* **2012**, *4* (6), 443–455.
(20) Walter, M.; Akola, J.; Lopez-Acevedo, O.; Jadzinsky, P. D.; Calero, G.; Ackerson, C. J.; Whetten, R. L.; Grönbeck, H.; Häkkinen, H. A Unified View of Ligand-Protected Gold Clusters as Superatom Complexes. *Proc. Natl. Acad. Sci. U. S. A.* **2008**, *105* (27), 9157–9162.
(21) Häkkinen, H. Atomic and Electronic Structure of Gold Clusters: Understanding Flakes, Cages and Superatoms from Simple Concepts. *Chem. Soc. Rev.* **2008**, *37* (9), 1847–1859.
(22) Mathew, A.; Pradeep, T. Noble Metal Clusters: Applications in Energy, Environment, and Biology. *Part. Part. Syst. Charact.* **2014**, *31* (10), 1017–1053.
(23) Bloomfield, V. A.; Crothers, D. M.; Tinoco Jr., I. *Nucleic Acids: Structures, Properties, and Functions*; University Science Books, 2000, Ed.; University Science Books, 2000.
(24) Seeman, N. C. Nucleic Acid Junctions and Lattices. *J. Theor. Biol.* **1982**, *99* (2), 237–247.
(25) Winfree, E.; Liu, F.; Wenzler, L. A.; Seeman, N. C. Design and Self-Assembly of Two-Dimensional DNA Crystals. *Nature* **1998**, *394* (6693), 539–544.
(26) Yin, P.; Hariadi, R. F.; Sahu, S.; Choi, H. M. T.; Park, S. H.; Labean, T. H.; Reif, J. H. Programming DNA Tube Circumferences. *Science* **2008**, *321* (5890), 824–826.
(27) Rothemund, P. W. K. Folding DNA to Create Nanoscale Shapes and Patterns. *Nature* **2006**, *440* (7082), 297–302.
(28) Douglas, S. M.; Dietz, H.; Liedl, T.; Högberg, B.; Graf, F.; Shih, W. M. Self-Assembly of DNA into Nanoscale Three-Dimensional Shapes. *Nature* **2009**, *459* (7245), 414–418.
(29) Dietz, H.; Douglas, S. M.; Shih, W. M. Folding DNA into Twisted and Curved Nanoscale Shapes. *Science* **2009**, *325* (5941), 725–730.
(30) Ke, Y.; Ong, L. L.; Shih, W. M.; Yin, P. Three-Dimensional Structures Self-Assembled from DNA Bricks. *Science* **2012**, *338* (6111), 1177–1183.
(31) Zheng, J.; Birktoft, J. J.; Chen, Y.; Wang, T.; Sha, R.; Constantinou, P. E.; Ginell, S. L.; Mao, C.; Seeman, N. C. From Molecular to Macroscopic via the Rational Design of a Self-Assembled 3D DNA Crystal. *Nature* **2009**, *461* (7260), 74–77.
(32) Marras, A. E.; Zhou, L.; Su, H.-J.; Castro, C. E. Programmable Motion of DNA Origami Mechanisms. *Proc. Natl. Acad. Sci. U. S. A.* **2015**, *112* (3), 713–718.
(33) Gerling, T.; Wagenbauer, K. F.; Neuner, A. M.; Dietz, H. Dynamic DNA Devices and Assemblies Formed by Shape-Complementary, Non-Base Pairing 3D Components. *Science (80-.).* **2015**, *347* (6229), 1446–1452.
(34) Zheng, J.; Constantinou, P. E.; Micheel, C.; Alivisatos, A. P.; Kiehl, R. A.; Seeman, N. C. Two-Dimensional Nanoparticle Arrays Show the Organizational Power of Robust DNA Motifs. *Nano Lett.* **2006**, *6* (7), 1502–1504.
(35) Schreiber, R.; Do, J.; Roller, E.-M.; Zhang, T.; Schüller, V. J.; Nickels, P. C.; Feldmann, J.; Liedl, T. Hierarchical Assembly of Metal Nanoparticles, Quantum Dots and Organic Dyes Using DNA Origami Scaffolds. *Nat. Nanotechnol.* **2014**, *9* (1), 74–78.
(36) Funke, J. J.; Dietz, H. Placing Molecules with Bohr Radius Resolution Using DNA Origami. *Nat. Nanotechnol.* **2015**, *advance on* (October), 1–6.

(37) Stein, I. H.; Schüller, V.; Böhm, P.; Tinnefeld, P.; Liedl, T. Single-Molecule FRET Ruler Based on Rigid DNA Origami Blocks. *Chemphyschem* **2011**, *12* (3), 689–695.
(38) Kuzyk, A.; Schreiber, R.; Fan, Z.; Pardatscher, G.; Roller, E.-M.; Högele, A.; Simmel, F. C.; Govorov, A. O.; Liedl, T. DNA-Based Self-Assembly of Chiral Plasmonic Nanostructures with Tailored Optical Response. *Nature* **2012**, *483* (7389), 311–314.
(39) Shen, X.; Asenjo-Garcia, A.; Liu, Q.; Jiang, Q.; García de Abajo, F. J.; Liu, N.; Ding, B. Three-Dimensional Plasmonic Chiral Tetramers Assembled by DNA Origami. *Nano Lett.* **2013**, *13* (5), 2128–2133.
(40) Pilo-Pais, M.; Watson, A.; Demers, S.; LaBean, T. H.; Finkelstein, G. Surface-Enhanced Raman Scattering Plasmonic Enhancement Using DNA Origami-Based Complex Metallic Nanostructures. *Nano Lett.* **2014**, *14* (4), 2099–2104.
(41) Cutler, J. I.; Auyeung, E.; Mirkin, C. A. Spherical Nucleic Acids. *Journal of the American Chemical Society*. 2012, pp 1376–1391.
(42) Rogers, W. B.; Manoharan, V. N. Programming Colloidal Phase Transitions with DNA Strand Displacement. *Sci.* **2015**, *347* (February), 639–642.
(43) Pinheiro, A. V.; Han, D.; Shih, W. M.; Yan, H. Challenges and Opportunities for Structural DNA Nanotechnology. *Nat. Nanotechnol.* **2011**, *6* (12), 763–772.
(44) Marzilli, L. G. Metal-Ion Interactions with Nucleic Acids and Nucleic Acid Derivatives; John Wiley & Sons, Inc.; pp 255–378.
(45) Peyser, L. a; Vinson, a E.; Bartko, a P.; Dickson, R. M. Photoactivated Fluorescence from Individual Silver Nanoclusters. *Science (80-.).* **2001**, *291* (5501), 103–106.
(46) Zheng, J.; Dickson, R. M. Individual Water-Soluble Dendrimer-Encapsulated Silver Nanodot Fluorescence. *J. Am. Chem. Soc.* **2002**, *124* (47), 13982–13983.
(47) Petty, J. T.; Zheng, J.; Hud, N. V; Dickson, R. M. DNA-Templated Ag Nanocluster Formation. *J. Am. Chem. Soc.* **2004**, *126* (16), 5207–5212.
(48) Gwinn, E. G.; O'Neill, P.; Guerrero, A. J.; Bouwmeester, D.; Fygenson, D. K. Sequence-Dependent Fluorescence of DNA-Hosted Silver Nanoclusters. *Adv. Mater.* **2008**, *20* (2), 279–283.
(49) Gwinn, E.; Schultz, D.; Copp, S.; Swasey, S. DNA-Protected Silver Clusters for Nanophotonics. *Nanomaterials* **2015**, *5* (1), 180–207.
(50) O'Neill, P. R.; Gwinn, E. G.; Fygenson, D. K. UV Excitation of DNA Stabilized Ag Cluster Fluorescence via the DNA Bases. *J. Phys. Chem. C* **2011**, *115* (49), 24061–24066.
(51) Ritchie, C. M.; Johnsen, K. R.; Kiser, J. R.; Antoku, Y.; Dickson, R. M.; Petty, J. T. Ag Nanocluster Formation Using a Cytosine Oligonucleotide Template. *J. Phys. Chem. C. Nanomater. Interfaces* **2007**, *111* (1), 175–181.
(52) Schultz, D.; Gwinn, E. G. Silver Atom and Strand Numbers in Fluorescent and Dark Ag:DNAs. *Chem. Commun. (Camb).* **2012**, *48* (46), 5748–5750.
(53) Schultz, D.; Gardner, K.; Oemrawsingh, S. S. R.; Markešević, N.; Olsson, K.; Debord, M.; Bouwmeester, D.; Gwinn, E. Evidence for Rod-Shaped DNA-Stabilized Silver Nanocluster Emitters. *Adv. Mater.* **2013**, *25* (20), 2797–2803.
(54) Schultz, D. Correlating Optical and Physical Properties of Few-Atom, Fluorescent Silver Clusters, University of California, Santa Barbara, 2013.
(55) Yan, J.; Gao, S. Plasmon Resonances in Linear Atomic Chains: Free-Electron Behavior and Anisotropic Screening of D Electrons. *Phys. Rev. B* **2008**, *78* (23), 235413.

(56) Guidez, E. B.; Aikens, C. M. Theoretical Analysis of the Optical Excitation Spectra of Silver and Gold Nanowires. *Nanoscale* **2012**, *4* (14), 4190–4198.
(57) Markešević, N.; Oemrawsingh, S. S. R.; Schultz, D.; Gwinn, E. G.; Bouwmeester, D. Polarization Resolved Measurements of Individual DNA-Stabilized Silver Clusters. *Adv. Opt. Mater.* **2014**, *2* (8), 765–770.
(58) Copp, S. M.; Schultz, D.; Swasey, S.; Pavlovich, J.; Debord, M.; Chiu, A.; Olsson, K.; Gwinn, E. Magic Numbers in DNA-Stabilized Fluorescent Silver Clusters Lead to Magic Colors. *J. Phys. Chem. Lett.* **2014**, *5* (6), 959–963.
(59) Swasey, S. M.; Karimova, N.; Aikens, C. M.; Schultz, D. E.; Simon, A. J.; Gwinn, E. G. Chiral Electronic Transitions in Fluorescent Silver Clusters Stabilized by DNA. *ACS Nano* **2014**, *8* (7), 6883–6892.
(60) Yuan, Z.; Chen, Y.-C.; Li, H.-W.; Chang, H.-T. Fluorescent Silver Nanoclusters Stabilized by DNA Scaffolds. *Chem. Commun. (Camb).* **2014**, *50*, 9800–9815.
(61) Yu, J.; Choi, S.; Richards, C. I.; Antoku, Y.; Dickson, R. M. Live Cell Surface Labeling with Fluorescent Ag Nanocluster Conjugates. *Photochem. Photobiol.* **2008**, *84* (6), 1435–1439.
(62) Patel, S. a; Richards, C. I.; Hsiang, J.-C.; Dickson, R. M. Water-Soluble Ag Nanoclusters Exhibit Strong Two-Photon-Induced Fluorescence. *J. Am. Chem. Soc.* **2008**, *130* (35), 11602–11603.
(63) Vosch, T.; Antoku, Y.; Hsiang, J.-C.; Richards, C. I.; Gonzalez, J. I.; Dickson, R. M. Strongly Emissive Individual DNA-Encapsulated Ag Nanoclusters as Single-Molecule Fluorophores. *Proc. Natl. Acad. Sci. U. S. A.* **2007**, *104* (31), 12616–12621.
(64) Guo, W.; Yuan, J.; Wang, E. Oligonucleotide-Stabilized Ag Nanoclusters as Novel Fluorescence Probes for the Highly Selective and Sensitive Detection of the Hg2+ Ion. *Chem. Commun. (Camb).* **2009**, 3395–3397.
(65) Yeh, H.-C.; Sharma, J.; Han, J. J.; Martinez, J. S.; Werner, J. H. A DNA--Silver Nanocluster Probe That Fluoresces upon Hybridization. *Nano Lett.* **2010**, *10* (8), 3106–3110.
(66) Yeh, H.-C.; Sharma, J.; Shih, I.-M.; Vu, D. M.; Martinez, J. S.; Werner, J. H. A Fluorescence Light-up Ag Nanocluster Probe That Discriminates Single-Nucleotide Variants by Emission Color. *J. Am. Chem. Soc.* **2012**, *134* (28), 11550–11558.
(67) Lan, G.-Y.; Huang, C.-C.; Chang, H.-T. Silver Nanoclusters as Fluorescent Probes for Selective and Sensitive Detection of Copper Ions. *Chem. Commun. (Camb).* **2010**, *46* (8), 1257–1259.
(68) Yang, S. W.; Vosch, T. Rapid Detection of microRNA by a Silver Nanocluster DNA Probe. *Anal. Chem.* **2011**, *83* (18), 6935–6939.
(69) Shah, P.; Rørvig-Lund, A.; Chaabane, S. Ben; Thulstrup, P. W.; Kjaergaard, H. G.; Fron, E.; Hofkens, J.; Yang, S. W.; Vosch, T. Design Aspects of Bright Red Emissive Silver nanoclusters/DNA Probes for microRNA Detection. *ACS Nano* **2012**, *6* (10), 8803–8814.
(70) Copp, S. M.; Bogdanov, P.; Debord, M.; Singh, A.; Gwinn, E. Base Motif Recognition and Design of DNA Templates for Fluorescent Silver Clusters by Machine Learning. *Adv. Mater.* **2014**, *26* (33), 5839–5845.
(71) Schultz, D.; Copp, S. M.; Markešević, N.; Gardner, K.; Oemrawsingh, S. S. R.; Bouwmeester, D.; Gwinn, E. Dual-Color Nanoscale Assemblies of Structurally Stable, Few-Atom Silver Clusters, as Reported by Fluorescence Resonance Energy Transfer.

ACS Nano **2013**, *7* (11), 9798–9807.
(72) Copp, S. M.; Schultz, D. E.; Swasey, S.; Gwinn, E. G. Atomically Precise Arrays of Fluorescent Silver Clusters: A Modular Approach for Metal Cluster Photonics on DNA Nanostructures. *ACS Nano* **2015**, *9* (3), 2303–2310.
(73) O'Neill, P. R.; Young, K.; Schiffels, D.; Fygenson, D. K. Few-Atom Fluorescent Silver Clusters Assemble at Programmed Sites on DNA Nanotubes. *Nano Lett.* **2012**, *12* (11), 5464–5469.
(74) Copp, S. M.; Faris, A.; Swasey, S. M.; Gwinn, E. G. Heterogeneous Solvatochromism of Fluorescent DNA-Stabilized Silver Clusters Precludes Use of Simple Onsager-Based Stokes Shift Models. *J. Phys. Chem. Lett.* **2016**, *7*, 698–703.
(75) Patel, S. A.; Cozzuol, M.; Hales, J. M.; Richards, C. I.; Sartin, M.; Hsiang, J.-C.; Vosch, T.; Perry, J. W.; Dickson, R. M. Electron Transfer-Induced Blinking in Ag Nanodot Fluorescence. *J. Phys. Chem. C. Nanomater. Interfaces* **2009**, *113* (47), 20264–20270.
(76) Swasey, S. M.; Leal, L. E.; Lopez-Acevedo, O.; Pavlovich, J.; Gwinn, E. G. Silver (I) as DNA Glue: Ag(+)-Mediated Guanine Pairing Revealed by Removing Watson-Crick Constraints. *Sci. Rep.* **2015**, *5*, 10163.
(77) Espinosa Leal, L. A.; Karpenko, A.; Swasey, S.; Gwinn, E. G.; Rojas-Cervellera, V.; Rovira, C.; Lopez-Acevedo, O. The Role of Hydrogen Bonds in the Stabilization of Silver-Mediated Cytosine Tetramers. *J. Phys. Chem. Lett.* **2015**, *6* (20), 4061–4066.
(78) Swasey, S. M.; Gwinn, E. G. Silver-Mediated Base Pairings: Towards Dynamic DNA Nanostructures with Enhanced Chemical and Thermal Stability. *New J. Phys.* **2016**, *18* (4), 45008.
(79) Schön, G.; Simon, U. A Fascinating New Field in Colloid Science: Small Ligand-Stabilized Metal Clusters and Possible Application in Microelectronics. *Colloid Polym. Sci.* **1995**, *273* (2), 101–117.
(80) Daniel, M.-C.; Astruc, D. Gold Nanoparticles: Assembly, Supramolecular Chemistry, Quantum-Size-Related Properties, and Applications toward Biology, Catalysis, and Nanotechnology. *Chem. Rev.* **2004**, *104* (1), 293–346.
(81) Toshima, N.; Shiraishi, Y.; Teranishi, T.; Miyake, M.; Tominaga, T.; Watanabe, H.; Brijoux, W.; Bönnemann, H.; Schmid, G. Various Ligand-Stabilized Metal Nanoclusters as Homogeneous and Heterogeneous Catalysts in the Liquid Phase. *Appl. Organomet. Chem.* **2001**, *15* (3), 178–196.
(82) Petty, J. T.; Fan, C.; Story, S. P.; Sengupta, B.; Iyer, A. S. J.; Prudowsky, Z.; Dickson, R. M. DNA Encapsulation of Ten Silver Atoms Produces a Bright, Modulatable, Near Infrared-Emitting Cluster. *J. Phys. Chem. Lett.* **2010**, *1* (17), 2524–2529.
(83) Sönnichsen, C.; Franzl, T.; Wilk, T.; Von Plessen, G.; Feldmann, J.; Wilson, O.; Mulvaney, P. Drastic Reduction of Plasmon Damping in Gold Nanorods. *Phys. Rev. Lett.* **2002**, *88* (7), 77402.
(84) Liu, Y.; Zhang, M.; Yin, B.; Ye, B. Attomolar Ultrasensitive MicroRNA Detection by DNA-Scaffolded Silver-Nanocluster Probe Based on Isothermal Amplification. *Anal. Chem.* **2012**, *84* (12), 5165–5169.
(85) Petty, J. T.; Sengupta, B.; Story, S. P.; Degtyareva, N. N. DNA Sensing by Amplifying the Number of near-Infrared Emitting, Oligonucleotide-Encapsulated Silver Clusters. *Anal. Chem.* **2011**, *83* (15), 5957–5964.
(86) Guo, W.; Yuan, J.; Dong, Q.; Wang, E. Highly Sequence-Dependent Formation of

Fluorescent Silver Nanoclusters in Hybridized DNA Duplexes for Single Nucleotide Mutation Identification. *J. Am. Chem. Soc.* **2010**, *132* (3), 932–934.
(87) Sengupta, B.; Ritchie, C. M.; Buckman, J. G.; Johnsen, K. R.; Goodwin, P. M.; Petty, J. T. Base-Directed Formation of Fluorescent Silver Clusters. *J. Phys. Chem. C* **2008**, 18776–18782.
(88) Schultz, D.; Gwinn, E. Stabilization of Fluorescent Silver Clusters by RNA Homopolymers and Their DNA Analogs: C,G versus A,T(U) Dichotomy. *Chem. Commun. (Camb).* **2011**, *47* (16), 4715–4717.
(89) Richards, C. I.; Choi, S.; Hsiang, J.-C.; Antoku, Y.; Vosch, T.; Bongiorno, A.; Tzeng, Y.-L.; Dickson, R. M. Oligonucleotide-Stabilized Ag Nanocluster Fluorophores. *J. Am. Chem. Soc.* **2008**, *130* (15), 5038–5039.
(90) Sharma, J.; Yeh, H.-C.; Yoo, H.; Werner, J. H.; Martinez, J. S. A Complementary Palette of Fluorescent Silver Nanoclusters. *Chem. Commun. (Camb).* **2010**, *46* (19), 3280–3282.
(91) Desireddy, A.; Kumar, S.; Guo, J.; Bolan, M. D.; Griffith, W. P.; Bigioni, T. P. Temporal Stability of Magic-Number Metal Clusters: Beyond the Shell Closing Model. *Nanoscale* **2013**, *5* (5), 2036–2044.
(92) O'Neill, P. R.; Velazquez, L. R.; Dunn, D. G.; Gwinn, E. G.; Fygenson, D. K. Hairpins with Poly-C Loops Stabilize Four Types of Fluorescent Ag N : DNA. **2009**, 4229–4233.
(93) Petty, J. T.; Fan, C.; Story, S. P.; Sengupta, B.; Sartin, M.; Hsiang, J.-C.; Perry, J. W.; Dickson, R. M. Optically Enhanced, near-IR, Silver Cluster Emission Altered by Single Base Changes in the DNA Template. *J. Phys. Chem. B* **2011**, *115* (24), 7996–8003.
(94) Han, B.; Wang, E. Oligonucleotide-Stabilized Fluorescent Silver Nanoclusters for Sensitive Detection of Biothiols in Biological Fluids. *Biosens. Bioelectron.* **2011**, *26* (5), 2585–2589.
(95) Farrag, M.; Thämer, M.; Tschurl, M.; Bürgi, T.; Heiz, U. Preparation and Spectroscopic Properties of Monolayer-Protected Silver Nanoclusters. *J. Phys. Chem. C* **2012**, *116* (14), 8034–8043.
(96) Udayabhaskararao, T.; Pradeep, T. New Protocols for the Synthesis of Stable Ag and Au Nanocluster Molecules. *J. Phys. Chem. Lett.* **2013**, *4* (9), 1553–1564.
(97) Desireddy, A.; Conn, B. E.; Guo, J.; Yoon, B.; Barnett, R. N.; Monahan, B. M.; Kirschbaum, K.; Griffith, W. P.; Whetten, R. L.; Landman, U.; et al. Ultrastable Silver Nanoparticles. *Nature* **2013**, *501* (7467), 399–402.
(98) Yang, H.; Wang, Y.; Huang, H.; Gell, L.; Lehtovaara, L.; Malola, S.; Häkkinen, H.; Zheng, N. All-Thiol-Stabilized Ag44 and Au12Ag32 Nanoparticles with Single-Crystal Structures. *Nat. Commun.* **2013**, *4*, 2422.
(99) Yang, H.; Lei, J.; Wu, B.; Wang, Y.; Zhou, M.; Xia, A.; Zheng, L.; Zheng, N. Crystal Structure of a Luminescent Thiolated Ag Nanocluster with an Octahedral Ag6(4+) Core. *Chem. Commun. (Camb).* **2013**, *49* (3), 300–302.
(100) Dhillon, H.; Fournier, R. Geometric Structure of Silver Clusters with and without Adsorbed Cl and Hg. *Comput. Theor. Chem.* **2013**, *1021*, 26–34.
(101) Pérez-Juste, J.; Pastoriza-Santos, I.; Liz-Marzán, L. M.; Mulvaney, P. Gold Nanorods: Synthesis, Characterization and Applications. *Coord. Chem. Rev.* **2005**, *249* (17–18), 1870–1901.

(102) Link, S.; Mohamed, M. B.; El-Sayed, M. A. Simulation of the Optical Absorption Spectra of Gold Nanorods as a Function of Their Aspect Ratio and the Effect of the Medium Dielectric Constant. *J. Phys. Chem. B* **1999**, *103* (16), 3073–3077.
(103) Chen, H.; Shao, L.; Li, Q.; Wang, J. Gold Nanorods and Their Plasmonic Properties. *Chem. Soc. Rev.* **2013**, *42* (7), 2679–2724.
(104) Zhang, Z.-Y.; Zhao, Y.-P. Optical Properties of Helical and Multiring Ag Nanostructures: The Effect of Pitch Height. *J. Appl. Phys.* **2008**, *104* (1), 13517.
(105) Zhang, Z.-Y.; Zhao, Y.-P. The Visible Extinction Peaks of Ag Nanohelixes: A Periodic Effective Dipole Model. *Appl. Phys. Lett.* **2011**, *98* (8), 83102.
(106) Karimova, N. V; Aikens, C. M. Time-Dependent Density Functional Theory Investigation of the Electronic Structure and Chiroptical Properties of Curved and Helical Silver Nanowires. *J. Phys. Chem. A* **2015**, *119* (29), 8163–8173.
(107) Ramazanov, R. R.; Kononov, A. I. Excitation Spectra Argue for Threadlike Shape of DNA-Stabilized Silver Fluorescent Clusters. *J. Phys. Chem. C* **2013**, *117* (36), 18681–18687.
(108) Case, D. A.; Darden, T. A.; Cheatham, III, T. E.; Simmerling, C. L.; Wang, J.; Duke, R. E.; Luo, R.; Walker, R. C.; Zhang, W.; Merz, K. M.; et al. AMBER 12, 2012.
(109) Walker, R. Simulating a Solvated Protein that Contains Non-Standard Residues (Simple Version) http://ambermd.org/tutorials/advanced/tutorial1_orig/.
(110) Humphrey, W.; Dalke, A.; Schulten, K. VMD: Visual Molecular Dynamics. *J. Mol. Graph.* **1996**, *14* (1), 33–38.
(111) Soto-Verdugo, V.; Metiu, H.; Gwinn, E. The Properties of Small Ag Clusters Bound to DNA Bases. *J. Chem. Phys.* **2010**, *132* (19), 195102.
(112) Wu, D. Y.; Hayashi, M.; Shiu, Y. J.; Liang, K. K.; Chang, C. H.; Yeh, Y. L.; Lin, S. H. A Quantum Chemical Study of Bonding Interaction, Vibrational Frequencies, Force Constants, and Vibrational Coupling of Pyridine−M_n (M = Cu, Ag, Au; N = 2−4). *J. Phys. Chem. A* **2003**, *107* (45), 9658–9667.
(113) Lin, F.; Wang, R. Systematic Derivation of AMBER Force Field Parameters Applicable to Zinc-Containing Systems. *J. Chem. Theory Comput.* **2010**, *6* (6), 1852–1870.
(114) Ofir, Y.; Samanta, B.; Rotello, V. M. Polymer and Biopolymer Mediated Self-Assembly of Gold Nanoparticles. *Chem. Soc. Rev.* **2008**, *37* (9), 1814–1825.
(115) Houlton, A.; Pike, A. R.; Angel Galindo, M.; Horrocks, B. R. DNA-Based Routes to Semiconducting Nanomaterials. *Chem. Commun. (Camb).* **2009**, No. 14, 1797–1806.
(116) Liu, J.; Uprety, B.; Gyawali, S.; Woolley, A. T.; Myung, N. V; Harb, J. N. Fabrication of DNA-Templated Te and Bi2Te3 Nanowires by Galvanic Displacement. *Langmuir* **2013**, *29* (35), 11176–11184.
(117) Menzer, S.; Sabat, M.; Lippert, B. Ag (I) Modified Base Pairs Involving Complementary (G , C) and Noncomplementary (A ,) Nucleobases . On the Possible Structural Role of Aqua Ligands in Metal-Modified Nucleobase Pairst. *J. Am. Chem. Soc.* **1992**, *114* (2), 4644–4649.
(118) Hall, M.; Frank, E.; Holmes, G.; Pfahringer, B.; Reutemann, P.; Witten, I. H. The WEKA Data Mining Software. *ACM SIGKDD Explor. Newsl.* **2009**, *11* (1), 10.
(119) Cortes, C.; Vapnik, V. Support-Vector Networks. *Mach. Learn.* **1995**, *20* (3), 273–297.
(120) Bradford, J. R.; Westhead, D. R. Improved Prediction of Protein-Protein Binding Sites

Using a Support Vector Machines Approach. *Bioinformatics* **2005**, *21* (8), 1487–1494.
(121) Brown, M. P. S.; Grundy, W. N.; Lin, D.; Cristianini, N.; Sugnet, C. W.; Furey, T. S.; Ares, M.; Haussler, D. Knowledge-Based Analysis of Microarray Gene Expression Data by Using Support Vector Machines. *Proc. Natl. Acad. Sci.* **2000**, *97* (1), 262–267.
(122) Teng, Y.; Yang, X.; Han, L.; Wang, E. The Relationship between DNA Sequences and Oligonucleotide-Templated Silver Nanoclusters and Their Fluorescence Properties. *Chemistry* **2014**, *20* (4), 1111–1115.
(123) Vens, C.; Rosso, M.-N.; Danchin, E. G. J. Identifying Discriminative Classification-Based Motifs in Biological Sequences. *Bioinformatics* **2011**, *27* (9), 1231–1238.
(124) Dhanda, S. K.; Vir, P.; Raghava, G. P. S. Designing of Interferon-Gamma Inducing MHC Class-II Binders. *Biol. Direct* **2013**, *8* (1), 30.
(125) Cilingir, G.; Lau, A. O. T.; Broschat, S. L. ApicoAMP: The First Computational Model for Identifying Apicoplast-Targeted Transmembrane Proteins in Apicomplexa. *J. Microbiol. Methods* **2013**, *95* (3), 313–319.
(126) Tinland, B.; Pluen, A.; Sturm, J.; Weill, G. Persistence Length of Single-Stranded DNA. *Macromolecules* **1997**, *30* (19), 5763–5765.
(127) Chang, C.-C.; Lin, C.-J. LIBSVM. *ACM Trans. Intell. Syst. Technol.* **2011**, *2* (3), 1–27.
(128) Ding, B.; Deng, Z.; Yan, H.; Cabrini, S.; Zuckermann, R. N.; Bokor, J. Gold Nanoparticle Self-Similar Chain Structure Organized by DNA Origami. *J. Am. Chem. Soc.* **2010**, *132* (10), 3248–3249.
(129) Pal, S.; Deng, Z.; Wang, H.; Zou, S.; Liu, Y.; Yan, H. DNA Directed Self-Assembly of Anisotropic Plasmonic Nanostructures. *J. Am. Chem. Soc.* **2011**, *133* (44), 17606–17609.
(130) Yao, H.; Yi, C.; Tzang, C.-H.; Zhu, J.; Yang, M. DNA-Directed Self-Assembly of Gold Nanoparticles into Binary and Ternary Nanostructures. *Nanotechnology* **2006**, *18* (1), 15102.
(131) Aldaye, F. A.; Sleiman, H. F. Sequential Self-Assembly of a DNA Hexagon as a Template for the Organization of Gold Nanoparticles. *Angew. Chemie Int. Ed.* **2006**, *45* (14), 2204–2209.
(132) Gaiduk, A.; Yorulmaz, M.; Orrit, M. Correlated Absorption and Photoluminescence of Single Gold Nanoparticles. *ChemPhysChem* **2011**, *12* (8), 1536–1541.
(133) Félix, C.; Sieber, C.; Harbich, W.; Buttet, J. Ag8 Fluorescence in Argon. *Phys. Rev. Lett.* **2001**, *86* (14), 2992–2995.
(134) Díez, I.; Ras, R. H. a. Fluorescent Silver Nanoclusters. *Nanoscale* **2011**, *3* (5), 1963.
(135) Yu, J.; Patel, S. A.; Dickson, R. M. In Vitro and Intracellular Production of Peptide-Encapsulated Fluorescent Silver Nanoclusters. *Angew. Chemie - Int. Ed.* **2007**, *46* (12), 2028–2030.
(136) Xu, H.; Suslick, K. S. Sonochemical Synthesis of Highly Fluorescent Ag Nanoclusters. *ACS Nano* **2010**, *4* (6), 3209–3214.
(137) Cathcart, N.; Mistry, P.; Makra, C.; Pietrobon, B.; Coombs, N.; Jelokhani-Niaraki, M.; Kitaev, V. Chiral Thiol-Stabilized Silver Nanoclusters with Well-Resolved Optical Transitions Synthesized by a Facile Etching Procedure in Aqueous Solutions. *Langmuir* **2009**, *25* (10), 5840–5846.
(138) Cathcart, N.; Kitaev, V. Silver Nanoclusters: Single-Stage Scaleable Synthesis of

Monodisperse Species and Their Chirooptical Properties. In *Journal of Physical Chemistry C*; 2010; Vol. 114, pp 16010–16017.
(139) Adhikari, B.; Banerjee, A. Facile Synthesis of Water-Soluble Fluorescent Silver Nanoclusters and HgII Sensing. *Chem. Mater.* **2010**, *22* (15), 4364–4371.
(140) Ledo-Suárez, A.; Rivas, J.; Rodríguez-Abreu, C. F.; Rodríguez, M. J.; Pastor, E.; Hernández-Creus, A.; Oseroff, S. B.; López-Quintela, M. A. Facile Synthesis of Stable Subnanosized Silver Clusters in Microemulsions. *Angew. Chemie - Int. Ed.* **2007**, *46* (46), 8823–8827.
(141) Liu, X.; Atwater, M.; Wang, J.; Huo, Q. Extinction Coefficient of Gold Nanoparticles with Different Sizes and Different Capping Ligands. *Colloids Surfaces B Biointerfaces* **2007**, *58* (1), 3–7.
(142) Baishya, K.; Idrobo, J. C.; Öğüt, S.; Yang, M.; Jackson, K.; Jellinek, J. Optical Absorption Spectra of Intermediate-Size Silver Clusters from First Principles. *Phys. Rev. B* **2008**, *78* (7), 75439.
(143) Harb, M.; Rabilloud, F.; Simon, D. Optical Absorption of Silver Clusters: A Study of the Effective Potential Core Size. *Chem. Phys. Lett.* **2009**, *476* (4–6), 186–190.
(144) Huang, Z.; Tao, Y.; Pu, F.; Ren, J.; Qu, X. Versatile Logic Devices Based on Programmable DNA-Regulated Silver-Nanocluster Signal Transducers. *Chemistry* **2012**, *18* (21), 6663–6669.
(145) Zhang, L.; Zhu, J.; Guo, S.; Li, T.; Li, J.; Wang, E. Photoinduced Electron Transfer of DNA/Ag Nanoclusters Modulated by G-Quadruplex/hemin Complex for the Construction of Versatile Biosensors. *J. Am. Chem. Soc.* **2013**, *135* (7), 2403–2406.
(146) Li, T.; Zhang, L.; Ai, J.; Dong, S.; Wang, E. Ion-Tuned DNA / Ag Fluorescent Nanoclusters as Versatile Logic Device. *ACS Nano* **2011**, *5* (8), 6334–6338.
(147) Han, B.; Wang, E. DNA-Templated Fluorescent Silver Nanoclusters. *Anal. Bioanal. Chem.* **2012**, *402* (1), 129–138.
(148) Driehorst, T.; O'Neill, P.; Goodwin, P. M.; Pennathur, S.; Fygenson, D. K. Distinct Conformations of DNA-Stabilized Fluorescent Silver Nanoclusters Revealed by Electrophoretic Mobility and Diffusivity Measurements. *Langmuir* **2011**, *27* (14), 8923–8933.
(149) Oemrawsingh, S. S. R.; Markešević, N.; Gwinn, E. G.; Eliel, E. R.; Bouwmeester, D. Spectral Properties of Individual DNA-Hosted Silver Nanoclusters at Low Temperatures. *J. Phys. Chem. C* **2012**, *116* (48), 25568–25575.
(150) Gutierrez, M.; Henglein, A. Formation of Colloidal Silver By" push-Pull" reduction of Silver (1+). *J. Phys. Chem.* **1993**, *97* (44), 11368–11370.
(151) Sharma, J.; Yeh, H.-C.; Yoo, H.; Werner, J. H.; Martinez, J. S. Silver Nanocluster Aptamers: In Situ Generation of Intrinsically Fluorescent Recognition Ligands for Protein Detection. *Chem. Commun. (Camb).* **2011**, *47*, 2294–2296.
(152) Förster, T. Zwischenmolekulare Energiewanderung Und Fluoreszenz (Intermolecular Energy Migration and Fluorescence, Translated by Knox RS). *Ann. Phys.* **1948**, *437*, 55–75.
(153) Förster, T. 10th Spiers Memorial Lecture Transfer Mechanisms of Electronic Excitation. *Discuss. Faraday Soc.* **1959**, *27*, 7–17.
(154) Markham, N. R.; Zuker, M. DINAMelt Web Server for Nucleic Acid Melting Prediction. *Nucleic Acids Res.* **2005**, *33* (Web Server issue), W577-81.
(155) Markham, N. R.; Zuker, M. UNAFold: Software for Nucleic Acid Folding and

Hybridization. In *Bioinformatics, Volume II: Structure, Function, and Applications*; Keith, J. M., Ed.; Methods in Molecular Biology™; Humana Press: Totowa, NJ, 2008; Vol. 453, pp 3–31.
(156) Stellwagen, E.; Muse, J. M.; Stellwagen, N. C. Monovalent Cation Size and DNA Conformational Stability. *Biochemistry* **2011**, *50* (15), 3084–3094.
(157) Clegg, R. M. [18] Fluorescence Resonance Energy Transfer and Nucleic Acids. *Methods Enzymol.* **1992**, *211*, 353–388.
(158) Johnson, H. E.; Aikens, C. M. Electronic Structure and TDDFT Optical Absorption Spectra of Silver Nanorods †. *J. Phys. Chem. A* **2009**, *113* (16), 4445–4450.
(159) Cui, Q.; Ma, K.; Shao, Y.; Xu, S.; Wu, F.; Liu, G.; Teramae, N.; Bao, H. Gap Site-Specific Rapid Formation of Fluorescent Silver Nanoclusters for Label-Free DNA Nucleobase Recognition. *Anal. Chim. Acta* **2012**, *724*, 86–91.
(160) Ma, K.; Cui, Q.; Liu, G.; Wu, F.; Xu, S.; Shao, Y. DNA Abasic Site-Directed Formation of Fluorescent Silver Nanoclusters for Selective Nucleobase Recognition. *Nanotechnology* **2011**, *22* (30), 305502.
(161) Zhang, M.; Guo, S.-M.; Li, Y.-R.; Zuo, P.; Ye, B.-C.; Zhang, M.; Yin, B. C.; Wang, X. F.; Ye, B. C.; Zhang, M.; et al. A Label-Free Fluorescent Molecular Beacon Based on DNA-Templated Silver Nanoclusters for Detection of Adenosine and Adenosine Deaminase. *Chem. Commun.* **2012**, *48* (44), 5488.
(162) Potier, N.; Van Dorsselaer, A.; Cordier, Y.; Roch, O.; Bischoff, R. Negative Electrospray Ionization Mass Spectrometry of Synthetic and Chemically Modified Oligonucleotides. *Nucleic Acids Res.* **1994**, *22* (19), 3895–3903.
(163) Guo, W.; Orbach, R.; Mironi-Harpaz, I.; Seliktar, D.; Willner, I. Fluorescent DNA Hydrogels Composed of Nucleic Acid-Stabilized Silver Nanoclusters. *Small* **2013**, *9* (22), 3748–3752.
(164) Murphy, M. C.; Rasnik, I.; Cheng, W.; Lohman, T. M.; Ha, T. Probing Single-Stranded DNA Conformational Flexibility Using Fluorescence Spectroscopy. *Biophys. J.* **2004**, *86* (4), 2530–2537.
(165) Iqbal, A.; Arslan, S.; Okumus, B.; Wilson, T. J.; Giraud, G.; Norman, D. G.; Ha, T.; Lilley, D. M. J. Orientation Dependence in Fluorescent Energy Transfer between Cy3 and Cy5 Terminally Attached to Double-Stranded Nucleic Acids. *Proc. Natl. Acad. Sci. U. S. A.* **2008**, *105* (32), 11176–11181.
(166) Ko, S. H.; Du, K.; Liddle, J. A. Quantum-Dot Fluorescence Lifetime Engineering with DNA Origami Constructs. *Angew. Chem. Int. Ed. Engl.* **2013**, *52* (4), 1193–1197.
(167) Lee, Y.-J.; Schade, N. B.; Sun, L.; Fan, J. A.; Bae, D. R.; Mariscal, M. M.; Lee, G.; Capasso, F.; Sacanna, S.; Manoharan, V. N.; et al. Ultrasmooth, Highly Spherical Monocrystalline Gold Particles for Precision Plasmonics. *ACS Nano* **2013**, *7* (12), 11064–11070.
(168) Guidez, E. B.; Aikens, C. M. Diameter Dependence of the Excitation Spectra of Silver and Gold Nanorods. *J. Phys. Chem. C* **2013**, *117* (23), 12325–12336.
(169) Yu, Y.; Luo, Z.; Chevrier, D. M.; Leong, D. T.; Zhang, P.; Jiang, D.; Xie, J. Identification of a Highly Luminescent Au22(SG)18 Nanocluster. *J. Am. Chem. Soc.* **2014**, *136* (4), 1246–1249.
(170) Yoon, B.; Luedtke, W. D.; Barnett, R. N.; Gao, J.; Desireddy, A.; Conn, B. E.; Bigioni, T. P.; Landman, U. Hydrogen-Bonded Structure and Mechanical Chiral Response of a Silver Nanoparticle Superlattice. *Nat. Mater.* **2014**, *13* (8), 807–811.

(171) Niihori, Y.; Matsuzaki, M.; Pradeep, T.; Negishi, Y. Separation of Precise Compositions of Noble Metal Clusters Protected with Mixed Ligands. *J. Am. Chem. Soc.* **2013**, *135* (13), 4946–4949.
(172) Xu, L.; Ma, W.; Wang, L.; Xu, C.; Kuang, H.; Kotov, N. A. Nanoparticle Assemblies: Dimensional Transformation of Nanomaterials and Scalability. *Chem. Soc. Rev.* **2013**, *42* (7), 3114–3126.
(173) Orbach, R.; Guo, W.; Wang, F.; Lioubashevski, O.; Willner, I. Self-Assembly of Luminescent Ag Nanocluster-Functionalized Nanowires. *Langmuir* **2013**, *29* (42), 13066–13071.
(174) Schiffels, D.; Liedl, T.; Fygenson, D. K. Nanoscale Structure and Microscale Stiffness of DNA Nanotubes. *ACS Nano* **2013**, *7* (8), 6700–6710.
(175) Schiffels, D. Design, Characterization and Functionalization of DNA Materials, Ludwig-Maximilians-Universität München, 2013.
(176) Wiggins, P. A.; van der Heijden, T.; Moreno-Herrero, F.; Spakowitz, A.; Phillips, R.; Widom, J.; Dekker, C.; Nelson, P. C. High Flexibility of DNA on Short Length Scales Probed by Atomic Force Microscopy. *Nat. Nanotechnol.* **2006**, *1* (2), 137–141.
(177) Obliosca, J. M.; Liu, C.; Yeh, H.-C. Fluorescent Silver Nanoclusters as DNA Probes. *Nanoscale* **2013**, *5* (18), 8443–8461.
(178) Antoku, Y.; Hotta, J.; Mizuno, H.; Dickson, R. M.; Hofkens, J.; Vosch, T. Transfection of Living HeLa Cells with Fluorescent Poly-Cytosine Encapsulated Ag Nanoclusters. *Photochem. Photobiol. Sci.* **2010**, *9* (5), 716–721.
(179) Wu, Z.; Jin, R. On the Ligand's Role in the Fluorescence of Gold Nanoclusters. *Nano Lett.* **2010**, *10* (7), 2568–2573.
(180) Wang, S.; Meng, X.; Das, A.; Li, T.; Song, Y.; Cao, T.; Zhu, X.; Zhu, M.; Jin, R. A 200-Fold Quantum Yield Boost in the Photoluminescence of Silver-Doped AgxAu25-X Nanoclusters: The 13th Silver Atom Matters. *Angew. Chemie - Int. Ed.* **2014**, *53* (9), 2376–2380.
(181) Suppan, P. Invited Review Solvatochromic Shifts: The Influence of the Medium on the Energy of Electronic States. *J. Photochem. Photobiol. A Chem.* **1990**, *50* (3), 293–330.
(182) Su, Y.-T.; Lan, G.-Y.; Chen, W.-Y.; Chang, H.-T. Detection of Copper Ions through Recovery of the Fluorescence of DNA-Templated Copper/silver Nanoclusters in the Presence of Mercaptopropionic Acid. *Anal. Chem.* **2010**, *82* (20), 8566–8572.
(183) Ma, K.; Shao, Y.; Cui, Q.; Wu, F.; Xu, S.; Liu, G. Base-Stacking-Determined Fluorescence Emission of DNA Abasic Site-Templated Silver Nanoclusters. *Langmuir* **2012**, *28* (43), 15313–15322.
(184) Zhang, L.; Liang, R.-P.; Xiao, S.-J.; Bai, J.-M.; Zheng, L.-L.; Zhan, L.; Zhao, X.-J.; Qiu, J.-D.; Huang, C.-Z. DNA-Templated Ag Nanoclusters as Fluorescent Probes for Sensing and Intracellular Imaging of Hydroxyl Radicals. *Talanta* **2014**, *118*, 339–347.
(185) Lippert, E. Dipolmoment Nnd Elektronenstruktur von Angereten Molekulen. *Zeitschrift fur Naturforsch. Part A- Astrophys. Phys. und Phys. Chemie* **1955**, *10* (7), 541–545.
(186) Mataga, N.; Kaifu, Y.; Koizumi, M. Solvent Effects upon Fluorescence Spectra and the Dipolemoments of Excited Molecules. *Bull. Chem. Soc. Jpn.* **1956**, *29* (4), 465–470.
(187) Onsager, L. Electric Moments of Molecules in Liquids. *J. Am. Chem. Soc.* **1936**, *58*

(8), 1486–1493.
(188) Díez, I.; Ras, R. H. A.; Kanyuk, M. I.; Demchenko, A. P. On Heterogeneity in Fluorescent Few-Atom Silver Nanoclusters. *Phys. Chem. Chem. Phys.* **2013**, *15* (3), 979–985.
(189) *CRC Handbook of Chemistry and Physics*, 95th ed.; Haynes, W. M., Ed.; CRC Press: Baton Rouge, FL, 2014.
(190) Akerlof, G. Dielectric Constants of Some Organic Solvent-Water Mixtures at Various Temperatures. *J. Am. Chem. Soc.* **1932**, *54* (11), 4125–4139.
(191) Lakowicz, J. R. *Principles of Fluorescence Spectroscopy*, 2nd ed.; Kluwer Academic/Plenum Publishers: New York, NY, 1999.
(192) Qu, F.; Dou, L. L.; Li, N. B.; Luo, H. Q. Solvatofluorochromism of Polyethyleneimine-Encapsulated Ag Nanoclusters and Their Concentration-Dependent Fluorescence. *J. Mater. Chem. C* **2013**, *1* (25), 4008.
(193) Marsh, D. Reaction Fields in the Environment of Fluorescent Probes: Polarity Profiles in Membranes. *Biophys. J.* **2009**, *96* (7), 2549–2558.
(194) Ooshika, Y. Absorption Spectra of Dyes in Solution. *J. Phys. Soc. Japan* **1954**, *9* (4), 594–602.
(195) Polewski, K. Spectral Properties of Adrenaline in Micellar Environment. *Physiol. Chem. Phys. Med. NMR* **2003**, *35* (1), 13–25.
(196) Zoon, P. D.; Brouwer, A. M. A Push-Pull Aromatic Chromophore with a Touch of Merocyanine. *Photochem. Photobiol. Sci.* **2009**, *8* (3), 345–353.
(197) Zhang, Q.; Luo, J.; Ye, L.; Wang, H.; Huang, B.; Zhang, J.; Wu, J.; Zhang, S.; Tian, Y. Design, Synthesis, Linear and Nonlinear Photophysical Properties and Biological Imaging Application of a Novel Λ-Type Pyrimidine-Based Thiophene Derivative. *J. Mol. Struct.* **2014**, *1074*, 33–42.
(198) Lee, C.; Takagi, C.; Truong, T.; Chen, Y.-C.; Ostafin, A. Luminescent Au Nanoparticles with a pH-Responsive Nanoparticle-Supported Molecular Brush. *J. Phys. Chem. C* **2010**, *114* (29), 12459–12468.
(199) Chalikian, T. V; Sarvazyan, A. P.; Plum, G. E.; Breslauer, K. J. Influence of Base Composition, Base Sequence, and Duplex Structure on DNA Hydration: Apparent Molar Volumes and Apparent Molar Adiabatic Compressibilities of Synthetic and Natural DNA Duplexes at 25 Degrees C. *Biochemistry* **1994**, *33* (9), 2394–2401.
(200) Dixit, S. B.; Mezei, M.; Beveridge, D. L. Studies of Base Pair Sequence Effects on DNA Solvation Based on All-Atom Molecular Dynamics Simulations. *J. Biosci.* **2012**, *37* (3), 399–421.
(201) Yildirim, A.; Sharma, M.; Varner, B. M.; Fang, L.; Feig, M. Conformational Preferences of DNA in Reduced Dielectric Environments. *J. Phys. Chem. B* **2014**, *118* (37), 10874–10881.
(202) Sprous, D.; Young, M. a.; Beveridge, D. L. Molecular Dynamics Studies of the Conformational Preferences of a DNA Double Helix in Water and an Ethanol / Water Mixture : Theoretical Considerations of the A ⇔ B Transition. **1998**, *102* (98), 4658–4667.
(203) Gell, L.; Kulesza, A.; Petersen, J.; Röhr, M. I. S.; Mitrić, R.; Bonačić-Koutecký, V. Tuning Structural and Optical Properties of Thiolate-Protected Silver Clusters by Formation of a Silver Core with Confined Electrons. *J. Phys. Chem. C* **2013**, *117* (28), 14824–14831.

(204) Bastos, M.; Castro, V.; Mrevlishvili, G.; Teixeira, J. Hydration of Ds-DNA and Ss-DNA by Neutron Quasielastic Scattering. *Biophys. J.* **2004**, *86* (6), 3822–3827.
(205) Dixit, S.; Crain, J.; Poon, W. C. K.; Finney, J. L.; Soper, A. K. Molecular Segregation Observed in a Concentrated Alcohol-Water Solution. *Nature* **2002**, *416* (6883), 829–832.
(206) Copp, S. M.; Schultz, D.; Swasey, S. M.; Faris, A.; Gwinn, E. G. Cluster Plasmonics: Dielectric and Shape Effects on DNA-Stabilized Silver Clusters. *Nano Lett.* **2016**, *16* (6), 3594–3599.
(207) Stockman, M. I. Nanoplasmonics : The Physics behind the Applications. *Phys. Today* **2011**, *64* (2), 39–44.
(208) Jain, P. K.; Eustis, S.; El-Sayed, M. A. Plasmon Coupling in Nanorod Assemblies: Optical Absorption, Discrete Dipole Approximation Simulation, and Exciton-Coupling Model. *J. Phys. Chem. B* **2006**, *110* (37), 18243–18253.
(209) Zuloaga, J.; Prodan, E.; Nordlander, P. Quantum Plasmonics: Optical Properties and Tunability of Metallic Nanorods. *ACS Nano* **2010**, *4* (9), 5269–5276.
(210) Ding, F.; Guidez, E. B.; Aikens, C. M.; Li, X. Quantum Coherent Plasmon in Silver Nanowires: A Real-Time TDDFT Study. *J. Chem. Phys.* **2014**, *140* (24), 244705.
(211) Guidez, E. B.; Aikens, C. M. Quantum Mechanical Origin of the Plasmon : From Molecular Systems to Nanoparticles. *Nanoscale* **2014**, *6*, 11512–11527.
(212) Bernadotte, S.; Evers, F.; Jacob, C. R. Plasmons in Molecules. *J. Phys. Chem. C* **2013**, *117* (4), 1863–1878.
(213) Nilius, N.; Wallis, T. M.; Ho, W. Development of One-Dimensional Band Structure in Artificial Gold Chains. *Science* **2002**, *297* (5588), 1853–1856.
(214) Yu, Y.; Luo, Z.; Chevrier, D. M.; Leong, D. T.; Zhang, P.; Jiang, D.; Xie, J. Identification of a Highly Luminescent Au22(SG)18 Nanocluster. *JACS* **2014**, *22*, 5–8.
(215) Pastor, N. The B- to A-DNA Transition and the Reorganization of Solvent at the DNA Surface. *Biophys. J.* **2005**, *88* (5), 3262–3275.
(216) Lisinetskaya, P. G.; Mitrić, R. *Ab Initio* Simulations of Light Propagation in Silver Cluster Nanostructures. *Phys. Rev. B* **2014**, *89* (3), 35433.
(217) Townsend, E.; Bryant, G. W. Which Resonances in Small Metallic Nanoparticles Are Plasmonic? *J. Opt.* **2014**, *16* (11), 114022.
(218) Mie, G. Beiträge Zur Optik Trüber Medien, Speziell Kolloidaler Metallösungen. *Ann. Phys.* **1908**, *330* (3), 377–445.
(219) Gans, R. Über Die Form Ultramikroskopischer Goldteilchen. *Ann. Phys.* **1912**, *342* (5), 881–900.
(220) Malola, S.; Lehtovaara, L.; Häkkinen, H. A DFT Study of Linear Gold-Thiolate Superclusters Absorbing in the Therapeutic NIR Window. *J. Phys. Chem. Lett.* **2014**, *5* (8), 1329–1334.
(221) Krauter, C. M.; Bernadotte, S.; Jacob, C. R.; Pernpointner, M.; Dreuw, A. Identification of Plasmons in Molecules with Scaled Ab Initio Approaches. *J. Phys. Chem. C* **2015**, *119* (43), 24564–24573.
(222) de Dormale, B.; Truong, V.-V. Nonlinear Optical Properties of Spheroidal Metallic Inclusions in a Dielectric Medium. *ISRN Nanotechnol.* **2011**, *2011*, 1–9.
(223) Johnson, P. B.; Christy, R. W. Optical Constants of the Noble Metals. *Phys. Rev. B* **1972**, *6* (12), 4370–4379.
(224) Mock, J. J.; Smith, D. R.; Schultz, S. Local Refractive Index Dependence of Plasmon

Resonance Spectra from Individual Nanoparticles. *Nano Lett.* **2003**, *3* (4), 485–491.
(225) Sekhon, J. S.; Verma, S. S. Tunable Plasmonic Properties of Silver Nanorods for Nanosensing Applications. *J. Mater. Sci.* **2012**, *47* (4), 1930–1937.
(226) McMahon, J. M.; Gray, S. K.; Schatz, G. C. Optical Properties of Nanowire Dimers with a Spatially Nonlocal Dielectric Function. *Nano Lett.* **2010**, *10* (9), 3473–3481.
(227) Young, M. A.; Jayaram, B.; Beveridge, D. L. Local Dielectric Environment of B-DNA in Solution: Results from a 14 Ns Molecular Dynamics Trajectory. *J. Phys. Chem. B* **1998**, *102* (39), 7666–7669.
(228) Senapati, S.; Chandra, A. Molecular Dynamics Simulations of Simple Dipolar Liquids in Spherical Cavity: Effects of Confinement on Structural, Dielectric, and Dynamical Properties. *J. Chem. Phys.* **1999**, *111* (3), 1223.
(229) Cuervo, A.; Dans, P. D.; Carrascosa, J. L.; Orozco, M.; Gomila, G.; Fumagalli, L. Direct Measurement of the Dielectric Polarization Properties of DNA. *Proc. Natl. Acad. Sci. U. S. A.* **2014**, *111* (35), E3624-30.
(230) Lee, K.; El-sayed, M. A. Gold and Silver Nanoparticles in Sensing and Imaging : Sensitivity of Plasmon Response to Size , Shape , and Metal Composition Gold and Silver Nanoparticles in Sensing and Imaging : Sensitivity of Plasmon Response to Size , Shape , and Metal Composition. *J. Phys. Chem. B* **2006**, *110* (39), 19220–19225.
(231) Al-Sherbini, A. S. A. M. Thermal Instability of Gold Nanorods in Micellar Solution of Water/glycerol Mixtures. *Colloids Surfaces A Physicochem. Eng. Asp.* **2004**, *246* (1–3), 61–69.
(232) Chen, H.; Kou, X.; Yang, Z.; Ni, W.; Wang, J. Shape- and Size-Dependent Refractive Index Sensitivity of Gold Nanoparticles. *Langmuir* **2008**, *24* (10), 5233–5237.
(233) Mayer, K. M.; Lee, S.; Liao, H.; Rostro, B. C.; Fuentes, A.; Scully, P. T.; Nehl, C. L.; Hafner, J. H. A Label-Free Immunoassay Based upon Localized Surface Plasmon Resonance of Gold Nanorods. *ACS Nano* **2008**, *2* (4), 687–692.
(234) Malinsky, M. D.; Kelly, K. L.; Schatz, G. C.; Van Duyne, R. P. Chain Length Dependence and Sensing Capabilities of the Localized Surface Plasmon Resonance of Silver Nanoparticles Chemically Modified with Alkanethiol Self-Assembled Monolayers. *J. Am. Chem. Soc.* **2001**, *123* (7), 1471–1482.
(235) Jensen, T.; Kelly, K. L.; Lazarides, A.; Schatz, G. C. Electrodynamics of Noble Metal Nanoparticles and Nanoparticle Clusters. *J. Clust. Sci.* **1999**, *10* (2), 295–317.
(236) Bonner, G.; Klibanov, A. M. Structural Stability of DNA in Nonaqueous Solvents. *Biotechnol. Bioeng.* **2000**, *68* (3), 339–344.
(237) Cheatham, T. E.; Kollman, P. A. Observation of the A-DNA to B-DNA Transition during Unrestrained Molecular Dynamics in Aqueous Solution. *J. Mol. Biol.* **1996**, *259* (3), 434–444.
(238) Feig, M.; Montgomery Pettitt, B. A Molecular Simulation Picture of DNA Hydration around A- and B-DNA. *Biopolymers* **1998**, *48* (4), 199–209.
(239) Bardeen, J.; Brattain, W. H. The Transistor, A Semi-Conductor Triode. *Phys. Rev.* **1948**, *74* (2), 230–231.
(240) Williams, E. D. Environmental Impacts of Microchip Manufacture. In *Thin Solid Films*; 2004; Vol. 461, pp 2–6.
(241) Whitesides, G. M.; Lipomi, D. J.; Gennes, P. G. de; Zhirnov, V. V.; Cavin, R. K.; Choi, H.; Mody, C. C. M.; Service, R. F.; Heath, J. R.; Stoddart, J. F.; et al. Soft Nanotechnology: “structure”vs.“function.” *Faraday Discuss.* **2009**, *143* (0), 373.

(242) Obliosca, J. M.; Babin, M. C.; Liu, C.; Liu, Y.-L.; Chen, Y.-A.; Batson, R. A.; Ganguly, M.; Petty, J. T.; Yeh, H.-C. A Complementary Palette of NanoCluster Beacons. *ACS Nano* **2014**, *8* (10), 10150–10160.
(243) Chen, Y.-A.; Obliosca, J. M.; Liu, Y.-L.; Liu, C.; Gwozdz, M. L.; Yeh, H.-C. NanoCluster Beacons Enable Detection of a Single N(6)-Methyladenine. *J. Am. Chem. Soc.* **2015**.
(244) Del Bonis-O'Donnell, J. T.; Vong, D.; Pennathur, S.; Fygenson, D. K.; Wetmur, J. G.; Tyagi, S.; Kramer, F. R.; Wang, K.; Tang, Z.; Yang, C. J.; et al. A Universal Design for a DNA Probe Providing Ratiometric Fluorescence Detection by Generation of Silver Nanoclusters. *Nanoscale* **2016**, *8* (30), 14489–14496.
(245) Valeur, B.; Berberan-Santos, M. N. *Molecular Fluorescence: Principles and Applications*, 2nd ed.; John Wiley & Sons: Weinheim, Germany, 2012.